Gerhard Steger

Experimental and numerical investigations of unsaturated soils with application to tunnelling under compressed air

Dissertation

Eingereicht an der Fakultät für Bauingenieurwissenschaften
der Technischen Universität Graz

Begutachter:

O.Univ.-Prof. Dipl.-Ing. Dr.techn. Stephan Semprich
Institut für Bodenmechanik und Grundbau
Technische Universität Graz

Prof. Dr. Eurípedes do Amaral Vargas Júnior
Departamento de Engenharia Civil
Pontifícia Universidade Católica do Rio de Janeiro

Graz, Juli 2010

Foreword

The present thesis is closely related to the long-standing field of research "tunnelling under compressed air" of the Institute of Soil Mechanics and Foundation Engineering of the Graz University of Technology. The advances in experimental and theoretical unsaturated soil mechanics during the past decade allow for a sophisticated analysis of this complex tunnelling method. However, specific experimental investigation techniques and numerical programs are necessary for this purpose. Together with already available research results the present thesis contributes a further step towards a comprehensive framework, which will prospectively allow for dealing with the relevant issues of a compressed air tunnel advance: air losses, surface settlements, tunnel face stability and blow outs. Beyond, the results of the conducted research are applicable to other problems in geotechnical engineering and geo-environmental engineering, which involve unsaturated soils.

I am grateful to Prof. Dr. S. Semprich for the encouragement and supervision of my PhD study. Prof. Semprich's wide knowledge and experience in the field of geotechnical engineering have been of great benefit to me.

I would like to thank Prof. Dr. E.A. Vargas for co-supervising me throughout my research work. My research stays under Prof. Vargas' guidance at the PUC Rio de Janeiro have been an outstanding scientific and personal experience.

DI J. Herdina, ÖBB Infrastruktur AG, is gratefully acknowledged for providing the data of the construction lot Tunnel Fritzens, Unterinntal in Tyrol.

I am also grateful to DI Morales-Calderon and Mr. P. Pucko for continuously supporting the unsaturated triaxial tests and other laboratory works. I would also like to thank my colleagues DI C. Lackner and DI F. Tschuchnigg for the cordial way of working together.

Abstract

Experimental and numerical investigations of unsaturated soils with application to tunnelling under compressed air

In the first part of the thesis, the development and application of a new two-phase flow field test are described. In particular, the test is meant to derive constitutive-model parameters for site applications with predominant air flow, e.g. compressed air tunnelling or remediation by soil venting. Initially, numerical simulations of the test performance and inverse modelling examples with synthetic data sets are conducted. Finally, three field tests are executed in silty-sandy soils. The installation of the experimental set-up, the measurement results and the inverse modelling of the tests are described.

In the second part of the dissertation, the correctness of unsaturated permeability data obtained by the steady-state method is investigated. In order to gain more knowledge of the distribution of matric suction and hydraulic permeability across the specimen, numerical simulations of steady-state tests are conducted. The obtained results are used to determine the error which is caused by assigning the measured permeability values to the linear mean-value of the suction. Finally, three different methods for an improved interpretation of steady-state derived permeability values are developed respectively applied and evaluated.

In the third part of the thesis, the mechanical behaviour of unsaturated soils is reviewed and investigated. A double-walled triaxial apparatus for unsaturated soils is designed and installed in the laboratory. The initial problems of the testing device and the measures in order to overcome the deficiencies are described. The double-walled cell is calibrated against different cell pressures and temperatures in order to improve the accuracy of volume change measurements of the soil specimens. A testing programme, which incorporates the investigation of the influence of hydraulic hysteresis, is designed. The first results of the testing series on a fine-sandy silt are presented.

As an application of unsaturated soil mechanics to civil engineering, the analysis and prediction of the air losses of the Tunnel Fritzens by means of numerical two-phase flow simulations are presented. The measured air losses during the advance of the first sections of the top-heading are used to back-calculate the permeability values of the soil and the artificial materials (e.g. shotcrete). Thereafter, various measures in order to reduce the air losses in the course of the further tunnel advance are elaborated. Additionally, a prediction of the air losses for the upcoming bench excavation is conducted.

Kurzfassung

Experimentelle und numerische Untersuchungen von teilgesättigten Böden mit Anwendung auf den Tunnelbau unter Druckluft

Im ersten Teil der Arbeit werden die Entwicklung und die Ausführung eines neuartigen Zweiphasenströmungs-Feldversuches beschrieben. Der Feldversuch ist im Besonderen für die Bestimmung von Parametern für Strömungsprobleme mit vorherrschender Luftphase vorgesehen, wie zum Beispiel beim Tunnelbau unter Druckluft oder beim Bodenbelüftungsverfahren. Zunächst werden theoretische numerische Simulationen des Feldversuches sowie inverse Modellierungen mit künstlich erzeugten Messdaten durchgeführt. In weiterer Folge werden drei Feldversuche in schluffig sandigen Böden ausgeführt und die zugehörigen Strömungsparameter durch inverse Modellierung berechnet.

Im zweiten Teil der Dissertation werden stationäre Durchlässigkeitsversuche an teilgesättigten Böden untersucht. Um vertiefte Kenntnisse der Kapillarspannungs- und Durchlässigkeitsverteilung in der Probe zu gewinnen, werden numerische Simulationen dieser Versuche durchgeführt. Die Ergebnisse werden im Weiteren dazu benutzt, um den Fehler, der bei der üblichen Zuweisung der gemessenen Durchlässigkeit zum Mittelwert der Kapillarspannung verursacht wird, zu quantifizieren. Danach werden drei verschiedene Methoden für eine verbesserte Dateninterpretation entwickelt bzw. vorgestellt und bewertet.

Im dritten Teil der Arbeit wird das mechanische Verhalten von teilgesättigten Böden untersucht. Eine entsprechende Triaxialanlage mit Doppelzelle wird dazu im Labor installiert. Die anfänglichen Probleme und deren Behebung bzw. Verbesserungen der Anlage werden beschrieben. Die Triaxialzelle wird gegen verschiedene Drücke und Temperaturwerte kalibriert. Ein Testprogramm, welches auch die Untersuchung des Einflusses von hydraulischer Hysterese vorsieht, wird vorgestellt. Die Ergebnisse der ersten Triaxialversuche an einem fein sandigen Schluff werden beschrieben.

Als Anwendungsbeispiel der Forschung auf praktische Problemstellungen wird die Analyse und Prognose von Luftverlusten beim Tunnel Fritzens vorgestellt. Dabei werden zwei- und dreidimensionale numerische Simulationen der auftretenden Zweiphasenströmung durchgeführt. Die Berechnungsergebnisse dienen unter anderem zur Erarbeitung von konstruktiven Maßnahmen zur Reduktion der Luftverluste im weiteren Vortriebsverlauf.

Table of contents

List of symbols and abbreviations

Small letters

b	[-]	vector containing actual values of estimated parameters
e	[-]	void ratio
h_c	[m]	capillary pressure head
$h_{w,1}$	[m]	water pressure head at first end face
$h_{w,2}$	[m]	water pressure head at second end face
i	[-]	discrete point in time or space
k(s)	[m/s]	unsaturated hydraulic conductivity as a function of suction
k_{perm}	[m/s]	conductivity obtained by a permeameter test
k_{plate}	[m/s]	conductivity of ceramic plates
k_{rnw}	[-]	relative permeability of non-wetting fluid
$k_{r\beta}$	[-]	relative permeability of phase β
k_{rw}	[-]	relative permeability of wetting fluid
$k_{S\&T}$	[m/s]	conductivity obtained by the Smiles and Towner method
k_{true}	[m/s]	true unsaturated water conductivity
k_{ws}	[m/s]	saturated water conductivity
l	[m]	length of soil specimen
l_i	[m]	length of specimen respectively ceramic plates
m	[-]	number of actual observations (in the objective function)
m	[-]	fitting parameter (in a water retention or permeability model)
m_{perm}	[-]	fitting parameter for permeability function
m_{ret}	[-]	fitting parameter for water retention function
m_y	[-]	mean value of weighted observations
$m_{y'}$	[-]	simulated equivalent to m_y
n	[-]	iteration counter (in inverse modelling)
n	[-]	pore number (soil property)
n	[-]	normal vector on the surface element Γ_n
p_a	[kPa]	air pressure
p_w	[kPa]	water pressure
$p_{w,b}$	[kPa]	hydrostatic pressure at the base of the tunnel
p_0*	[kPa]	isotropic yield stress
q	[-]	imposed water flux (in permeameter tests)
q	[kPa]	deviatoric stress (in triaxial tests)
q	[kg/s]	flow in sinks and sources (in multi-phase flow modelling)
$q_{a,max}$	[m³/min]	maximum air loss rate
q_a	[l/min]	air injection rate
q_w	[l/min]	water infiltration rate

r	[m]	length of centrifuge arm
r_1	[m]	radius of the meniscus surface
r_2	[m]	radius of the liquid bridge at the neck
s	[kPa]	suction respectively matric suction
s_b	[kPa]	suction at the base of the specimen
s_{mean}	[kPa]	linear mean value of suction
s_t	[kPa]	suction at the top of the specimen
t_s	[N/m]	surface tension of water
u_a	[kPa]	air pressure
u'_a	[kPa/m]	excess pore pressure gradient of air
$\mathbf{u}_b$	[m/s]	Darcy-velocity vector
u_w	[kPa]	water pressure
u'_w	[kPa/m]	excess pore pressure gradient of water
v	[m/s]	Darcy velocity (in flow problems)
v	[-]	specific volume (in triaxial tests)
v_a	[m/s]	seepage velocity of air
v_w	[m/s]	seepage velocity of water
y_{hi}	[-]	i^{th} pressure observation being matched by the regression
y'_{hi}	[-]	simulated pressure corresponding to the i^{th} pressure observation
y_i	[-]	i^{th} observation value
y'_i	[-]	i^{th} simulated value corresponding to i^{th} observation value
y_{pk}	[-]	k^{th} prior information included in the regression
y'_{pk}	[-]	simulated value corresponding to the k^{th} prior information
y_{qj}	[-]	j^{th} flow observation being matched by the regression
y'_{qj}	[-]	simulated flow corresponding to the j^{th} flow observation
x	[-]	distance along the specimen
z	[-]	number of consecutive iterations

Capital letters

A	[m²]	cross section of the specimen
C^{ep}_{ijhk}	[-]	elasto-plastic constitutive matrix
C^{s}_{ijhk}	[-]	constitutive matrix that relates suction increments to strain increments
F	[kg/s]	mass or heat flux
H	[m]	potential at a distance x along the specimen
H_0	[m]	potential at $x = 0$
H_l	[m]	potential at $x = l$
K_i	[m²]	intrinsic permeability
M	[kg, J]	mass or energy per volume
$P_{c\beta}$	[kPa]	capillary pressure in phase β

P_g	[kPa]	gas pressure
$P_ß$	[kPa]	fluid pressure in phase *ß*
Q_a	[m³]	total amount of air need
S_β	[-]	degree of saturation of phase *β*
S_{ew}	[-]	effective degree of water saturation
S_w	[-]	degree of water saturation
S_{wr}	[-]	residual water saturation
U	[-]	uniformity coefficient
V_{corr}	[cm³]	volume change correction
V(ε)	[-]	variance-covariance matrix of the true errors

Greek letters

α	[1/m]	fitting parameter of the water retention function
β	[-]	index for fluid phases
δ_a	[kg/m³]	density of the air phase
ε_1	[-]	axial strain
ε_v	[-]	volumetric strain
ε_{ij}	[-]	strain tensor
θ_w	[cm³/cm³]	volumetric water content
θ_{wr}	[cm³/cm³]	residual volumetric water content
θ_{ws}	[cm³/cm³]	saturated volumetric water content
κ	[-]	index for fluid components
$\lambda(s)$	[-]	slope of normal compression lines at different suction values
μ	[-]	function of suction and/or the degree of water saturation
μ_β	[kg/s·m]	viscosity with respect to phase *β*
ξ	[-]	constitutive variable, which is a function of suction and/or the degree of saturation respectively other soil parameters
ρ_d	[g/cm³]	dry density of soil
ρ_s	[g/cm³]	grain density
ρ_w	[g/cm³]	density of water
ρ_β	[g/cm³]	density of phase *β*
σ	[kPa]	total stress
σ_3	[kPa]	cell pressure
σ_i^2	[-]	variance of the true error of the observation *i*
σ'_{ij}	[kPa]	effective stress tensor
Γ	[-]	surface element
τ	[-]	tortuosity factor

φ'	[°]	effective friction angle
X_{β}^{κ}	[-]	mass fraction of component κ present in phase β
χ	[-]	effective stress parameter
ω	[rad/s]	rotation velocity (of a centrifuge permeameter)
ω	[-]	weight assigned to the residual (of an objective function)
ω_{hi}	[-]	weight of i^{th} pressure observation
ω_{qj}	[-]	weight of j^{th} flow observation
ω_{pk}	[-]	weight of k^{th} prior information
ϖ	[-]	arbitrary loss function

Abbreviations

AIC	Akaike's information criterion
AICc	modified Akaike's information criterion
BIC	Bayes information criterion
Cov_{jk}	covariance between parameters j and k
maxChange	maximum computed parameter change
ND	total number of observations
NH	number of pressure head observations
NP	number of parameters
NPR	number of prior information values
NQ	number of flow observations
pcc(j,k)	parameter correlation coefficient of parameters j and k
res	weighted residual
tolObj	maximum allowed change of the objective function
tolPar	maximum allowed parameter change
Var_j	variance of parameter j
Var_k	variance of parameter k

1 Introduction and outline of the thesis

1.1 Research on unsaturated soils

It is generally agreed that modern soil mechanics started with Terzaghi's proposal of the effective stress concept (1936). In this context, it is interesting to point out that the title of this publication, "*The shearing resistance of saturated soils*", includes the restriction "saturated". It can be concluded that Terzaghi was well aware that the complexity of unsaturated soil behaviour needed further research effort and enhanced mathematical frameworks in order to be able to describe their mechanical behaviour.

An analogous starting point for the theoretical research on unsaturated soils was probably given by Bishop (1959). Bishop recognized that the presence of two fluids (air and water) in the pore space required an extension of Terzaghi's original effective stress concept. Bishop introduced a parameter χ (effective stress parameter), which relates the different magnitudes of pore water and pore air pressure to the effective stress. The title of Bishop's publication, "*The principle of effective stress*", already makes clear that with the extended formulation a validity for saturated as well as for unsaturated soils was assumed.

Bishop's extended effective stress proposal was not as unanimously received as Terzaghi's effective stress concept for saturated soils. Jennings and Burland (1962), Burland (1964), Fredlund et al. (1978) and many others strongly criticized Bishop's stress and doubted its correctness. As a result of the criticism, the extended effective stress concept has been abandoned and has not been employed for decades. Nowadays, it is understood that in the majority of cases Bishop's stress was misconceived, because it was not viewed in the context of plastic soil behaviour. Bishop's stress has finally been "rediscovered" and is now frequently employed for advanced constitutive models of unsaturated soils.

However, after Bishop's controversially discussed effective stress concept, the research efforts on unsaturated soils were intensified. Major development steps were e.g. the state surfaces presented by Matyas and Radhakrishna (1968), the proposal of a shear strength equation with two independent stress state variables by Fredlund and Morgenstern (1977) and the first constitutive model for unsaturated soils in the framework of elasto-plasticity by Alonso et al. (1990).

Since then, research on unsaturated soils experienced a boom. Significant advances in the development of theoretical concepts as well as experimental laboratory and field methods have been achieved. An outstanding large number of research efforts have been dedicated to the determination and modelling of the

water retention curve, which represents a key issue in unsaturated soil mechanics. Another means was the development of elasto-plastic models for unsaturated soils. Nowadays, for better or for worse, unsaturated soil mechanics has established as own research discipline in extension to saturated soil mechanics.

1.2 Open issues

Research on both experimental and theoretical unsaturated soil mechanics has reached a very advanced level. A large number of constitutive models are available for use. In particular, the stress-strain models are highly sophisticated and are able to describe evermore aspects of unsaturated soil behaviour (e.g. the effects of bimodal pore systems). Laboratory testing and measuring techniques are continuously improving. Still, there are a lot of open issues to deal with.

One problem is certainly associated with the complexity of many of the elasto-plastic constitutive models. Often, they are developed based on limited experimental evidence, and sometimes solely based on a single triaxial testing series. Thus, these constitutive models show a good performance for a distinct soil but prove to be inapplicable for other soil types, or even for the same soil but compacted at different water content. Additionally, the often high number of necessary parameters makes these models unusable for practical applications.

The triaxial testing of unsaturated soils is extremely time-consuming, in particular if the hysteretic effects of the water retention behaviour are also of interest. If the limited amount of published data from extended triaxial testing series is compared with the large number of published constitutive models, it becomes clear that their experimental validation cannot keep up with the theoretical advances. Hence, there are a large number of elasto-plastic models whose general performance has not yet been sufficiently evaluated.

The state of the art concerning the water retention and unsaturated water-flow behaviour respectively models is somewhat different. A number of models, which are well-validated in the field of unsaturated zone hydrology, are available. Recently, efforts have been made towards the development of flexible models, which allow for the consideration of bimodal pore systems. However, in contrast to the water permeability models, the validity of air permeability functions has been studied and evaluated much less, in particular in the context of two-phase flow problems in unsaturated soils. This deficiency appears to be a consequence of the limited number of applications to site problems.

The measurement of matric suction with different methods is nowadays a routine procedure in experienced laboratories. On the contrary, the measurement of

unsaturated air and water conductivity remains challenging and does not always yield reliable results. An additional problem is that the measurement techniques are often conceptually very different from the aimed applications. To overcome this deficiency, other procedures like the inverse modelling of transient flow experiments have been used with increasing intensity during the last years.

Another issue concerns the coupling of the water retention with the permeability models. The water respectively air permeability functions are usually derived by integration of the water retention relationship into the functions; that means that an identical set of parameters is used in both constitutive laws. This approach has been proved right for certain soils but has also been found misleading for other soils. Recently, there is a trend towards the decoupling of water retention and permeability functions.

As a conclusion of the latter considerations, three important means of future research activities on unsaturated soils are formulated:

- **Evaluation of appropriate stress-strain constitutive models**
  As already mentioned before, constitutive models for unsaturated soils are often developed based on limited experimental evidence. Therefore, it is necessary to compare the model predictions with independent experimental data from other triaxial testing series. That way, the models' general capability of describing unsaturated soil behaviour can be evaluated. For this purpose, more experimental data from triaxial tests need to be produced. Another aspect which needs to be investigated further concerns the necessary level of model complexity. Likely, many engineering applications do not require a highly complex model that can account for "all" aspects of unsaturated soil behaviour. Summarized, the focus of the evaluation should be on the identification of appropriate constitutive modelling concepts for the purpose of their future application to engineering problems.

- **Parameter identification for permeability models**
  Different methods for the determination of the unsaturated air and water permeability are available. Many of these methods were developed in the field of agricultural engineering. Hence, the way of deriving the permeabilities may be conceptually very different from civil engineering problems and can make the obtained parameters inapplicable. As a consequence, the different methods for parameter identification, such as the direct measurement or the instantaneous profile method should be reviewed in the light of the aimed applications. Alternative methods, e.g. inverse modelling, for the effective parameter identification should be applied and evaluated. That way, appropriate and efficient procedures for the parameter identification of water and air permeability models can be detected respectively developed further with focus on the aimed applications.

- **Application to civil engineering problems**
  A severe drawback of bringing forward unsaturated soil mechanics is their so far limited application to site problems. In the majority of cases, unsaturated soil mechanic principles are solely used for two-dimensional slope stability analyses. The reason for the gulf between the available theoretical concepts and their practical application is probably that unsaturated soil mechanics is still under development and that a consolidation phase of the existing knowledge has not yet taken place. The conduction of case studies would be of particularly great importance in order to establish unsaturated soil mechanics in civil engineering practice. However, the conduction of case histories is hampered by a lack of field data.

In closing, another aspect is pointed out, which is likely to contribute to the above mentioned gulf between theory and application. With increasing research efforts, unsaturated soil mechanics finally has become an own research area that has been uncoupled from "classical" soil mechanics. Nowadays, both disciplines seem to coexist side-by-side rather than to complete each other. This is a trend that in fact impedes a unified soil mechanics framework and should be intended to turn back.

1.3 Focus and outline of the thesis

The present thesis aims at addressing some of the highlighted deficiencies in the previous section. Thus, the thesis focuses on applied research, e.g. on methods of parameter identification, rather than on the development of new theoretical concepts. Additionally, it is intended to produce experimental data to enable the evaluation of multi-phase flow and mechanical constitutive models. Various topics of the thesis are associated with tunnelling under compressed air.

The main part of this thesis consists of the development and inverse modelling of a two-phase field test, the numerical investigation of steady-state permeameters, a triaxial testing device for unsaturated soils and a practical application to tunnelling under compressed air. Because of the relatively wide range of research, the described topics of the thesis are treated exhaustively in independent chapters. Each of these chapters is organised into the following scheme: firstly, an introduction to the specific topic; secondly, a review of published research on the topic and selected theoretical aspects; thirdly, the conducted research work and its results; and finally, a discussion respectively summary of the results. It is further assumed that the reader of the thesis is familiar with the basics of unsaturated soil behaviour and multi-phase flow. In this context, the books of Fredlund and Rahardjo (1993), Lu and Likos (2004) and Bear (1988) are recommended.

In the following, the main chapters of the thesis and their contents are outlined:

- **Design of and theoretical studies of a new two-phase flow field test (chapter 2)**
  A new two-phase flow field test is developed. The test consists of a water infiltration and a subsequent air injection phase. The aim is to derive multi-phase flow parameters for site applications with predominant air flow, e.g. compressed air tunnelling or remediation by soil venting. A computational framework for the numerical simulation and the inverse modelling of the field test is developed. The test performance, i.e. water infiltration and air injection rates as well as water pressure and saturation distributions at reference points in the ground, is simulated exemplarily. Theoretical inverse modelling examples with different synthetic observation data sets are conducted. Based on the obtained results, recommendations for the practical application of the field test and its inverse modelling are given.

- **Execution and inverse modelling of air injection field tests (chapter 3)**
  The two-phase flow field test developed in chapter 2 is realised. In a variation of the original design, air is injected into a shallow groundwater table. The installation of the experimental set-up and measuring equipment in the field is explained and illustrated. Thereafter, the execution of three field tests in different soils is described and the corresponding measuring results are presented. For two of the field tests, the measurements are used for an inverse modelling of the multi-phase flow parameters. Because of the encountered irregularities of the measured air flow rates, an inverse modelling of the third field test is not conducted. Instead, the test performance is interpreted in the light of compressed air tunnelling. Finally, suggestions for specific research activities in order to advance the proposed field test are given.

- **Numerical investigations of steady-state unsaturated conductivity tests (chapter 4)**
  The correctness of unsaturated permeability data obtained by the steady-state method is investigated. A problem associated with the testing method is that a suction gradient across the specimen is necessary. In order to gain more knowledge of the distribution of suction and hydraulic permeability across the specimen, numerical simulation series of steady-state tests are conducted by using different parameter sets. The obtained results are used to determine the error which is caused by assigning the measured permeability values to the linear mean value of suction. Finally, three different methods for a better interpretation of steady-state derived permeability values are developed respectively evaluated. In detail, these methods are: firstly, the proposal of a new reference suction; secondly, the application of the Smiles and Towner method (1968); and thirdly, the inverse modelling of the permeability tests.

- **Installation, calibration and first test results of a triaxial testing device (chapter 5)**
  A double-walled triaxial testing device for unsaturated soils is configured and installed in the laboratory. The initial problems of the device and the improvements in order to overcome these deficiencies are described. Thereafter, the sensibility of the volume change-measuring device to temperature and pressure variations is investigated. Subsequently, the double-walled cell is calibrated against different cell pressures in order to enable accurate volume change measurements of the soil specimens. After the installation and calibration process, a first testing series with a fine-sandy silt is started. The testing of this material is of interest with respect to tunnelling under compressed air. The triaxial tests are conducted at constant suction. The effects of the degree of saturation (hysteresis of the water retention curve) on shear strength and strain behaviour are investigated by rigorous testing on drying respectively wetting paths. The obtained results are discussed with respect to previously published experimental results of similar materials.

- **Case study: Tunnel Fritzens - analysis and prediction of air losses (chapter 6)**
  In this chapter, an application of unsaturated soil mechanics to tunnelling under compressed air is presented. At the beginning, the project Tunnel Fritzens and its complex construction environment and driving concept are described. The numerical simulation of the two-phase flow of water and air which is induced by the tunnel advance is explained. The measured air losses during the excavation works of the first sections of the top-heading are analysed and divided into air losses through the tunnel lining respectively the tunnel face. Subsequently, the corrected air losses are used to back-calculate the permeability values of the soil and the artificial materials (e.g. shotcrete). The reasons for the high air losses during the top-heading advance are identified. Thereafter, various measures in order to reduce the air losses in the course of the further tunnel advance are elaborated and their effectiveness is investigated by means of numerical simulations. Additionally, a prediction of the air losses for the upcoming bench excavation is conducted.

- **Conclusions and outlook (chapter 7)**
  First of all, the conducted research and the most important results are highlighted. Afterwards, the achieved progresses but also the encountered problems of the researched topics are discussed. The discussion particularly takes place in the light of the intended application of the research for practical problems. In the closing outlook, suggestions and visions for further research activities are presented.

2 Design and theoretical studies of a new two-phase flow field test

2.1 Introduction

A number of geo-environmental problems require the consideration of two-phase flow of water and air: Tunnelling under compressed air, remediation by soil venting or rainfall infiltration over a shallow water table (for example). The design and analysis of these problems require the knowledge of the water retention capacity and water and air conductivity behaviour of the involved materials. Numerous laboratory and field techniques are available to determine these functions. However, for multi-phase flow systems it is difficult to obtain appropriate parameters from laboratory and field measurements. They may be process and scale dependent; that is, the measured parameters are often conceptually and thus numerically different from the effective parameters required by the site-specific numerical model (Finsterle 2004).

In recent years, an alternative method has gained increasing attention by unsaturated zone scientists: parameter identification by inverse modelling. Here, analytical or numerical models are calibrated against measurement data of transient flow experiments. This procedure provides some significant advantages over direct measurement methods. Firstly, the experimental set-up is generally simple and may be adapted to the problem focused on. Thus, the determined parameters are conceptually identical with the field problem. Secondly, all the fluid related unsaturated soil parameters can be determined simultaneously in a relatively fast, time-efficient way (van Dam et al. 1994). Additionally, the reliability of the obtained parameters can be expressed by stochastic characteristics (Finsterle 1999).

Draining column, imbibition and one-step respectively multi-step flow experiments are employed in order to obtain observation data sets for the parameter identification by inverse modelling. A review of the scientific literature indicates that in general a single-phase flow approach is adopted for the numerical modelling of the experiments. However, Schultze et al. (1999) encountered dynamic non-equilibrium effects during multi-step outflow/inflow experiments. They referred these effects to non-negligible resistance of the air flow at higher degrees of water saturation. Consequently, they suggest using a two-phase flow approach in order to accurately account for the flow behaviour.

A common problem of the employed transient flow experiments in literature is the nature of the induced flow. The soil specimen is usually collocated between

one high air and one low air entry disk. Hydraulic and/or pneumatic boundary conditions are applied behind the plates. During inflow and outflow tests, air replaces water respectively is replaced by water in the soil pores. However, air does not flow "through" the soil in a constant manner. Thus, the inverse modelling of these tests may yield parameters that are not appropriate for applications where air is the prevailing flow phase, e.g. soil venting or tunnelling under compressed air. Exceptions are so-called pneumatic tests (e.g. Kramer and Semprich 1989, Huang et al. 1999, Vesselinov et al. 2001a, 2001b), where air is injected into deep bore holes. However, these tests generally focus on the determination of the intrinsic permeability and/or porosity of porous rock mass, and not on transient multi-phase flow characteristics.

In order to determine parameters that are conceptually similar to multi-phase flow problems with prevailing air flow, a transient field experiment is developed in this chapter. The original idea of such a field test came from Vargas (personal communication, Dec. 2006). The intended test includes a water infiltration and a subsequent air injection phase. The preliminary water infiltration phase can be cancelled if the initial water saturation is high enough to allow for a significant desaturation of the soil by the air injection. On the other hand, the execution and inverse modelling of both test phases allow the determination of parameter sets that are characteristic for multi-phase flow problems with predominant water flow and predominant air flow, respectively.

The chapter starts with a literature review on inverse modelling theory. Subsequently, different experimental setups are designed, and their advantages and disadvantages are discussed. A computational framework for inverse modelling of the field tests is developed. Exemplary numerical simulations of the test performance are carried out. Inverse modelling studies with synthetic data are carried out. The aim of these investigations is to gather information on the type and amount of observations which is needed for the successful inverse modelling of the field test. Finally, the gained knowledge is summarized and recommendations for the practical execution of the proposed field test are given.

2.2 Literature review: inverse modelling theory

2.2.1 General principle

Inverse modelling is usually defined as the process of estimating model-related parameters by matching a numerical model to measured data representing the system response (e.g. flow problem) at discrete points in space and time. Model calibration, history matching and non-linear regression are equivalent terms for this estimation procedure (Finsterle 2004), and will be used throughout the work.

Independently of the type and nature of the investigated problem, inverse modelling incorporates the following essential components:

- A physical process respectively measurements representing the true, unknown system response.
- A numerical model of the physical process respectively computed values of the modelled process.
- An objective function which basically contains the differences between the measured and computed system response.
- A minimization algorithm which minimizes the deviations between the true and modelled system response by perturbation of the model parameters.

The physical system is the basis for the development of the numerical model. It contains constitutive relationships whose parameters are optimized by the inverse modelling. The objective function contains the weighted residuals and prior information for parameter estimation. The minimization algorithm computes the sensitivity of the objective function to the individual parameters and derives a corrected parameter set. This cycle is repeated until a specified convergence criterion is met. Figure 2.1 illustrates the principle of inverse modelling.

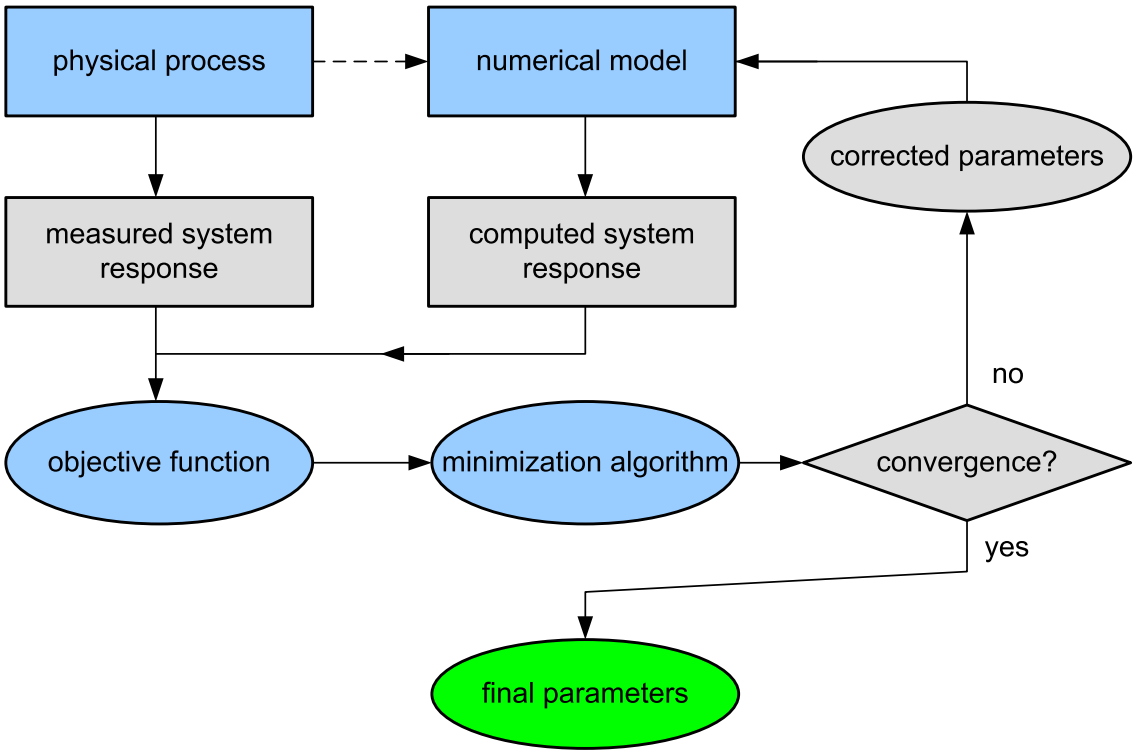

Figure 2.1: The principle of parameter estimation by inverse modelling.

Theoretically, a least-squares objective function can be used to derive a parameter set that accurately describes the true system behaviour if only three conditions are met (Hill and Tiedeman 2007):

- The relevant physical processes, the system geometry, and so on are adequately represented by the numerical model. This applies especially to the employed constitutive models.

- The true errors of the observations and prior information are random and have a mean of zero. Thus, every effort needs to be made to eliminate bias (i.e. systematic errors) in the observations.

- The weighted true errors are independent. That implies that the weighting of the observations needs to be proportional to the inverse of the variance-covariance matrix of the observation errors.

2.2.2 Objective function and minimization

The purpose of the objective function is to provide an integral measure of misfit between the model predictions and the measurements. The objective function can be extended to include prior information or regularization terms (Carrera and Neumann 1986). Prior information can be measured parameter values. While the use of prior information may lead to a solution of the inverse problem, it may also be misleading. For example, the measurement of permeability in the laboratory may be conceptually inconsistent with the flow problem in field, and the difference in scale may compromise the solution (Finsterle 1999).

In general, the objective function ***S(b)*** has the following form:

$$S(\mathbf{b}) = \sum_{i=1}^{m} \varpi \cdot (res_i ; \mathbf{b}) \qquad (2.1)$$

ϖ	arbitrary loss function
m	number of actual observations
i	discrete point in time or space
res	weighted residual
b	vector containing actual values of the estimated parameters

The specific form of the objective function may be derived from maximum likelihood theory. For example, assuming the final residuals follow a Gaussian distribution, maximum likelihood estimates are obtained by minimizing the sum of weighted squared residuals, i.e. by solving a weighted least-squares problem (Carrera and Neumann 1986). Weighted squared residuals can be written as:

$$res_i = \omega\left\{y_i - y_i'(\mathbf{b})\right\}^2 \tag{2.2}$$

ω weight assigned to the residual
y_i i^{th} observation value
y'_i i^{th} simulated value corresponding to i^{th} observation value

In groundwater and multi-phase flow modelling, least-squares objective functions are most commonly used. If water pressure and flow observations, and further prior information are used in the model calibration, the specific objective function *S(**b**)* reads:

$$\begin{aligned} S(\mathbf{b}) = &\sum_{i=1}^{NH} \omega_{hi}\left\{y_{hi} - y'_{hi}(\mathbf{b})\right\} + \sum_{j=1}^{NQ} \omega_{qj}\left\{y_{qj} - y'_{qj}(\mathbf{b})\right\} \\ &+ \sum_{i=1}^{NPR} \omega_{pk}\left\{y_{pk} - y'_{pk}(\mathbf{b})\right\} \end{aligned} \tag{2.3}$$

NH number of pressure head observations
NQ number of flow observations
NPR number of prior information values
y_{hi} i^{th} pressure observation being matched by the regression
$y'_{hi}(\mathbf{b})$ simulated pressure corresponding to the i^{th} pressure observation (a function of the parameter vector **b**)
y_{qj} *j*th flow observation being matched by the regression
$y'_{qj}(\mathbf{b})$ simulated flow corresponding to the j^{th} flow observation (a function of the parameter vector **b**)
y_{pk} k^{th} prior information included in the regression
$y'_{pk}(\mathbf{b})$ simulated value corresponding to the k^{th} prior information (a function of the parameter vector **b**)
ω_{hi} weight of i^{th} pressure observation
ω_{qj} weight of j^{th} flow observation
ω_{pk} weight of k^{th} prior information

The aim of the optimization procedure is to find the minimum of the objective function. Since the model output ***y***(***b***) depends on the parameters, the fit can be improved by changing the elements of the parameter vector ***b***. The search for the minimum takes place in the *n*-dimensional parameter space. A number of algorithms are available to minimize the objective function. The majority of the search methods are iteratively; that is, they start with an initial guess parameter set, and an updated vector is computed at each iteration. A step is successful if the new parameter set ***b*** at iteration (n+1) leads to a reduction of the objective function value:

$$S(\mathbf{b}_{n+1}) < S(\mathbf{b}_n) \tag{2.4}$$

If the optimization problem has a unique minimum, and the objective function is smooth enough, optimization methods that use calculated sensitivities (e.g. Gauss-Newton method) can be applied advantageously because they are computationally very efficient. They are called gradient methods because they generally use the gradient of the objective-function surface to determine how to proceed to the minimum. If the objective function contains multiple minima respectively is very irregular, global search methods are more useful. Global search methods (e.g. swarm optimization) do not use sensitivities. Instead, they proceed to the next set of parameters using a long history of the model fit produced by previous sets of parameters. The methods differ from the way in which the previous sets are used. The disadvantage of global search methods is that they are computationally intensive, often requiring computation times that are ten or hundreds of times as long as the execution times required by gradient-search methods (Hill and Tiedeman 2007).

In the course of the further work, the Levenberg-Marquardt algorithm is used for the optimization problems. It is a modification of the original Gauss-Newton method for nonlinear least-squares optimization. The so-called Levenberg parameter (Levenberg 1944) is introduced into the search algorithm. The Marquardt scheme (1963) of adapting the search direction and step length provides the flexibility needed for the minimization of the objective function with a complex topology. The Levenberg-Marquardt method can be viewed as a flexible combination of the robustness of the Steepest Descent Method and the efficiency of a second order Gauss-Newton method (Finsterle 1999).

2.2.3 Weighting of observations and prior information

Except for cases with only one kind of observation at apparently equal error variance, weighting is an important issue in optimization problems and performs to related functions: First, in case of more than one type of observations, the measurements are normalized to the same units, so that they can be squared and summed using Equation (2.3). Second, weighting needs to relate the influence of observations and prior information according to their accuracy. Both functions relate directly to the theoretical requirement that the weight matrix $\boldsymbol{\omega}$ is proportional to the inverse of the variance-covariance matrix of the true errors (Draper and Smith 1998):

$$\boldsymbol{\omega}^{1/2} \propto \mathbf{V}(\boldsymbol{\varepsilon})^{-1} \tag{2.5}$$

$\mathbf{V}(\boldsymbol{\varepsilon})$ variance-covariance matrix of the true errors

For uncorrelated measurements, a diagonal weight matrix $\boldsymbol{\omega}_i$ can be employed. Equation (2.5) can then be expressed as:

$$\boldsymbol{\omega}_i \propto 1/\sigma_i^2 \tag{2.6}$$

σ_i^2 variance of the true error of observation *i*

The difficulty is that statistic characteristics of a measurement are usually not available, because only one measurement is taken at each calibration point at one time. Further, for any observation, errors may result from many sources. Examples are the limited accuracy of the measurement device, the geometrical position of the measurement points etc. It is noted that in many cases the standard deviation of a measurement device is larger than its defined accuracy.

Finsterle (1999) states that one is often forced to estimate the standard deviation based on the variability of one measured data at many calibration points. Hill and Tiedeman (2007) suggest deriving the variance of the observations through estimations on the probability of a specific measurement deviation. To illustrate this approach, the following example is considered:

- Based on the known accuracy of a pressure transducer and on experience, it is estimated that the true value with a probability of 97.5 % is within ±100 Pa of the measured value.

- Thus, the significance level of the measurement is 2.5 %. Assuming a normal distribution of the error, the standard normal curve gives a critical *z*-value of 2.24.

- Now, from the assumed confidence interval of 100 Pa, the estimated standard deviation s_{yi} of the measurement y_i can be computed:

$$100 = 2.24 \cdot s_{yi} \quad \Rightarrow \quad s_{yi} = 44.6 \text{ Pa} \tag{2.7}$$

The weighting of prior information and of selected data requires special considerations. For example, in groundwater modelling there are often many head observations but very few flow observations. It may thus be useful for model calibration to increase the influence of the underrepresented observations respectively prior information relative to the prevailing kind of observations. Here, it is best to think the purpose of the covariance matrix as a weighting matrix (Finsterle 1999). If, for example, a single flow observation should receive a weight comparable to 20 head observations, then the standard deviation of the flow observation should be taken to 5 % (=100/20) of the actual measurement uncertainty.

In practice, it is generally impossible to exactly identify and account for all the errors that contribute to an observation. Yet, it is rarely difficult to determine weights that adequately represent errors in regression. If one poses different

levels of potential error, almost always some of them can clearly be identified as realistic while others are not realistic. While the resulting statistics are not rigidly defined, such an assumption based approach is usually able to determine the weights well enough. This is because the regression results are generally not sensitive to moderate variation in the weighting: nearly identical results are typically obtained given weighting within a range that reasonably represents the likely observation error. However, if the weighting is changed beyond reasonable ranges, large variations in the regression results may occur, causing the regression to loose meaning and become arbitrary (Hill and Tiedeman 2007).

2.2.4 Convergence

Convergence criteria are needed to determine when to stop an optimization process. The best-case scenario is when the global minimum of the objective function is identified. Theoretically, the minimum is identified if all elements of the gradient vector $\partial S / \partial \boldsymbol{b}$ are zero. According to Cooley and Naff (1990), model calibrations employing modified Gauss-Newton respectively Levenberg-Marquardt algorithms, typically converge within a number of iterations equal to five or twice the number of parameters.

In practice, two different convergence criteria are employed. In analogy to their specifications, they are called parameter-value criterion respectively model-fit criterion (Hill and Tiedeman 2007). By the first criterion, convergence is achieved when the parameter values change only by a small fraction from one optimization-iteration to the next. This indicates that at the current regression iteration, the parameter values lie in a flat area (valley) that is a minimum of the objective function. For untransformed parameters this condition is achieved if for all parameters the maximum calculated change by the minimization algorithm is smaller than a user specified tolerance limit:

$$\text{maxChange}_j < \text{tolPar}_j \qquad \text{for all } j = 1, \text{NP} \tag{2.8}$$

maxChange	maximum computed parameter change
tolPar	maximum allowed parameter change
NP	number of parameters

Hill and Tiedeman (2007) suggest that *tolPar* is typically no more than 0.01 respectively 0.001 for final model calibrations. However, for preliminary regressions it may be advantageous to use larger values.

By the second convergence criterion, the optimization procedure converges if the model fit improves little or no more; that is, the value of the least-squares

objective function does not reduce significantly in the course of a specified number of consecutive regression-iterations:

$$\Delta S(\mathbf{b}) = [S(\mathbf{b})_{i+n} - S(\mathbf{b})_i] < \text{tolObj} \quad \text{for all n = 1 to z} \tag{2.9}$$

tolObj	maximum allowed change of the objective function
n	iteration counter
z	number of consecutive iterations

This convergence criteria is typically specified with *tolObj* = 0.01 and *z* = 3. Poeter et al. (2005) recommend using this model-fit convergence criterion in early stages of the calibration process. Because it does not provide as strong an indication that a minimum has been reached as the parameter-value criteria, for final model calibrations the satisfaction of the latter one is preferable (Hill and Tiedeman 2007).

Other stopping criteria are a maximum number of iterations or a maximum number of forward simulations (Finsterle 1999). However, these criteria are due to practical reasons (e.g. limiting the computation time) and, if met, indicate an ill-posed inverse problem rather than the identification of a unique parameter set.

2.2.5 Evaluation of model fit

After a converged parameter optimization, the quality of the model fit needs to be evaluated. Additionally, criteria are necessary in order to be able to quantitatively compare different optimization runs of the same problem (e.g. evaluation of constitutive models). The value of the objective function is only an informal information to indicate model fit. It is rarely employed for more formal comparisons because their values nearly always decrease with the number of optimized parameters (Hill and Tiedeman 2007). In the following, selected aspects respectively criteria of model fit evaluation are presented.

- **Magnitude of residuals and weighted residuals**
  The evaluation of the largest residuals and weighted residuals accompanies the model calibration throughout. In initial model runs, the largest weighted residuals often indicate gross errors in the model or in the observation data sets. To detect such problems, it is useful to evaluate the percent contribution of the largest weighted residuals to the value of the objective function. Weighted residuals that disproportionally highly contribute to the objective-function value are suspect and must be checked carefully. For example, single observations can be identified as outliers and subsequently excluded from the model regression.

- **Calculated error variance and standard error**
  A common indicator of the overall model fit respectively the overall magnitude of the weighted residuals is the calculated error variance s^2, which after Cooley and Naff (1990) and Ott (1993) equals:

$$s^2 = \frac{S(\mathbf{b})}{ND + NPR - NP} \tag{2.10}$$

  ND total number of observations
  NPR number of prior information values
  NP number of parameters

  The standard error of regression s is the square root of the calculated error variance. The interpretation of both, s^2 and s, is related to the weighing. If the calculated error variance is significantly different from 1.0, this indicates that the model fit is inconsistent with the weighting (Hill 1998).

- **AIC, AIC_C and BIC statistics**
  Several authors (e.g. Brockwell and Davis 1987, and Burnham and Anderson 2002) criticized the calculated error variance and standard error of regression for not sufficiently accounting for the drawbacks associated with an increasing number of parameters. The AIC, AIC_C (a modified version of the first one) and BIC statistics were developed in order to address this criticism.

  In principal, the maximum-likelihood objective function value $S'(\mathbf{b})$ is penalized by the number of parameters and/or observations. The AIC (Akaike 1973, 1974), AIC_C (Sugira 1978) and BIC (Akaike 1978) statistics read:

$$AIC = S'(\mathbf{b}) + 2 \cdot NP \tag{2.11}$$

$$AIC_C = S'(\mathbf{b}) + 2 \cdot NP + \frac{2 \cdot NP \cdot (NP + 1)}{ND + NPR - NP - 1} \tag{2.12}$$

$$BIC = S'(\mathbf{b}) + NP \cdot \ln(ND + NPR) \tag{2.13}$$

  For the cited statistics, smaller values generally indicate a more accurate model. If the statistics for a model with fewer parameters are only slightly larger than for a model with more parameters, Hill and Tiedeman (2007) state that it may be preferable to select the model with the fewer parameters. Burnham and Anderson (2002) suggest that out of the three statistics, the AIC_C has distinct advantages.

- **Correlation coefficient**
  The correlation coefficient between the weighted observations and the weighted simulated values measures how well the trends in the weighted

simulated values match those of the weighted observed values. A plot of weighted or unweighted observations against simulated equivalents shows this trend graphically.

The described correlation coefficient *R* can be calculated for a diagonal weight matrix as (Cooley and Naff 1990):

$$R = \frac{\sum_{i=1}^{ND}\left(\omega_i^{1/2} y_i - m_y\right)\cdot\left(\omega_i^{1/2} y'_i - m_{y'}\right)}{\left\{\sum_{i=1}^{ND}\left(\omega_i^{1/2} y_i - m_y\right)^2\right\}^{1/2}\cdot\left\{\sum_{i=1}^{ND}\left(\omega_i^{1/2} y'_i - m_{y'}\right)^2\right\}^{1/2}} \qquad (2.14)$$

ND	total number of observations
y_i	*i*th observation value
y'_i	*i*th simulated equivalent to y_i
ω_i	weight of the *i*th observation
m_y	mean value of weighted observations
$m_{y'}$	simulated equivalent to m_y

Generally, a value of *R* that is greater than 0.90 indicates that the trends in the weighted simulated values closely match those of the weighted observations. However, *R* depends on the range of the values and wide ranges are common when using different kinds of data (Hill and Tiedeman 2007). Thus, the informative value of the correlation coefficient may be limited in some cases.

- **Plot of weighted residuals versus weighted simulated values**
  These plots can be applied advantageously to detect systematic misfit or other erroneous trends in model calibration. However, weighting of observations and prior information has to fulfil the criteria outlined previously in this chapter. Figure 2.2 shows two example-plots of weighted residuals versus weighted simulated values that reveal erroneous model trends.

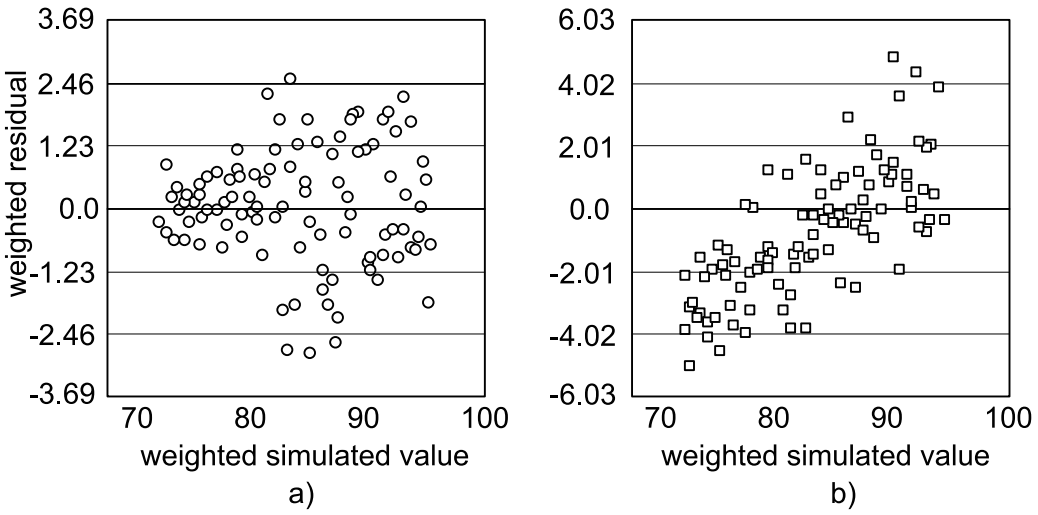

Figure 2.2: Plot of weighted residuals (after Hill and Tiedeman 2007).

Theoretically, weighted residuals of observations with random errors only, are scattered evenly about 0.0 for the entire range of values on the horizontal axis. In Figure 2.2a), the weighted residuals associated with smaller weighted simulated values vary less, i.e. they have a smaller variance. In Figure 2.2b), the weighted residuals increase with increasing weighted simulated values.

If different kind of data and/or prior information is employed for the calibration, it is advisable to display the residuals with different plot symbols. Further discussion and possible constrains of the described and similar plots are provided by Hill (1994).

- **Parameter correlations**
  The problem of parameter correlation is not directly linked to the model fit, but is an issue concerning the uniqueness of the inverse solution. The parameter correlation coefficient *pcc* of two parameters *j* and *k* is calculated as their covariance, divided by the product of their standard deviations:

$$\mathrm{pcc}(j,k) = \frac{\mathrm{Cov}_{jk}}{\mathrm{Var}_j^{1/2} \cdot \mathrm{Var}_k^{1/2}} \tag{2.15}$$

Cov_{jk} covariance between parameters *j* and *k*
Var_j variance of parameter *j*
Var_k variance of parameter *k*

After a successful model calibration, the parameter correlations are computed for each pair of parameters. The possible correlation range is from -1.0 to +1.0. If the absolute value of the correlation coefficient for a pair of parameters is close to 1.0, the two parameters generally cannot be estimated uniquely. On the contrary, if the absolute values of all parameter correlation coefficients are less than about 0.95, it is likely that all parameters can be estimated uniquely (Finsterle 1999, Poeter et al. 2005). The limit of 0.95 is a rule of thumb; unique estimates can sometimes be obtained even with absolute *pcc* values that are very close to 1.0 (Hill and Tiedeman 2007).

2.3 Computational framework

2.3.1 General

The inverse modelling of two-phase flow experiments requires a numerical model respectively simulation tool for forward computations, and an optimization software for parameter estimation. A numerical tool, which is capable of switching boundary conditions, integrated data evaluation and fully

automated communication with the optimization tool, is developed for the forward simulations. The programmed features allow for an efficient inverse modelling of the field tests. The program is called FT_2009.

For the parameter estimation, the universal optimization code UCODE_2005 (Poeter et al. 2005) is used. A similar inverse modelling framework is employed by Chinkulkijniwat (2006). However, due to special features of FT_2009 and the employed communication scheme with UCODE_2005, the computation procedure is more straightforward and does not require manual interaction.

2.3.2 FT_2009

The numerical forward code must be able to accurately simulate the induced two-phase flow of water and air of the planned field test. FT_2009 makes use of the TOUGH2-EOS3 (Pruess et al. 1999) finite-difference routines for solving the governing equations for the two-phase flow of water and air. Thus, previously to the actual program development, the used mass balance equations and flow vectors of TOUGH2-EOS3 respectively FT_2009, are described.

The mass and energy balance equations for the fluid components κ (water and air) have the general form:

$$\frac{\partial}{\partial t}\int_{V_n} M^{\kappa} dV_n = \int_{\Gamma_n} \mathbf{F}^{K} \bullet \mathbf{n} d\Gamma_n + \int_{V_n} q^{\kappa} dV_n \tag{2.16}$$

M mass or energy per volume
V_n element volume (bounded by the closed surface Γ_n)
F mass or heat flux
q sinks and sources
n normal vector on the surface element Γ_n (pointing inward V_n)

The total mass accumulation term of a component M^{κ} is obtained by summing over the fluid phases β (e.g. liquid, gas):

$$M^{\kappa} = n\sum_{\beta} S_{\beta}\rho_{\beta}X_{\kappa}^{\beta} \tag{2.17}$$

n porosity
S_β degree of saturation of phase β
ρ_β density of phase β
X_β^κ mass fraction of component κ present in phase β

The total mass flux $\boldsymbol{F^{\kappa}}$ is a sum over the individual phase fluxes $\boldsymbol{F_{\beta}}$ of each fluid component κ:

$$\boldsymbol{F}^{\kappa} = \sum_{\beta} X_{\beta}^{\kappa} \boldsymbol{F}_{\beta} \boldsymbol{n} \tag{2.18}$$

The introduction of the intrinsic permeability K_i allows a multiphase formulation of Darcy's law for the computation of the phase fluxes $\boldsymbol{F}_{\beta}$:

$$\mathbf{F}_{\beta} = \rho_{\beta} \mathbf{u}_{\beta} = -\mathrm{K}_{\mathrm{i}} \frac{\mathrm{k}_{\mathrm{r}\beta} \rho_{\beta}}{\mu_{\beta}} \left(\nabla \mathrm{P}_{\beta} - \rho_{\beta} \mathbf{g} \right) \tag{2.19}$$

$\mathbf{u_b}$ Darcy-velocity vector (volume flux)
$k_{r\beta}$ relative permeability of phase *β*
μ_{β} viscosity with respect to phase *β*
P_{β} fluid pressure in phase *β* (= $P_g + P_{c\beta}$)
P_g gas pressure
$P_{c\beta}$ capillary pressure in phase *β* (≤ 0)

All thermophysical properties are represented by the steam table equations as given by the International Formulation Committee (1987). Air is approximated as an ideal gas. Additivity is assumed for air and vapour partial pressures in the gas phase ($P_g = P_a + P_v$). The viscosity of air-vapour mixture is computed as given by Hirschfelder et al. (1954) and the solubility of air in liquid water is represented by Henry's law. The primary unknowns are the thermodynamic variables of the grid blocks (pressure, saturation and temperature). Boundary conditions as pressure, saturation and temperature refer to the gas phase (Pruess et al. 1999). Isothermal problems as well as non-isothermal problems can be handled.

The planned field test consists of a water infiltration and subsequent air injection phase. Further, the infiltration respectively injection occurs at different pressure steps. Thus, for the numerical simulation of the field test and the automated communication with UCODE_2005, the following features are required for FT_2009 (additionally to the actual flow simulation):

- **Division of the test simulation into single steps:**
  The stepwise execution of the water infiltration and air injection requires a consecutive series of flow simulations. Each pressure step requires one simulation run.

- **Modification of the initial and boundary conditions:**
  The initial conditions of the model domain at pressure step (*i+1*) correspond to the final conditions of pressure step *i*. Additionally, the Dirichlet-boundary conditions simulating the water infiltration respectively air injection pressure need to be increased after each pressure step.

- **Switching of the boundary conditions:**
  After the completion of the water infiltration phase respectively the corresponding number of pressure steps, the boundary condition simulating

the water infiltration needs to be replaced by a boundary condition simulating the air injection.

- **Data evaluation:**
  For the communication with the optimization code, the flow simulation must provide simulated equivalents to the measurements of the field test. Therefore, after each forward simulation, time series of water infiltration and air injection rates need to be provided. Additionally, water saturation, air and water pressure distributions of selected elements must be evaluated.

The latter requirements were used to develop the general structure of FT_2009. A flowchart of the program is shown in Figure 2.3. For parameter estimation modes, the program execution is managed by UCODE_2005.

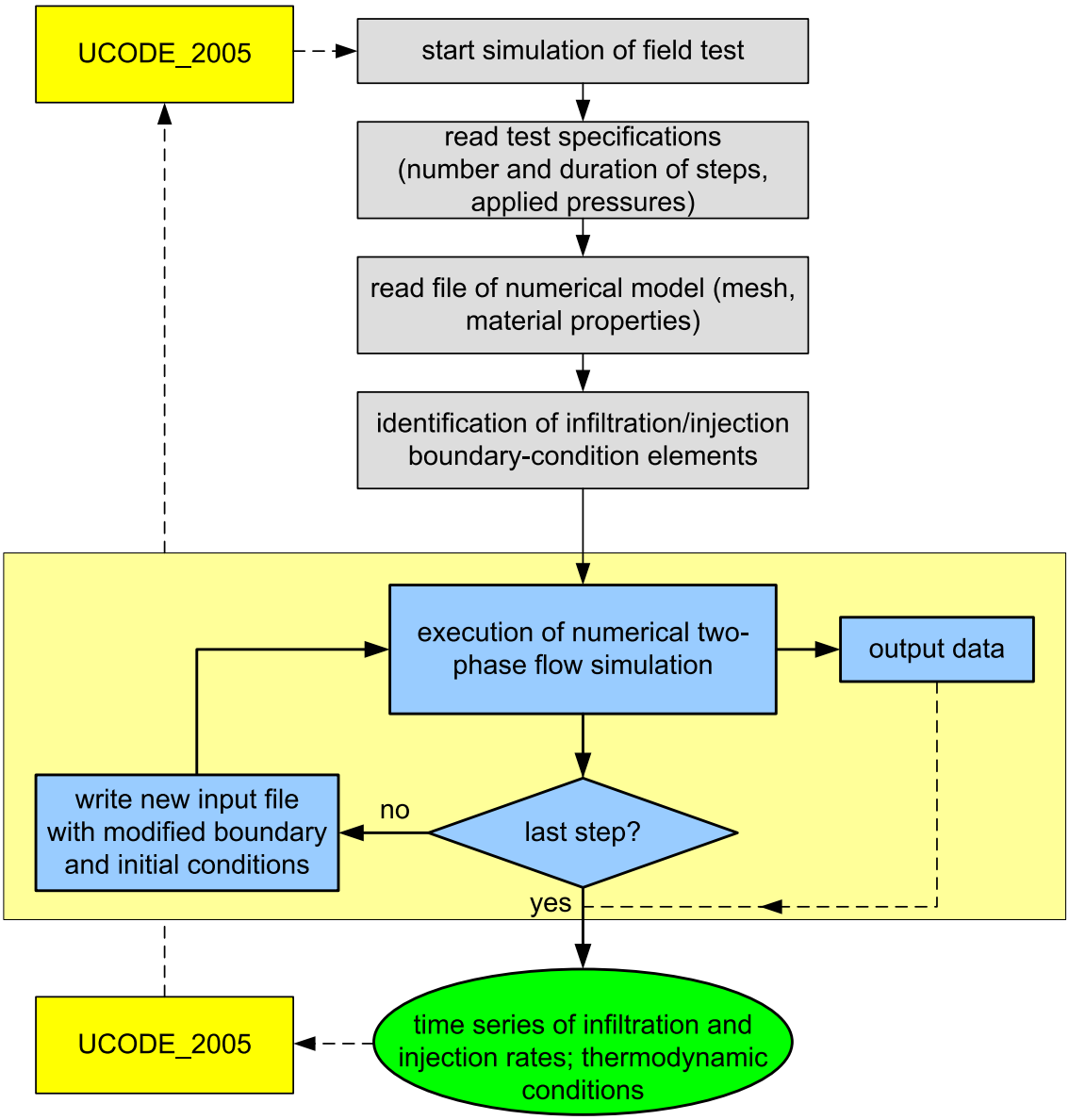

Figure 2.3: Principle functioning of the program FT_2009.

After program initialization through UCODE_2005, the field test specifications are read from the file “test_execution.txt”. This is a file with loose format, which contains the number and duration of water infiltration respectively air injection steps, and the pressure magnitudes and their duration. For field tests with air injection phases only, one pseudo-water infiltration phase with a time duration equal to zero needs to be defined.

Thereafter, the input file of the numerical model of the field test is read. The input file contains the mesh geometry, the initial conditions, boundary conditions and the material properties of the involved materials. The selected constitutive models must be specified. The elements, for which time series of water pressures or saturation degrees are desired, must be listed in the file. For a detailed description of the numerical model, see section 2.5.

Next, FT_2009 identifies the boundary-condition elements which model the water infiltration respectively air injection phases of the field test. For this purpose, these elements need to be named “TUNEL” in the input file of the numerical model. The corresponding flow connections from the simulated boundary conditions to model domain elements are identified and written at the end of the input-file.

After this preliminary program phase, the two-phase flow simulation of the first pressure step of the water infiltration phase is executed. The pressure and duration of this first step are read directly from the input file. Nevertheless, they must also be specified concordantly in the test-specification file. The flow simulation produces a number of output files. Among these are water respectively air flow rates of all relevant flow connections and the thermodynamic conditions of the elements listed in the input file of the model.

If the executed simulation of the pressure step is not the last one, FT_2009 proceeds with the writing of a new input file for the subsequent pressure step. For this purpose, the output file of the preliminary pressure step is read in order to obtain the initial conditions for the subsequent pressure step. The pressure magnitudes and the duration of the new test step are read from the test-specification file and assigned accordingly in the input file. If the program additionally has to switch from water infiltration to air injection, the corresponding boundary conditions (described in detail in section 2.5) are changed, too.

The cycle of a two-phase flow simulation - writing a new input file is repeated until the simulation of the last pressure step has been executed. Thereafter, a subroutine reads the output files of all test phases and evaluates the time series of the water infiltration and air injection rates during the duration of the whole test. Additionally, times series of air, water and capillary pressure of the selected

elements in the input file of the numerical model are produced. The files containing these times-series data provide the simulated equivalents to observations that are used for the model calibration. Finally, control is handed over to UCODE_2005 to perform the next step of the parameter estimation.

Of course FT_2009 can also be employed for forward simulations, solely. Moreover, the program is able to simulate any type of multi-step two-phase flow experiment (e.g. multi-step outflow experiments). Some requirements apply to the structure of the input file of the numerical model. These requirements are specified in the "Read-me" file of the program code (see CD ROM).

2.3.3 Constitutive laws

The numerical modelling of the two-phase flow of water and air requires three constitutive laws: First, a function describing the water retention capacity of the soil; second, a function describing the relative permeability behaviour; and third, a function describing the relative permeability behaviour of air. For these functions, numerous models can be found in literature. FT_2009, too, contains a number of selected constitutive relations. However, in the following only the constitutive laws that are used for the inverse modelling of the field test are described.

The capillary pressure-saturation relationship is modelled after Van Genuchten (VG; 1980). The VG model is one of the most commonly used water retention models (Chen et al. 1999). In original form, it reads:

$$S_{ew} = \left\{1 + \left(\alpha \cdot h_c\right)^n\right\}^{-m} \tag{2.20}$$

S_{ew} effective degree of water saturation;

$$S_{ew} = \left(\theta_w - \theta_{wr}\right)/\left(\theta_{ws} - \theta_{wr}\right) \tag{2.21}$$

θ_w volumetric water content
θ_{ws} saturated volumetric water content
θ_{wr} residual volumetric water content
h_c capillary pressure head
α fitting parameter that is inversely proportional to the air entry pressure
m, n fitting parameters that are inversely proportional to the width of pore-size distribution; usually it is assumed that m = 1-1/n

The Van Genuchten-Mualem (VGM) model is employed to describe the relative permeability functions of water and air. The VGM permeability model is

obtained by integrating the Van Genuchten water retention model into the permeability model of Mualem (1976). The permeability functions read:

$$k_{rw} = S_{ew}^{\tau}\left\{\frac{\int_0^{Se}\frac{dS_e}{h_c}}{\int_0^1\frac{dS_e}{h_c}}\right\}^2 = S_{ew}^{\tau}\left\{1-\left(1-S_{ew}^{1/m}\right)^m\right\}^2 \qquad (2.22)$$

$$k_{rnw} = \left(1-S_{ew}\right)^{\tau}\left\{\frac{\int_{S_e}^1\frac{dS_e}{h_c}}{\int_0^1\frac{dS_e}{h_c}}\right\}^2 = \left(1-S_{ew}\right)^{\tau}\left\{1-S_{ew}^{1/m}\right\}^{2m} \qquad (2.23)$$

k_{rw} relative permeability of wetting fluid; i.e. water
k_{rnw} relative permeability of non-wetting fluid; i.e. air or other gases
τ tortuosity factor

The ability of the VGM functions to model unsaturated water flow has been studied and proved by numerous authors (e.g. Eching and Hopmans 1993, Chen et al. 1999, Hwang and Powers 2003). However, the suitability of the model for active air flow has been far less investigated. Moreover, Kammerer (2000), Chinkulkijniwat et al. (2005) and Steger et al. (2006) found that for multi-phase flow in porous media with prevailing air flow, the air permeability may be governed by macro flow paths. The macro flow paths may develop due to erosion forces of the air and/or deformations due to elevated air pressures.

In the case of macro pores, the flow behaviour may become similar to that of fractured porous media (e.g. fractured tuffs). For these materials, the air flow takes primarily place in the fractures and the matrix remains at high degrees of water saturation (Vesselinov and Neumann 2001). Although for soils it is not to be expected that the flow behaviour is governed by the macro pores only, the VGM and similar models are likely to underestimate the occurring air flow.

In order to account for increased air permeability at high degrees of water saturation, two additional air constitutive functions are developed for use in combination with the VGM water permeability model. The new functions allow convex shapes of the air permeability functions. Theoretically, a convex shape can also be generated by using negative values for the tortuosity factor τ. While this may be a reasonable approach for the water permeability function (compare Wösten and Van Genuchten 1988), it is a misleading concept for the air permeability. Every tortuosity factor lower than zero yields relative air permeability values larger than 1.0 in a distinct saturation range. Moreover, negative τ-values always yield an increase of the air permeability with increasing

water saturation in a distinct saturation range. Obviously, this approach is physically inconsistent and is therefore not employed in FT_2009.

The first new air permeability function is a simple modification respectively enhancement of the original VGM model. The power function "2 · m" of Equation (2.23) is replaced by "x · m". The variable *x* is allowed to vary between 0.5 and 2.0. The new function is called VGM-mod, and reads:

$$k_{rnw} = (1 - S_{ew})^{\tau} \left\{ 1 - S_{ew}^{1/m} \right\}^{x \cdot m} \qquad \text{where } 0.5 \le x \le 2.0. \qquad (2.24)$$

The second new model is a pure fitting function and computes the air permeability as exponential function of the VGM-water permeability. The exponent *p* is allowed to vary between 1.0 and 5.0. The obtained air permeability function is called (1-k_{rw})-EXP model:

$$k_{rnw} = \left[1 - k_{rw}(\mathrm{VGM}) \right]^{p} = \left[1 - S_{ew}^{\tau} \left\{ 1 - \left(1 - S_{ew}^{1/m} \right)^{m} \right\}^{2} \right]^{p} \qquad (2.25)$$

where $1.0 \le p \le 5.0$.

Figure 2.4 illustrates the different relative permeability functions. For all displayed functions, the *m*-value and the τ-factor are 0.75 and 0.50, respectively. For the VGM-mod model, the chosen *x*-value is 0.5. It can be seen that a strongly convex shape of the air permeability curve can be achieved with the extended model. The chosen *p*-value of the (1-k_{rw})-EXP model is 5.0. Here, low air permeability is obtained in the range of residual air saturation. Subsequently, a steep increase is predicted by the function.

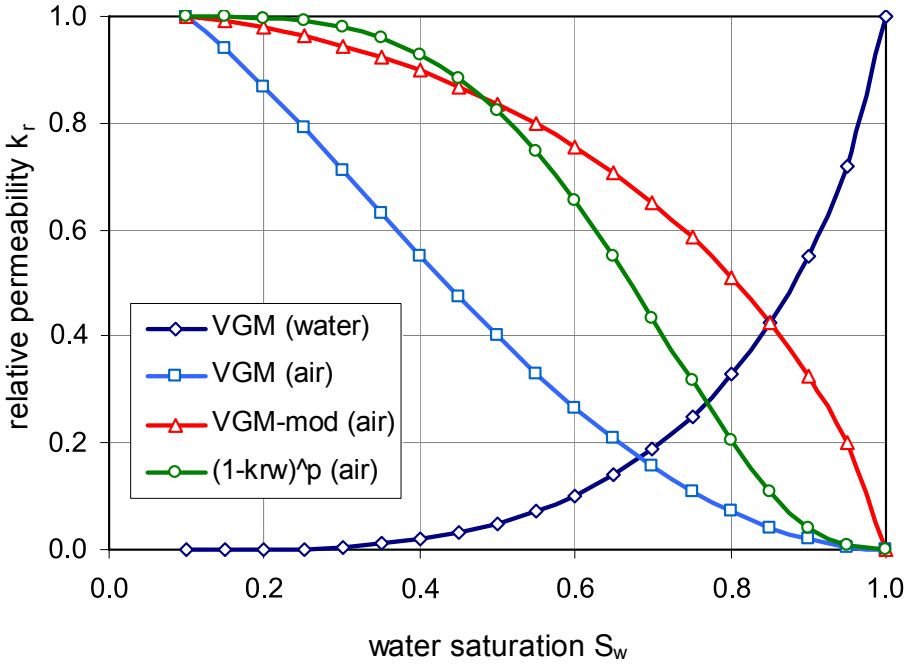

Figure 2.4: Characteristic shapes of employed relative permeability functions.

2.3.4 UCODE_2005

UCODE_2005 (Poeter et al. 2005) is a public-domain inverse modelling software. Any process model or set of models can be used; the only requirements are that models have numerical (ASCII or text only) input and output files, that the numbers in these files have sufficient significant digits, that all required models can be run from a single batch file or script, and that simulated values are continuous functions of the parameter values. The main use of the code is in groundwater model calibration.

UCODE_2005 can be used efficiently in model calibration through its sensitivity analysis capabilities and its ability to estimate parameter values that result in the best possible fit to the observations. Parameters are estimated using nonlinear regression: a weighted least-squares objective function is minimized with respect to the parameter values using a modified Gauss-Newton method (= Leveret-Marquardt method) or a double-dogleg technique. Statistics are calculated and printed for use in (1) diagnosing inadequate data and identifying parameters that probably cannot be estimated; (2) evaluating estimated parameter values; and (3) evaluating how well the model represents the simulated processes (Poeter et al. 2005).

Figure 2.5 shows the principle functioning of the parameter-estimation mode of UCODE_2005. After problem initialization, process-model input file(s) using the initial guess parameters are created. Subsequently, a first execution of the process models is conducted. From the output files, simulated values equivalent to the employed observations for model calibration are extracted respectively computed. The value of the objective function is computed with the evaluated weighted residuals.

Next, the parameter sensitivity loop is started. All parameters are perturbed step by step. The process model simulations are executed each time. With the so obtained simulated observation equivalents, the sensitivity of the objective function to the individual parameters is computed. UCODE_2005 offers the options of forward, backward and central-difference sensitivities.

After the perturbation of the last parameter, the Levenberg-Marquardt method is employed to compute a set of updated parameters. A detailed description of the Levenberg-Marquardt method can be found in Hill and Tiedeman (2007). Convergence of parameter estimation is checked against two criteria: Firstly, changes in estimated parameter values; secondly, changes of the sum of the objective function. If the changes are larger than the specified criteria (compare section 2.2.4), and the maximum number of iterations has not been reached, the next parameter-optimization step is initialized.

When parameter optimization converges, or the maximum number of iterations has been reached, sensitivities are calculated using the more accurate central-difference method. The additional accuracy is needed to compute a sufficiently accurate parameter variance-covariance matrix (Hill and Tiedeman 2007), from which a number of statistics (e.g. parameter correlations) are computed. If parameter optimization converged, the final parameters are considered to be optimized (Poeter et al. 2005).

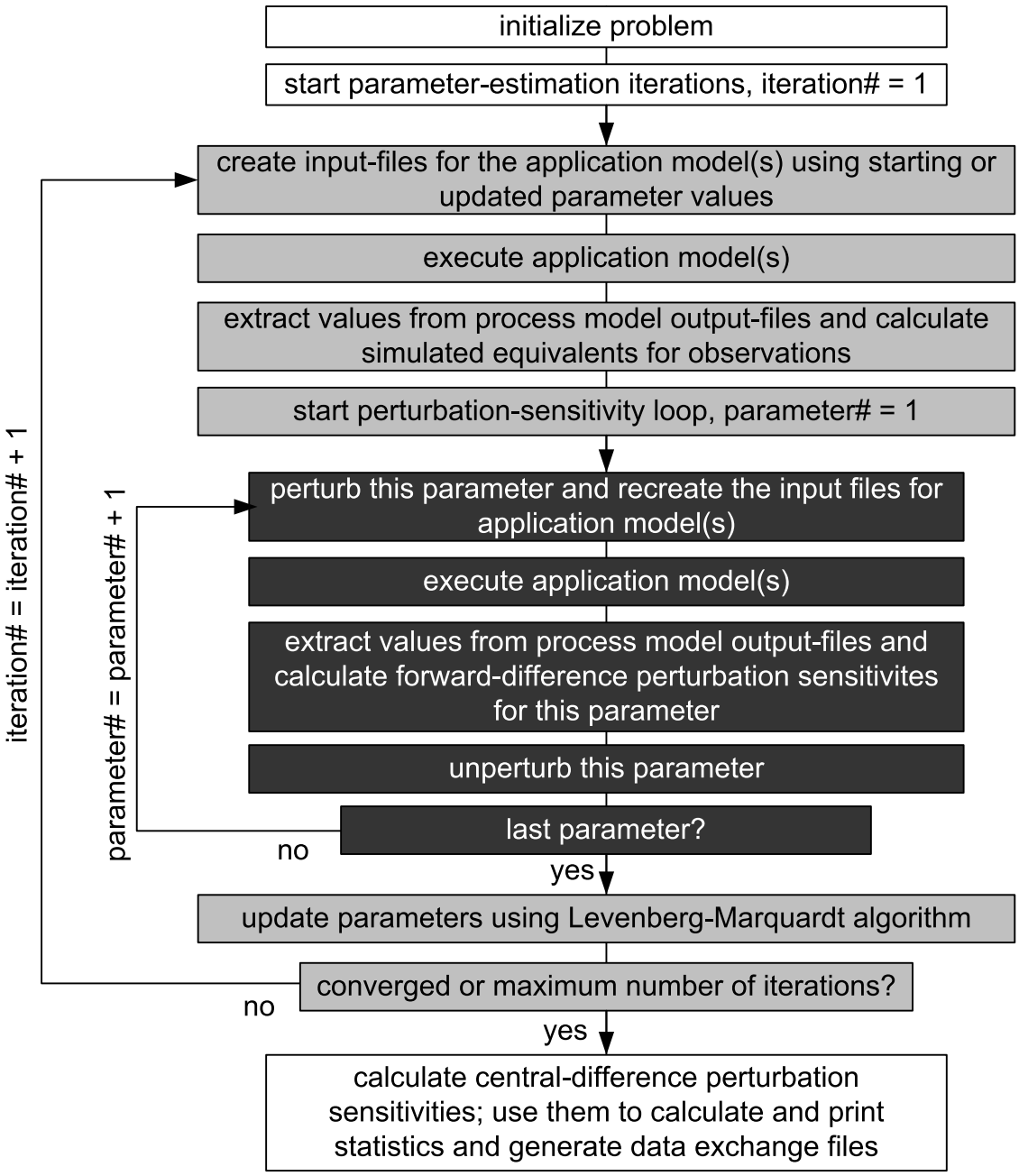

Figure 2.5: Flow chart showing the major steps in the UCODE_2005 parameter-estimation mode (after Poeter et al. 2005).

2.3.5 Executing a UCODE_2005 - FT_2009 parameter optimization

The execution of a parameter optimization with the developed framework is straightforward and efficient. However, at least three files are necessary for (1) the exact definition of the optimization procedure and (2) the communication between UCODE_2005 and FT_2009. In the following, the use and contents of the three files are briefly described. For a detailed description of the file formats and alternative file options, the reader is referred to the UCODE_2005 manual.

The mandatory files are:

- **Main input file:**
  The main input file defines details of the parameter optimization for UCODE_2005, e.g. initial guess parameter values, parameter change quantities and convergence criteria. The observation values and their statistics may also be written in this file. Further, the command for the process model execution, the names of the model input file, model output file, template file and instruction file are defined.

- **Template file:**
  The template file is identical with the input file of the numerical model with the only exception that the parameters which are optimized are replaced by substitution symbols. Based on the template file, UCODE_2005 creates input files with updated parameter values. FT_2009 executes the updated input files in the course of the sensitivity and parameter estimation modes.

- **Instruction file:**
  The instruction file indicates UCODE_2005 how to extract simulated equivalents to observation data from the model output file(s). The instruction file can be of two types. Either, the extraction of the simulation equivalents is carried out by specification of its exact position (line and column number), or through a search by means of specified keywords.

With the three described files and the UCODE_2005 and FT_2009 executables, any parameter estimation can be conducted. However, in case of many observation data and different kind of observation data, it is advantageous to write the data in separate files. If more than one process model is used, theoretically a template and an instruction file are needed for each of them. Alternatively, FT_2009 can be employed to generate a central output file from the individual model output files. The execution of the process models is advantageously carried out through a batch file. Figure 2.6 illustrates the interaction between the different data files and executable files.

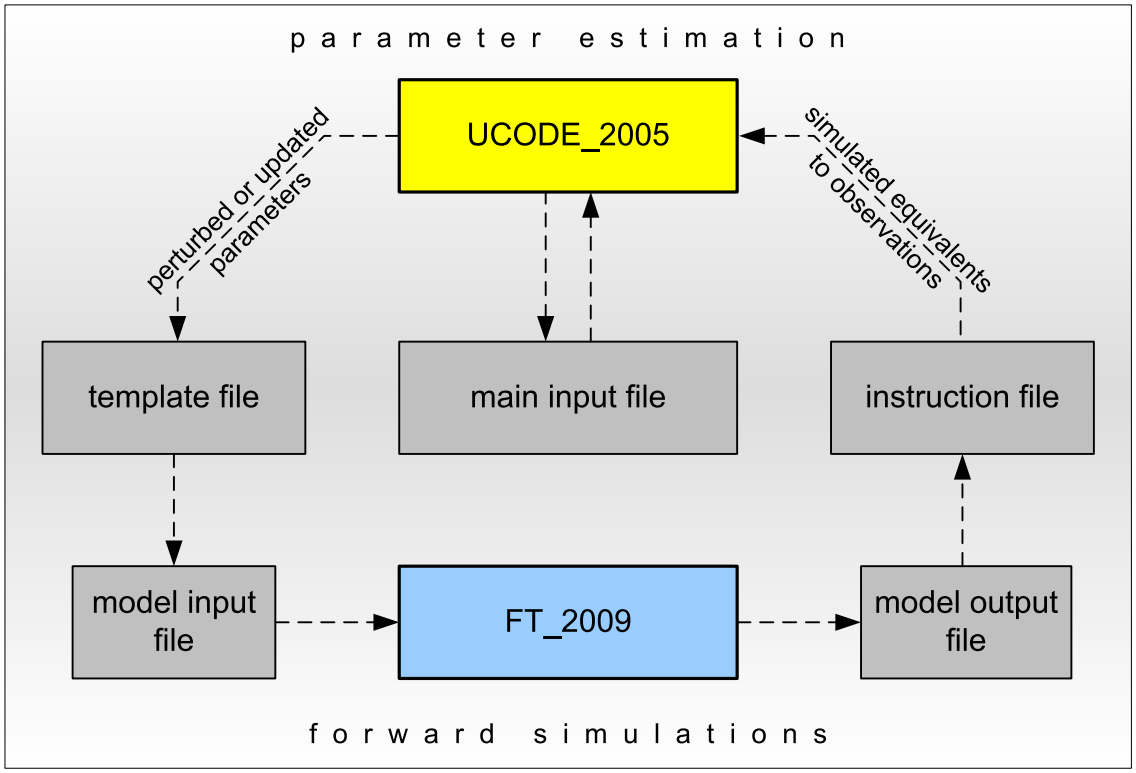

Figure 2.6: UCODE_2005 – FT_2009 communication scheme.

2.4 Design of the field test and numerical simulation of the test performance

2.4.1 Experimental setup

The proposed field test consists of a water infiltration and subsequent air injection phase. The test is meant for soils with medium permeability, i.e. fine to coarse sands with different silt contents, and residual soils. Steger et al. (2007) investigated different experimental setups for the proposed field test. The design was supported by numerical simulations. Concerns about soil fissuring respectively macro-pore development during the air injection phase and the advantage of a relatively uniform saturation distribution favoured the selection of a test setup with a vertical, partly perforated pipe as infiltration/injection device.

The principle of the designed experimental setup is to infiltrate water respectively to inject air at some depth below the soil surface. In comparison to water infiltration and air injection directly on the surface, this test design offers several advantages: Firstly, it increases the flow-path length from the injection device to the atmosphere and therewith the gradient and the erosion forces of the air; secondly, it reduces the influence of altered soil properties which frequently

occur on or close to the surface on the test results; and thirdly, the soil acts as natural dead load to prevent heaving especially during the air injection phase.

For test execution, a pipe with 1 to 2 m length and a diameter of 5 to 10 cm is placed into a vertical bore hole in the ground. The lower part of the pipe is perforated. Depending on the soil type, it may be favourable to drill the borehole with a larger diameter than the pipe. For that case, a filter is installed around the perforation, whereas the upper part of the hole is refilled with a tight material (e.g. clay). On the surface, an additional dead load may be placed on a steel plate. A tight connection between the plate and the infiltration pipe has to be ensured in order to have proper boundary conditions for the numerical modelling of the test. Figure 2.7 illustrates the designed experimental setup.

In the soil around the perforated part of the pipe, different measurement devices may be installed, e.g. TDR-probes, tensiometers and air pressure gauges. Secondary pipes with small diameter may be necessary for the installation of the devices. The distance of the measuring devices from the pipe has to be adapted to the expected water retention and relative permeability behaviour of the soil, but will in general vary between 15 and 30 cm. A data logger is employed to record the measurement series.

It is mentioned that measurements in the soil are not mandatory for the subsequent inverse modelling of the field test. Some multi-step outflow experiments are calibrated with cumulative water outflow measurements, only. During the field test execution, the water infiltration and air injection rates are measured. However, at least one additional kind of measurement data in the soil will facilitate the convergence of the inverse modelling and assure a higher accuracy of the estimated parameters (van Dam et al. 1994, Durner et al. 1999).

A Mariotte disposal is used to generate constant pressures during the water infiltration phase. The infiltrating water increases the water saturation and decreases the capillary pressures in the soil. This process is continued until a steady or quasi-steady state of the infiltration rate or of the saturation degree at the measurement point is reached. Thereafter, the Mariotte disposal is lifted to a higher level and the next pressure step is executed. In total, the execution of three to five pressure steps is planned for the water infiltration phase.

After completion of the water infiltration, the air injection phase starts. For this purpose, the top of the pipe is connected to an air pressure line. The air supply is by means of an air tank or by an air compressor. The air pressure is controlled by a high precision regulation system. For the air injection phase of the field test, one pressure step is continued until a steady state or quasi steady state is reached, too, and in total three to five steps are executed. In order to enable a test execution in one day, both test phases shall not exceed five to six hours, each.

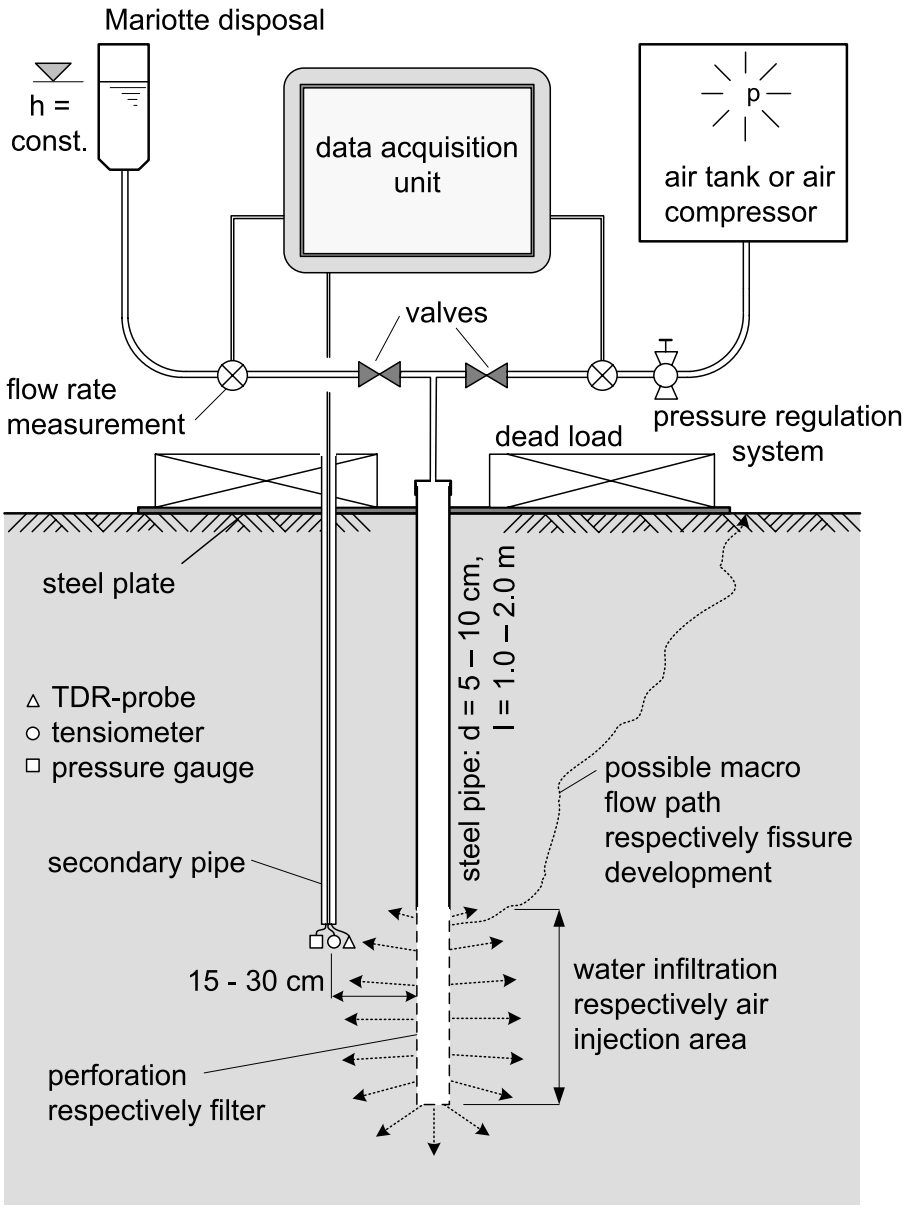

Figure 2.7: Experimental setup of the proposed field test.

During the water infiltration phase, the air pressure in the soil remains constant at atmospheric level, except for occluded air bubbles. Thus, the tensiometer measurements at the same time are representative for negative water respectively capillary pressures. During the subsequent air injection phase, immediately after application of a new pressure step, the pore air pressure and the pore water pressure are translated to a higher level. As a consequence, the tensiometer measurements are representative for the water pressure, only. Capillary pressures cannot be measured with tensiometers because they use differential pressure transducers with the atmospheric pressure as reference level. The penetrating air continuously desaturates the soil and water pressures will decrease concurrently, but may remain positive throughout the duration of the air injection phase.

Special consideration has to be given to the magnitude of the applied air injection pressures. The elevated pore air pressures and high flow velocities may cause alterations of the soil texture. Extensions of the pore space may occur and macro flow channels may develop. Adherent phenomena are pressure drops in the soil and/or an abruptly increasing air flow rate. The problem is that the field test is no longer representative for the undisturbed soil if alterations of the original soil texture occur. On the other hand, if such effects are conceptually similar to the targeted site problem, it might be useful to intentionally produce them. However, as a general rule of thumb, the applied air pressure heads should not be larger than the weight of the soil above the air injection area. Alternatively, additional dead loads can be applied to the soil surface.

2.4.2 Numerical model and soil parameters

An axis-symmetric model is used for the numerical simulation of the proposed field test. The model dimensions are 2.0 m and 3.0 m in radial and vertical direction, respectively. The pipe for the infiltration of water respectively injection of air is modelled with a length of 1.0 m and a diameter of 5 cm. At the lower part of the pipe, a length of 25 cm is perforated. On the surface, a steel plate with a radius of 50 cm is modelled around the pipe. Figure 2.8 depicts a schematic view of the model and the assigned boundary conditions.

A rectangular mesh with 32 element rows in radial and 36 elements in vertical direction is used to model the described geometry of the experimental setup. Reference elements for evaluation of the transient thermodynamic conditions during the test simulation are situated at 15, 30 and 45 cm distance from the pipe. The assigned initial conditions in the model domain are a water saturation $S_w = 0.30$ and an air pressure p_a = 100 kPa. The simulations are conducted isothermally at a temperature of 20° Celsius.

Neumann-boundary conditions with zero flux are applied to the symmetry axis, the upper, impermeable part of the steel pipe and the steel plate. The bottom, lateral and top model boundaries are modelled with Dirichlet-conditions with p_a = 100 kPa and S_w = 0.30. Full water and air permeability (k_{rw} = k_{ra} = 1.0) is assumed for the simulated atmospheric conditions at the top of the model. The right lateral and bottom boundary conditions have identical relative-permeability properties with the soil elements.

The infiltration of water respectively injection of air is modelled with Dirichlet-boundary conditions, too. The assigned pressures are total pressures (atmospheric pressure + excess pressure Δp_i). Full water and zero air permeability are modelled during the water infiltration. On the contrary, full air and zero water

permeability are modelled during the air injection steps. In detail, this is achieved with Grant functions (Grant 1977) in combination with water saturations of 0.999 and 0.001 for the water infiltration and air injection, respectively.

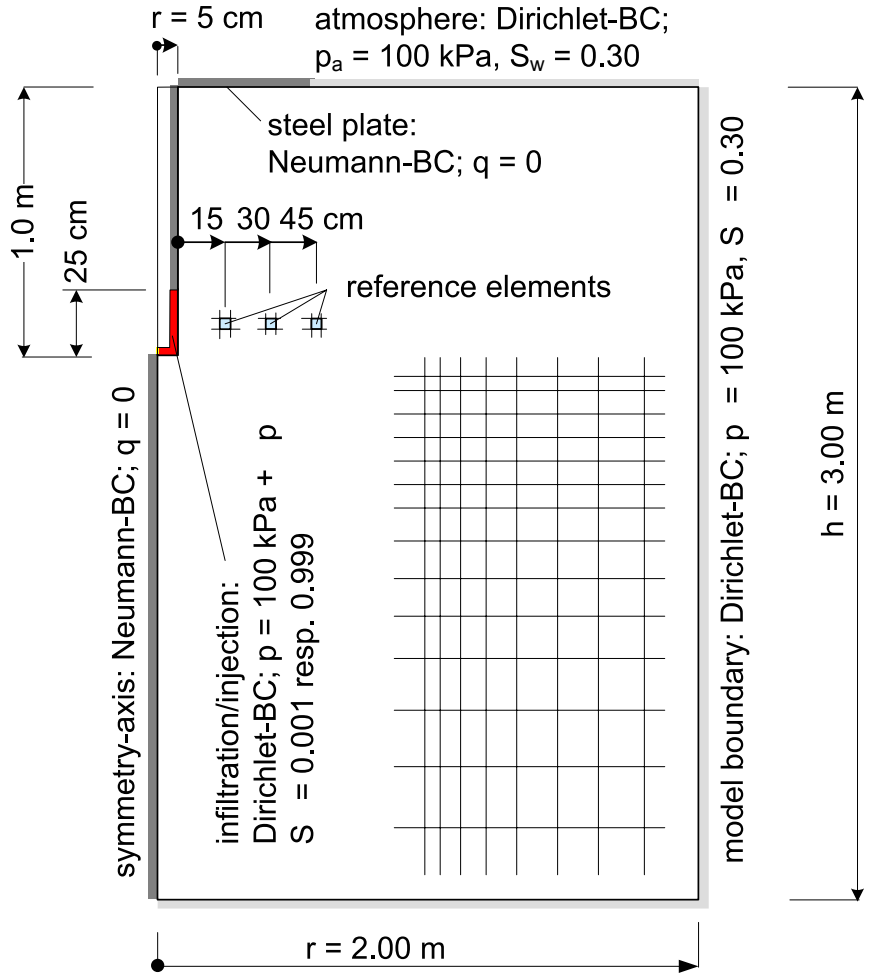

Figure 2.8: Numerical model of the field test with assigned boundary conditions.

The modelled soil represents a silty sand, a typical soil targeted with the proposed field test. The saturated water permeability k_w is $5.0 \cdot 10^{-6}$ m/s and the air entry value p_0 is 2.5 kPa. The Van Genuchten-Mualem model is used to model the water retention and relative permeability function. Table 2.1 gives the employed soil parameters for the numerical simulation.

Table 2.1: Soil parameters for the Van Genuchten-Mualem model

k_w	θ_{wr}	θ_{ws}	m	τ	α
[m/s]	[-]	[-]	[-]	[-]	[1/m]
$5.0 \cdot 10^{-6}$	0.07	0.35	0.50	0.50	3.9

The field test is simulated with six pressure steps; three water infiltration and three air injection steps. The total time duration of the test is 43,200 s respectively 12 h. Table 2.2 gives the magnitudes of the pressure steps and their duration. For the water infiltration steps, a pressure of 0 kPa corresponds to a water level of the Mariotte disposal at the ground surface.

Table 2.2: Pressure steps and duration of the modelled field test.

step number	**type**	**pressure**	**time**
-	-	[kpa]	[s]
1	water infiltration	0	5,400
2	water infiltration	10	5,400
3	water infiltration	20	5,400
4	air injection	20	9,000
5	air injection	35	9,000
6	air injection	50	9,000

2.4.3 Simulation results

A numerical simulation of a hypothetical field test with the numerical model and soil parameters specified in the previous section was carried out. In this section, the computation results for water and air flow rates, and the distributions of water saturation, water and air pressures are presented and discussed.

Figure 2.9 illustrates the development of water infiltration and air injection rates during the field test. The water infiltration rates q_w are generally much lower than the air injection rates q_a. The q_w - distribution is relatively steady during the individual pressure steps. A maximum value of 0.94 l/min is reached for the pressure step 20 kPa. For the same pressure, the air injection rate is 13.4 l/min. A maximum flow rate of 51.7 l/min is obtained for the final pressure step. A steady state is not reached during the individual steps.

Figure 2.10 depicts the distribution of water saturation at the three reference points at 15, 30 and 45 cm distance from the pipe. During the water infiltration, the water saturation increases from the initial value of 0.3 to 1.0 at al reference points. For the closest reference point full water saturation is encountered after 25 min, whereas at 45 cm distance this value is only reached after 3 hours. The subsequent air injection leads to a constant decrease of the water saturation to final values between 0.49 and 0.63. The curves are smooth and hardly reflect the

pressure elevations in the pipe. As can be recognized from Figure 2.10, despite the higher applied pressures and longer duration of the air injection steps, the drainage of the soil needs much more time than the wetting of the soil. This phenomenon is linked to the capillary pressures. During the water infiltration, they suck the water into the soil, whereas during the air injection they present an increasing resistance to the further desaturation of the soil.

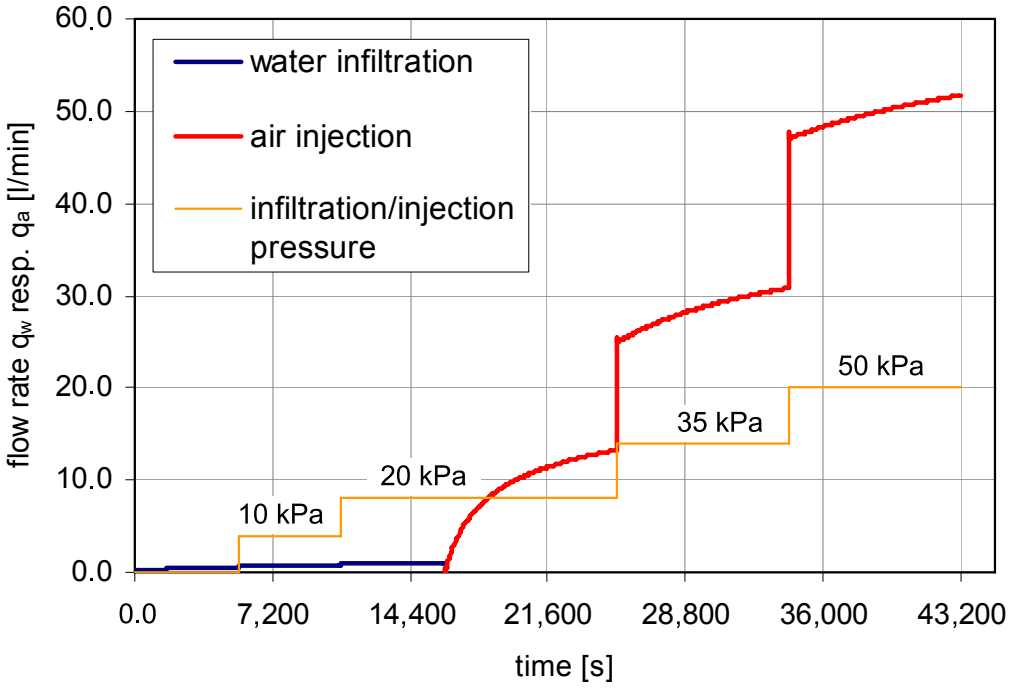

Figure 2.9: Water infiltration and air injection rates.

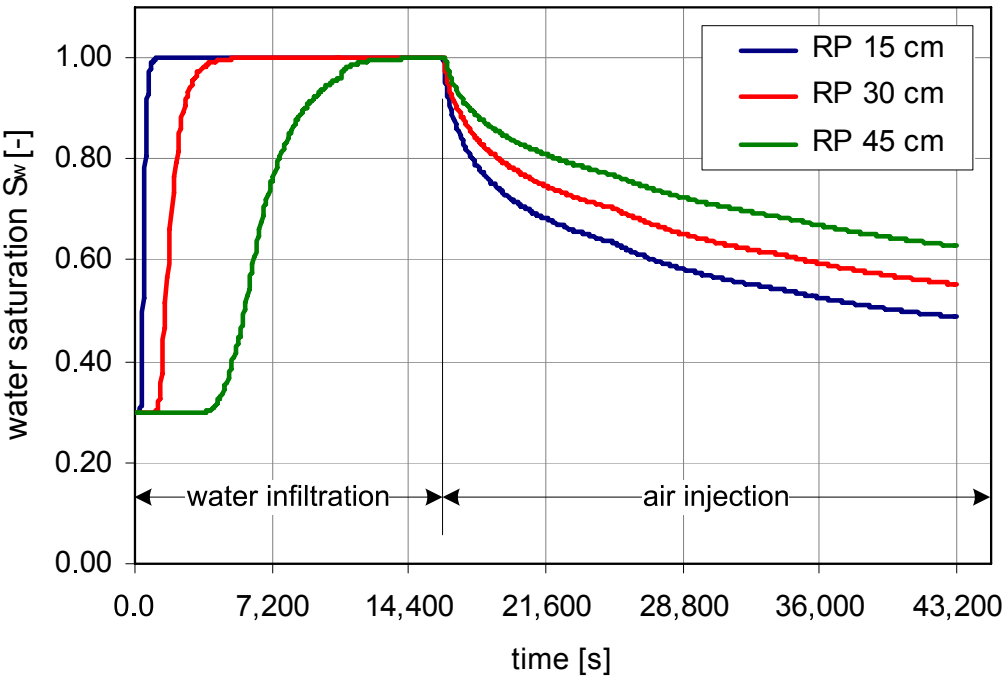

Figure 2.10: Water saturation during water infiltration and air injection phase.

Figure 2.11 illustrates the spherical development of water saturation fronts at different test phases. The depicted sections have a size of 1.25 m · 2.25 m. At the end of the water infiltration phase, a water saturated zone extends with a radius of approximately 50 cm around the centre of the infiltration area. Beyond a radius of 80 cm, the soil remains unaffected by the water infiltration. At the beginning of the air injection phase, the water saturated zone dissolves rapidly. Already after 500 seconds, a 75 % water saturation front is beginning to develop. By comparison, the desaturation is occurring with decreasing intensity after the end of the first air injection step. At the end of the air injection phase, a large circular zone with 50 – 60 % water saturation extends around the injection area.

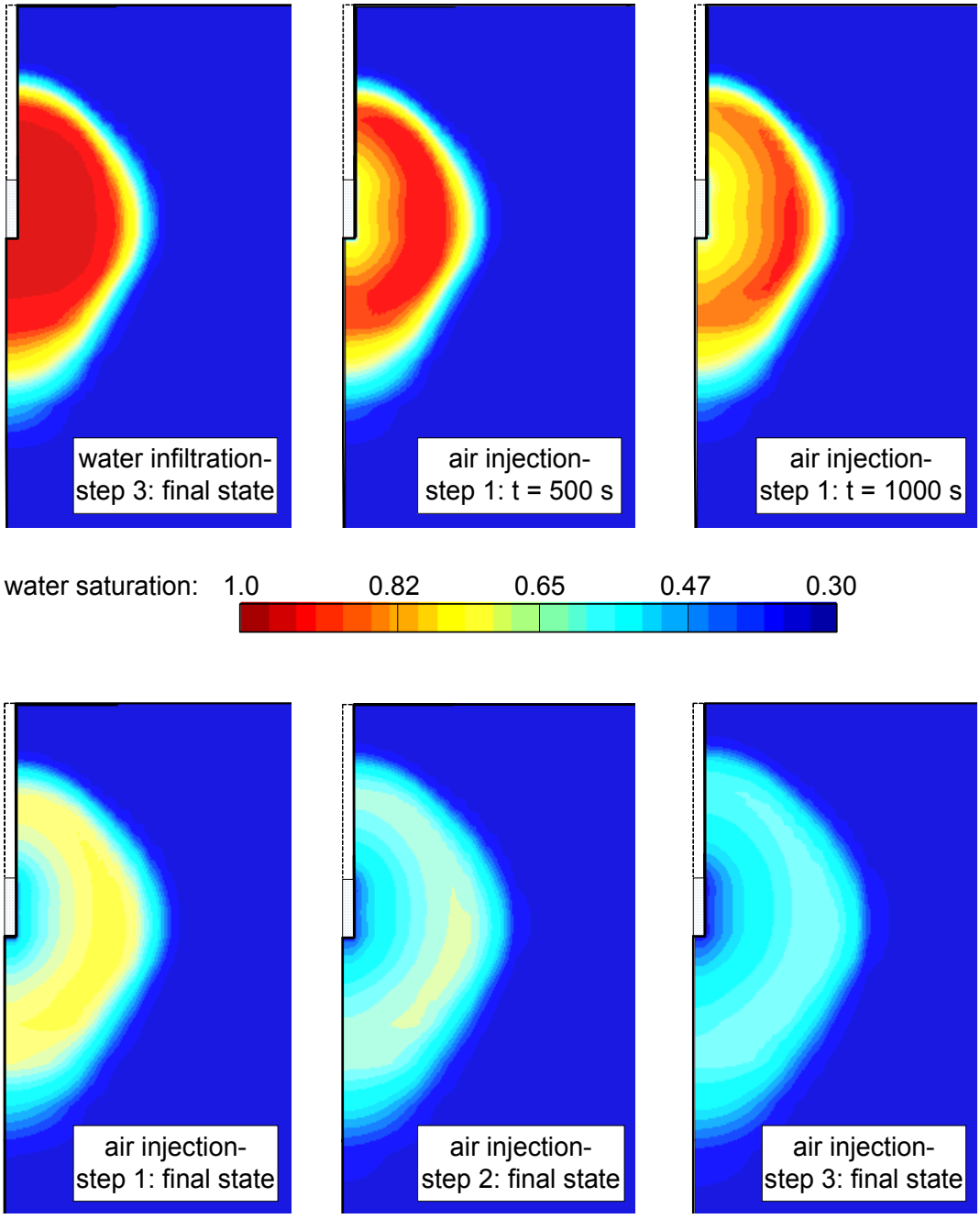

Figure 2.11: Areal extension of water saturation fronts during the test phases.

Figure 2.12 shows the capillary pressure distributions at the reference points. Their shapes are similar to the water saturation curves. From the initial value of 20 kPa, a reduction to 0 kPa occurs in the course of the water infiltration. The subsequent air injection yields a constant but slow increase of the capillary pressures. The maximum capillary pressures at the reference points vary between 3.95 and 6.49 kPa at the end of the air injection phase, only. A further increase of the capillary pressures would require very long testing times for this soil type.

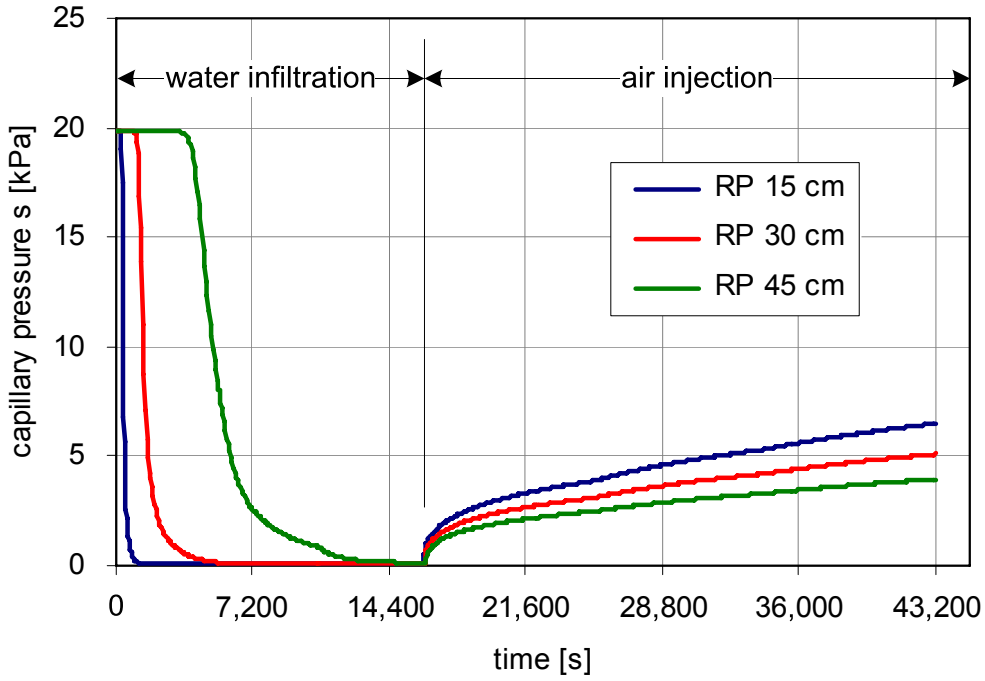

Figure 2.12: Capillary pressures during water infiltration and air injection.

It has already been mentioned that tensiometers during the air injection phase measure the water and not the capillary pressure. In order to obtains simulated equivalents for the inverse modelling of the field test, the water pressures have to be computed as the difference between the air pressure and the capillary pressure ($p_w = p_a - s$). The air pressure is a primary variable of the employed mass balance equations and therefore a direct output of the numerical solution.

Figure 2.13 shows the air pressure distributions for the reference points. The total pressures are presented. The increase of the pressure at the beginning of the individual steps is clearly reflected by the curves. During the water infiltration, when a saturation state close to 1.0 is reached, the pressure of entrapped air bubbles increases and is identical with the water pressure. During the air injection phase, a peak value is encountered at the beginning of each test step. Thereafter, the air pressure decreases. This behaviour is best pronounced for the first air injection step. At this time, the soil around the injection area is water saturated and an air pressure accumulation is the consequence. With advancing air injection, the fully saturated zone dissolves and the air pressure drops.

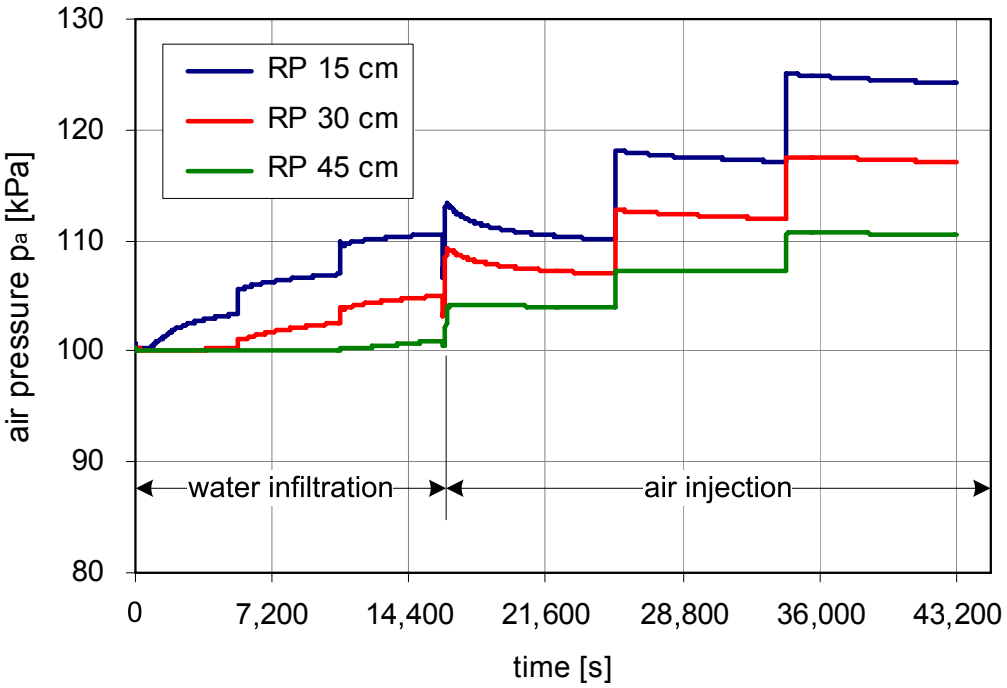

Figure 2.13: Air pressures during water infiltration and air injection phase.

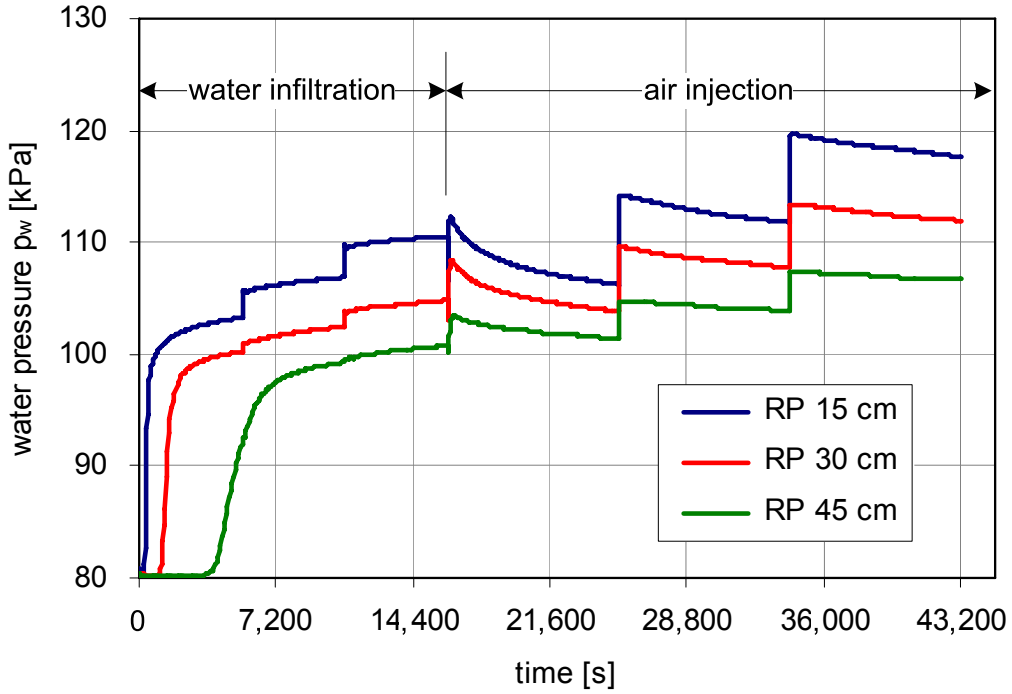

Figure 2.14: Water pressures during water infiltration and air injection phase.

Figure 2.14 finally depicts the distribution of water pressures, which is obtained from the difference of air and capillary pressures. A significant increase occurs during the water infiltration phase. Here, the development of the water pressures is only determined by the decreasing capillary pressures. When full saturation is reached at the reference points (see Figure 2.10), air and water pressures are identical (compare Figure 2.13 and 2.14). During the air injection phase, the

water pressures are determined both by the air pressure and the increasing suction. The pressure elevation at the beginning of the individual steps results in an equal increase of air and water pressure. Subsequently, the water pressure decreases with the advancing desaturation of the soil and the adherently increasing capillary pressure. For all three reference points the water pressure is above atmospheric level during the whole air injection phase of the field test.

2.5 Inverse modelling studies with synthetic observation data

2.5.1 General description

The results of the conducted forward simulation of the field test in the previous chapter are used for theoretical inverse modelling examples. The aim of the investigations is to study the suitability of different kind of data for a successful parameter optimization of an actually conducted field test. Beyond, the functioning of the developed inverse modelling framework is checked.

Three different variants are investigated. The employed synthetic observation sets are flow rates only (variant 1), water pressures only (variant 2) and flow rates and water pressures (variant 3). These are common data used for the inverse modelling of water infiltration tests and laboratory outflow experiments. Water saturation data is usually not used because its distribution is often rather non-uniform (especially in coarse textured soils; e.g. fingering phenomenon). Air pressure data is not used due to its relatively low variation over time during a pressure step.

For each variant, optimization runs with three, four and five free parameters are conducted. It is investigated in which cases the true parameter set can be detected by the inverse modelling of the field test. A particular interest of the investigations is to show whether measurements of the water and air flow rates alone are able to produce unique parameter estimations, or if a second kind of observation data (e.g. water pressures) is additionally necessary.

For assessing the uniqueness of the inverse solution, the following criterion is used: It is assumed that the inverse solution is unique if each value of all the optimized parameters differs no more than 1 % from the true parameter value. This criterion must be fulfilled for optimization runs with different initial guess parameter sets. The initial guess parameters are chosen with different deviations but within a physically reasonable range of the true parameters. A similar approach is used by Eching et al. (1994), Simunek and Van Genuchten (1996) as well as Hwang and Powers (2003).

Additionally, critical parameter correlations and the sensitivity of the inverse solution to the different parameters are investigated. Parameter correlations are defined as critical if the correlation coefficient is larger than 0.95 (compare section 2.2.5). The sensitivity of the inverse solution with respect to a certain parameter is defined as low if the composite scaled sensitivity for this parameter is less than 5.0 % of the maximum sensitivity.

2.5.2 Variant 1

Variant 1 uses synthetic water and air flow rate observations for the parameter optimization, only. For each pressure step, the data points are selected 100 seconds after beginning with the step and each subsequent 1,000 seconds of the time period (compare Figure 2.9). Thus, a total number of 48 observations is obtained. For weighting, a standard deviation of 1 % is assigned to each water flow rate. Because the measurement of air flow rates is more uncertain, a standard deviation of 2.0 % is assigned to these observations. This type of weighting corresponds to a constant relative measurement error.

For each optimization problem (with three, four and five free parameters), a series of five regressions with different initial guess parameters was carried out. All regressions converged in a straightforward manner and yielded excellent model fits. For all optimization runs, the coefficient of determination is close to 1.0. Other characteristics (e.g. AIC-value) are not discussed here because their values are not significant for the conducted inverse modelling examples.

Two of the optimizations with five free parameters indicated non-uniqueness of the inverse solution. The optimized parameter value S_{wr} deviated 2.1 respectively 3.8 % from the true value. Generally, the inverse solutions showed low sensitivity with respect to this parameter. The remaining parameters, however, were all within the defined 1 % limit. Critical correlations were encountered for two regressions with five parameters. Table 2.3 summarizes the most important findings and gives the average number of iterations for the regression series.

Table 2.3: Summary of findings for the optimization runs of variant 1.

series	optimized parameters	uniqueness	critical correlation	low sensitivity	number of iterations
-	-	-	-	-	-
1	m, α, S_{wr}	yes	no	no	5
2	K_i, m, α, S_{wr}	yes	no	yes: α	6
3	τ, K_i, m, α, S_{wr}	no	yes: (S_{wr}-τ)	yes: α, S_{wr}	9

The obtained results suggest that unique parameter estimations can be obtained by the inverse modelling of the field test with flow rate observations, only. However, great care is recommended if a five parameter-fit of the field test is aimed. Here, a larger number of runs with initial guess parameters varying within a wide range and a comprehensive analysis of the regression statistics will be necessary to exclude the possibility of only having detected a local minimum.

2.5.3 Variant 2

Variant 2 uses 48 synthetic water pressure observations of the reference point at 15 cm distance from the pipe for the parameter optimization. For each pressure step, the data points are selected 100 seconds after beginning with the step and each subsequent 1,000 seconds of the time period (compare Figure 2.14). For weighting, a standard deviation of 500 Pa is assigned to all water pressure values; that means that the relative measurement error increases with smaller measured values. This type of measurement error and the according weighting implies that observations with larger absolute values tend to have a disproportionately high influence on the regression and vice versa.

For each optimization problem (with three, four and five free parameters), a series of five regressions with different initial guess parameters was carried out. All optimization runs converged, but only the regressions with three parameters yielded unique solutions. A high number of 13 iterations (on the average) was required to reach convergence. For the optimizations with four and five parameters, rather different parameter sets were computed. In particular, high deviations up to 28 % from the true values were obtained for the parameters *m*-value and S_{wr}. These two parameters showed high correlations, too. Nevertheless, the coefficient of determination is close to 1.0 for all runs. Table 2.4 summarizes the obtained results. It is interesting to see that the regressions that yielded non-uniqueness needed a significantly lower number of iterations for convergence. Obviously, at these regressions the parameter search ended relatively fast in one of the various local minima instead in the detection of the global minimum.

Table 2.4: Summary of findings for the optimization runs of variant 2.

series	optimized parameters	uniqueness	critical correlation	low sensitivity	number of iterations
-	-	-	-	-	-
1	m, α, S_{wr}	yes	yes: (S_{wr}-m)	no	13
2	K_i, m, α, S_{wr}	no	yes: (S_{wr}-m)	no	6
3	τ, K_i, m, α, S_{wr}	no	yes: (S_{wr}-m)	no	7

The problem associated with the non-uniqueness of optimized parameters is that they usually do correctly represent all aspects of the physical process. To illustrate this fact, one of the conducted optimization runs with five free parameters is considered. The final parameters K_i, m-value and S_{wr} deviated 8.0, 15 and 28 % from the true values, respectively. Nevertheless, the regression fits the employed water pressure observations very well. However, the flow rates are not correctly represented by the parameter set, see Figure 2.15. Similar deviations are obtained for water saturation and air pressure distribution. The detected parameter set is therefore not representative for the true flow behaviour.

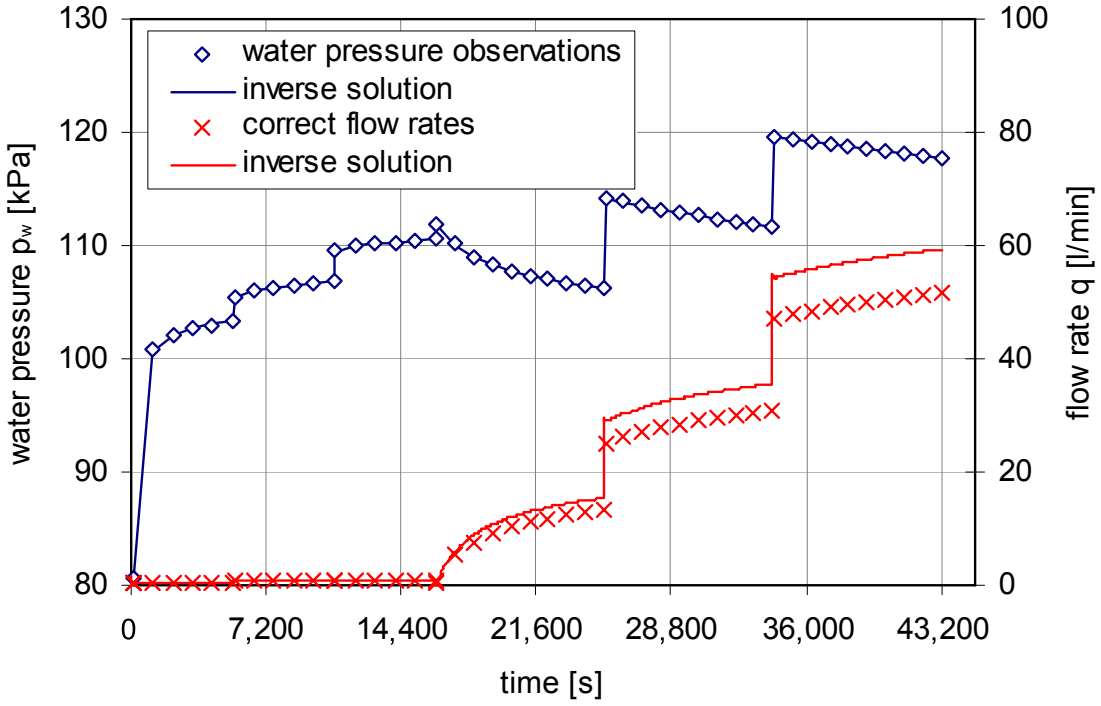

Figure 2.15: Consequences of a non-unique parameter set.

The results of the conducted optimization runs indicate that a unique inverse solution for water pressures as single observation data set can only be obtained for three parameters. The performance of the regression can possibly be improved if measurements at a second reference point are included into the observation data. This should be subject of further investigations.

2.5.4 Variant 3

Variant 3 uses synthetic flow rates and water pressure observations for the parameter optimization. For each pressure step, the data points are selected 100 seconds after beginning with the step and each subsequent 1,000 seconds of time period (compare Figure 2.15). In total, 96 observations are used for the regression. For weighting, a standard deviation of 1 % is assigned to each water

flow rate and a standard deviation of 2.0 % to each air flow rate. A constant standard deviation of 500 Pa is assigned to all water pressure values.

For each optimization problem (with three, four and five free parameters), a series of five with different initial guess parameters was carried out. All optimization runs converged and yielded excellent model fits. In analogy, the computed coefficients of determination are close to 1.0. Even the regressions with five optimized parameters of variant 3 do not exhibit problems of non-uniqueness or low sensitivities. The average number of necessary iterations for convergence is similar to variant 1. Table 2.5 summarizes the obtained findings.

Table 2.5: Summary of findings for the optimization runs of variant 3.

series	optimized parameters	uniqueness	critical correlation	low sensitivity	number of iterations
-	-	-	-	-	-
1	m, α, S_{wr}	yes	no	no	5
2	K_i, m, α, S_{wr}	yes	no	no	7
3	τ, K_i, m, α, S_{wr}	yes	no	no	9

The obtained results clearly show that unique parameter sets can be obtained by inverse modelling of the field test with flow rates and water pressures as regression data. Problems with non-uniqueness or parameter correlations are not to be expected.

2.6 Summary and conclusions

In this chapter, theoretical research on the development of a two-phase flow field test and its inverse modelling was carried out. The aim of the research was to gain more knowledge of the anticipated practical test performance and to provide a sound basis for the future realization of the proposed field test. The parameters obtained by the inverse modelling of the test are particularly meant for site applications with predominant air flow, e.g. soil venting or tunnelling under compressed air.

In the first part, the principles of inverse modelling were reviewed. The least-squares objective function and different methods for its minimization were described. Important issues like weighting, convergence and the problem of parameter correlations were discussed. Finally, different methods of evaluating model fit after a successful optimization run were presented. Different stochastic characteristics and a graphical interpretation method were described.

Subsequently, a computational framework for the inverse modelling of the aimed field test was developed. The framework consists of the two-phase flow program FT_2009 and the universal inverse modelling software UCODE_2005 (Poeter et al. 2005). FT_2009 is able to simulate any type of multi-step inflow/outflow experiments. Modified respectively new air permeability functions that account for a different flow behaviour than the commonly used models were implemented into the program. The integrated data evaluation of FT_2009 and the straightforward communication scheme with UCODE_2005 ensure an efficient inverse modelling procedure.

The proposed experimental setup of the field test was outlined. The test procedure with a water infiltration and subsequent air injection phase was described. The problem of tensiometer measurements at non-atmospheric air pressures was discussed. At non-atmospheric air pressures tensiometers do not measure capillary pressures but water pressures. Additionally, the possibility of soil heaving and macro-pore development during the air injection was addressed. It was concluded that the applied pressure head during air injection phases should not exceed the dead load of the soil above the injection area. Alternatively, additional dead loads should be applied to the surface.

The program FT_2009 was employed to carry out simulations of the field test performance. A hypothetical test with three water infiltration steps and three air injection steps was simulated. The water and air flow rates were computed. For selected reference points in the soil, the water saturation, the capillary pressure, the air and water pressure distributions were evaluated. A rather distinct distribution of the water pressures was computed for the air injection phase: despite the unsaturated soil state, the water pressures at the reference points were above atmospheric level during all air injection steps. The simulation results also indicated that the drainage of the soil takes significantly more time than its wetting.

The simulation results of the hypothetical field test were used for extended inverse modelling studies. The aim was to check the functioning of the development computational framework and to study the characteristics of the regression for a different number of optimized parameters and observation data. It proved that the use of flow rates as single observation data set yields enough information for the unique estimation of four parameters. If solely water pressures were used for the regressions, only the optimization runs with three parameters resulted in unique solutions. A combination of flow rates and water pressure data showed that the inverse problem is well-posed even in the five parameter objective-function space. If for some constrains the number of optimized parameter needs to be reduced, the residual water saturation is a suitable choice, because for the majority of the conducted regressions the objective function showed the lowest sensitivity with respect to this parameter.

In summary, the following recommendations are given for the practical application and inverse modelling of the field test:

- **Preliminary numerical simulations:**
  To optimize the experimental setup, it is useful to conduct preliminary numerical simulations of the field test. For this purpose, the soil parameters can be estimated from the grain size distribution (e.g. Jackson 1972, Arya et al. 1999) or unsaturated soil data bases (e.g. UNSODA). That way the dimensions of the infiltration/injection pipe can be determined and the capacity of the air supply equipment can be estimated. Additionally, the best locations for measurement devices in the soil can be determined.

- **Test execution:**
  The numerical simulations showed that the drainage of the soil by air injection occurs much more slowly than its wetting. It is therefore recommended to conduct a significantly longer air injection phase than water infiltration phase. If possible, the individual pressures steps should be continued until a steady-state is reached. The application of pressure heads higher than the dead load of the soil above the injection area has to be done with care. A subsequent analysis of the air flow rates will give hints whether or not the soil texture experienced alterations during the test execution.

- **Inverse modelling of the field test:**
  In principle, the obtained results suggest that the inverse modelling of the field test can be carried out with flow rates as single regression data. However, the integration of water pressure data will facilitate the convergence of the inverse solution and yield more accurate parameters. The regression of the field test with water pressure data only, will at least require measurements at two different reference points. It is also recommended to measure the water content in the soil to allow qualitatively checks of the inverse solution. Water content measurements, despite their mentioned uncertainties, can give valuable hints on the type of the air permeability function (e.g. indication of a convex shape due to macro-pore development). If significantly hysteretic water retention behaviour is expected, it may be necessary to execute two inverse modelling cycles (Durner et. al 1999): one for the water infiltration phase and one for the air injection phase.

It has been stated that the parameters obtained by the inverse modelling of the field test are especially meant for applications with predominant air flow. Whether the parameters are of general use for the determination of the water retention and relative permeability functions has to be evaluated by comparing the measurements which are, for example, obtained by steady-state methods. For this purpose and the general validation of the developed field test, a number of applications in different soil types is desirable.

3 Execution and inverse modelling of air injection field tests

3.1 Introduction

This chapter deals with the execution and inverse modelling of the two-phase flow field test that has been designed and studied in the previous section. In comparison to the original design no water infiltration phase is conducted. Instead, the air is injected into fully saturated ground in a short distance below a shallow groundwater table. A total number of three tests in three different soils is executed.

There are several reasons for the modified test procedure. Firstly, the aimed main application of the field test is tunnelling under compressed air. Here, the escaping air drains the soil from an originally saturated state to an unsaturated state. The air injection into originally saturated ground is therefore conceptually identical with the site specific conditions. Secondly, the problem of dealing with hysteretic soil behaviour is avoided. Thirdly, the initial conditions for the numerical model can be determined more readily according to full water saturation and hydrostatic pressure distribution below the groundwater table. Additionally, it is considered advantageous to start with a simple procedure because the field test is realized for the first time; more complex features (e.g. numerical modelling of hysteresis) can be incorporated step by step in subsequent applications.

The chapter starts with a literature review on the inverse modelling of different transient flow experiments. Subsequently, the general procedure of the field test execution is outlined. The test location and the ground conditions are described. The installation of the experimental equipment, measuring devices and data acquisition systems is explained. Thereafter, the practical execution of the test is specified. In order to study the applicability respectively the effects of high air injection pressures, the excess pressure is increased stepwise to a maximum value of 50 kPa in the last test step.

Subsequently to the description of the general test procedure, each of the three field tests is dealt with in a separate section. To begin with, the measurement results for air flow rates, water pressures and saturation distributions are presented. The selection of observation data for the inverse modelling of the tests is explained. The detailed inverse modelling of the field tests is described. Thereafter, the obtained results are discussed and interpreted. Finally, the results are summarized and recommendations for the further development of the field test are given.

3.2 Literature review: inverse modelling of transient flow experiments

3.2.1 General information

The review focuses on selected examples of the inverse modelling of transient flow experiments. A wide range of different tests is covered: transient one-step and multi-step as well as one-phase flow and two-phase flow experiments are reviewed. Different findings concerning the type and number of parameters that are used for model calibrations are evaluated. The literature examples are compared with the conclusions from the theoretical inverse modelling examples of the previous chapter. The aim of the review is to get more input for the inverse modelling of the subsequently conducted field tests.

3.2.2 Examples

- **Van Dam et al. (1994)**
  The suitability of data from outflow experiments with Tempe pressure cells using the one-step and multi-step method is investigated. It is found that the one-step method does not realistically represent field conditions because of the large initial gradient. Moreover, in many cases non-unique inverse solutions are obtained. It is concluded that four to five parameters of the Van Genuchten-Mualem model (Van Genuchten 1980; Mualem 1976) can be estimated by using only outflow data of multi-step outflow experiments. It is recommended to determine the residual water content θ_{wr} and the saturated water content θ_{ws} by independent measurements. In order to maintain a sufficient flexibility of the permeability function the tortuosity factor τ should be optimized and not fixed at the common value of 0.5.

  Another point that is addressed concerns the initial conditions of the flow experiments. Outflow experiments starting from saturated conditions show non-uniform flow (Hopmans et al. 1992). This violates the Darcian flow concept which is based on uniform flow. To reduce this problem, it is recommended to exclude the water permeability k_{ws} from the optimization procedure if the experiment incorporates water saturated and very dry states.

- **Eching et al. (1994)**
  Multi-step outflow, evaporation and infiltration experiments are used for parameter optimization. In order to avoid interference of the results with non-uniform flow behaviour, the experiments are started under unsaturated conditions. Richards' equation (Richards 1931) and the VGM model are

employed to numerically simulate the unsaturated water flow. Cumulative water flow volume and simultaneously measured water pressure heads are used in the objective function.

In general, four parameters are optimized. The tortuosity factor τ is fixed at a value of 0.5. The saturated water content θ_{ws} is measured independently. Very good agreements between optimized values and direct measurements are obtained for the water retention curve. For the investigated sandy soil, large deviations between optimized values and direct measurements are obtained for the hydraulic conductivity function at high water saturation.

The optimization results indicate that the problem of non-uniqueness of the estimated parameters is reduced greatly if cumulative water outflow and simultaneously measured water pressure values are used in the objective function. However, if the saturated water conductivity k_{ws} is incorporated into the optimization procedure, it is found to be a fitting parameter without physical meaning. Since the experiments are started with unsaturated specimens, the obtained results are not accurate in the low suction range (Van Dam et al. 1992).

- **Chen et al. (1999)**
  A modified multi-step outflow method is used to provide experimental data for the inverse parameter optimization of different two-fluid flow systems. The investigated materials are sand and a fine sandy loam. Seven different parametric models are tested in their ability to fit the observation data. A two-phase flow approach is employed for the numerical simulations. Cumulative water outflow, water pressure head data and a directly measured value of the water retention curve are used in the objective function. An arbitrarily fixed weighting factor of 15 is assigned to the prior information.

  At the different optimization runs, three respectively four parameters are optimized. The saturated water content θ_{ws} and the tortosity factor τ are fixed. It is argued that fixing the saturated water conductivity k_{ws} overcontrains the permeability relationship. It is found that the Van Genuchten-Mualem model (Van Genuchten 1980, Mualem 1976), the Kosugi-Mualem model (Kosugi 1994, Mualem 1976) and the Brutsaert-Burdine model (Brutsaert 1967, Burdine 1953) fit the observation data very well. Despite having one parameter less, also the Gardner-Mualem model (Gardner 1958, Mualem 1976) shows a very good performance. The Brooks-Corey (1964) types of models do not converge in several cases respectively yield poor model fits.

- **Durner et al. (1999)**
  A state-of-the-art report on the inverse modelling of inflow/outflow experiments is presented. Different variants and aspects of these types of

experiments are investigated. Richards' equation (Richards 1931) and the VGM model are used for the numerical simulations. Additionally, a bimodal water retention model (Durner 1994) is employed.

Durner et al. (1999) conclude that inflow/outflow experiments provide sufficient information to obtain unique optimizations of up to five parameters of the water retention and hydraulic conductivity function. However, for soils with structured pore systems, the use of bimodal hydraulic functions is necessary. Omitting the saturated respectively nearly saturated state is likely to leave the parameters of a structural pore system unidentifiable.

The multi-step method is proved to be superior to the one-step method, which is mathematically ill-posed in many cases. The continuous method with a gradually changing pressure gradient is an attractive alternative but requires independent measurements of either the saturated hydraulic conductivity k_{ws} or the residual and saturated water content θ_w. An important aspect is that k_{ws} can never be estimated accurately by an inflow/outflow experiment because the conductivity function becomes very insensitive towards saturation.

Although a hysteretic modelling approach is employed, the inverse modelling of a combined inflow/outflow experiment can only be accomplished successfully with independent sets of parameters for the outflow and backflow phase. The encountered problems are referred to the non-negligible resistance of air flow, which cannot be accounted for by using Richard's equation. Furthermore, Durner et al. conclude that progress will continue towards de-coupling of the conductivity and retention characteristics.

- **Hwang and Powers (2003)**
  The capability of six soil hydraulic models to yield unique parameter sets for sandy soils from multi-step outflow data is investigated. An additional focus of the research concerns the saturated water conductivity k_{ws}. A single-phase flow model is adopted. The experiments are started from unsaturated conditions. Cumulative water outflow, water pressure head data and the initial water content of the specimen are used in the objective function. An arbitrarily fixed weighting factor of 15 is assigned to the water content value.

  The optimization of differently constituted parameter sets is investigated. It shows that parameter estimations including both the residual and saturated water content θ_w are generally not unique. Also, non-unique parameter sets are obtained for optimization runs if k_{ws} is used as fitting parameter. In these cases, the permeability values are generally estimated too low; this is due to the significant drop of conductivity in the range of high water saturation for soils with narrow pore size distribution. On the contrary, very good fits are obtained if the tortuosity factor τ is employed as fitting parameter.

As a consequence, Hwang and Powers recommend fixing k_{ws} at its independently measured value; otherwise, k_{ws} loses its physical significance and should be viewed as an empirical parameter that yields the best fit in the optimization problem. Hwang and Powers conclude that τ has a key function in describing the steep increase of the hydraulic conductivity function of sandy soils. It should be included into the optimization rather than being fixed at 0.5. In order to maintain the physical meaning of the saturated water content and to obtain unique parameter sets, fixing the saturated water content θ_{ws} at its measured value is recommended, too. Among the investigated constitutive laws, the Kosugi-Mualem model yielded the best fits. However, also the Van Genuchten-Mualem model showed an excellent performance.

- **Chinkulkijniwat (2005)**
  The inverse modelling of a two-phase flow air injection laboratory experiment is conducted. Air is injected at the bottom of an originally water saturated soil column by air injection. The investigated material is fine-medium sand. Air pressure and volumetric water content measurements are used for the optimization. The Van Genuchten-Mualem model respectively the Corey-gas permeability function (Corey 1954) are used to describe the fluid related properties of the sand.

  Four respectively five parameters are optimized. The saturated hydraulic conductivity k_{ws} and the saturated water content θ_{ws} are measured independently. The tortuosity factor τ is optimized. Appropriate initial guess parameters are derived from the grain size distribution. That way, convergence is achieved efficiently. However, relatively poor model fits are obtained. The parameter α seems too low for the relatively coarse soil. A comparison with independently measured values of the water retention curve, for example, is not available. The analysis of residuals and model run statistics indicates model bias (Chinkulkijniwat 2005).

  Chinkulkijniwat states that macro pore development was observed in the course of the flow experiment. This alteration of the original soil texture probably causes different air relative permeability behaviour than described by the Van Genuchten-Mualem function and similar models. However, the macro pore development is not explicitly accounted for.

- **Velloso et al. (2007)**
  A field water infiltration test with simple experimental set-up is developed. The infiltration takes place at constant pressure head. Two tests in a young residual soil are conducted. Richards' equation (Richards 1931) and the VGM model are used for the numerical simulations. Tensiometer measurements at 12 cm distance from the infiltration area constitute the optimization data.

Three parameters are optimized; among these the saturated water permeability k_{ws}. The tortuosity factor τ is fixed at a value of 0.5. The residual and saturated water contents θ_w are obtained from independent measurements. Good model fits and agreements with independently measured water retention characteristics are obtained. However, for one of the presented optimizations, a critical parameter correlation of 0.96 is obtained between the saturated water conductivity k_{ws} and the n-value. The correlation indicates that (1) the saturated water conductivity can only be estimated with relatively high uncertainty and that (2) unique optimizations of more than three parameters are probably not possible. More observation data, e.g. additional tensiometer measurements at a second reference point or water flow rates, would be necessary for this purpose.

3.2.3 Conclusions

The review shows that different approaches are chosen for the inverse modelling of transient flow experiments. The major differences concern the kind of data that are used for the optimization procedure and the type of the estimated parameters. Some authors (e.g. Van Dam et al. 1994) state that flow rate observations of multi-step outflow experiments provide sufficient information for parameter optimization; other authors (e.g. Eching et al. 1994) state that additional water pressure head measurements inside the specimen are necessary to obtain unique parameter estimations. Similarly, different opinions exist whether the τ-factor and k_{ws} should be optimized or measured independently.

Despite the described different approaches and findings, some agreements are common to most of the examples:

- The Van Genuchten-Mualem model is generally able to fit the model regressions well. However, this relates principally to the water retention curve and the water permeability function. The suitability of the air permeability function has been studied far less intensively.

- Among the five or six parameters of the constitutive models, the parameters α and m (respectively n) are always optimized.

- Independently of the number of optimized parameters, either the tortuosity τ or the saturated water conductivity k_{ws} is estimated, but never both simultaneously.

- If the saturated water conductivity is estimated, it is subject of relatively high uncertainty and its physical meaning is weakened.

- Using water pressure head data additionally to flow rates facilitates convergence and yields more accurate parameter estimates.

- Multi-step flow experiments are more suitable to provide data sets for parameter optimization than one-step flow experiments.

The conclusions from the reviewed literature examples are mostly consistent with the findings from the conducted theoretical inverse modelling examples in chapter 2. For example, it was found that the use of only one series of tensiometer measurements allows the estimation of three parameters and that the use of flow rates and water pressure head data yields more accurate parameters. On the other hand, the low sensitivity of the saturated water conductivity could not be derived from the investigations in chapter 2. Here, a low sensitivity was identified for the residual water content θ_{wr}.

It has to be kept in mind those rather different experimental set-ups and boundary conditions were employed in the reviewed examples. Thus, some findings may only apply for a specific type of experiment while others may have general validity. Probably the best way to get information on the inverse modelling of transient flow experiments is to carry out preliminary optimizations with synthetic observation data. However, for these theoretical examples there is no measurement noise and no modelling error. Thus, the obtained results (e.g. on the number of parameters that can be estimated) should be considered as best case scenario that does not always apply in field conditions.

3.3 General test procedure

3.3.1 Test site and ground conditions

The test site is located in the municipal area of Stuhlfelden, Austria, approximately 20 km west of Zell am See. The field tests are executed in pasture land owned by the Dorfner-Bauer, approximately 300 - 500 m south of the Pirtendorfer Salzachbrücke. The test site can be accessed via dirt road. The geographical location of the test area is depicted in Figure 3.1.

The regional geography is dominated by the Salzachtal, which extends in east-west direction in this area. Approximately in the middle of the valley floor the river Salzach is located. From the surface to shallow depths, the soils are principally constituted by silts and sands which have been deposited during flooding events of the Salzach. During the period of the conduction of the field tests (September/October 2010), the ground water level was encountered between 0.8 and 1.5 m below the ground surface.

Figure 3.1: The location of the test area in Stuhlfelden/Salzburg (Sagis 2009).

The ground surface is covered by a 5 - 7 cm thick sod-humus layer, which is rooted in a 25 - 30 cm thick compact clayey silt layer of low water permeability. Below, sands with greater or lesser finer content are encountered. The sands reach a mightiness of at least 2.5 m. The ground was not explored to greater depths. The properties of the sand layer vary strongly within small horizontal distances, but are relatively homogeneous over the depth. Within a distance of 200 m, three locations with three different soils were selected to execute the field tests. Due to their sedimentary origin, the sands show a pronounced horizontal texture. Figure 3.2 shows the three soils in disturbed and undisturbed conditions.

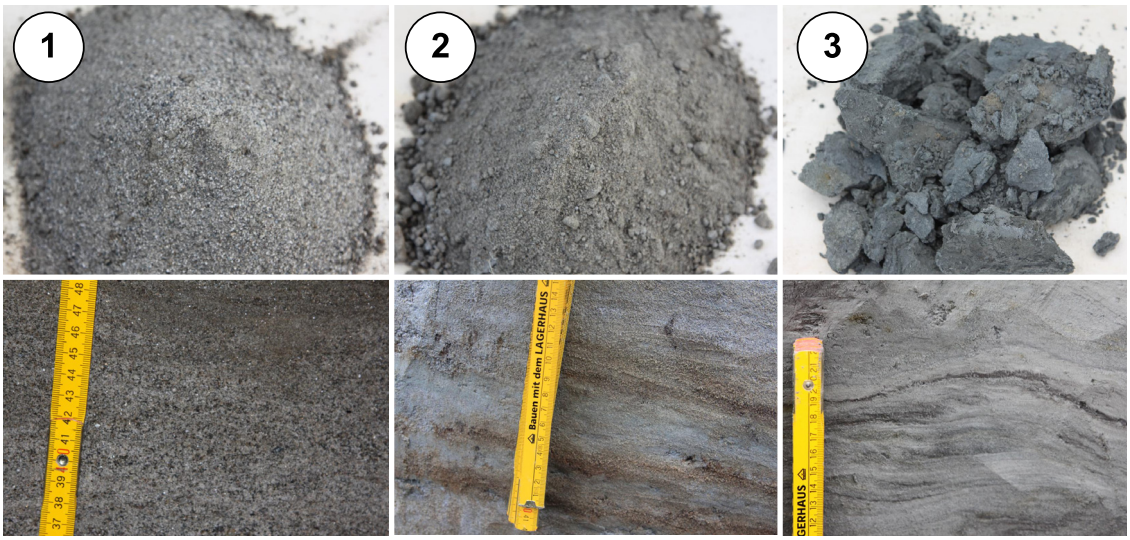

Figure 3.2: The soils in which the field tests are executed (Hirscher 2010).

The three soil types in which the field tests are executed are a (1) medium-coarse sand, a (2) silty fine sand and a (3) silt-fine sand. Only the silt-fine sand shows an apparent cohesion. Of each of the three soils, four to six undisturbed samples were investigated in the laboratory. The grain size distribution, the water permeability, porosity and dry density were determined. Table 3.1 summarizes the results of the laboratory investigations. The water permeability is related to a temperature of 10° Celsius. The permeability tests of soil 1 in horizontal direction could not be conducted successfully.

Table 3.1: Characterization of soil types.

	unit	**soil 1**	**soil 2**	**soil 3**
soil type	**-**	medium-coarse sand	silty fine sand	silt – fine sand
gravel	[mass%]	3.2	-	-
sand	[mass%]	96.8	79.0	50.9
silt	[mass%]	-	21.0	49.1
uniformity-coefficient U	[-]	2.0	5.0	3.0
grain density ρ_s	[g/cm³]	2.73	2.72	2.70
dry density ρ_d	[g/cm³]	1.61	1.45	1.46
porosity n	[-]	0.41	0.46	0.46
water permeability-horizontal $k_{ws,h}$	[m/s]	-	$1.55 \cdot 10^{-5}$	$4.15 \cdot 10^{-6}$
water permeability-vertical k_{wv}	[m/s]	$2.0 \cdot 10^{-4}$	$1.40 \cdot 10^{-5}$	$3.10 \cdot 10^{-6}$

3.3.2 Installation of the experimental set-up

The test installation begins with a circular excavation of 3.0 m diameter. The top soil and the 25 cm thick silt layer are removed. This measure is carried out in order to encourage air flow towards the surface and not below the relatively impermeable silt layer. The excavation is continued down to a level of + 75 cm with respect to the groundwater table.

Subsequently to the preliminary excavation, a 120 cm deep borehole is excavated with help of a secondary pipe with 10 cm diameter. A steel pipe with a filter at the end is placed into the borehole. The filter has a diameter of 10 cm and a height of 20 cm. An impermeable base plate is adjacent to the filter. The

injection of the air takes place in a distance of 10 to 30 cm below the shallow groundwater table. After the installation of the filter and the steel pipe, the secondary pipe is removed and simultaneously refilled with a clayey soil.

In the soil around the filter, four tensiometers and four TDR-probes are installed at two different radii (approximately 20 and 35 cm). Two tensiometers and two TDR-probes are installed at each radial distance. The exact distance is adapted to the soil type. The measuring devices have a shaft length of 120 cm and are installed with help of a lance borer of 28 mm diameter. After the installation of the air injection lance and the measuring devices, a 30 cm thick gravel layer is filled into the excavation pit. This additional dead load is meant to prevent pneumatic ground break due to the pressure gradient of the injected air. The layout of the experimental setup is depicted in Figure 3.3.

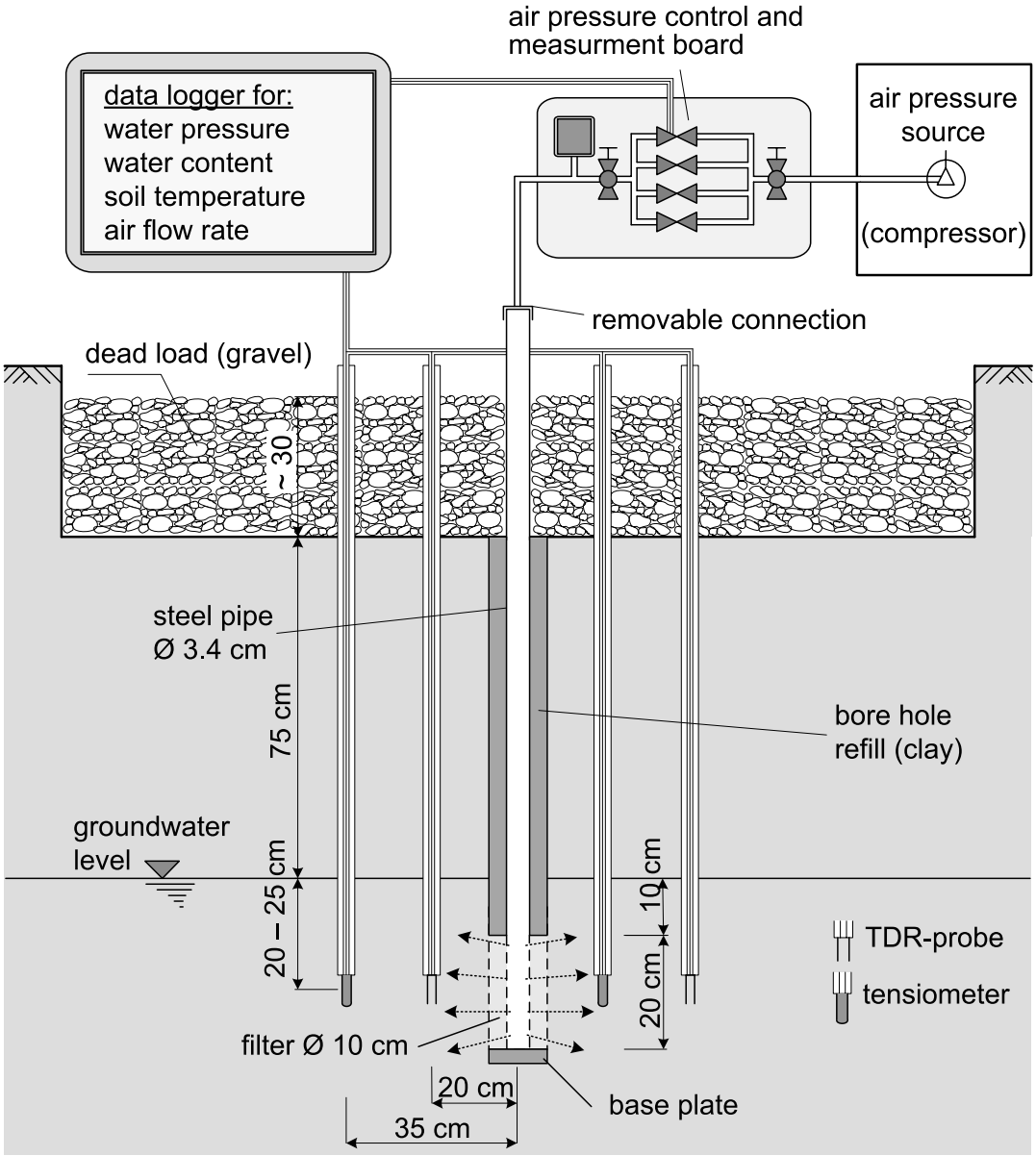

Figure 3.3: The experimental system of the field tests (after Hirscher 2010).

The compressed air during the execution of the field test is delivered by a compressor with a free air capacity of 4.9 m³/min. The air pressure and the air flow rate are controlled respectively measured by a fabricated control board. A data logger stores the measurements of water pressure, water content and soil temperature. A notebook is used for the continuous visualisation and control of the test performance. A series of pictures in Figure 3.4 illustrates the installation and final setup of the field test.

a) Preliminary excavation-covered with a membrane to prevent excessive evaporation.

b) Secondary pipe for filter installation; boring of holes for the TDR-probes and tensiometers.

c) Installed air injection pipe and measuring devices; beginning of back filling with coarse gravel.

d) Measuring points for levelling measurements; gravel refill.

e) Completed field test set-up during test execution.

Figure 3.4: Photo series of field test installation and execution.

The field tests are conducted at constant pressure magnitudes, which are increased stepwise. The corresponding air flow rates are measured. The opposite procedure is usually employed for pneumatic tests in fractured rocks: constant air flow rates are injected and the steady-state pressures in the pipe and other bore holes in the ground are measured. However, in soils such a procedure could produce pressure accumulations that results in large deformations respectively alterations of the soil structure. Therefore, this approach is considered as not suitable for granular materials.

3.3.3 Air pressure control and measurement

The control and measurement of the air injection pressure respectively of the air flow rate is a key issue of the field tests. A control board was designed and fabricated for this purpose; basically, it consists of two pressure regulators, a manometer and four measuring valves. Figure 3.5 shows a picture of the employed air injection control and measuring board.

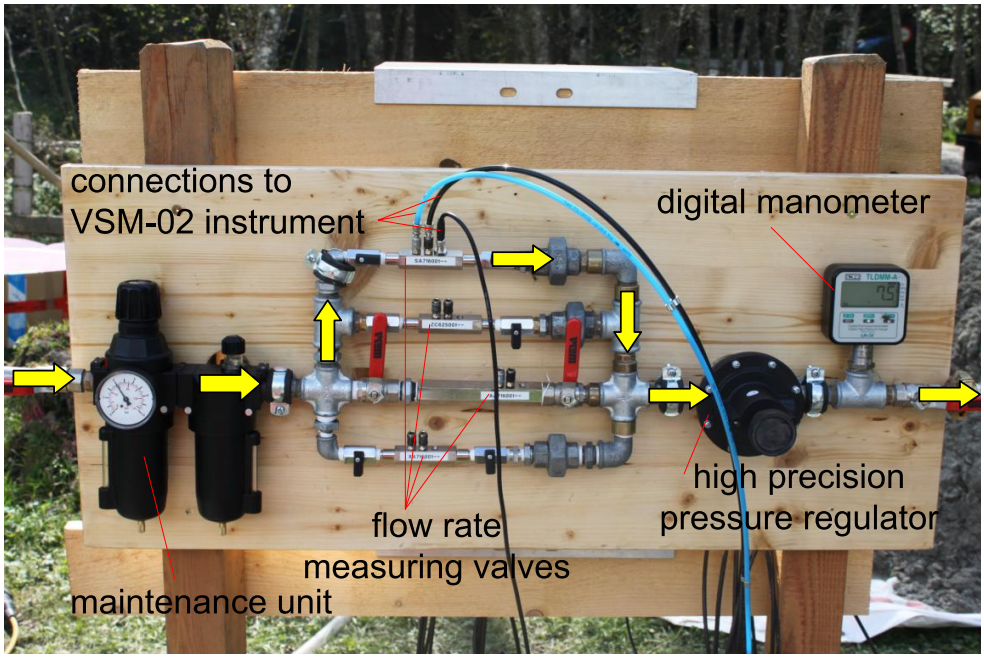

Figure 3.5: Air pressure control and measuring board.

Compressed air is supplied by the compressor with a pressure up to 8.2 bar. The maintenance unit of the control board serves to reduce the pressure to 4 bar and to filter the compressed air. A high precision pressure regulator (0 - 0.7 bar) with an accuracy of 0.07 kPa is used for the final regulation of the air pressure. Because of the initially low air injection pressures of only 5 kPa, a high flow capacity of this pressure regulator is required. A digital manometer (0 - 1 bar) allows the measurement of the air pressure with an accuracy of 0.1 kPa.

The measuring of the air flow rate is based on differential pressure measurements. Four calibrated valves with different flow capacities are mounted on the control board. Only one valve is active at the same time, see Figure 3.5. The valves have a short constriction of the cross section. The VSM-02 instrument (Optiservice GbR 2000) measures the pressure at two different positions of the constriction. The temperature of the air is also measured. The air flow rate is computed as a function of the pressure difference between the two measurement points. The flow rate can be normalized to a specific pressure and/or temperature.

The use of four different measurement valves allows the determination of air flow rates ranging from as low as 0.5 l/min to values as high as 3,125 l/min. The producer of the air measurement equipment (Optiservice GbR, Hellbronn) gives an accuracy of the air flow rates of ± 2.5 % in relation to each measurement.

Further details on the air control and measurement system are provided by Hirscher (2010). The employed tensiometers respectively TDR-probes and their specifications are also described by Hirscher.

3.3.4 Inverse modelling specifications

- **General**
  The inverse modelling of the field tests is conducted with the developed computational framework FT_2009 - UCODE_2005. Different combinations of parameters are optimized in order to obtain the best agreements of simulated and measured values of the conducted tests. The model fit is checked by means of statistical characteristics and also presented graphically.

- **Numerical model**
  The numerical model is basically as described in chapter 2. However, some modifications are necessary due to a different geometry and different initial conditions. Additionally, the dimensions of the model are extended to 4.0 m in horizontal and vertical direction. The filter is modelled with a diameter of 10 cm and a height of 20 cm. Because of the base plate, the bottom of the filter is modelled as impermeable.

  The excavation pit is modelled according to its actual depth and width. Its surface, which is covered by the gravel refill, is modelled as fully water and air permeable. The humus and the silt layer are modelled as impermeable barrier. Thus, the injected air can either flow directly to the surface or can escape below the impermeable layer.

  A hydrostatic pressure distribution is assumed in the area below the groundwater level for the initial conditions. In order to avoid numerical problems, an air saturation of 0.001 is assigned here. Above the groundwater level, an atmospheric pressure of 100 kPa is simulated. Here, the assignment of water respectively air saturation in the model is based on selective TDR-measurements along the vertical profile above the groundwater level.

- **Observation data and their weighting:**
  Air flow rates and water pressure data are employed for the inverse modelling. The TDR-measurements are not used for the regressions, because of their partially problematic performance. However, they constitute additional information for the interpretation of the obtained results.

  Trial runs of the air flow rate measuring equipment showed that for higher flow rates a much better accuracy is achieved than for low flow rates. Thus, for all values larger than 500 l/min, a standard deviation of 2.5 % is used for the weighting. For the lowest measureable flow rate of 0.5 l/min, a standard deviation of 10.0 % is assumed. Intermediate values are linearly interpolated. According to the accuracy of the employed tensiometers, a standard deviation of 500 Pa is assigned to each water pressure value.

3.4 Field test 1

3.4.1 General

Field test 1 is executed in the medium-coarse sand (soil 1; see Table 3.1). The saturated water permeability k_w is approximately $2 \cdot 10^{-4}$ m/s. Thus, relatively high air flow rates are expected even at low injection pressures. Four tensiometers and four TDR-probes are installed in 28 respectively 43 cm distance from the centre point of the filter.

For the identification of possible soil heaving, geodetic height measurements are taken at 10 distinct points by a theodolite. Measurements are taken in three different radial directions at 25, 50 and 75 cm distance from the injection lance (compare Figure 3.4 d). Also, the top level of the injection lance is levelled. Test measurements showed that vertical movements of the measuring points can be detected with an accuracy of at least 1 mm.

The field test is conducted in nine steps with air injection pressures Δp_a ranging from 5 to 50 kPa. The duration of the steps is adapted to the necessary amount of time in which steady-state conditions are reached. The total testing period is 4.75 hours. Table 3.2 gives the duration and pressure magnitudes of the individual steps.

Table 3.2: Duration and injection pressures of field test 1.

step number	**injection pressure Δp_a**	**time t**
-	[kpa]	[s]
1	5.0	240.0
2	7.5	3,600
3	10.0	3,600
4	12.5	2,700
5	15.0	1,800
6	20.0	1,800
7	25.0	1,200
8	37.5	900.0
9	50.0	900.0

3.4.2 Presentation and discussion of measurement results

- **Air flow rate:**
  Figure 3.6 shows the measured air flow rates q_a over the testing time. The air injection pressures Δp_a are also depicted. At 5.0 kPa injection pressure the air does not yet penetrate into the saturated soil. However, already the next pressure step with 7.5 kPa yields a maximum flow rate of 118 l/min. The flow-rates show a jump at the beginning of each subsequent pressure step. A maximum flow rate of 2,047 l/min is reached at the end of the field test.

  The development of the air flow rate is plausible and in agreement with the expected behaviour until the fifth pressure step (15.0 kPa); that is, the flow rate increases at the beginning of each pressure step and reaches a steady value, which is approximately proportional to the pressure increase, towards the end of the step. Some scatter of the measurements is encountered at the beginning of pressure step 5. Here, problems with condenser water falsified the measurements.

  After the fifth step, the flow rates are partially significantly lower than the injection pressure might lead one to expect. A more or less constant air flow is measured from the beginning to the end of the steps. It is supposed that a limiting factor of the air pressure line (e.g. friction in tubes) is the reason for this behaviour.

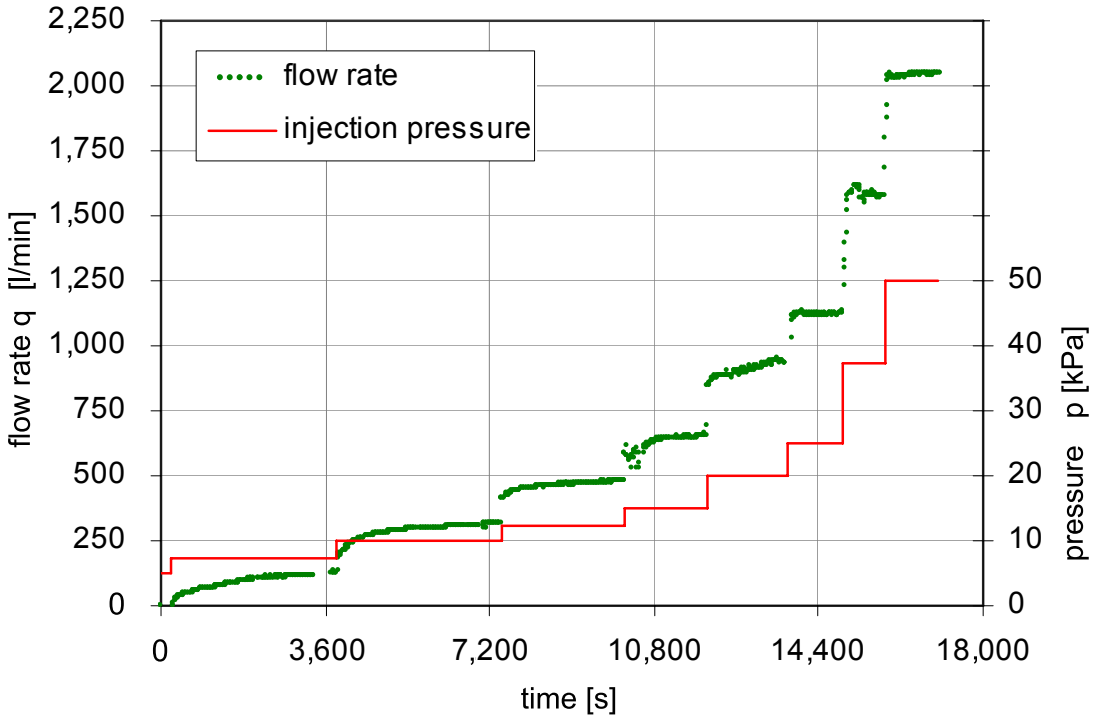

Figure 3.6: Development of air flow rate at field test 1.

- **Tensiometer measurements:**
  Figure 3.7 illustrates the tensiometer measurements of field test 1. Total water pressures are depicted. The distributions are consistent with the theoretical investigations of chapter 3. At the beginning of each test step, the water pressures increase due to the elevated air injection pressure. Subsequently, the water pressures decrease due to the continuous desaturation of the soil. During the whole test duration, the water pressures remain positive, i.e. above the atmospheric pressure of 100 kPa. The tensiometer measurements at the same distance but in different positions are relatively similar. The outer tensiometers give lower pressure magnitudes than inner ones. It can thus be concluded that (1) the measurements are reliable and that (2) the flow regime in the soil is homogenous.

  Generally, the measured water pressure values are relatively low in relation to the applied air injection pressures. Similarly, the variation due to the different air injection pressures is small. The peak values vary between 105.5 and 107.75 kPa for the tensiometers at 28 cm distance, and 105.1 and 107.1 kPa for the tensiometers at 43 cm distance.

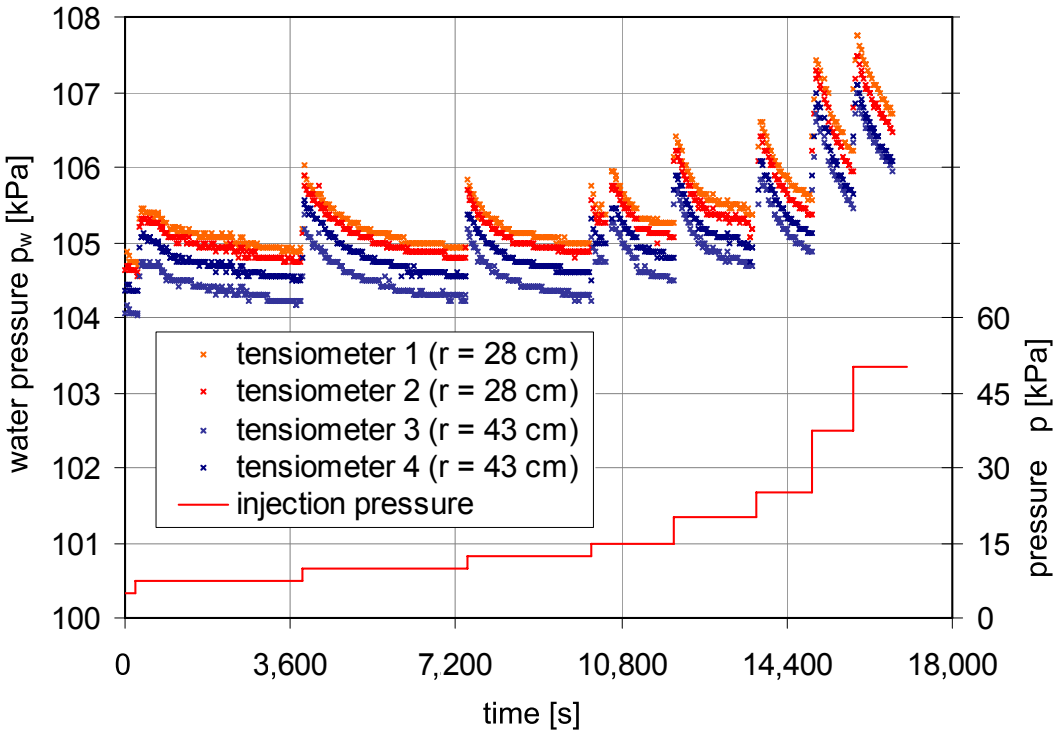

Figure 3.7: Water pressure distributions at field test 1.

- **Water content measurements:**
  The installation of the TDR-probes proved to be difficult. Due to the coarse soil, the bore hole for the installation of the probes was not stable in the area below the groundwater table. As a consequence of the difficult installation, two TDR-probes did not provide data because the measuring shanks bent

respectively broke. Figure 3.8 shows the development of the air saturation at the two remaining measurement points. The air saturation is computed from the water content measurements and the soil porosity.

The initial air saturation of the ground in the injection area is zero. Subsequently, the penetrating air leads to a continuous water desaturation of the soil. However, the air saturation increases rather slowly. Despite the high air flow rate of 314 l/min at the third pressure step (10 kPa), the air saturation reaches only values between 5 and 7.5 % at the two measuring points.

The further measurements of the air saturation are inconsistent with the expected behaviour. The TDR-probe at 43 cm distance from the air injection area shows a higher air saturation than the TDR-probe at 28 cm distance. This behaviour can only be explained by erroneous measurements or a disturbed soil structure due to the air injection. It is likely that the TDR-probe at 43 cm distance gives wrong results because of the sudden jump of more than 10 %, which is obtained when the injection pressure is increased to 20 kPa. However, the final air saturation values are 30.5 and 44.5 % at the inner and outer measuring point, respectively. In general, the observed behaviour of the TDR-probes yields doubts on the reliability of the obtained measurements.

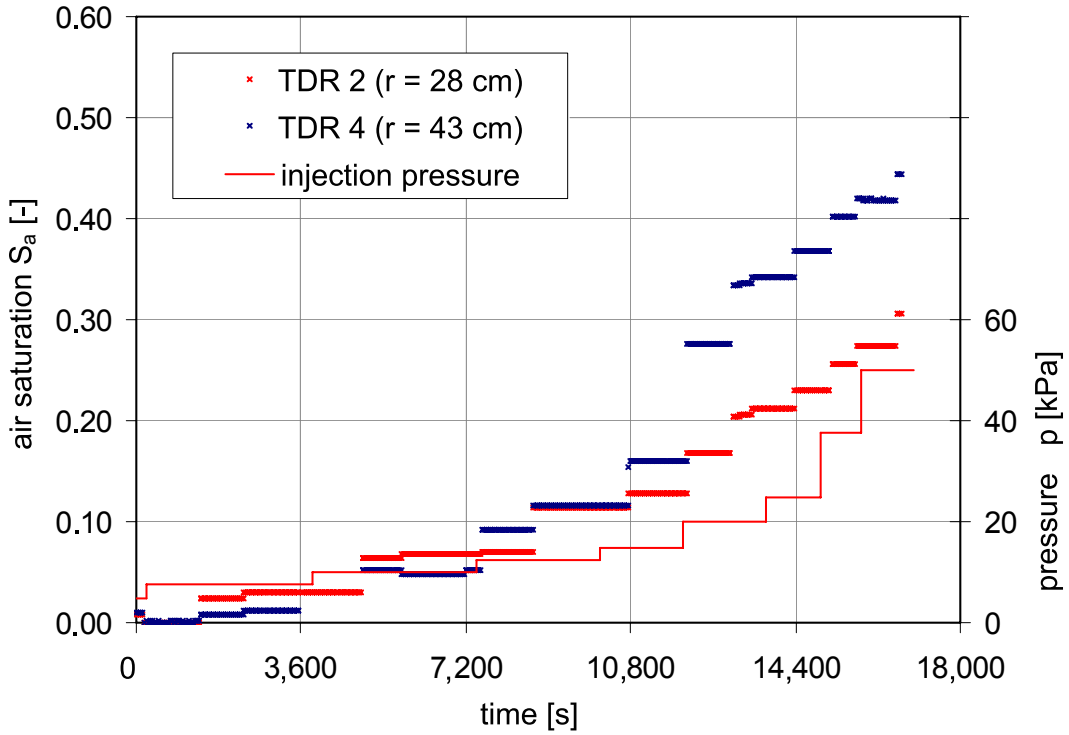

Figure 3.8: Air saturation distributions at field test 1.

- **Temperature measurements:**
  The temperature of the soil respectively of the pore water during test execution is obtained from the TDR-probes. From the beginning of the test

until the fifth pressure step (15 kPa), the temperature is constant at 13.5 ° Celsius at all probes. Towards the end of the test, there is a small drop to values between 12 and 13.1 ° Celsius. For more details, see Hirscher (2010). The environment temperature during the test execution varied between 13 and 15° Celsius.

- **Surface heaving:**
  The level of the 10 reading points remained unchanged during the whole test duration.

3.4.3 Inverse modelling

- **Selection of observation values:**
  The inverse modelling of the field test is conducted with 25 flow rate and water pressure measurements, each. The data is selected in time intervals of approximately 500 seconds from the second until the fifth pressure step. The measurement curves during this period are smooth and in agreement with the theoretical behaviour (see section 3.3.3). No values are selected in the first half of the second pressure step (irregular development of the flow rate; probably due to non-Darcian flow behaviour) and at the beginning of the fifth pressure step (wide data scatter).

  The air injection pressure of the fifth test step is 15 kPa. This value is considerably larger than the estimated air entry value of the investigated soil. Therefore, it is thought that the selected observation data covers a sufficiently wide range to allow an accurate inverse modelling of the field test. The weighting of the observations is carried out by means of the standard deviations specified in section 3.3.4.

- **Approach 1**
  Approach 1 assumes a homogeneous flow regime in the soil, i.e. possible macro pore developments or pore space extensions are not taken into account explicitly. Preliminary trials showed that unique inverse solutions with five optimized parameters cannot be obtained. Furthermore, it proved that the optimization of the intrinsic permeability K_i yields significantly lower permeabilities than those obtained from laboratory tests. Thus, it was decided to fix the intrinsic permeability at its independently measured value.

  The VGM, VGM-mod and (1-k_{rw})-EXP model (see chapter 2) with differently constituted sets of four free parameters are used for the final optimization runs of the field test. The best model fit is achieved with the VGM-mod model in combination with an independent optimization of the *m*-value of the

water retention function (m_{ret}) and the permeability function (m_{perm}). The decoupling of the constitutive functions is consistent with a suggestion of Durner et al. (1999). However, the residual water content θ_{wr} and the saturated water content θ_{ws} are fixed for both functions at values which are derived from laboratory tests. If employed, the exponent p is also fixed at values derived from trial and error runs. The α-value and the tortuosity τ are the additional free parameters. Table 3.3 gives the optimized parameters and their 95 % - confidence intervals. Additionally, the fixed parameters and how they were derived are given.

Table 3.3: Optimization results of approach 1 (with VGM-mod model).

optimized parameters	**unit**	**value**	**confidence intervals**
m_{perm}	[-]	0.651	(0.57 – 0.74)
m_{ret}	[-]	0.415	(0.39 – 0.45)
τ	[-]	0.181	(0.15 – 0.22)
α	[1/m]	12.1	(10.2 – 14.2)
fixed parameters	**unit**	**value**	**origin**
K_i	[m²]	$2.27 \cdot 10^{-11}$	permeability test
θ_{wr}	[-]	0.03	pressure cell test
θ_{ws}	[-]	0.42	= soil porosity
p	[-]	1.0	trial and error runs

The parameter correlations from the regression vary between 0.04 and 0.83. The maximum value is obtained for the α - m_{perm} correlation. This is far from the critical value of 0.95 (Finsterle 1999, Hill and Tiedeman 2007) and suggests that the parameters can be estimated in a unique manner.

A heuristic testing of the uniqueness of the inverse solution by optimization runs with different initial guess parameters revealed contradictory results. The minimized values of the objective function are almost identical, whereas some of the obtained parameter values change more than 1 % between the different runs; this criterion was also used to prove uniqueness in chapter 2. That means that the four-dimensional parameter space of the least-squares objective function has a global minimum in form of a flat large valley and further that a strictly unique estimation of the parameters is not possible. However, the deviations of the optimized parameters are within a limited range (maximal 5 %). Thus, the flow process is assumed to be represented correctly by the obtained parameter sets.

- **Approach 2**
  An analysis of the measurement results shows that rather low air saturation values are obtained throughout the field test. Although the TDR-measurements due to their difficult installation are likely to be falsified, the general trend of the air saturation is supposed to be represented correctly to a greater or lesser extent. Thus, the obtained air saturation curves indicate that the desaturation of the soil respectively the two-phase flow does not take place in the whole pore space but predominantly in macro pores. In this case the macro pores dewater relatively fast, large areas of the pore space remain at high degrees of water saturation at the same time.

  The assumption of the above described flow behaviour results in two consequences. Firstly, the air permeability function shows a steep increase at high water saturation values. Secondly, the estimation of the water retention curve is complicated due to the low change of the water content during the experiment. Thus, the inverse modelling of the field test must be conducted with independent measurements of the water retention curve. Further, the employed constitutive function for the air phase must be flexible enough to reproduce convex shapes of the relative permeability curve.

  Consequently, only the parameters of the permeability functions of water and air are optimized at approach 2. For the water retention function, steady-state measurements from pressure plate tests are used to derive the corresponding constitutive parameters directly. This approach is favoured against using the steady-state measurements as prior information in the inverse modelling. In the latter case, the necessarily assigning of high weights to the steady-state measurements could cause the regression lose meaning and become arbitrary (Hill and Tiedeman 2007).

  Similar to approach 1, four parameters are optimized and the intrinsic permeability K_i is a fixed parameter. Instead of α and m_{ret}, the exponent p and the residual water content are estimated. Table 3.4 gives the fixed and the optimized parameters and their 95 % - confidence intervals.

Table 3.4: Optimization results of approach 2 (with VGM-mod model).

optimized parameters	unit	value	confidence intervals
m_{perm}	[-]	0.357	0.31 – 0.41
p	[-]	1.90	1.40 – 2.70
τ	[-]	0.201	0.13 – 0.31
θ_{wr}	[-]	0.168	0.13 – 0.21

fixed parameters	unit	value	origin
K_i	[m²]	$2.27 \cdot 10^{-11}$	permeability test
m_{ret}	[-]	0.72	pressure cell test
α	[1/m]	4.17	pressure cell test
θ_{ws}	[-]	0.42	= soil porosity

The optimized parameters show correlations ranging from 0.09 to 0.94. The value of 0.94 is obtained for the correlation between the exponent *p* and the tortuosity *τ*. The heuristic check of uniqueness indicates an irregular surface of the objective function. Various optimization runs with different initial guess parameters do not converge. However, the converged runs yield rather similar if not identical parameters.

- **Evaluation of model fit:**
  Table 3.5 gives some statistical characteristics and information on the presented inverse modelling runs for approach 1 and 2. The lower objective-function value and AIC_C criterion indicate a better model fit for approach 1. The negative AIC_C value is a consequence of a negative value of the maximum likelihood objective function value (from which the AIC_C criterion is computed, see chapter 2.2). The coefficients of determination are close to 1.0 in both cases. The presented characteristics principally indicate good model fits for both approaches with slight advantages for approach 1.

Table 3.5: Characteristic values of model fit for approach 1 and 2.

characteristic	approach 1	approach 2
objective function value	13.03	18.75
AIC_C criterion	-55.8	-37.7
coefficient of determination	0.9999	0.9998
standard error of regression	0.532	0.638

A further evaluation of the model fit is given by the analysis of the weighted residuals. The ratio between positive and negative residuals is 27:23 and 25:25 for approach 1 and 2, respectively. However, the distributions of the residuals around 0 are not fully random, as can be seen from the plots in Figure 3.9. The weighted residuals of the flow rates from 200 to 600 l/min are largest and shift from predominantly positive to predominantly negative values. This trend is identical for both approaches. A more evenly distribution is obtained for the water pressure residuals of approach 1. On the contrary, an

anomalistic distribution is given for approach 2. With increasing water pressures, the residuals shift from the positive into the negative range.

The described irregularities may be caused by an incomplete numerical model respectively by constitutive laws that are not fully capable of modelling the flow behaviour in the soil. Another error source are systematic measurement errors. However, it has to be kept in mind that the displayed residuals are from a highly complex two-phase flow field problem and an accordingly complex numerical model. Thus, apart from the described single irregularities, the overall distribution of the weighted residuals is satisfying.

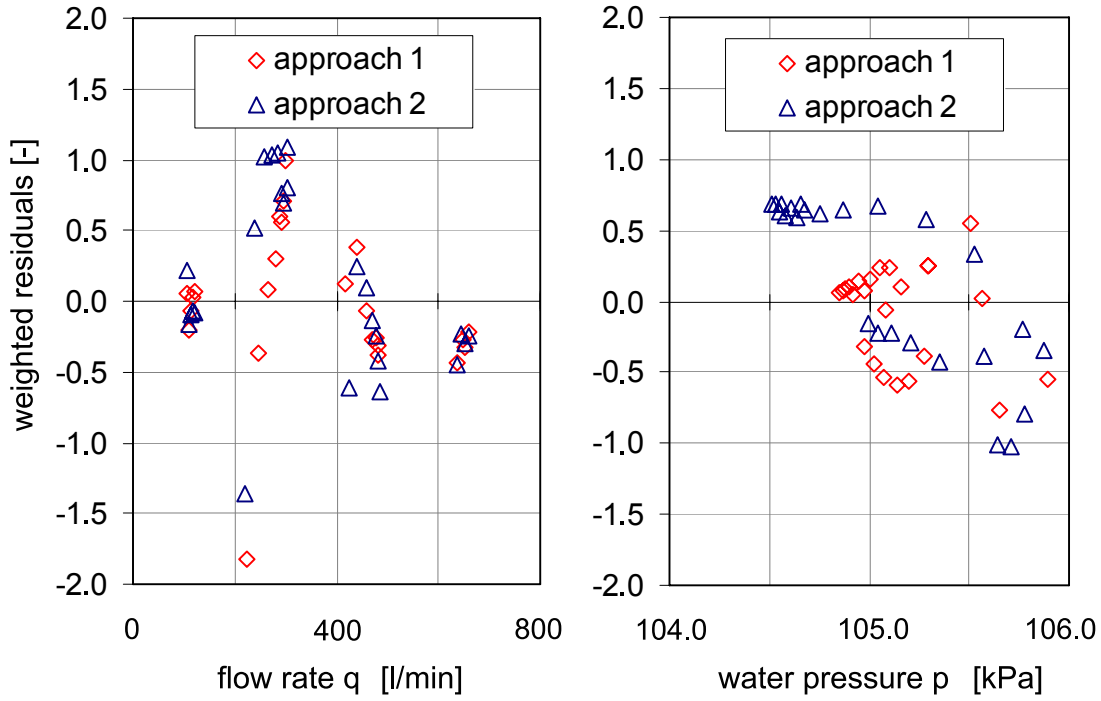

Figure 3.9: Distribution of weighted residuals for approach 1 and 2.

- **Graphical comparison between measured and optimized model response:** Figure 3.10 and 3.11 depict the employed observations and the simulated distributions of the air flow rate and the water pressures, respectively. The range of measuring uncertainty of the observations is additionally depicted.

  The optimized flow rates match the observations very well. A slightly better fit can be recognized for the inverse-modelling approach 1. All simulated values are within the limit of measured value ± measuring accuracy (2.5 – 7.5 % of the measured value). The largest deviations appear between 3,600 and 7,200 s of testing time. Large deviations between the measured and the simulated air flow rates also appear in the initial test phase (approximately during the first half hour; not depicted). Here, the deviations are supposed to be due to the non-uniform flow in the fully saturated soil. For this reason no measurements during this period were used for the optimization.

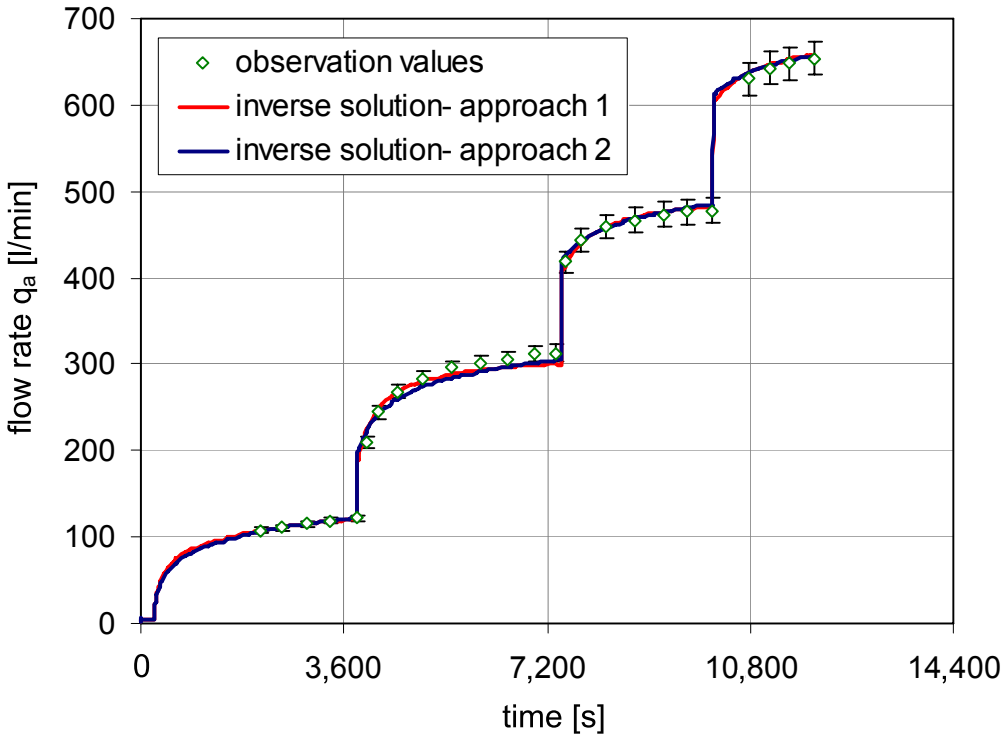

Figure 3.10: Comparison of measured and optimized air flow rates.

The optimized water pressures are all within the measurement accuracy of the tensiometers (± 500 Pa), see Figure 3.11. Approach 1 fits the observations very well, except for the first pressure step. The systematic misfit of the water pressures for approach 2 can be recognized. The simulated values are initially too low, and towards the end they become increasingly too high.

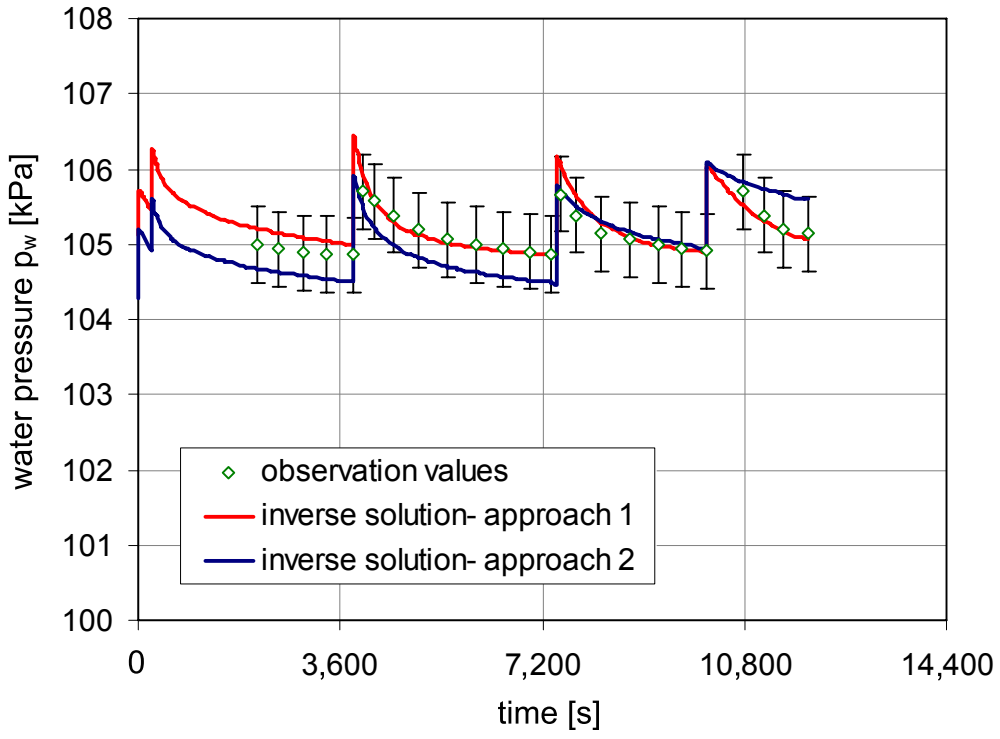

Figure 3.11: Comparison of measured and optimized water pressures.

3.5 Field test 2

3.5.1 General

Field test 2 is executed in the silty fine sand (soil 2; see Table 3.1). The saturated water permeability k_{ws} of $1.55 \cdot 10^{-5}$ m/s in horizontal direction is approximately 15 times lower than in field test 1. Due to the lower permeability, the tensiometers and TDR-probes are installed in a closer distance to the filter. The radial distances are 20 and 35 cm for the first and second set of instruments, respectively. Geodetic height measurements are not taken at field test 2.

The field test is conducted in eight steps with air injection pressures ranging from 7.5 to 50 kPa. The duration of the steps is adapted approximately to the necessary amount of time in which steady-state conditions are reached. The total testing period is 9.75 hours. Table 3.6 gives the duration and pressure magnitudes of the individual steps.

Table 3.6: Duration and injection pressures of field test 2.

step number	**injection pressure Δp_a**	**Time t**
-	[kPa]	[s]
1	7.5	1,970
2	10.0	2,700
3	15.0	3,600
4	20.0	5,400
5	27.5	5,400
6	35.0	6,300
7	42.5	5,400
8	50.0	4,600

3.5.2 Presentation and discussion of measurement results

- **Air flow rate:**
  Figure 3.12 shows the development of the air flow rate over the testing time. Similar to field test 1, the graph shows a jump at the beginning of each

pressure step. At the end of the first step (7.5 kPa), a steady-state flow rate of 7.2 l/min is measured. A maximum flow rate of 1,121 l/min is obtained for the final pressure step of the field test (50 kPa).

The development of the air flow rate is plausible and in agreement with the expected theoretical behaviour until the end of the sixth pressure step (35 kPa); that is, the increase of the flow rate is strong at the beginning and it subsequently develops towards a steady state. Due to the higher water retention potential of soil 2 than soil 1, proportionality between air injection pressure and flow is not given. No data is available for a short period during the sixth pressure step. Here, problems with condenser water hindered useable measurements.

At the two final pressure steps (42.5 and 50 kPa), an approximately constant air flow is measured from the beginning to the end of the steps. Possibly, the pore space experienced an extension which immediately caused a desaturation of the macro pores and thus a steady-state flow. A judgement of this assumption is difficult as no geodetic height measurements of the surface are available. The measurements additionally show a strong scatter which is partially caused by problems with condenser water in the air pressure line.

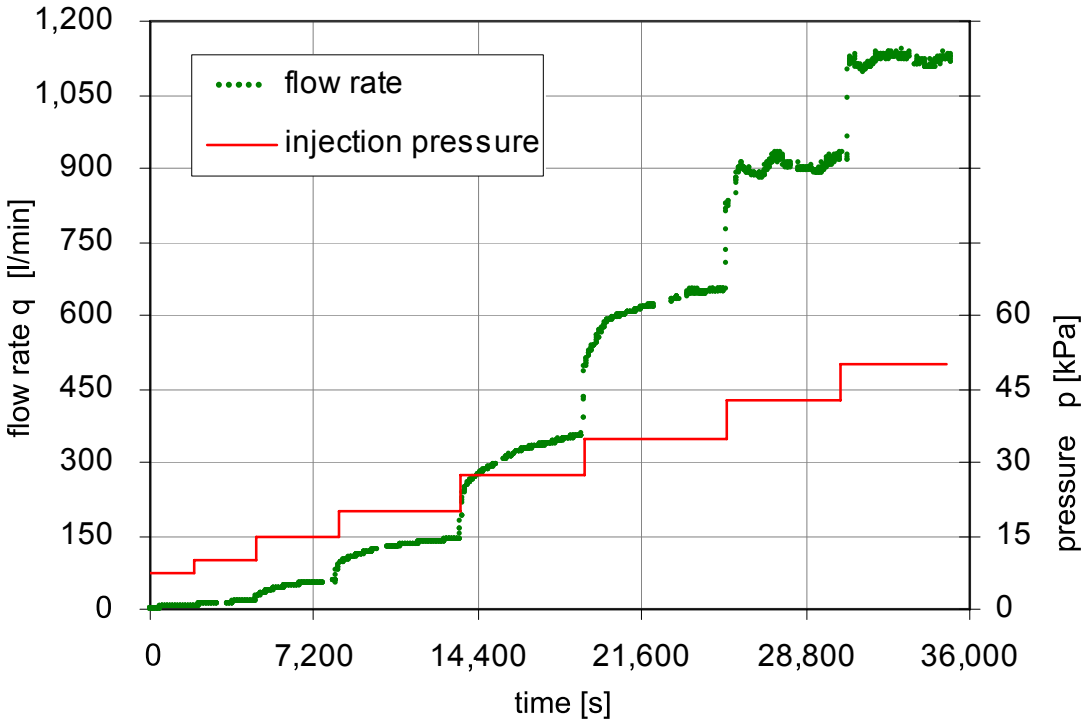

Figure 3.12: Development of air flow rate at field test 2.

Although proportionality is only given to a limited extent, it is interesting to compare the measurements of field test 1 and 2. Flow rates of 7.2 and 121 l/min are measured at 7.5 kPa air injection pressure, respectively. The ratio

between the flow rates corresponds approximately to the ratio of the saturated water permeabilities of the two soils (16.8 and 14.3, respectively). At 15.0 kPa the ratio decreases to 11.9, which is probably due to the higher water retention potential of soil 2. However, the final air flow rates only differ by a factor of 1.8. This clearly indicates a limited air supply capacity at field test 1 and/or an extension of the pore space at field test 2 in the final testing phases.

- **Tensiometer measurements:**
  Figure 3.13 illustrates the tensiometer measurements at field test 2. Similarly to field test 1, the distributions are consistent with the theoretical investigations of chapter 3. The outer tensiometers give lower pressure magnitudes than the inner ones. Due to the higher water retention potential of soil 2 in comparison to soil 1, the water pressure reductions during the individual test steps are more pronounced. However, the water pressures remain positive throughout the test conduction.

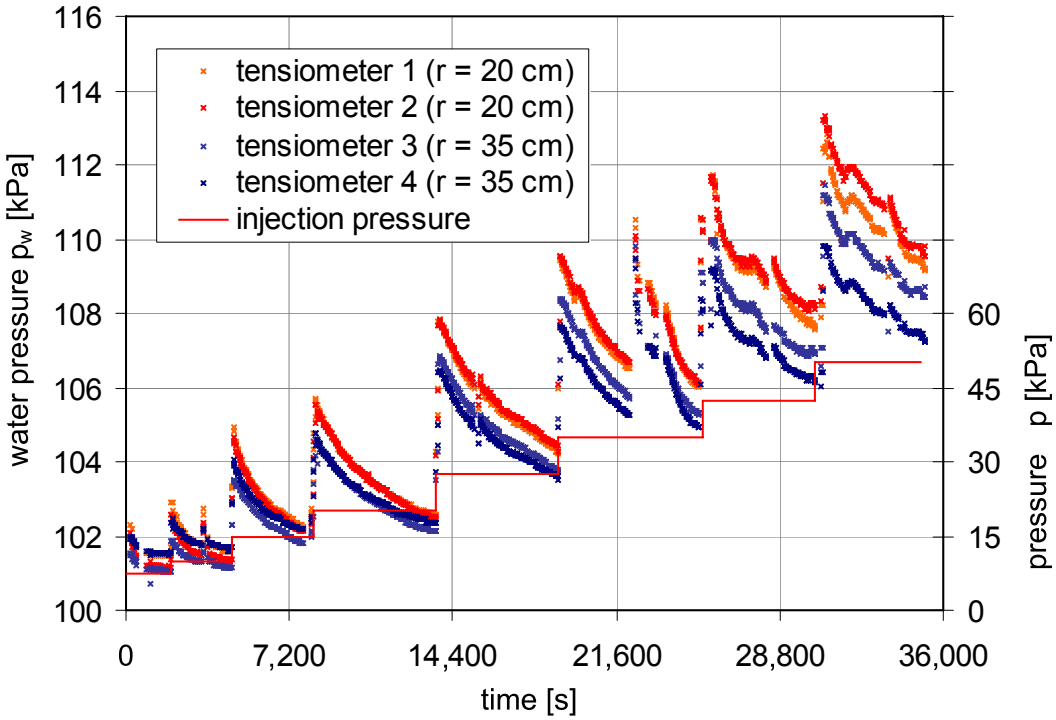

Figure 3.13: Water pressure distributions at field test 2.

Although the measured water pressure values are higher than in field test 1, they are relatively low in relation to the applied air injection pressures. The peak values vary between 103.25 and 113.50 kPa for the tensiometers at 20 cm distance, and 102.0 and 111.5 kPa for the tensiometers at 35 cm distance. For the two final pressure steps, larger deviations between the tensiometer measurements at the same distance but different positions around the filter are encountered. This behaviour is another indication of a disturbed soil structure in the final test phase.

- **Water content measurements:**
  The installation of the TDR-probes in the silty fine sand proved to be less difficult than in the medium-coarse sand of field test 1. Still, the collocation was troubled by the unstable bore hole below the groundwater level. Figure 3.14 shows the development of the air saturation at the four measurement points. The air saturation is computed from the water content measurements and the soil porosity.

  The obtained air saturation values are generally low, similar to field test 1. In opposition to the measured flow rates and water pressures, the behaviour during the two last pressure steps does not deviate significantly from the preliminary test phase. The TDR-probes at different distances from the air injection filter give relatively identical values. The final air saturation values are between 28.0 and 30.5 %.

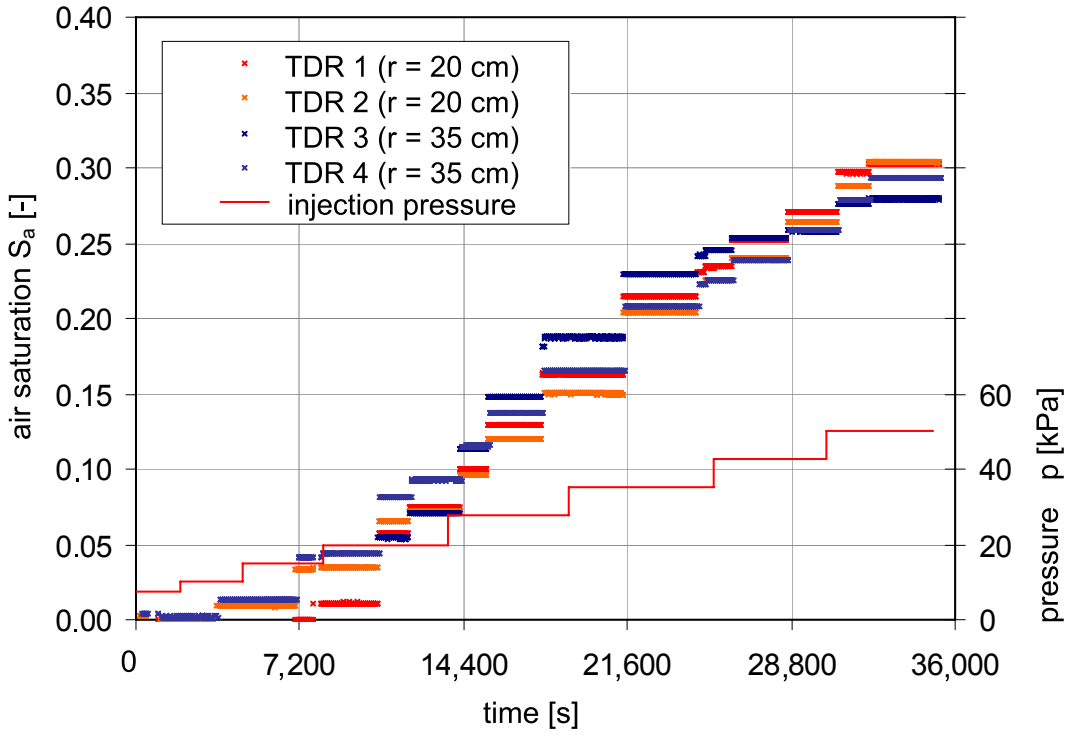

Figure 3.14: Air saturation distributions at field test 2.

- **Temperature measurements:**
  The temperature of the soil respectively of the pore water during the test execution is obtained from the TDR-probes. At 20 cm distance from the centre point of the filter, the temperature varies between 11.1 and 12.7 ° Celsius for the first six pressure steps. At the two final pressure steps, the temperature increases up to 19.2 ° Celsius because of the hot delivered air of the overheated compressor engine. At 35 cm distance from the centre point of the filter, the temperature varies between 12.0 and 13.1 ° Celsius during all

test phases. For more details, see Hirscher (2010). The environment temperature during test execution varied between 13 and 18° Celsius.

- **Surface heaving:**
  No geodetic height measurements were carried out at field test 2; only the top of the injection pipe was controlled by a water level at the beginning and end of the field test. The top level at the test end was 3 mm higher than at the beginning.

3.5.3 Inverse modelling

- **Selection of observation values:**
  The inverse modelling of the field test is carried out with 33 flow rates and 30 water pressure measurements. The data is selected in intervals of 750 - 1,000 seconds from the second to the fifth pressure step. The measurement curves are smooth and in agreement with the expected theoretical behaviour during this period. At the sixth and seventh test step the air flow rate already reaches a steady state at the beginning and shows anomalous behaviour subsequently. No observation values are selected from the first pressure step (irregular development of the flow rate; probably due to non-Darcian flow behaviour). At the end of the fifth pressure step, water pressures values are omitted from the optimization because of the large data scatter in this period.

  The air injection pressure of the sixth pressure step is 35 kPa. This value is considerably larger than the estimated air entry value of the investigated soil. Therefore, it is thought that the selected observation data covers a sufficiently wide range to allow an accurate inverse modelling of the field test. The weighting of the observations is carried out by means of the standard deviations specified in section 3.3.4.

- **Approach 1**
  Approach 1 assumes a homogeneous flow regime in the soil, i.e. possible macro pore developments or pore space extensions are not explicitly taken into account. Equal to field test 1, preliminary trials showed that unique inverse solutions with five optimized parameters cannot be obtained. On the contrary, the inverse runs would not converge if the intrinsic permeability K_i were not optimized. As a consequence of the preliminary inverse runs, the ratio between the permeabilities in horizontal and vertical direction was increased to 1.5, whereas the laboratory tests yielded an average value of 1.1.

  Even with K_i as free parameter, convergence is difficult to achieve and the inverse solutions are generally not unique. Many times the optimizations fail

because of numerical problems. The numerical failures are caused by physically unrealistic parameters that were derived from the optimization iterations. The computation of physically unrealistic parameters is a strong indicator of an ill-posed optimization problem.

The converged inverse modelling runs show generally an erroneous model fit, particularly for the flow rates (see Figure 3.16). They are computed too high during the first pressure steps and too low at the final pressure steps. This result suggests that an increase of the intrinsic permeability occurred during the execution of the field test at the higher air injection pressures, e.g. by an extension of the pore volume or macro pores. The measured elevation of the injection pipe of 3 mm supports this hypothesis. The change of the intrinsic permeability cannot be described in a physically consistent way by the employed numerical models. For the sake of further analyses in subsequent sections, Table 3.7 exemplarily gives the parameters of a (misleading) optimization run of field test 2. The m_{perm}-value was constrained at its lower limit of 0.25 and therefore no confidence intervals could be computed.

Table 3.7: Optimization results of approach 1 (with VGM-mod model).

optimized parameters	**unit**	**value**	**confidence intervals**
K_{iv}	[-]	$2.94 \cdot 10^{-12}$	$(2.6 – 3.2 \cdot 10^{-12})$
m_{perm}	[-]	0.250	constrained
m_{ret}	[-]	0.754	(0.60 – 0.94)
α	[1/m]	0.772	(0.62 – 0.96)
fixed parameters	**unit**	**value**	**origin**
τ	[-]	0.5	standard value
θ_{wr}	[-]	0.07	pressure cell test
θ_{ws}	[-]	0.46	= soil porosity
p	[-]	1.0	trial and error runs

- **Approach 2**
  The optimization runs of approach 1 indicate a rather irregular surface of the objective function surface. Many local minima are encountered. In such a case, the parameter identification with a gradient based search method is complicated and a global optimization procedure may be superior. In order to escape the local minima, approach 2 tries to achieve a better model fit by a combination of trial and error runs and UCODE_2005 runs.

In agreement with approach 1, four parameters are optimized and four parameters are fixed. The intrinsic permeability K_i, the *m*-value, α and the exponent *p* are optimized. The ratio between the permeability in horizontal and vertical direction is fixed with 1:1.5. Based on preliminary trials, a constant value of 0.25 is assigned to the tortuosity τ. The VGM, VGM-mod and (1-k_{rw})-EXP model are employed for the optimizations.

Even with the combined optimization approach, the simulated equivalents can only be matched well either to the flow rate or water pressure observations, but not to both of them simultaneously. An additional problem is that the obtained parameter values from various optimization runs which yield good model fits differ considerably from physical correct parameters. Table 3.8 presents the parameters of an optimization with the VGM-mod model that gives a good fit of the flow rates. Confidence intervals are not available due to the combined inverse modelling procedure.

Table 3.8: Optimization results of approach 2 (with VGM-mod model).

optimized parameters	**unit**	**value**	**confidence intervals**
K_{iv}	[-]	$7.267 \cdot 10^{-12}$	-
$m_{perm,ret}$	[-]	0.817	-
α	[1/m]	0.354	-
p	[-]	0.859	-
fixed parameters	**unit**	**value**	**origin**
τ	[-]	0.25	estimation
θ_{wr}	[-]	0.07	pressure cell test
θ_{ws}	[-]	0.46	= soil porosity
p	[-]	1.0	trial and error runs

Of the optimized parameters, the intrinsic permeability K_i and the α-value of the water retention function show large deviations from results that are obtained from laboratory investigations. It seems that these two parameters together have an opposite fitting function in the optimization rather than a physical meaning. The low *a*-value causes the computation of too high flow rates in the first test phase. On the contrary, the high intrinsic permeability K_i enables the simulation of high flow rates at the higher pressure steps. That way, the misfit of the flow rates in approach 1 is overcome. The expense is that the optimized parameter set produces water pressure values that deviate heavily from the observations.

- **Evaluation of model fit**
  Because of the different inverse modelling procedures, the objective-function value and AIC_C-criterion of approach 1 and 2 are not comparable, and their absolute values are meaningless. Thus, Table 3.9 gives only the coefficient of determination and the standard error of regression. The high coefficient of correlation for approach 1 (0.995) would indicate a good model fit. However, because of the two different kind and wide range of observation data, its meaning is reduced (compare Hill and Tiedeman 2007). The standard error of regression for approach 1 is high (3.60) and beyond acceptable limits for approach 2 (145.3).

Table 3.9: Characteristic values of model fit for approach 1 and 2.

characteristic	**approach 1**	**approach 2**
coefficient of determination	0.995	0.357
standard error of regression	3.60	145.33

The analysis of the weighted residuals once more indicates the problems of both optimization approaches, see Figure 3.15. For approach 1, the weighted residuals are negative for low flow rates and positive for high flow rates. On the contrary, the weighted residuals of the water pressures are relatively evenly distributed around zero. The same applies for the distribution of the weighted flow-rate residuals of approach 2. However, here the water pressure residuals are extremely large, and all of them show positive values.

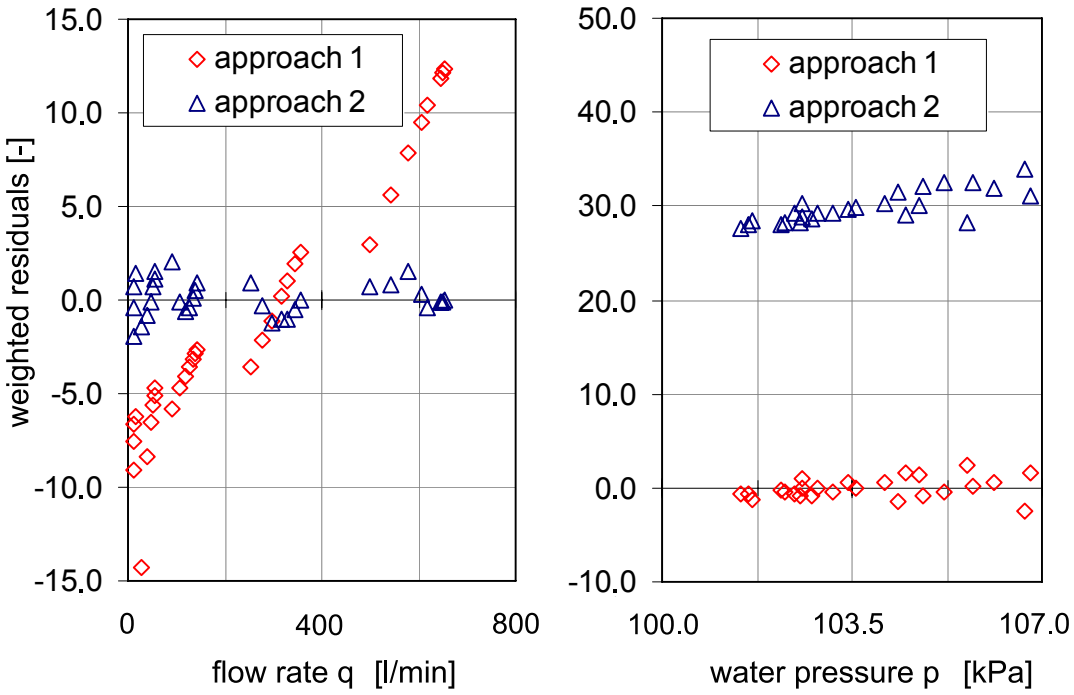

Figure 3.15: Distribution of weighted residuals for approach 1 and 2.

The described irregularities of the weighted residuals may be caused from an incomplete numerical model respectively constitutive laws which are not capable of modelling the true flow behaviour in the soil. Another reason may be systematic measurement errors, particularly of the water pressures. In summary, the analysis of the weighted residuals shows that the optimized parameter sets are not able to represent the true physical flow process.

- **Graphical comparison between measured and optimized model response:** Figure 3.16 and 3.17 depict observations and the optimized distributions of air flow rates and water pressures, respectively. The measuring accuracy of the observations is also depicted (2.5 – 7.5 % of the measurement for the flow rates and a constant value of 500 Pa for each water pressure measurement).

  In Figure 3.16, the totally erroneous representation of the air flow-rate curve by the parameter set of approach 1 can be recognized. This misinterpretation is caused by the water pressure observations, which apparently dominated the regression. The trial and error based inverse modelling of approach 2 yields a good fit of the flow rates. Here, the majority of the simulated flow rates lie within the uncertainty interval of the measurements.

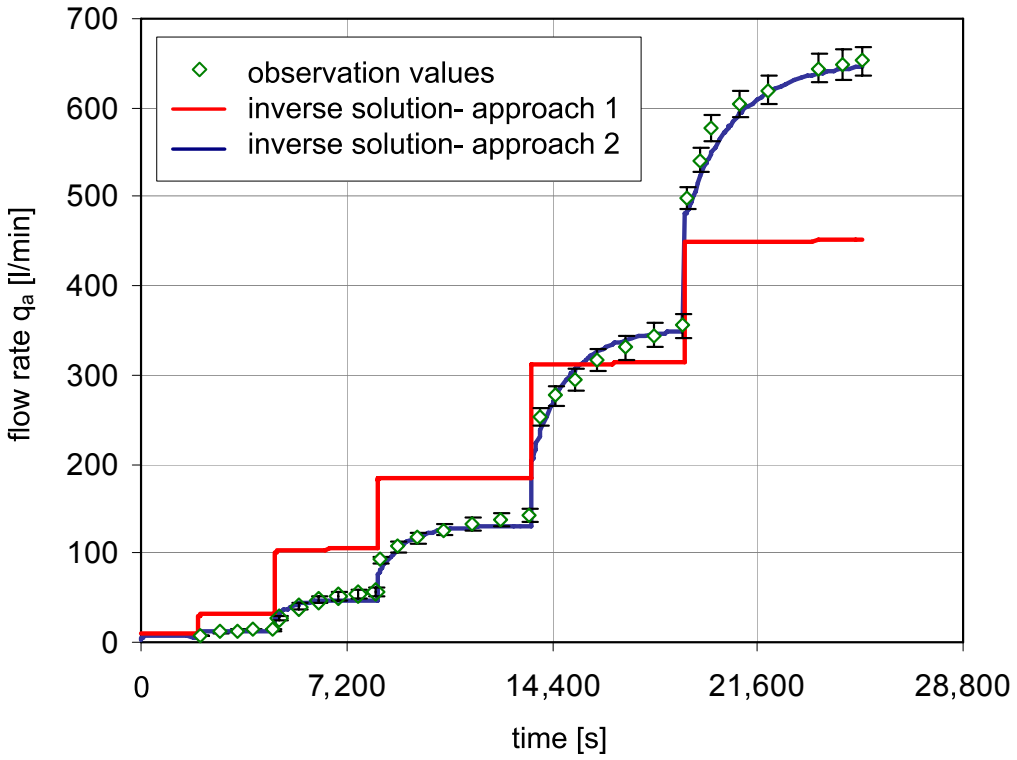

Figure 3.16: Comparison of measured and optimized air flow rates.

The measured and simulated water pressures of approach 1 are displayed in Figure 3.17. The simulated values are generally too low at the beginning of the pressures steps and too large towards the end of the pressure step. In between, the

agreement between the observations and their simulated equivalents is better. However, the general trend indicates a systematic misfit. Because of the large deviations, the simulated water pressures of approach 2 are not depicted. On average, the values are computed 15 kPa too low. These large deviations are a consequence of the focus of approach 2 on fitting the air flow rates.

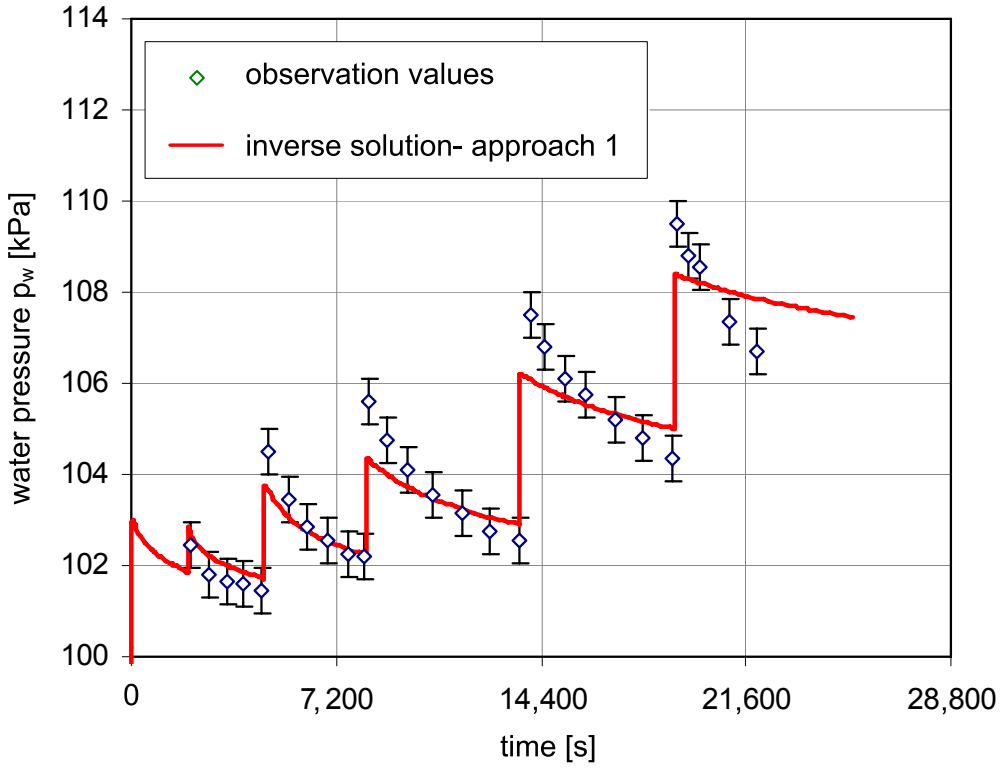

Figure 3.17: Comparison of measured and optimized water pressures.

3.6 Field test 3

3.6.1 General

Field test 3 is executed in silt - fine sand soil (soil 3; see Table 3.1). The horizontal saturated water permeability k_{ws} is approximately $4.2 \cdot 10^{-6}$ m/s. Thus, the expected flow rates are significantly lower than in field test 1 and 2. Four tensiometers and two TDR-probes are installed in 17 respectively 33 cm distance from the centre point of the filter. Geodetic height measurements are taken by a theodolite at 10 distinct points. Measurements are taken in three different radial directions at 25, 50 and 75 cm distance from the injection lance (compare Figure 3.4 b). Additionally, the top level of the injection lance is levelled.

The field test is conducted in ten steps with air injection pressures ranging from 5 to 50 kPa. The duration of the steps is adapted to the necessary amount of time in which steady-state conditions are reached. The total testing period is

approximately 8.5 hours. Table 3.10 gives the duration and pressure magnitudes of the individual steps.

Table 3.10: Duration and injection pressures of field test 3.

step number	**injection pressure Δp_a**	**time t**
-	[kpa]	[s]
1	5.0	900.0
2	7.5	900.0
3	10.0	1,800
4	12.5	2,700
5	15.0	6,300
6	20.0	9,000
7	25.0	3,000
8	30.0	1,800
9	40.0	1,800
10	50.0	2,100

3.6.2 Presentation and discussion of measurement results

- **Air flow rate:**
  Figure 3.18 depicts the measured air flow rates over the testing time. The low flow rates during the initial test phase are displayed in a window with larger scale. At 5 kPa injection pressure the air does not yet penetrate into the saturated soil. At the subsequent pressure step of 7.5 kPa the flow rate increases from initially 0.69 to 0.90 l/min. During the subsequent test stages, the development of the air flow rate is characterized by smooth increases at the beginning and steady states towards the end of the steps.

  At the end of the fifth pressure step (20 kPa), an anomalous increase can be recognized, see the window in Figure 3.18. The subsequent pressure increase to 25 kPa yields an explosive jump of the flow rate. The pressure elevation of 5 kPa would lead to expect a maximum increase of 25 % of the flow rate, whereas the actual increase is more than tenfold. A constant value of 325 l/min is obtained soon after a small drop of the peak value.

The pressure elevation to 30 kPa yields an approximately pressure-proportional increase of the flow rate, which is nearly constant from the beginning to the end of the step. Another large jump is encountered when the pressure is increased to 40 kPa. The air flow rate doubles from approximately 450 to 900 l/min. Subsequently, a slight decrease can be observed. A maximum flow rate of 1,105 l/min and a similar subsequent drop is measured at the final pressure step of 50 kPa.

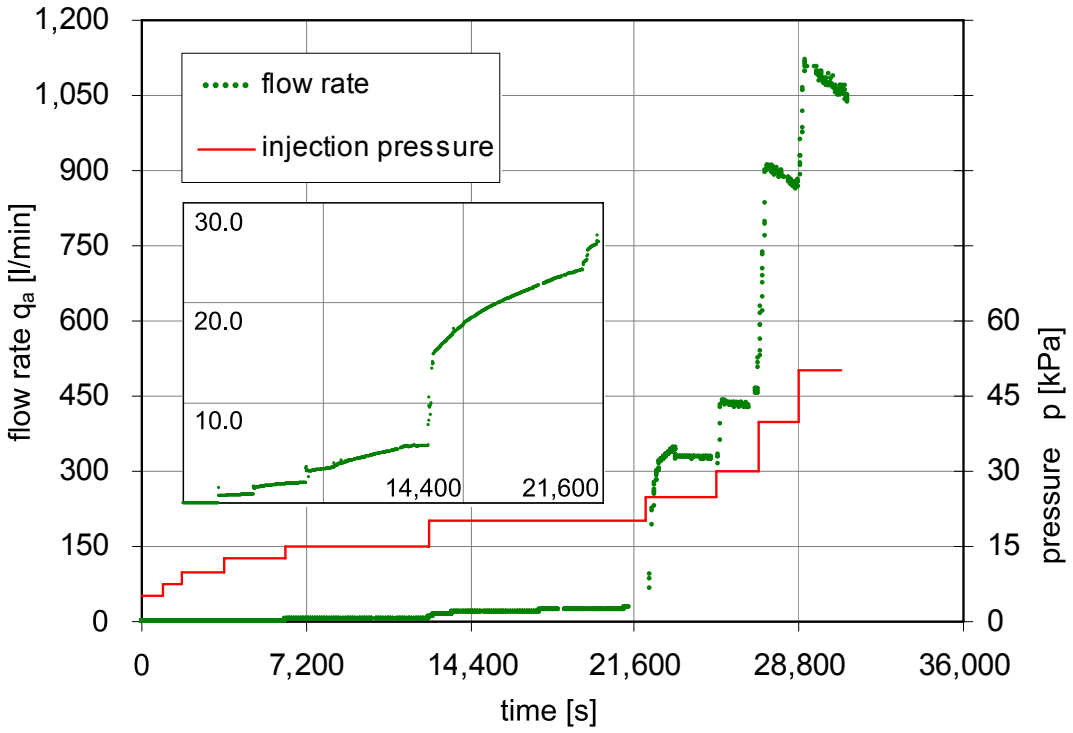

Figure 3.18: Development of air flow rate at field test 3.

- **Tensiometer measurements:**
  Figure 3.19 depicts the water pressure distributions during the execution of field test 3. At the first test phase, the tensiometers reflect the pressure increases but show only low variations over time. During the pressure steps five and six (15 and 20 kPa), the distributions are consistent with the theoretically expected behaviour; that is, the initial jumps due to the pressure elevations decrease subsequently due to the continuous desaturation of the soil. At these two steps, the initial peak values of 105.75 and 109.5 kPa drop to 105 and 108 kPa, respectively. The tensiometer measurements at the same distance but in opposed radial directions are virtually identical. The tensiometers at the inner radius give only insignificantly higher pressure magnitudes than the tensiometers at the outer radius.

  After the pressure increase to 25 kPa, the water pressure behaviour changes. The measurements show strong scatter and anomalous developments. Additionally, large deviations between the readings at the same distance but

opposed radial directions are obtained. Despite the large water retention potential of the soil in which field test 3 is executed, the measured water pressure values during the final test phase are lower than at field test 2.

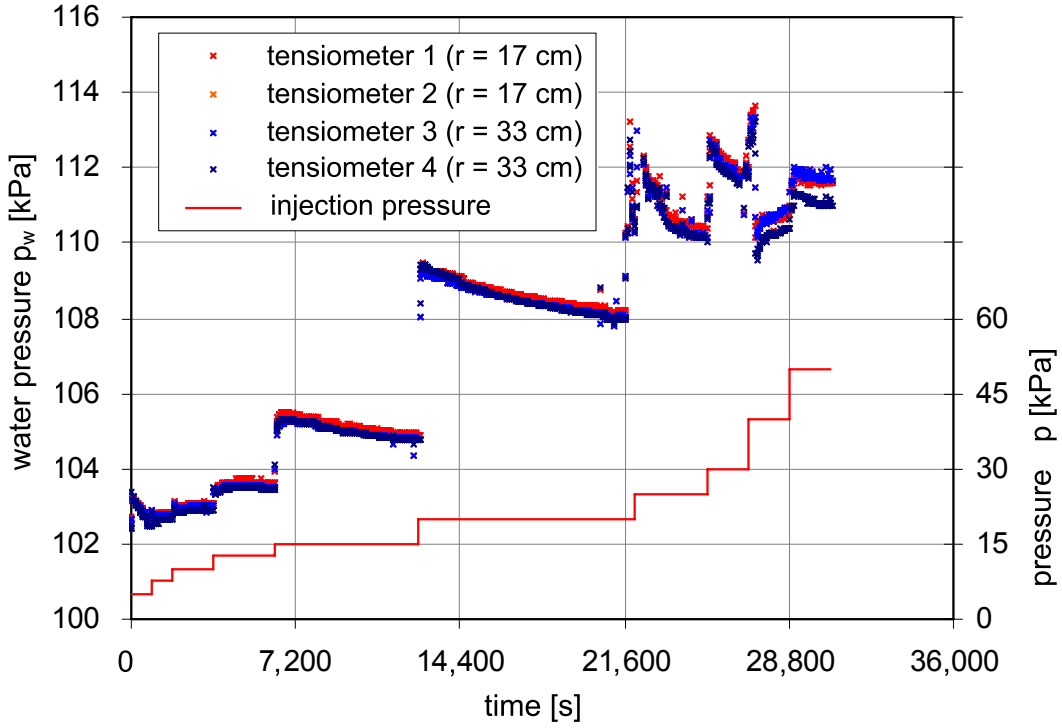

Figure 3.19: Water pressure distributions at field test 3.

- **Water content measurements:**
  The installation of the two available TDR-Probes in the silt - fine sand was less complicated than in the soils of field test 1 and 2. The apparent cohesion of the soil ensured a stable bore hole even in the area below the groundwater table for a limited time. However, one TDR-probe did not transmit signals to the data logger due to an electronic problem. Figure 3.20 shows the development of the air saturation at the remaining device at 17 cm distance from the centre point of the filter. The air saturation is computed from the water content measurements and the soil porosity.

  The desaturation of the soil starts at an air injection pressure of 10 kPa. Here, an air saturation of 1 to 3 % is measured. Relatively large jumps are obtained with some time delay after the pressure elevations at the subsequent test steps. For example, the pressure elevation from 10 to 12.5 kPa yields a sudden increase of the air saturation from 19 to 34 % after a delay of 0.5 hours. The delay reflects the necessary amount of time for the extension of the new saturation front from the filter to the measurement point.

  It is remarkable that during the pressure step that caused the first explosive increase of the air flow rate (25 kPa), only a very small increase of the air

saturation is measured. This is a hint that large parts of the air escape through a developed macro pore respectively gap. However, the subsequent pressure steps yield again significant jumps. A maximum air saturation of 58.5 % is obtained at the end of the field test.

The comparison of the air saturation distribution with the other two conducted field test shows that for all pressure steps the lowest water contents respectively highest air saturation values are measured at field test 3. This is remarkable because of its high water retention potential it would be expected that the lowest saturation values were encountered in this test. Supposing that the TDR-measurements are reliable, the conclusion is that in the silt –fine sand the air flow affects the pore space in a more homogenous way than at field test 1 and 2, in which the air flow rather takes place in macro pores.

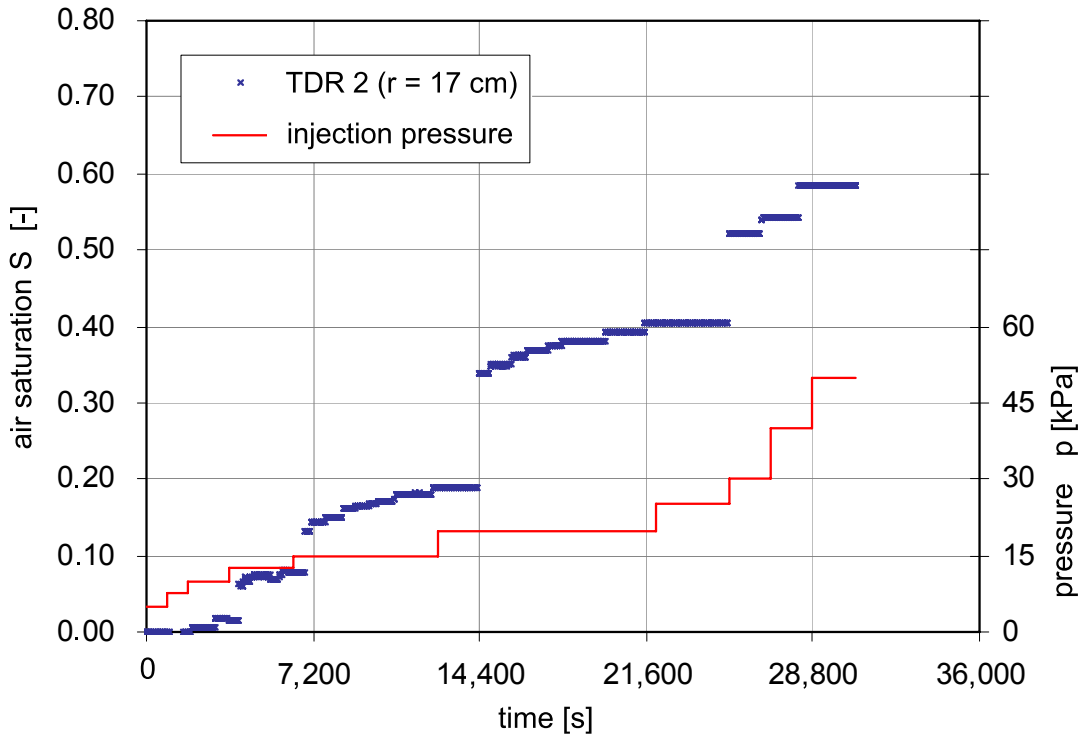

Figure 3.20: Air saturation distribution at field test 3.

- **Surface heaving:**
  The geodetic height measurements are relatively similar for the reading points at 25, 50 and 75 cm distance of the same radial direction. On the contrary, large differences are measured between the reading points at the three different radial directions. Thus, Figure 3.21 shows the relative levels of the three measuring points at 50 cm distance and of the top of the injection pipe. Hirscher (2010) presents the results of all measuring points.

  The level of the measuring points remains equal until the injection pressure of 15 kPa. After the pressure elevation to 20 kPa, two of the three measuring

points show elevations of 1 and 4 mm, respectively. The subsequent test step (25 kPa) yields large elevations at all three radial reading points. However, by far the highest value of 14 mm is obtained for the measuring point 3. Thereafter, the levels of the measuring points continue to increase but with lower intensity. The final elevations are 11, 14 and 17 mm for the measuring points 1, 2 and 3, respectively. The centre point (air injection pipe) experiences a level change of only 5 mm at the pressure step with 40 kPa. The low elevation in comparison to the other reading points is supposed to be due to the counterpressure of the base plate of the filter, which is fixed to the pipe.

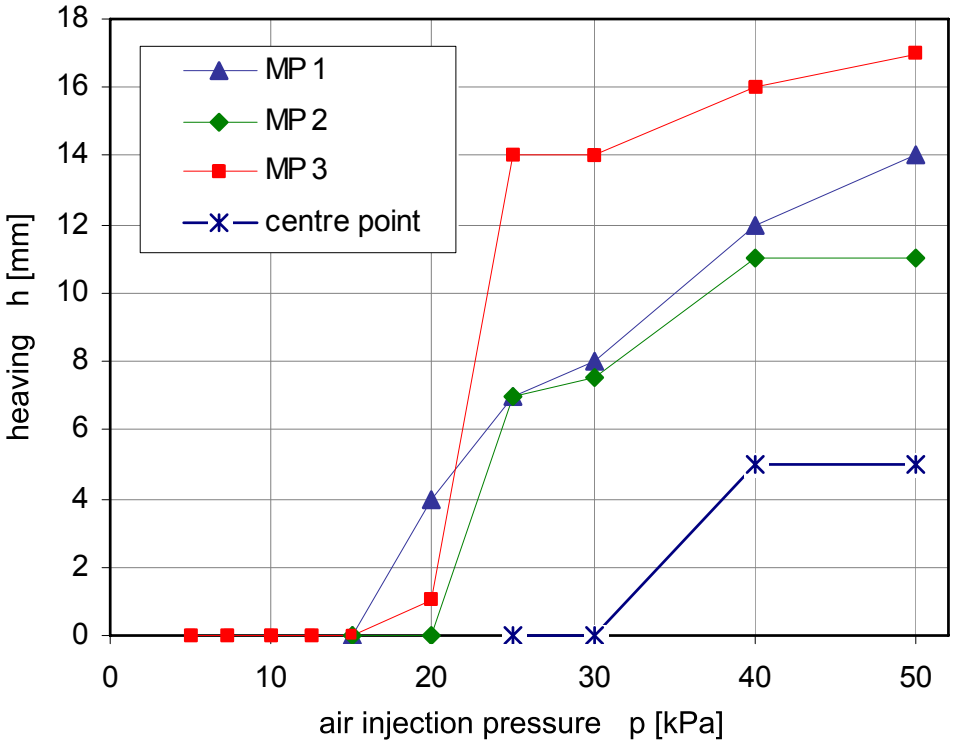

Figure 3.21: Soil heaving at field test 3.

- **Temperature measurements:**
  The temperature of the soil respectively of the pore water during the execution of the test is obtained from the TDR-probe. During the test conduction, the temperature varies between 13.0 and 13.6° Celsius. For more details, see Hirscher (2010). The environment temperature during the test execution varied between 10 and 16° Celsius.

3.6.3 Interpretation of the test performance

The measurement results of the air flow rate and the water pressures are characterized by various irregularities. The first time, an anomalous development of the air flow rate occurs during the fifth pressure step (15 kPa). Here, the flow rate increases with low intensity after the characteristic jump at the beginning

and is constant at the end of the step (see the window in Figure 3.18). In between, a stronger increase of the graph can be recognized. Such a trend is not consistent with the theoretical distribution of the air flow rate and must have been caused by the extension of the pore and/or the development of (a) macro pore(s).

Because of the encountered irregularities in the measurement results, an inverse modelling of field test 3 is not conducted. The data range from 0 – 12.5 kPa is not sufficient because of the expected high air entry value of the silt-fine sand. Instead, a short interpretation of the observed test behaviour in the context of the compressed air tunnelling is given. A detailed interpretation of the test behaviour and of observed air bubbles below the sod outside the excavation pit is provided by Hirscher (2010).

Additional to the above described irregularity, disproportionally high increases of the air flow rate occur at the beginning of the seventh pressure step (from 25 to 325 l/min) and at the beginning of the ninth pressure step (from 450 to 900 l/min. Such an explosive increase of the air flow rate is known as blow out in compressed air tunnelling.

In general, blow outs can occur if the applied pressure head is higher than the dead load of the soil above the underground space which is exposed to the compressed air (Arz et al. 1994). There are two different forms of blow outs, depending on the soil type. In coarse grained soils with no or low apparent cohesion, the erosion forces of the flowing air favour the development of macro pores. In the case of a blow out, single macro pores progressively extend to large so-called flow chimneys in which large amounts of compressed air escape. In fine grained soils, the flow velocities are lower and the cohesion hinders soil erosion. Instead, the pressure accumulation in the air injection area can cause a fracture of the soil structure. The air then escapes in the developed cracks respectively gaps.

In the field test, the first blow out occurs immediately after the test step with 20 kPa air injection pressure. This pressure magnitude corresponds approximately to the dead load of the soil and gravel above the air injection area. The analysis of the geodetic height measurements indicates the second type of blow out. The explosive increases of the air flow rate occur simultaneously with significant heavings of the soil surface, see Figure 3.21. Before and after the blow outs, the level changes of the measuring points are small.

An example of the fracturing of the soil is illustrated in Figure 3.22. The photo shows an extended horizontal fracture of the soil, which was caused by the air pressure accumulation in the soil. The photo was taken after the test execution in 50 cm distance from the injection pipe in a depth of 25 cm below the level of the excavation pit.

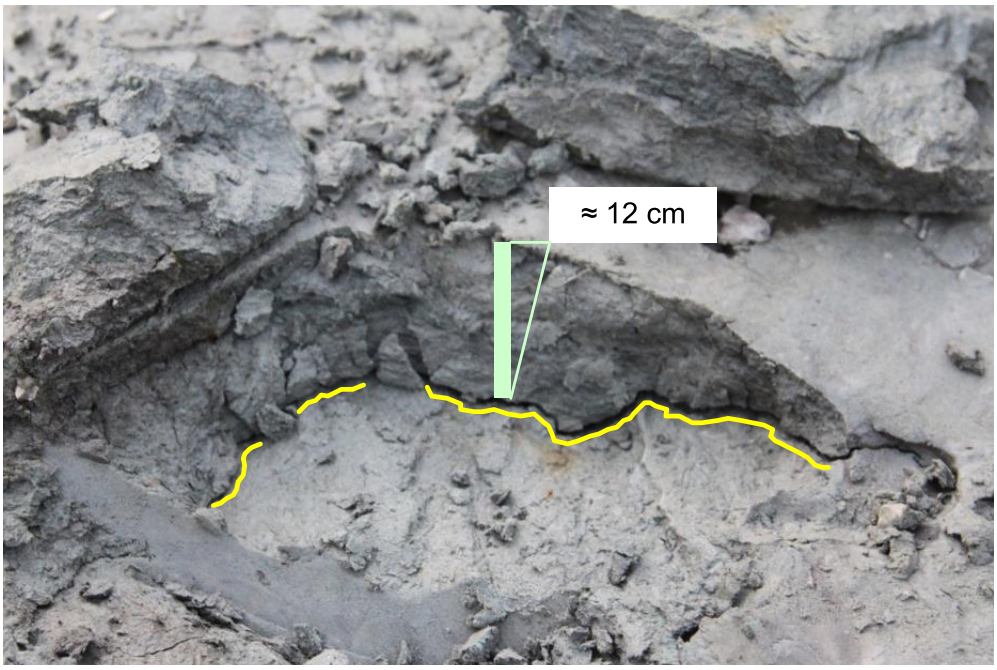

Figure 3.22: Soil fracturing due to air injection (pneumatic ground break).

With respect to compressed air tunnelling, the observed field test performance supports the assumption that a critical state is reached, when the applied excess pressure equals the dead load of the soil above the tunnel. However, this statement is principally valid for fine grained soils; similar effects, for example, did not occur in the significantly coarser soil of field test 1.

3.7 Discussion of results

Generally, it proved that the optimization of fluid flow parameters from the field test data is not as straight forward as from the synthetic data of the theoretical investigation in chapter 3. In field, the measurements have a noise, the original soil texture may be altered and the employed constitutive models may not be able to account for all aspects of the flow process. Additionally, the inverse modelling of a two-phase flow experiment is more complex than the regression of an unsaturated water flow experiment.

From this point of view, the concept of unique inverse solutions has to be questioned critically. Beyond, if an apparently unique parameter set is identified, this does not automatically mean correctness (Durner et al. 1999). Consider for example the different inverse modelling approaches of field test 1. Here, approach 1 did not explicitly take into account macro pore development and the resulting consequences of predominant air flow respectively of a reduced water mobility in the quasi-saturated matrix. On the contrary, in approach 2 only the

parameters of the permeability function were optimized. The parameters of the water retention function were derived from steady-state pressure plate tests. Also a unique inverse solution was obtained here. However, the identified parameters differ significantly from the parameters of approach 1. The obtained water and air relative-permeability functions are depicted in Figure 3.23.

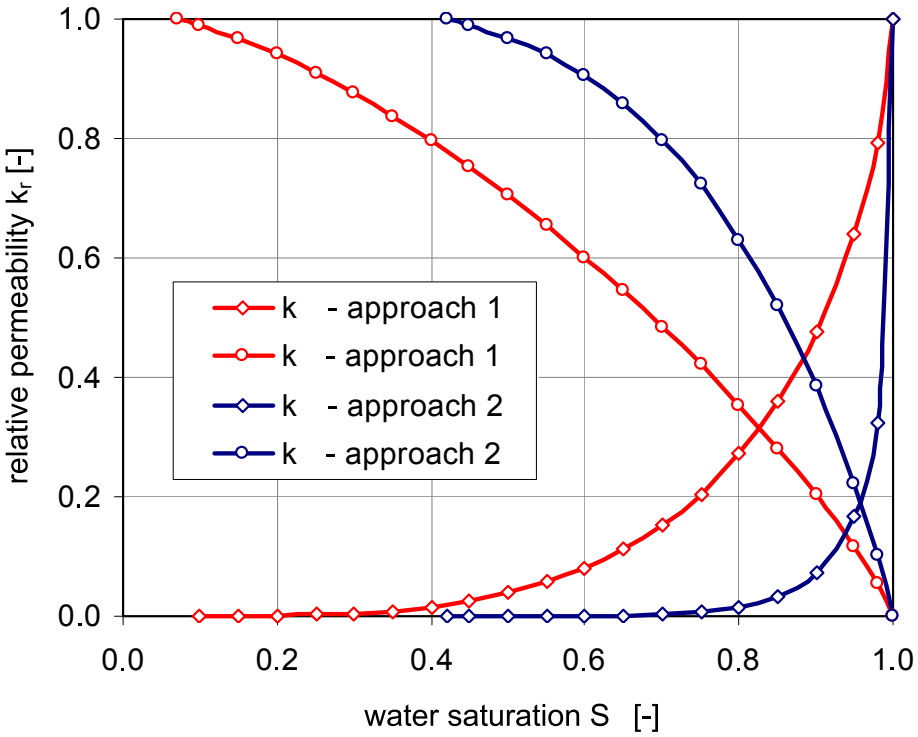

Figure 3.23: Optimized relative permeability functions for the soil of field test 1.

The depicted permeability functions clearly illustrate the differences between approach 1 and 2. The curve shapes of approach 1 are typical for a classical relative permeability problem with stable pore structure. The curve shapes of approach 2 reflect the assumed predominant air flow in macro pores. The air permeability shows a steep increase at high degrees of water saturation, whereas the water mobility is strongly reduced. A comparison of the computed air saturation values with the TDR-measurements indicates that approach 2 is physically more realistic. With the parameters of approach 1, the air saturation is computed too high.

The inverse modelling of field test 2 was complicated by convergence problems. Even with the combined systematic-trial and error optimization procedure, good model fits could only be obtained for one kind of observation data (flow rates or water pressures) at the same time, but not for both of them simultaneously. Consequently, the identified parameters cannot be considered as representative for the true flow behaviour. Their application in site problems is unlikely to produce appropriate results.

There are three possible reasons for the bad inverse modelling results of field test 2: Firstly, the measured air flow rates are biased; secondly, the measured water pressures are biased; and thirdly, the true flow behaviour cannot be described sufficiently accurate with the employed modelling approach. The measurement of the flow rates is considered as reliable. The tensiometer readings are more likely to be biased. Their practical performance at multi-phase flow problems with predominant air flow has not been investigated thoroughly yet. This should be the focus of investigations in controlled laboratory conditions.

If an alteration respectively extension of the pore space caused an increase of the intrinsic permeability, an alternative modelling approach would have to be considered for field test 2. For example, the flow simulation could be coupled with a stress-strain simulation. Because of the relatively low capillary pressures, it is supposed that the consideration of the pore air pressures in the soil is sufficient for the mechanical model.

The measurements of field test 3 were not used for an inverse modelling because of the encountered irregularities of the measuring results. Instead, an interpretation with respect to compressed air tunnelling was conducted. The occurred explosive increases of the flow rate were identified as blow outs. Sufficient observation data for the inverse modelling of the multi-phase flow parameters of this soil can only be obtained if the air injection takes place in greater depths. However, the installation of measuring instruments becomes increasingly difficult in this case.

3.8 Summary and conclusions

The chapter focused on the application and inverse modelling of air injection field tests. The design and theoretical research on the field test have been conducted in a previous chapter. In a variation to the original design, the field tests were only carried out with an air injection phase, which took place in a shallow groundwater table.

The chapter started with a literature review on the inverse modelling of selected unsaturated water and two-phase flow experiments. Most of the findings from the literature review are consistent with the results of the theoretical investigations of chapter 2. However, a major difference concerns the optimization of the intrinsic permeability. While in the conducted investigations in chapter 2 the accurate identification of this parameter was achieved without problems, several authors came to the conclusion that the estimation of the intrinsic permeability is difficult and subject of high uncertainty.

Thereafter, the installation of the experimental equipment and the execution of the field tests were described. The tests were carried out in Stuhlfelden, Salzburg. Three tests in three different sandy soils were conducted. The soils were a medium-coarse sand, a silty fine-sand, and a coarse silt - fine sand. The practical application of the field tests was completed successfully. The experimental set-up, the measuring instrumentation and data acquisition system showed a good performance. An exception are the TDR-probes, whose installation was complicated by the cohesionless soils below the groundwater table.

The flow rate and water pressure measurements of field test 1 and field test 2 were used for an inverse modelling of the multi-phase flow parameters of the soils. The inverse modelling of field test 1 could be conducted successfully. The evaluation of the model fit showed very good agreements between the observations and their simulated equivalents. Because of the consideration of the effects of macro-pores on the flow process, the parameter set of approach 2 is supposed to be superior to approach 1. This assumption is supported by the realistic simulation of the low air saturation in the soil by approach 2.

The inverse modelling of field test 2 was complicated. It is supposed that either biased tensiometer measurements or an incomplete modelling approach falsified the optimization process. The latter aspect refers to a possible extension of the pore space during the experiments. The resulting increase of the intrinsic permeability cannot be described in a physically consistent way by the employed constitutive models. The coupling of the fluid flow model with a mechanical model could overcome this deficiency. However, it would also require the determination of the intrinsic permeability at different bulk densities in the laboratory. Beyond, the use of a coupled approach in the parameter optimization process brings further uncertainties which have to be investigated in further studies.

The performance of field test 3 was interpreted in the context of compressed air tunnelling. Because of the various irregularities in the measurement curves, the data was considered as unsuitable for an inverse modelling. The analysis of the flow rates together with the geodetic height measurements of the surface identified two occurred blow outs, i.e. explosive increases of the air flow rate.

Although the fluid-flow related parameters could not be identified from field test 3, a valuable conclusion with respect to compressed air tunnelling was drawn. It was concluded that a critical state with respect to blow outs is reached when the applied excess pressure equals the dead load of the soil above the tunnel. This statement is principally valid for fine grained soils. Because no blow outs and no surface heaving occurred at field test 1, it can on the other hand be concluded that the application of higher pressures in medium-coarse sandy soils with little or no finer content is less critical.

The conducted testing series only constitutes the starting point for the further development of the field test. Nevertheless, valuable information on the practical test performance and on the inverse modelling was gained. Several deficiencies could be identified and can thus be improved in the next testing series. In order to bring forward the further development of the field test, the following research activities are suggested:

- **Laboratory investigations:**
  The performance of tensiometers should be studied and evaluated in unsaturated soil columns which are exposed to an air pressure gradient. The tensiometers should be installed in different angles with respect to the flow direction. The development and the effects of macro pores should also be investigated in unsaturated soil columns. Different gradients should be applied to the specimen and their intrinsic permeability should be determined subsequently to each test. Thus, critical air pressure gradients and their effects on the permeability can be characterized.

- **Practical application:**
  In order to avoid an excessive stress of the pore structure, the execution of the field tests should be conducted with small pressure steps. A stepwise elevation of the air injection pressure by 2.5 kPa seems appropriate, especially in the finer grained soils. An interesting alternative could be the so-called continuous flow method (Durner et al. 1999), in which the air pressure is increased continuously. Beyond, in order to move a step further, field tests with preliminary water infiltration and subsequent air injection phase should be conducted.

- **Enhanced modelling approaches:**
  The inverse modelling of field test 2 was supposed to be hindered by an incomplete modelling approach, which cannot account for the increase of the intrinsic permeability in a physically correct way. In order to overcome this deficiency, enhanced numerical modelling approaches should be considered in such cases. Firstly, the flow simulation could be coupled with a mechanical model. Thus, the intrinsic permeability could be computed as a function of the pore volume. Secondly, the numerical flow simulation could be enhanced by a function, which computes the intrinsic permeability depending on the pressure gradient between the single elements. The results of the suggested laboratory investigations could be used to develop such a function.

A final aspect concerns the general validity of the optimized multi-phase flow parameters of the water retention and permeability functions. Given the experiences from the conducted field tests, doubts arise whether the determined parameters can also be used for unsaturated water flow problems. A certain drawback is that the unsaturated air permeability functions (which in fact

dominate the optimization of the field tests) are far less investigated and validated than the water permeability functions. It is supposed that parameters with general validity are most likely to be derived from field tests which are conducted in soils with a relatively stable pore structure and with air injection pressures not higher than the dead load of the soil. Particularly young residual soils, in which relatively coarse grains are embedded in a stiff clay matrix, may be suitable for such applications.

Despite the encountered difficulties in the inverse modelling, there are no alternatives to the proposed field test or at least similar air flow tests for multi-phase flow problems, which incorporate predominant air flow in deformable soils. Parameters which are derived from standard outflow experiments or the grain size distribution are generally not able to appropriately describe a multi-phase flow problem with non-negligible air flow. For example, the numerical simulation of air losses in compressed air tunnelling with such parameters may yield totally misleading results (e.g. much too low flow rates; compare Steger et al. 2006).

For the final verification of the appropriateness of the proposed field test, the application in combination with a site problem is of particular interest, e.g. a compressed air tunnelling project in a sandy soil. The field test could be conducted in the ground where the tunnel is driven. With the optimized parameters, a forward prediction of the air losses would be conducted. If a good agreement between the predicted and the measured air losses during tunnel construction can be achieved, even the further development of the field test towards a commercial application is of interest.

4 Numerical investigations of steady-state unsaturated conductivity tests

4.1 Introduction

In analogy to saturated soil testing, the steady-state method can also be used for hydraulic conductivity measurement of unsaturated soils. The water flux through the soil sample and the gradient are maintained constant with time. Three different steady-state techniques for unsaturated soils are described in the following section. From a physical point of view all permeameter methods are based on the same principle, regardless the different experimental setups: Ceramic plates at both end faces of a cylindrical specimen are employed to transmit water pressure to the soils solids. Suction is generated by independent control of the pore air pressure, using the axis-translation technique.

Theoretically, the steady-state method is the most accurate procedure for determination of the unsaturated hydraulic conductivity (Benson and Gribb 1997, Huang et al. 1998). There are, however, various difficulties associated with this method. Experimental challenges include the long testing periods and the adherent problems of water losses, air diffusion and measurement uncertainties. System head losses may also falsify the obtained conductivity values. Calibration tests are employed to minimize the experimental errors.

There is a further aspect which may contribute to the misinterpretation of unsaturated hydraulic conductivity data that is hardly accounted for: The non-uniform distribution of matric suction in the soil specimens. In order to induce respectively to maintain a constant flow, different magnitudes of pore water pressure act behind the two ceramic plates at the end faces of the soil sample. The air pressure in the specimen is the same everywhere. Necessarily, this results in a matric suction gradient across the soil specimen.

Like in saturated soil tests, the unsaturated hydraulic conductivity is computed using Darcy's law:

$$v = -k(s) \cdot (h_{w,1} - h_{w,2}) / l \tag{4.1}$$

v Darcy velocity
$k(s)$ unsaturated hydraulic conductivity at a specific suction
$h_{w,1}$ water pressure head at first end face
$h_{w,2}$ water pressure head at second end face
l length of soil sample

In consequence of the non-uniform distribution of suction, the water content varies along the axis of the sample and therewith the hydraulic conductivity. The steady flow velocity is everywhere the same. Considering Eq. 4.1, it follows that the hydraulic gradient varies along the length of the specimen, being high where the conductivity is low and vice versa.

Taking into account the latter statements, Childs (1957) concludes that the conductivity at a given water content must be obtained by measuring the potential gradient at the point where the water content prevails. Because of the experimental complications and because of concerns about interfering with the water flow, all the recently presented steady-state permeameters in literature have abandoned measuring pore water pressures inside the specimen. The distributions of matric suction, hydraulic conductivity and the potential gradient across the soil specimen are therefore unknown.

However, the hydraulic conductivity obtained from the permeameter tests has to be referred to a specific suction respectively water content. This “average” suction value is usually computed as linear mean of the suction at the base and the top of the soil sample. However, it has long been recognized that the measured average water conductivity does not necessarily correspond to the applied average matric suction (Childs 1957, Benson and Gribb 1997).

In order to avoid respectively to reduce the problem of the non-uniform distribution of matric suction, Benson and Gribb (1997) suggest maintaining the suction gradients as small as possible while maintaining measurable flow rates. Similarly, Lu et al. (2006) argue that the problem could be greatly reduced in future due to progresses achieved in reducing the magnitude of the imposed flow rates of constant-flow permeameters.

Improvements of the experimental systems will certainly allow applying lower flow rates and measuring lower head differences and vice versa. Apart from the experimental limitations there are, however, other limitations which have to be taken into account. Firstly, low flow rates respectively low suction gradients result in low flow velocities. Times to reach steady state increase rapidly and are fast beyond practical limits for silty and clayey soils. Adherent with long testing times, the problems of water losses and air diffusion become more severe.

Secondly, below a certain threshold gradient water shows non-linear flow behaviour. Especially in fine grained soils, this may result in a flow which is not obeying the Darcy-law or in no flow at all before a minimum gradient is exceeded. For clay soils the threshold gradient may exceed 30 (Bear 1988). Due to the latter considerations it follows that the non-uniform distribution of matric suction will continue an important issue in steady-state testing of unsaturated water respectively air conductivity.

Theoretical research respectively numerical investigations of the steady-state technique and how to deal with the described problems are spare. In order to overcome this deficiency, a detailed analysis of the non-uniform suction distribution in the specimen and its consequences to the measured hydraulic conductivity are carried out in this chapter. The investigations are based on numerical simulations of hypothetical unsaturated permeameter tests. Moreover, different methods for interpreting the measured average conductivity are discussed respectively developed.

The research was initiated by an ongoing steady-state permeameter development at PUC Rio de Janeiro (Moncada 2008). Inconsistent results emphasised the need to gain deeper knowledge of the hydraulic conditions inside the soil specimen. Parts of the work have already been published in Steger et al. (2008).

4.2 Literature review: steady-state methods

4.2.1 The constant-head method

Like in conventional testing of saturated soils, a constant gradient over the specimen is achieved by applying different pressure heads behind the two ceramic plates at the end faces. Suction is controlled by the axis translation technique, using an external air pressure source. The air entry value of the ceramic plates must be larger than the maximum suction applied during hydraulic conductivity testing. Once a steady-state flow is established, the corresponding flow rate is measured. Darcy's law is assumed to be valid for computing the hydraulic conductivity corresponding to specific levels of applied matric suction (Fredlund & Rahardjo 1993).

In order to compute correctly the hydraulic conductivity, it is necessary to isolate the internal head losses from system head losses. This is particularly important for coarse grained soils and for testing near saturation. Here, the head losses in the end caps may be significantly larger than the specimen head loss. The total head loss must be corrected for the impedance of the ceramic plates and the overall system head losses. This impedance may be measured prior to testing by permeating a "blank" specimen having negligible head loss, e.g. a cylinder or free water (Lu and Likos 2004).

Constant-head permeameters may be either rigid-walled or flexible-walled. Rigid-wall permeameters do not allow control of the stress level in the specimen. Thus, with increasing suction and adherent soil shrinking, the sample is likely to lose contact with the side walls. In unsaturated soil specimens, the air pressure is higher than the water pressure and water flow is bound to the soil grains.

Sidewall leakage is therefore not a problem in unsaturated conductivity testing. The air pressure is usually supplied through a side port in the permeameter wall and distributed around the perimeter of the sample using filter paper strips situated along the internal wall of the cell.

Flexible-wall permeameters allow hydraulic conductivity testing at different stress levels. A confining cell system enables isotropic or triaxial stress control. For flexible-wall systems both the water and air pressure are commonly applied at the bottom respectively top of the sample. Special ends caps comprising both high air entry (water pressure) and low air entry (air pressure) materials are required (Benson and Gribb 1997).

Recently, constant-head permeameters have been developed by Huang et al. (1998), Gan and Fredlund (2000) and Samingan et al. (2003). Figure 4.1 shows a schematic view of the experimental setup used by Gan and Fredlund (2000). On each end face of the specimen, a 1 bar ceramic plate is placed. Air pressure is applied by a lateral inlet. The head difference is generated by means of an elevated constant head tank. The water flows into a glass vial with a hypodermic needle. For tests at very low suctions, a slightly different arrangement with high permeability porous brass disks is employed.

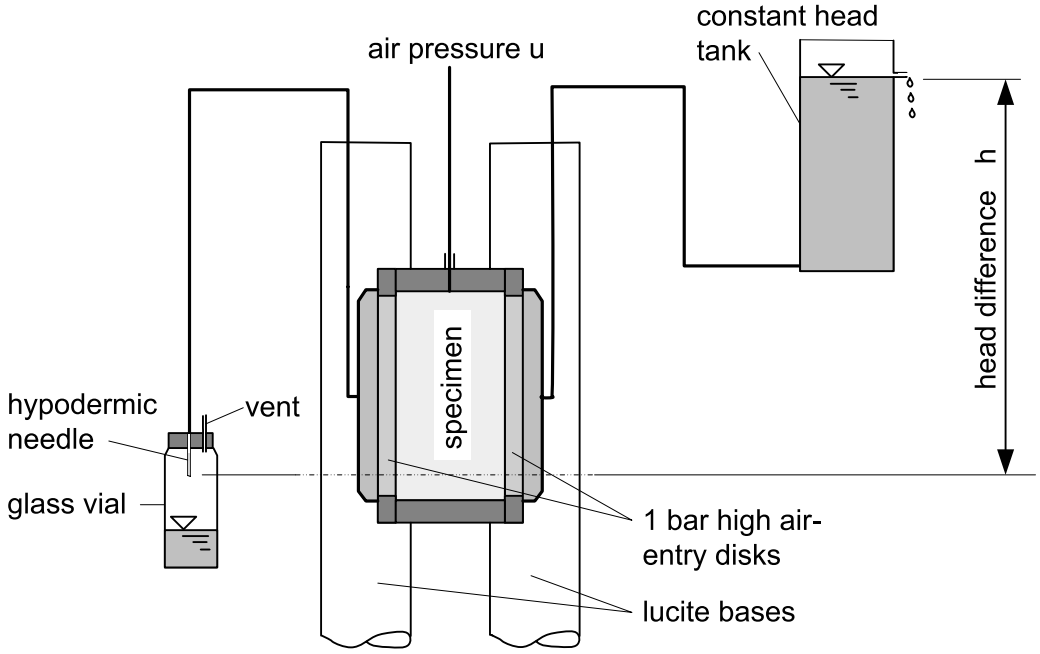

Figure 4.1: Constant-head permeameter (after Gan and Fredlund 2000).

The primary advantage of the constant-head method is its simplicity and its relatively widespread use. Because the test may be conducted in a triaxial cell, hydraulic conductivity may be examined under stress controlled and simulated in situ conditions. Hydraulic conductivity measurements as low as 10^{-11} m/s are generally possible (Lu and Likos 2004).

Primary disadvantages are the often lengthy amounts of time for steady-state to be achieved and difficulties associated with measuring extremely low flow rates with sufficient accuracy. Because a gradient is required to induce flow, the suction along the length of the specimen, and thus the hydraulic conductivity, is non-uniform. Furthermore, in case of a flexible-walled permeameter system, combined end plates will yield a not strictly one-dimensional flow behaviour. The application of a one-dimensional expression of the Darcy equation is therefore problematic, and the two-dimensional flow field is unknown.

4.2.2 The constant-flow method

The constant flow method also requires a suction gradient over the length of the specimen in order to induce a flow. Thus, the constant-head and constant-flow permeameters are similar testing techniques. The key difference is that in the latter case the flow rate through the soil sample is controlled rather than measured. Constant-flow syringe pumps are used to impose precisely controlled flow rates, which may be as low as 10^{-9} cm³/s respectively 0.01 cm³/d. Hydraulic conductivities as low as 10^{-16} m/s can theoretically be measured (Lu et al. 2006).

For computation of the hydraulic conductivity, a constant hydraulic head is maintained at one side of the specimen whereas the water pressure increase due to the imposed flow rate is measured at the other side. Once the head measurement becomes steady, the hydraulic conductivity may be computed using Darcy's law.

Ceramic plates are situated at both end sides of the specimen, just like for constant-head permeameters. Also, constant-flow permeameters can be rigid-walled or flexible-walled. A specific value of suction is achieved by either lowering the water pressure or elevating the air pressure in the specimen. Depending on the chosen system, the air pressure is supplied through a side port in the permeameter wall respectively via a combined end cap.

Constant-flow permeameters were developed by Kunkel et al. (1995), Lu et al. (2006) and Moncada (2008). Figure 4.2 depicts the experimental layout designed by Lu et al. (2006). A dual-chamber syringe pump is used to impose a constant flow rate. In order to reduce time for steady-state conditions, a "water content" pump is employed additionally to achieve the desired suction value of the specimen. The head difference Δh is measured with a differential pressure transducer. Specifically designed high air entry disks are fabricated for this purpose. The developed experimental system is complex but allows concurrently measuring the hydraulic conductivity and water retention curve of the soil specimen.

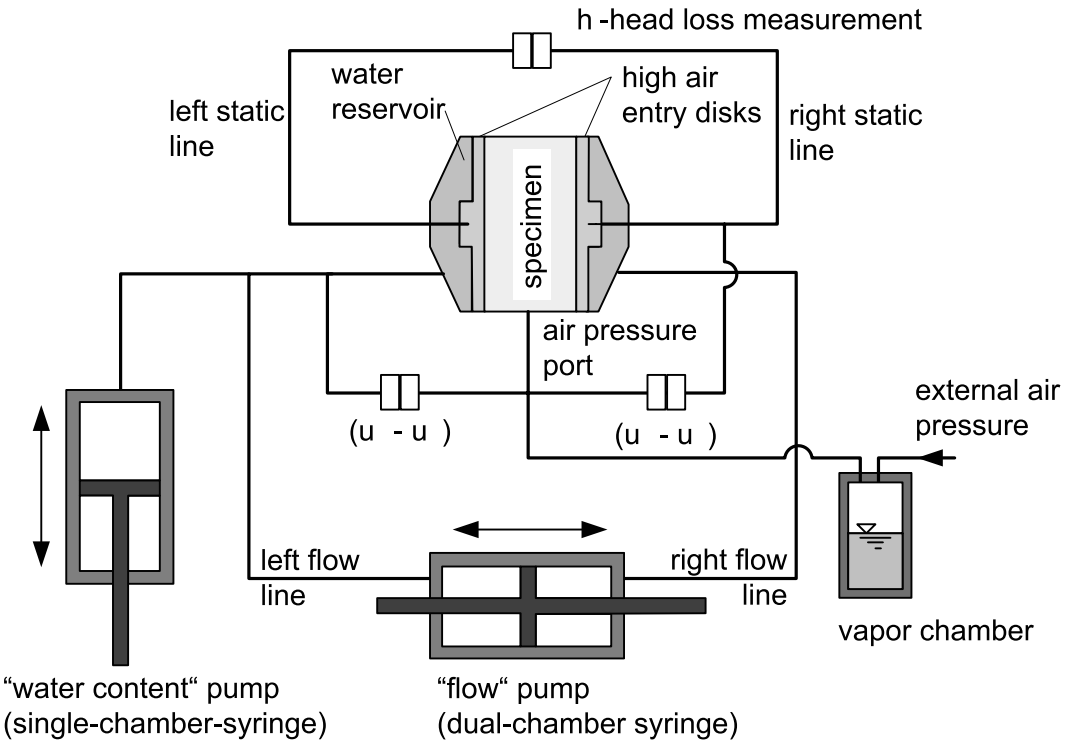

Figure 4.2: Constant-flow permeameter (after Lu et al. 2006).

The advantages and disadvantages of constant-flow permeameters are principally the same as for constant-head systems. Testing times are long (typically at least one month for one material) and the experimental procedure is tedious. Because of the necessary gradient, the suction distribution is non-uniform in the sample. Furthermore, there is the problem of inducing a non one-dimensional flow when combined end caps are used. However, some authors, e.g. Lu et al. (2006), consider the constant-flow method superior to the constant-head method. They argue that the application of extremely low flow rates can be done with higher accuracy than their measurement, thus favouring the constant-flow technique.

4.2.3 The centrifuge method

The steady-state centrifugation method is a hydraulic conductivity measuring technique that uses a spinning centrifuge to generate an elevated gravitational gradient. The amount of time to reach a steady-state flow through an unsaturated specimen can be reduced significantly. It is assumed that Earth’s gravity field is negligible compared to the centrifuge gravity field. Fluid flow through the specimen may then be considered as one-dimensional (Nimmo and Akstin 1988).

Theoretically, two driving gradients may induce the fluid flow in a centrifuge permeameter: firstly, a suction gradient across the specimen, and secondly the centrifugal gravity gradient. Fluid flow respectively the hydraulic conductivity

for a given suction condition can then be described in terms of these two gradients:

$$v = -k(s) \cdot \left[\rho_w \omega^2 r + \frac{\partial s}{\partial r} \right] \tag{4.2}$$

ρ_w density of water
ω rotation velocity
s local suction
r length of centrifuge arm

Nimmo et al. (1992) showed that the radial suction gradient can be neglected at sufficiently high rotational speed. The experimental setup of the permeameters itself is similar to the constant-head respectively constant-flow method but requires special techniques in order to control the fluid flow through the specimen. Typically, specimens are run from an initially saturated condition and then desaturated in a stepwise fashion. Detailed descriptions are provided by Nimmo et al (1992).

The primary advantage of the centrifuge method is the short testing time required in comparison to other steady-state techniques. Times for steady state range from a few hours for determining relatively large hydraulic conductivities to over 24 hours for relatively low conductivities (Nimmo and Akstin 1988). Another advantage is that no suction gradient is necessary to induce flow, thus the problem of the non-uniform suction distribution can be avoided. Major disadvantages are the high costs of centrifuge testing and its limited application to incompressible materials, such as dense sands or overconsolidated materials. For compressible or highly structured materials the high centrifugal forces can alter the soil fabric and thus influence the hydraulic conductivity measurements (Lu and Likos 2004).

4.3 Numerical simulations

4.3.1 Permeameter system and general concept

A constant-flow permeameter system is adopted for the numerical investigations. The gained simulations results and analyses, however, are equally valid for any constant-head and constant-flow systems, and do not depend on a specific permeameter system.

The modelled experimental setup is similar to the PUC permeameter (Moncada 2008). The difference is the lateral application of the air pressure by means of a filter paper around the perimeter of the specimen rather than by combined end

caps. This modification is made in order to ensure a strictly one-dimensional flow field once a steady state is reached. Thus, a dependence of the investigation results on a specific design is avoided. Figure 4.3 depicts the details of the experimental system which are relevant for the numerical modelling.

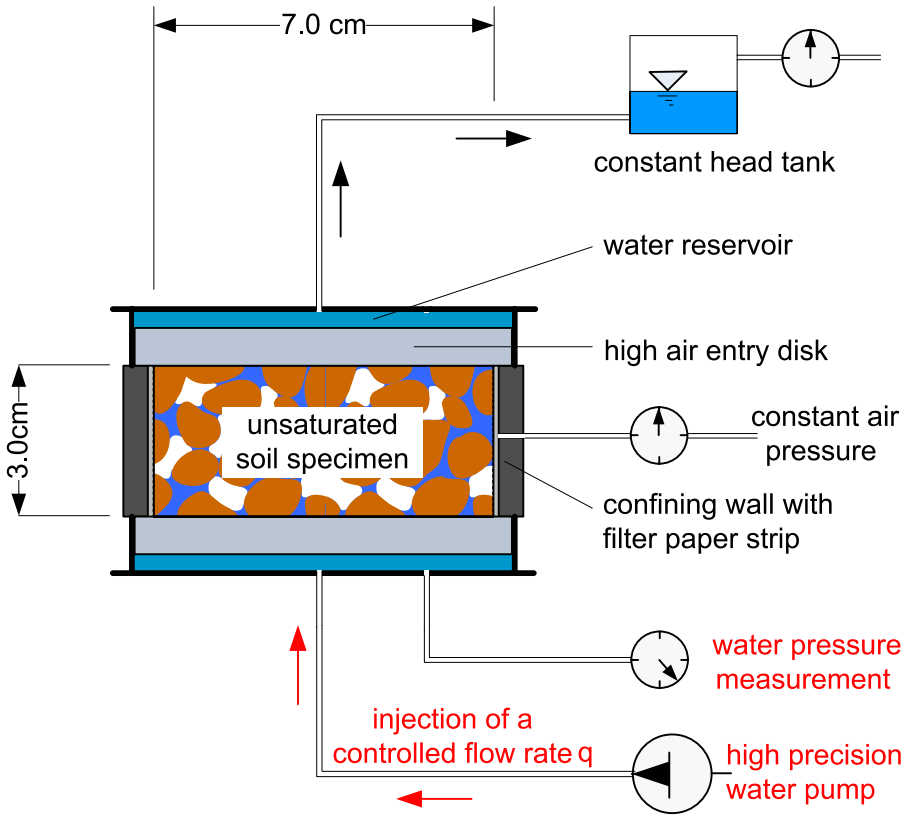

Figure 4.3: Experimental system of modelled permeameter.

The sample is assumed to be situated in a rigid confining ring. The specimen has a diameter of 7.0 cm and a height of 3.0 cm, a common sample size in steady-state testing of unsaturated conductivity (e.g. Samingan et al 2003, Lu et al. 2006, Moncada 2008). The ceramic plates at the upper and lower end face of the specimen have a thickness of 0.7 cm. Water reservoirs are located behind the ceramic plates. Air pressure is applied via a lateral port. For its uniform distribution, a filter paper strip is situated along the internal wall of the confining ring.

A water pump imposes a controlled flow rate to the lower reservoir of the permeameter. A constant air pressure, corresponding to the desired suction value, is applied to the sample. The water pressure head at the upper water reservoir is maintained constant by means of a constant head tank. It is mentioned that for the numerical simulations, flow is assumed to take place in horizontal direction. The pressure increase due to the imposed flow rate in the lower reservoir is measured. The obtained head difference, corrected for the impedance of the ceramic plates, is directly proportional to the hydraulic conductivity of the sample *k(s)*:

$$k(s)_{soil} = v\frac{l_{soil}}{\Delta h_{soil}}$$

$$= \frac{q}{A}\frac{l_{soil}}{\Delta h_{tot} - 2\frac{q}{A}\frac{l_{plate}}{k_{plate}}} \tag{4.3}$$

q imposed water flux
A cross section of the specimen
Δh_i head loss in specimen respectively ceramic plates
k_{plate} conductivity of ceramic plates
l_i length of specimen respectively ceramic plates

First of all, the numerical simulations are carried out to gain knowledge about the distribution of suction and hydraulic conductivity inside the specimen. In the second step, the inherent error if the measured hydraulic conductivity is referred to the linear mean value of suction is investigated.

For this purpose, two numerical simulation series of unsaturated steady-state permeameter tests with two different soils are carried out. The parameters describing the water retention respectively hydraulic conductivity function are obtained from literature data. Theoretically, any physically reasonable set of parameters could be used for the numerical investigations. The distribution of suction and hydraulic conductivity can readily be obtained by analyzing the final pressure and saturation values of the single grid block elements.

In order to reveal the error caused by referring the measured hydraulic conductivity to the linear mean of suction, the numerically computed pressure increase in the lower water reservoir is treated like an experimental result. Together with the imposed flow rate it is used to compute the hydraulic conductivity with Equation (4.3). The so obtained conductivity k_{perm} is then referred to the linear mean of matric suction at the base respectively top of the specimen:

$$k_{perm} \Rightarrow k\left(\frac{s_b + s_t}{2}\right) \tag{4.4}$$

s_b suction at base of the specimen
s_t suction at top of the specimen

Using the latter approach corresponds to the common interpretation of conductivity values obtained with steady-state permeameter for unsaturated soils. However, in the subsequent step, the correct hydraulic conductivity k_{true} for the linear mean value of suction is computed from the parameters of the hydraulic conductivity function used in the numerical simulation. Finally, the values obtained from the numerical simulation (k_{perm}) and from the conductivity

function (k_{true}) are compared. Thus, the error when steady-state conductivity measurements are referred to the linear mean value of suction is obtained:

$$\text{error}[\%] = \frac{1}{k_{true}} k_{perm} \cdot 100 - 100 \tag{4.5}$$

4.3.2 Numerical model and material parameters

An axis-symmetric model with a radius of 3.5 cm and a height of 4.4 cm is employed. A rather fine-meshed grid with 720 blocks in total, 72 rows in radial and 10 element rows in axial direction, is used. The materials that are covered by the mesh are the soil and the adjacent high air entry disks. The water reservoirs behind the ceramic disks are not incorporated. Instead, boundary conditions are applied directly. The same applies for the filter paper strip around the specimen. The cross section of the numerical model and the assigned boundary conditions are shown in Figure 4.4.

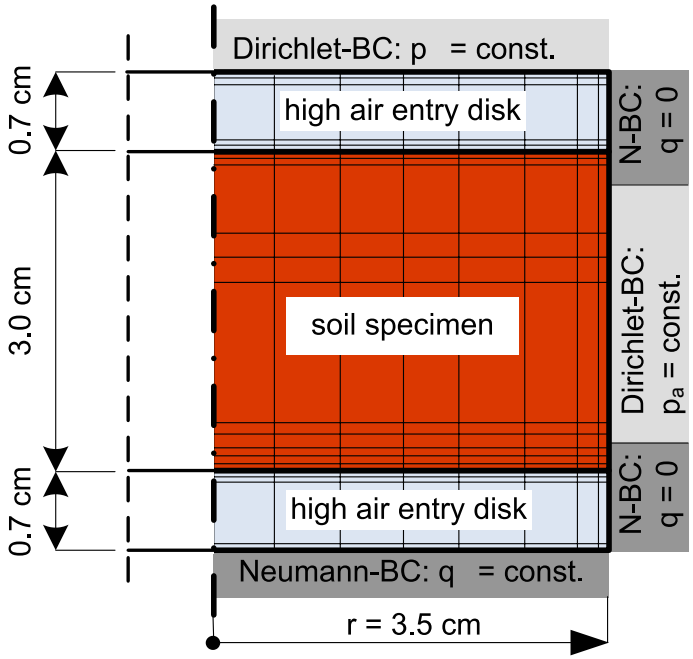

Figure 4.4: Numerical model of permeameter and boundary conditions.

A Neumann-boundary condition with constant flux according to the injected flow rate is assigned to the grid blocks of the lower ceramic plate. Due to the axis-symmetric model, the injection rates of the single grid blocks have to be computed according to their different cross sections. The constant water pressure behind the upper high air entry disk is represented by a Dirichlet-condition, i.e. a constant water pressure is simulated. Full mobility of the water phase and zero air conductivity is modelled for these two boundary conditions. In order to avoid numerical problems, a water saturation of 0.999 instead of 1.0 is assigned.

The filter paper strip along the perimeter of the specimen is also simulated with a Dirichlet-boundary condition. In order to desaturate the sample to different suction values, a constant but higher pressure than behind the upper ceramic disk has to be modelled. Full air mobility and zero water mobility are assigned here as well. An air saturation of 0.999 is assigned to the lateral boundary grid blocks.

Below and above the filter paper, Neumann boundary conditions with zero flux are assigned to the remaining lateral wall of the sample respectively the ceramic plates. This is simply achieved by cutting all flow connections in lateral direction. For the same reason, no phase specific conductivity functions and no phase saturations need to be assigned here.

In order to obtain relevant results, two different soils, which are well known in the specific literature, are used in the numerical simulation series. The first one, Esperance Sand, is a poorly-graded, medium-fine, clean sand characterized by Lu et al. (2006). The second one, Beit Netofa Clay, was investigated by van Genuchten (1980). For both soils the water retention curve and the hydraulic conductivity function are described by the van Genuchten model (1980) respectively the Van Genuchten-Mualem model (Van Genuchten 1980, Mualem 1976). The air conductivity is modelled after Corey (1954).

In order to model the physical behaviour of the high air entry disks it is necessary to adopt a very high *n*-value. Thus, full water saturation even at the highest modelled suction value can be ensured. α has to be chosen high enough such that air cannot penetrate into the disks. For the numerical simulations, these two parameters were chosen arbitrarily in order to be able to model the desired behaviour numerically. Depending on the magnitude of the modelled suction value, a 0.5 bar high flow (HF) respectively a 1.0 bar high flow disk, are employed for the numerical simulations. The parameters of Esperance Sand, Beit Netofa Clay and ceramic plates are summarized in Table 4.1.

Table 4.1: Material parameters.

material	$\mathbf{k_{sat}}$	$\mathbf{\theta_s}$	$\mathbf{S_{r,w}}$	$\mathbf{S_{r,air}}$	$\boldsymbol{\alpha}$	**n**
	[m/s]	[-]	[-]	[-]	[m^{-1}]	[-]
Esperance Sand	$4.9 \cdot 10^{-7}$	0.39	0.02	0.02	1.80	1.60
Beit Netofa Clay	$9.5 \cdot 10^{-9}$	0.45	0.00	0.02	0.15	1.17
Ceramic 0.5 bar HF	$8.6 \cdot 10^{-6}$	0.40	0.20	0.02	0.1	100
Ceramic 1 bar HF	$8.6 \cdot 10^{-8}$	0.40	0.20	0.02	0.2	100

The program TOUGH2 (Pruess et al. 1999) together with the EOS3 module (two phase flow of air and water) is employed to solve the flow problem constituted by the described numerical permeameter model and its boundary conditions. The program and its different flow modules are described in more detail in chapter 3. Theoretically, if only the steady-state conditions were of interest, also the EOS9 module (single phase water flow) could be employed.

4.3.3 Simulation results

In the following, the results of 4 simulation series are presented. For Esperance Sand, suction values of 5 respectively 20 kPa were applied to the upper ceramic plate of the permeameter. Six different flow rates for each of these two values were assigned to the lower ceramic plate in order to generate different suction gradients across the soil specimen. The same procedure was carried out for the simulations with Beit Netofa Clay, but the suction values at the top were 20 respectively 70 kPa. A total number of 24 simulations were conducted.

The computation results are summarized in tables and figures. Displayed results are the head loss Δp due to the imposed flow rate q, the average gradient *grad*, the permeameter conductivity k_{perm} and the "true" conductivity k_{true}. The main information, the inherent error when the permeameter conductivity is referred to the linear average suction, is given in the last column of the tables. Additionally, figures illustrate the computed distributions of matric suction respectively hydraulic conductivity in the soil specimen.

- **Esperance Sand 5 kPa**
  The imposed flow rates range from $q = 1 \cdot 10^{-5}$ cm³/s to $5 \cdot 10^{-3}$ cm³/s. The lower limit of the flow rates is due to numerical constraints. Here, the flow rate of $q = 1 \cdot 10^{-5}$ cm³/s yields an extremely low gradient of 0.1, and this was the smallest flow rate that allowed a successful simulation run. The largest flow rate was chosen such that the sample still remained unsaturated at the lower end face, where the injection is simulated.

  Table 4.2 shows the simulation results for the applied suction of $s_t = 5$ kPa behind the upper ceramic plate. It can be seen that the conductivity interpretation errors range from 2.6 to 32.5 %, depending on the magnitude of the imposed flow rate. However, the obtained gradients for the four lower flow rates are rather small. Thus, in order to maintain reasonable equilibrium times and to avoid problems of non-Darcyan flow, only the flow rates of $q = 2.5 \cdot 10^{-5}$ cm³/s respectively $q = 5 \cdot 10^{-3}$ cm³/s should be used for permeameter tests with soils similar to Esperance Sand. The obtained conductivities, however, will then at least incorporate an error of 20 %.

Table 4.2: Simulation results for Esperance Sand (s_t = 5 kPa).

flow rate q	**Δs**	**s_{mean}**	**grad**	**k_{perm}**	**k_{true}**	**error**
[cm³/s]	[kPa]	[kPa]	[-]	[m/s]	[m/s]	[-]
$5.0 \cdot 10^{-3}$	4.200	2.900	14.0	$9.31 \cdot 10^{-8}$	$7.03 \cdot 10^{-8}$	32.5
$2.5 \cdot 10^{-3}$	1.907	3.454	10.2	$6.41 \cdot 10^{-8}$	$5.36 \cdot 10^{-8}$	19.6
$1.0 \cdot 10^{-3}$	1.804	4.087	6.04	$4.31 \cdot 10^{-8}$	$3.99 \cdot 10^{-8}$	7.9
$5.0 \cdot 10^{-4}$	1.086	4.451	3.62	$3.57 \cdot 10^{-8}$	$3.40 \cdot 10^{-8}$	4.9
$1.0 \cdot 10^{-4}$	0.264	4.867	0.88	$2.94 \cdot 10^{-8}$	$2.85 \cdot 10^{-8}$	3.2
$1.0 \cdot 10^{-4}$	0.028	4.986	0.09	$2.78 \cdot 10^{-8}$	$2.71 \cdot 10^{-8}$	2.6

Figure 4.5 illustrates the computed distributions of matric suction in the specimen for the largest four flow rates. The head losses in the ceramic plates are not shown. At a sample length of 30 mm a constant suction value of s = 5 kPa is maintained for all flow rates due to the specified boundary condition. At the lower end face of the specimen, matric suction is strongly decreased for higher flow rates. Particularly for the two highest simulated flow rates, the computed distributions are strongly non-linear.

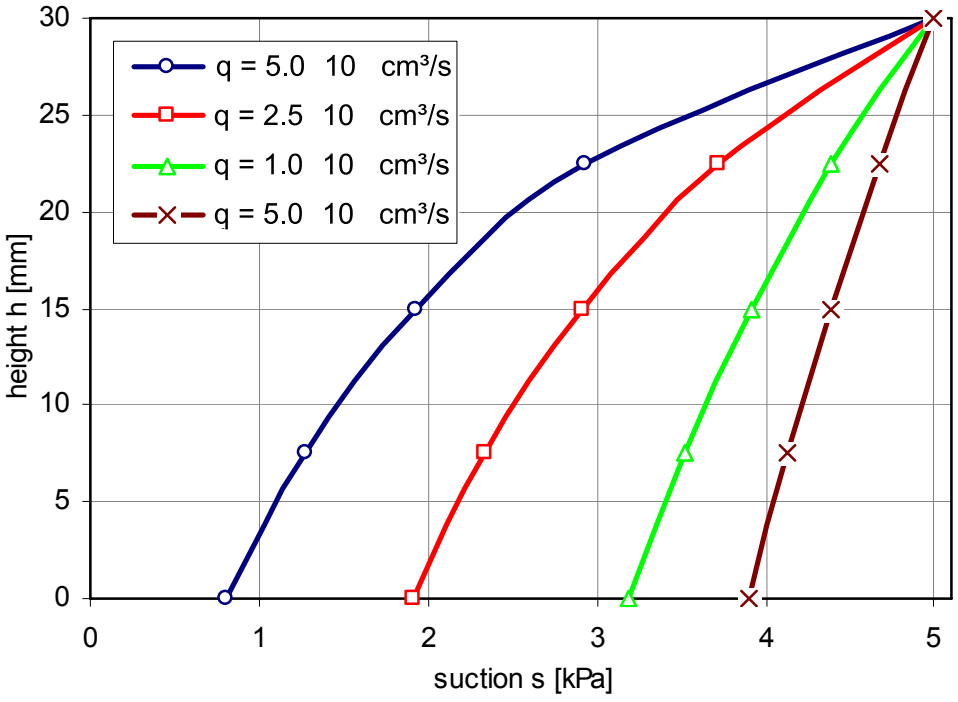

Figure 4.5: Distributions of matric suction for Esperance Sand (s_{top} = 5 kPa).

- **Esperance Sand 20 kPa**
  The imposed flow rates range from $q = 1 \cdot 10^{-7}$ cm³/s to $1 \cdot 10^{-3}$ cm³/s. The flow rate of $q = 1 \cdot 10^{-7}$ cm³/s yields an extremely low gradient of 0.04 and is the lowest one that allows a successful simulation run. The largest flow rate is chosen such that the sample still remains unsaturated at the lower end face, where the injection takes place. The average gradient of 46.9 for this simulation is still in a commonly used range for permeameter tests.

  Table 4.3 contains the simulation results for an applied suction of $s = 20$ kPa at the top ceramic plate. It can be seen that the maximum conductivity interpretation error is as large as 102 % for the largest flow rate. For the flow rates of $q = 1 \cdot 10^{-5}$ cm³/s and lower, the obtained gradients are too small for practical application. Thus, in order to maintain reasonable equilibrium times and to avoid problems of non-Darcyan flow, only flow rates larger than approximately $q = 1.0 \cdot 10^{-4}$ cm³/s should be used for permeameter tests at s = 20 kPa with soils similar to Esperance Sand. The obtained conductivities, however, are likely to incorporate relatively high errors.

Table 4.3: Simulation results for Esperance Sand ($s_t = 20$ kPa).

flow rate q	**Δs**	**s_{mean}**	**grad**	**k_{perm}**	**k_{true}**	**error**
[cm³/s]	[kPa]	[kPa]	[-]	[m/s]	[m/s]	[-]
$1.0 \cdot 10^{-3}$	14.079	12.372	46.9	$5.38 \cdot 10^{-9}$	$2.67 \cdot 10^{-9}$	102.0
$5.0 \cdot 10^{-4}$	12.129	13.634	40.4	$3.16 \cdot 10^{-9}$	$1.99 \cdot 10^{-9}$	58.5
$1.0 \cdot 10^{-4}$	6.417	16.728	21.4	$1.20 \cdot 10^{-9}$	$1.06 \cdot 10^{-9}$	13.1
$1.0 \cdot 10^{-5}$	1.126	19.427	3.75	$6.85 \cdot 10^{-10}$	$6.60 \cdot 10^{-10}$	3.8
$1.0 \cdot 10^{-6}$	0.122	19.939	0.41	$6.20 \cdot 10^{-10}$	$6.07 \cdot 10^{-10}$	2.1
$1.0 \cdot 10^{-7}$	0.011	19.995	0.04	$6.02 \cdot 10^{-10}$	$6.00 \cdot 10^{-10}$	-0.2

Figure 4.6 shows the computed distributions of matric suction in the specimen for the largest four flow rates. Only head losses in the specimen are displayed. At a sample height of 30 mm a constant suction value of $s = 20$ kPa is maintained for all flow rates due to the specified boundary condition. At the base of the specimen, matric suction is reduced strongly for the higher flow rates. The lowest suction value of $s = 5.5$ kPa is obtained for the flow rate of $q = 1 \cdot 10^{-3}$ cm³/s. The suction distributions for the two highest flow rates show strong non-linearity.

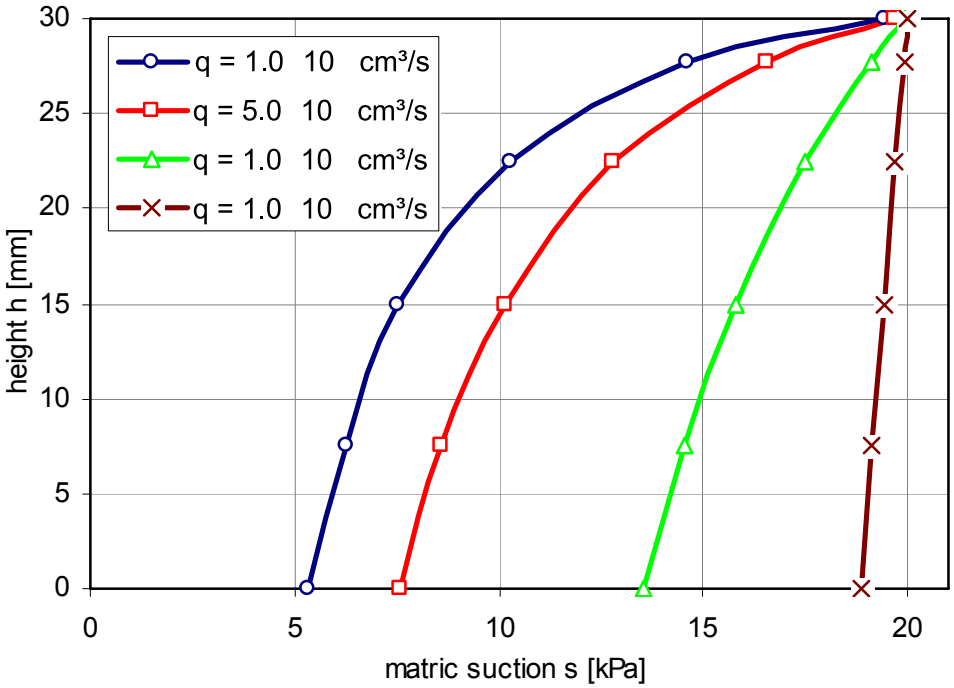

Figure 4.6: Distributions of matric suction for Esperance Sand (s_t = 20 kPa).

In Figure 4.7 additionally the extremely wide range of hydraulic conductivity for this simulation series is depicted. At the top, a value of $k_w = 6.6 \cdot 10^{-10}$ m/s is maintained for all flow rates due to the constant suction boundary condition. At the base, the hydraulic conductivities are strongly increased. For example, a value of $k_w = 2.4 \cdot 10^{-8}$ m/s is obtained for the flow rate of $q = 1 \cdot 10^{-3}$ cm³/s, which is 36 times higher than at the top.

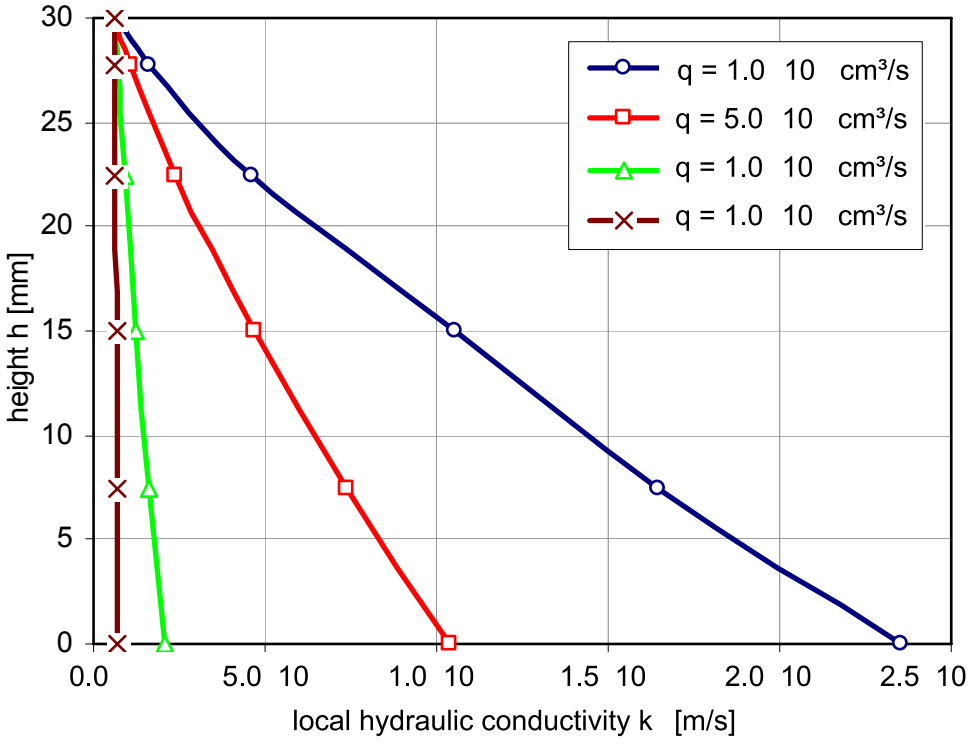

Figure 4.7: Distributions of hydraulic conductivity for Esp. Sand (s_t = 20 kPa).

- **Beit Netofa Clay 20 kPa**
  This soil has a significantly higher air entry value than Esperance sand. At 5 kPa suction Beit Netofa Clay remains almost saturated. Therefore, a suction of 20 kPa is the lower value that is used for the first simulation series. The minimum and maximum flow rates are $q = 1 \cdot 10^{-7}$ cm³/s and $2 \cdot 10^{-4}$ cm³/s, respectively. Larger flow rates cause full water saturation of the lower surface of the specimen, and numerical simulations with lower flow rates do not converge.

  Table 4.4 summarizes the results for the six conducted simulations. The conductivity errors are generally lower than for Esperance Sand. The maximum error is 22.7 % for the highest flow rate. For lower flow rates, significantly smaller errors are predicted by the numerical simulations. The two flow rates $q = 1 \cdot 10^{-4}$ cm³/s and $5 \cdot 10^{-5}$ cm³/s yield errors of 8.7 and 4.7 %, respectively. The according gradients of 41.2 and 25.0 should allow for acceptable equilibrium times. It can therefore be concluded that steady-state permeameter tests of Beit Netofa Clay at $s_t = 20$ kPa suction yield sufficiently accurate conductivity values. For the lowest flow rate of $q = 1 \cdot 10^{-7}$ cm³/s an error of -0.1% is computed. Here, because of the extremely low gradient of 0.06, the accuracy of the numerical simulations reaches its limits.

Table 4.4: Simulation results Beit Netofa Clay ($s_t = 20$ kPa).

flow rate q	**Δs**	**s_{mean}**	**grad**	**k_{perm}**	**k_{true}**	**error**
[cm³/s]	[kPa]	[kPa]	[-]	[m/s]	[m/s]	[-]
$2.0 \cdot 10^{-4}$	17.913	10.878	59.7	$8.6 \cdot 10^{-10}$	$7.0 \cdot 10^{-10}$	22.7
$1.0 \cdot 10^{-4}$	12.352	13.741	41.2	$6.3 \cdot 10^{-10}$	$5.8 \cdot 10^{-10}$	8.7
$5.0 \cdot 10^{-5}$	7.487	16.215	25.0	$5.2 \cdot 10^{-10}$	$4.9 \cdot 10^{-10}$	4.7
$1.0 \cdot 10^{-5}$	1.949	19.018	6.50	$4.3 \cdot 10^{-10}$	$4.2 \cdot 10^{-10}$	2.8
$1.0 \cdot 10^{-6}$	0.198	19.901	0.66	$4.1 \cdot 10^{-10}$	$4.0 \cdot 10^{-10}$	2.1
$1.0 \cdot 10^{-7}$	0.019	19.991	0.06	$4.0 \cdot 10^{-10}$	$4.0 \cdot 10^{-10}$	-0.1

Figure 4.8 depicts the computed distributions of matric suction for the flow rates from $q = 2 \cdot 10^{-4}$ cm³/s to $1 \cdot 10^{-5}$ cm³/s. At a sample height of 30 mm a constant suction value of $s = 20$ kPa is maintained for all flow rates due to the specified boundary condition. The head losses range from $s = 2$ to 17 kPa. In comparison with the simulations with Esperance Sand, the distributions do

not show such a strong non-linearity. These computation results explain the smaller deviations of the simulated conductivities from the true conductivities. However, that does not mean that a linear distribution of suction yields error free conductivities, as can be seen for the flow rate of $q = 1 \cdot 10^{-5}$ cm³/s in Figure 4.8 respectively in Table 4.4.

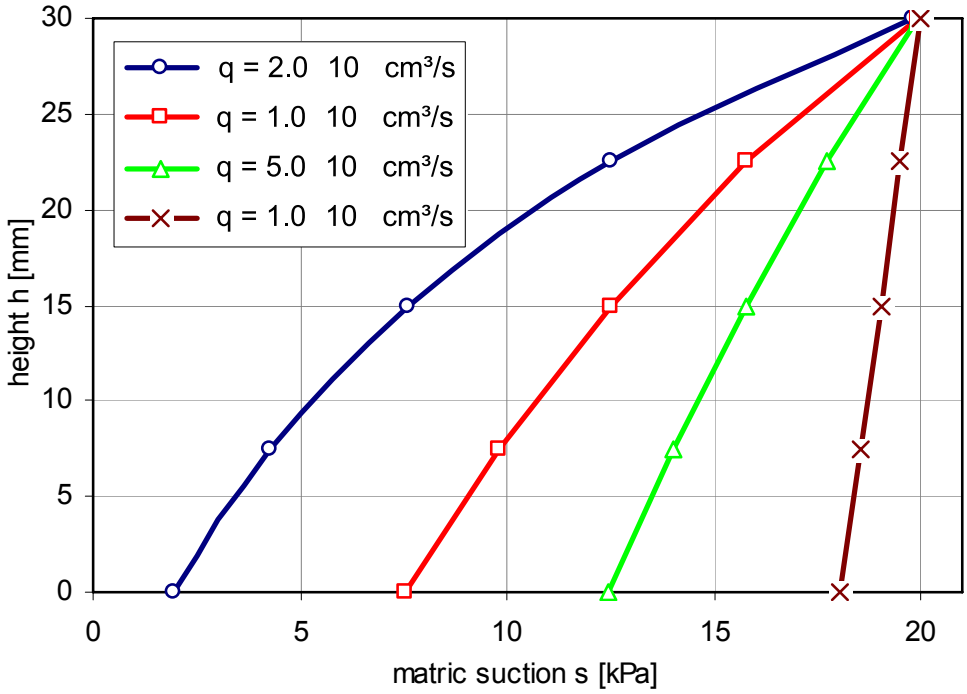

Figure 4.8: Distribution of matric suction for Beit Netofa Clay ($s_t = 20$ kPa).

- **Beit Netofa Clay 70 kPa**
  The values of the six simulated flow rates are the same as for the simulations with a suction of $s_t = 20$ kPa at the top end. Because of the reduced hydraulic conductivities at $s = 70$ kPa, the head losses due to the imposed flow rates are generally larger than for the first simulation series.

  Table 4.5 contains the corresponding computation results. The maximum conductivity error is 46.0 % for the largest flow rate. The corresponding average gradient of 200.1 is relatively high. The lower flow rates of $q = 1 \cdot 10^{-4}$ cm³/s and $q = 5 \cdot 10^{-5}$ cm³/s lead to errors of 20.3 % and 9.3 %, respectively, and the according gradients are in a common range for steady state tests. The next imposed flow rate of $q = 1 \cdot 10^{-5}$ cm³/s yields a conductivity error of only 3.2 % but in a significantly lower gradient of 30.9 as well. Because of a possibly high threshold gradient and the long testing time for this soil-type, this flow rate may already be too low for permeameter tests. Therefore, practicable steady-state tests of Beit Netofa Clay with $s = 70$ kPa applied suction at the upper end face are likely to incorporate inacceptable deviations of the true soil conductivities.

Table 4.5: Simulation results for Beit Netofa Clay (s_t = 70 kPa).

flow rate	**Δs**	**s_{mean}**	**grad**	**k_{perm}**	**k_{true}**	**error**
[cm³/s]	[kPa]	[kPa]	[-]	[m/s]	[m/s]	[-]
$2.0 \cdot 10^{-4}$	60.039	38.252	200.1	$2.6 \cdot 10^{-10}$	$1.8 \cdot 10^{-10}$	46.0
$1.0 \cdot 10^{-4}$	46.422	46.421	154.7	$1.7 \cdot 10^{-10}$	$1.4 \cdot 10^{-10}$	20.3
$5.0 \cdot 10^{-5}$	32.090	53.770	107.0	$1.2 \cdot 10^{-10}$	$1.1 \cdot 10^{-10}$	9.3
$1.0 \cdot 10^{-5}$	9.275	65.323	30.9	$8.4 \cdot 10^{-10}$	$8.1 \cdot 10^{-11}$	3.2
$1.0 \cdot 10^{-6}$	1.033	69.480	3.44	$7.5 \cdot 10^{-11}$	$7.3 \cdot 10^{-11}$	2.7
$1.0 \cdot 10^{-7}$	0.105	69.948	0.35	$7.3 \cdot 10^{-11}$	$7.2 \cdot 10^{-11}$	1.6

In Figure 4.9 the computed distributions of matric suction for the largest four flow rates are illustrated. At a sample height of 30 mm a constant suction value of s_t = 70 kPa is maintained. For the three higher flow rates large head losses, ranging from s = 20 to 60 kPa, are computed. Similar to the second simulation series with Esperance Sand, the computed suction distributions for the two largest flow rates show a strong curvature.

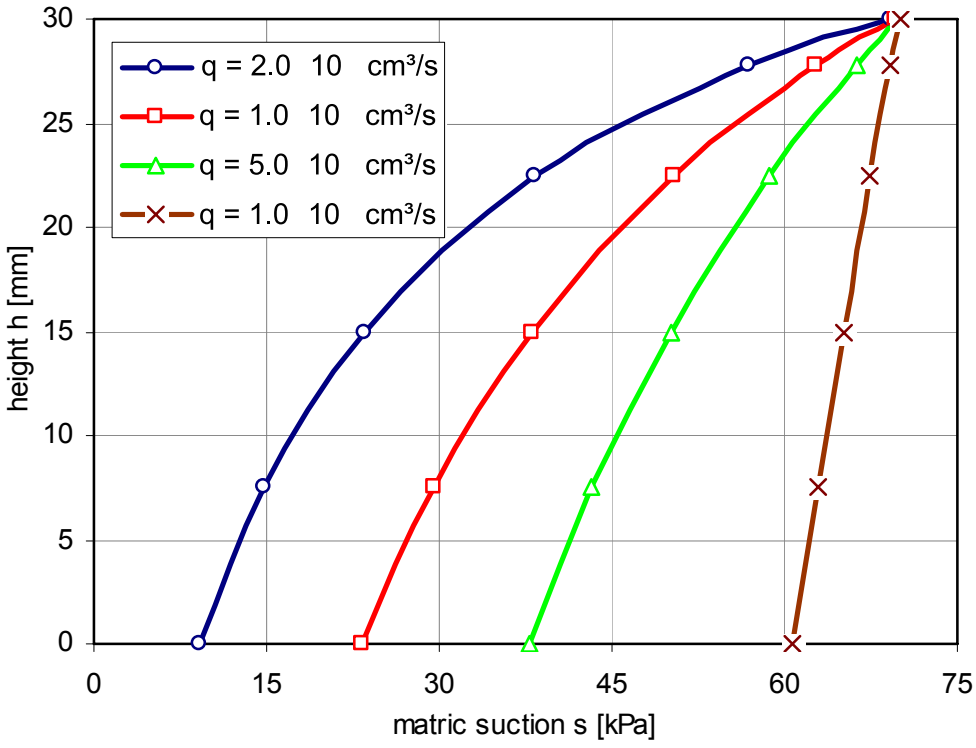

Figure 4.9: Distribution of matric suction for Beit Netofa Clay (s_t = 70 kPa).

Figure 4.10 depicts the computed hydraulic conductivity distribution for the four largest flow rates. At the top, a value of $k_w = 7.2 \cdot 10^{-11}$ m/s is maintained for all flow rates due to the constant suction boundary condition. For the flow rate of $q = 2 \cdot 10^{-4}$ cm³/s, a conductivity value of $k_w = 8.0 \cdot 10^{-10}$ m/s is obtained at the base of the specimen. The wide range of hydraulic conductivity in the sample illustrates the large error potential of conductivity interpretation of Beit Netofa Clay at this suction level.

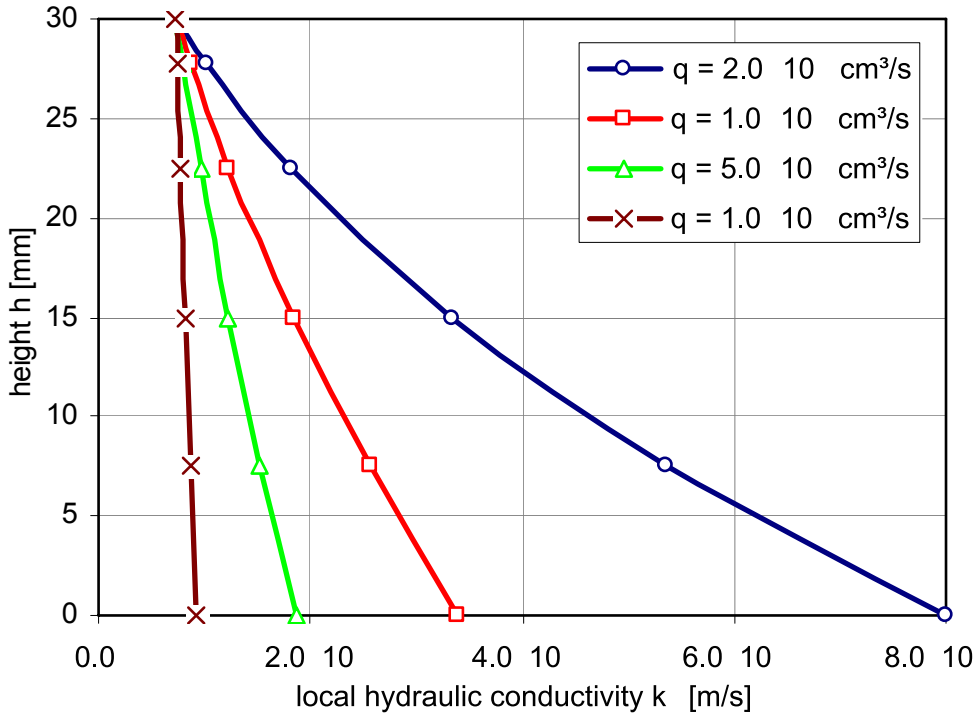

Figure 4.10: Distributions of hydraulic conductivity for B.N. Clay (s_t = 70 kPa).

4.3.4 Discussion and interpretation of results

The four numerical simulation series of the constant flow permeameter system could be carried out successfully. Detailed knowledge of the hydraulic processes and conditions "inside" the specimen was gained from the simulations. The correctness of the numerical model has been confirmed by the vanishing deviations between true and permeameter derived conductivity at the lower imposed flow rates.

To sum up, the conducted numerical simulations with Esperance Sand and Beit Netofa Clay show that

- large head losses across the specimens may occur at appropriate flow rates.
- the suction distribution along the specimens may exhibit strong non-linearity.

- hydraulic conductivity generally varies within a wide range in the specimens.

- an average conductivity at an average suction is measured rather than a specific conductivity value at a corresponding specific suction value.

- the common approach of assigning the measured average conductivity to the linear mean value of suction is likely to be highly erroneous.

The effects of the above summarized problems depend on the soil type, the magnitude of the applied suction boundary condition and the imposed flow rate. The difficulties with the non-uniform distribution of suction and associated problems become less severe at lower flow rates respectively suction gradients. However, in many cases the problem cannot be avoided because of experimental and hydraulic constrains.

In order to maintain manageable equilibrium times a certain suction gradient is necessary. The resulting non-uniform suction distribution in the permeameter is particularly a problem for low-suction soils, e.g. sands with little or no finer content. For these soils, already a low suction difference may lead to a large water saturation variation in the specimen. This results in a wide range of hydraulic conductivity in the specimen and the related problem of the correct conductivity value.

For low permeability soils, a so called threshold gradient has to be exceeded in order to induce water flow. Below this critical gradient the flow behaviour may show non-linear flow behaviour respectively no flow takes place at all. For clay soils the threshold gradient can even exceed 30 (Bear 1988). Therefore, this is another limiting factor respectively lower bound for suction differences that can be used in the permeameter tests.

From a saturated soil mechanics point of view, errors in the order of 100 % and lower (or even higher) may seem negligible. However, when unsaturated flow or transport processes are to be considered, a higher accuracy is indispensable for two reasons: Firstly, incorrect conductivity values may bias or even prevent the calibration of a relative permeability-saturation respectively permeability-suction constitutive model. Secondly, most unsaturated flow problems are time-dependent respectively transient. Here, errors in the used conductivity data may result in totally misleading predictions of flow or transport processes.

Due to the latter aspects, it seems necessary to reconsider the common practice of referring the conductivities from steady-state tests to the linear mean value of suction. Moreover, it appears desirable to apply respectively to develop new techniques that allow for more appropriate conductivity values. In the following section, three different methods and their effectiveness are investigated.

4.4 Correcting the steady-state derived conductivity

4.4.1 The Smiles and Towner method

Smiles and Towner (1968) presented a method of analysis for use with steady-state measurements of unsaturated hydraulic conductivity. The method itself is relatively simple but requires additional conductivity tests. The same magnitude of suction has to be maintained at one side of the sample during a number of tests. The increased testing effort may make the method appear less attractive. On the other hand, it is especially well suited for constant-flow permeameters.

To highlight the basic idea of the Smiles and Towner method, an analysis which is after Crank (1964) is presented. An unsaturated soil column of the length l is considered. The analysis starts with a differential form of the Darcy- equation:

$$v = -k\frac{\partial H}{\partial x} \tag{4.6}$$

H potential at a distance x along the specimen

Equation (4.6) can be integrated with respect to x over the total length of the considered specimen:

$$v \cdot l = -\int_{H_0}^{H_l} k \cdot dH = -k \cdot \left(H_l - H_0\right) \tag{4.7}$$

H_0 potential at $x = 0$
H_l potential at $x = l$

Differentiating equation (4.7) with respect to H_l, and assuming H_0 as a constant, yields the relationship:

$$\frac{\partial v}{\partial H_l} \cdot l = -k \tag{4.8}$$

Equation (4.8) in principle states that the slope of a function $l \cdot v(H_l)$, supposed a constant H_0, corresponds to the hydraulic conductivity for specific values of H_l. Experimentally, this curve can be obtained by carrying out a number of tests with different flow rates while maintaining the suction head at the other end face of the specimen constant. The Darcy-velocity v is given by the injected flow rate, and the according suction head H_l at the base can be measured.

Figure 4.11 shows a plot, which illustrates graphically the application of the Smiles and Towner method. The data points were obtained from the second simulation series with Esperance Sand, where a suction of $s = 20$ kPa was applied to the upper end face of the specimen.

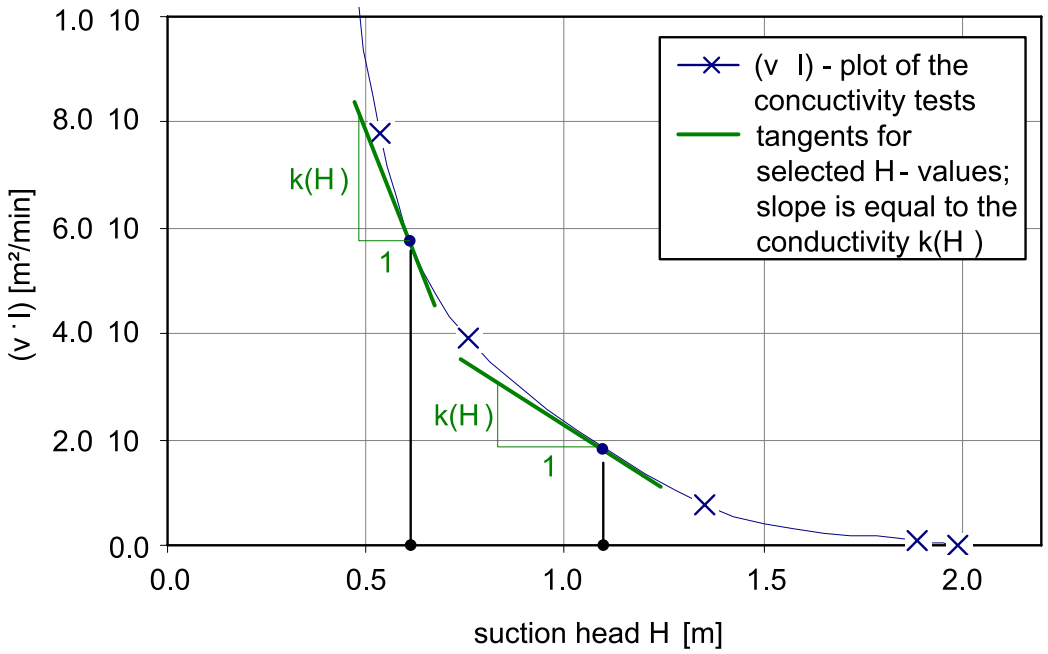

Figure 4.11: Illustration of the Smiles and Towner method.

Obviously, the more experiments are carried out, the higher the accuracy of the obtained hydraulic conductivities will be. At one side of the specimen the suction head is maintained constant throughout the tests. Thus, equilibrium times when switching from one flow rate to the other are relatively fast in comparison with a test with a different suction head and flow rate. Further, the additional experimental time effort can be considered as duly because various conductivities at different suctions can be derived from such a testing series.

A possible complication of the Smiles and Towner method is the impedance of the ceramic plates. Equation (4.8), in a strict sense, requires H_0 to be constant at one end surface of the specimen. However, H_0 can only be controlled behind the ceramic plate. It is therefore important to use ceramic plates with negligible resistance compared to the probed soil. In this favourable case, the potential drop across the plates can be neglected. Smiles and Towner (1968) additionally presented a way to deal with cases in which the latter condition cannot be maintained. This method is based on the same analytical analysis, but requires a set of ($v \cdot l$) versus H_l curves. More extensive testing series at different H_o-values are necessary, making this alternative method extremely tedious.

- **Example of use:**
  The Smiles and Towner method is applied to the simulations series with Esperance Sand (s_t = 20 kPa) and Beit Netofa Clay (s_t = 70 kPa). The plot shown in Figure 4.11 and an analogous plot for Beit Netofa Clay are used. The hydraulic conductivity values are derived for three different suction values for both considered simulation series. The results are summarized in

Table 4.6. For the different suction values, the conductivity obtained with the Smiles and Towner method $k_{S\&T}$ and the true conductivity k_{true} are presented.

Table 4.6: Application of the Smiles and Towner method (1968).

simulation series	**suction**	$\mathbf{k_{S\&T\ (1968)}}$	$\mathbf{k_{true}}$	**error**
-	[kPa]	[m/s]	[m/s]	[-]
Esperance Sand with s_t = 20 kPa	10.0	$5.19 \cdot 10^{-9}$	$5.28 \cdot 10^{-9}$	-1.7
	12.5	$2.67 \cdot 10^{-9}$	$2.59 \cdot 10^{-9}$	3.2
	15.0	$1.39 \cdot 10^{-9}$	$1.49 \cdot 10^{-9}$	-6.7
Beit Netofa Clay with s_t = 70 kPa	30.0	$2.59 \cdot 10^{-10}$	$2.51 \cdot 10^{-10}$	3.3
	40.0	$1.64 \cdot 10^{-10}$	$1.71 \cdot 10^{-10}$	-4.3
	50.0	$1.32 \cdot 10^{-10}$	$1.24 \cdot 10^{-10}$	6.7

The obtained results indicate that the Smiles and Towner method is particularly effective for large suction gradients across the specimen. The average and the maximum error of the obtained conductivity values are 4.3 and 6.7 %, respectively. By comparison, errors up to 100 % would be obtained if the linear mean value of suction was referred to the conductivity values. When the suction, for which the conductivity is to be determined, approaches the applied suction on the upper end side of the specimen, the inaccuracy of the graphical interpretation becomes a limiting factor. This tendency can already be observed for the obtained conductivities in Table 4.6.

4.4.2 A new reference suction

From the numerical simulations and the computed distributions of matric suction along the height of the specimens it can be recognized that the true average matric suction is always lower than the linear mean suction. It seems therefore logical that the measured hydraulic conductivity from permeameter tests is always predicted too high when the linear mean value of suction is employed as reference suction. The analysis of the numerical simulations confirms this assumption. On the other hand, this clear tendency does not yet imply that the true average suction corresponds exactly to the permeameter conductivity.

It is of theoretical interest, however, to investigate the latter assumption. For this purpose, the largest flow rates of each of the four simulation series are taken into account. These are the simulations that yielded the largest errors of the obtained conductivities. Based on the computed distributions of matric suction, the true mean suction is computed and subsequently referred to the conductivity derived from the permeameter simulations. This value is finally compared to the correct conductivity of the computed mean suction.

To begin with, the suction distributions of the four simulations are approximated with fourth or fifth order polynomials as functions of the height *s(h)*. The true mean suction s_{mean} is subsequently computed with the line integral:

$$s_{mean} = \frac{1}{h_o - h_u} \int_{h_u}^{h_o} s(h) \cdot dh \qquad (4.9)$$

In Figure 4.12 the problem of linear mean suction and true mean suction is highlighted for the simulation with Esperance Sand at s_t = 20 kPa and q = $1.0 \cdot 10^{-3}$ cm³/s. The suction at the upper end of the specimen is slightly reduced to a value of s = 19.4 kPa due to the head loss in the ceramic plate. At the base of the specimen suction is reduced to a value of s = 5.3 kPa. In between these values the distribution is strongly non-linear. The common approach, computing a linear mean suction, gives a value of s_{mean} = 12.4 kPa. The true mean value s_{true} = 9.7 kPa is encountered at a height of 22 mm. If the computed true mean suction is referred to the conductivity value obtained from the permeameter simulation, the deviation from the correct conductivity is only -1.7 %.

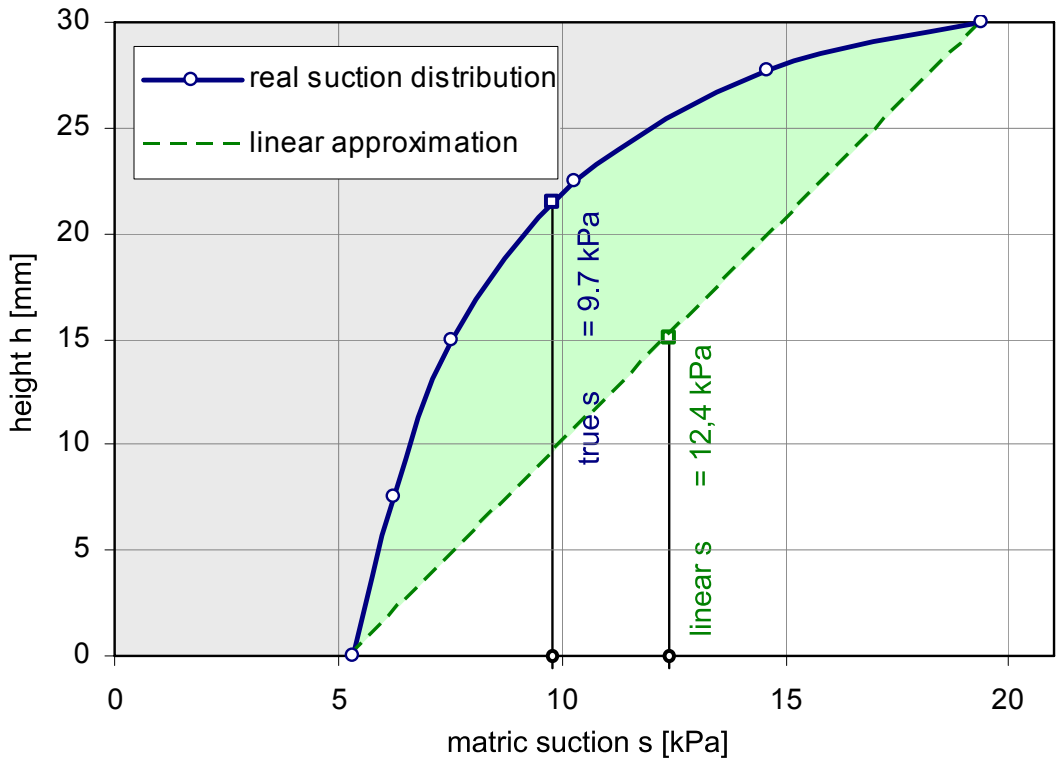

Figure 4.12: Linear mean value and true mean value of the suction distribution.

The same procedure was carried out for the largest simulated flow rates of Esperance Sand (s_t = 5 kPa), Beit Netofa Clay (s_t = 20 kPa and 70 kPa). The results of the analyses are summarized in Table 4.7. The first three columns show the conductivity value obtained from the permeameter simulation k_{perm}, the corresponding linear mean suction and the true mean suction. Finally, the conductivities for the true mean suctions and their deviations from the permeameter values are presented. The average error of 4.0 % is very low in comparison to the average error of 50.8 % which is caused by referring the linear mean value of suction to the permeameter results (compare section 4.3.3).

Table 4.7: Conductivity errors for true mean suction (for the largest flow rate of each simulation series).

simulation	**k_{perm}**	**linear s_{mean}**	**true s_{mean}**	**k (true s_{mean})**	**error**
-	[m/s]	[kPa]	[kPa]	[m/s]	[-]
Esperance Sand s_t = 5 kPa	$9.31 \cdot 10^{-8}$	2.90	2.13	$9.89 \cdot 10^{-8}$	6.3
Esperance Sand s_t = 20 kPa	$5.38 \cdot 10^{-9}$	12.37	9.75	$5.29 \cdot 10^{-9}$	-1.7
Beit Netofa Clay s_t = 20 kPa	$8.64 \cdot 10^{-10}$	10.88	9.07	$8.36 \cdot 10^{-10}$	-3.4
Beit Netofa Clay s_t = 70 kPa	$2.57 \cdot 10^{-10}$	38.90	28.60	$2.69 \cdot 10^{-10}$	4.7

The results presented in Table 4.7 suggest that the true mean suction corresponds closely to the average hydraulic conductivity measured by steady-state tests. However, the distribution of suction and therefore the true mean suction are not known respectively cannot be computed a priori to the conductivity tests. Even after the conduction of the tests the computation of the true mean suction would be problematic due to the a priori unknown errors of the conductivities from the permeameter tests. An iterative numerical procedure would be required.

From a practical point of view it seems more attractive to develop a formula for a new reference suction that does not require additionally numerical analyses. This formula has to take into account the curved shape of the suction distribution in the specimens in the permeameters. The suction computed by the new formula should aim representing the true mean suction as accurately as possible.

Two additional simulation series, one with a clayey and one with a sandy soil type, were carried out in order to generate a larger data pool. Subsequently, numerous attempts at developing a formula for the new reference suction were undertaken. These attempts included consideration of the pore size distribution

factor, air entry value etc. Many of these approaches yielded good results for one or two simulation series but failed for others with different soil types. Finally, the best solution proved to be a simple formula which only incorporates the suction values at both end faces of the specimen. In principle, the linear mean suction is corrected for the weighted suction difference between the base and the top of the specimen, respectively. The proposed new reference suction s_{ref} further considers two cases, depending on the magnitude of the suction gradient:

If $(s_t - s_b) \leq \frac{s_t}{2}$:

$$s_{ref} = \frac{1}{2}(s_b + s_t) - \frac{1}{8}(s_b - s_t) = \frac{5}{8}s_b + \frac{3}{8}s_t \tag{4.10}$$

If $(s_t - s_b) > \frac{s_t}{2}$:

$$s_{ref} = \frac{1}{2}(s_b + s_t) - \frac{1}{6}(s_b - s_t) = \frac{2}{3}s_b + \frac{1}{3}s_t \tag{4.11}$$

s_b suction at the base of the specimen
s_t suction at the top of the specimen

For all conducted simulations, equation (4.10) respectively (4.11) proved to be considerably more appropriate than the common approach with the linear mean suction. Most remarkable improvements are obtained for the higher flow rates. Here, the conductivity error is often reduced by a factor of 10. In general, assigning the new reference suction to the conductivities of permeameter tests yields deviations of less than 10 % of the true value, even for very high suction gradients.

It is to be expected that employing the suggested new reference suction for future steady-state permeameter tests yields a significant improvement of the obtained conductivity values. In case of other permeameter systems, it is noted that for application of Equation (4.10) and (4.11), s_b is always the lower suction value, and s_t is always the larger suction value.

- **Example of use:**
  In order to show the appropriateness of the new reference suction, another simulation series with Esperance Sand is conducted. The simulations carried out in section 4.3.3 are not suitable because they primarily focused on the effects of different flow rates at the same suction. For the determination of an actual hydraulic conductivity function, a number of tests at different applied suction values at the upper end of the specimen are necessary.

  A hypothetical set of permeameter tests at six different suction values, ranging from ***s*** = 5 kPa to 150 kPa, is simulated. The procedure is the same as

in section 4.3.3. The parameters of Esperance Sand given in Table 4.1 are used for the numerical simulations. The hydraulic conductivities k_{perm} are computed with Darcy's law. The gradient is obtained from the pressure increase at the water reservoir at the lower ceramic plate. Instead of employing the linear mean suction, Equation (4.10) respectively (4.11) is employed to compute the new reference suctions s_{ref}. Subsequently, the true hydraulic conductivities for the reference suction $k(s_{ref})$ are determined with the constitutive model function. Finally, the deviations of the conductivities $k(s_{ref})$ from the permeameter conductivities k_{perm} are computed.

Table 4.8 contains the results of the conducted investigations. The absolute errors, when the conductivity values k_{perm} are referred to the new reference suction, vary from 0.1 to 9.9 %. The average error of the six simulated tests is 4.0 %. If the commonly used linear mean suction is assigned to the conductivities obtained from the permeameter tests, the minimum error is 20.2 % and the maximum error is 61.8 %. The average error for this case is 40.9 %. These results confirm the appropriateness of the proposed new reference suction.

Table 4.8: Example of the use of the new reference suction.

test number	$\mathbf{s_{top}}$	$\mathbf{k_{perm}}$	$\mathbf{s_{ref}}$	$\mathbf{k\ (s_{ref})}$	**error**
	[kPa]	[m/s]	[kPa]	[m/s]	[-]
1	5.0	$8.21 \cdot 10^{-8}$	2.96	$8.85 \cdot 10^{-8}$	**-7.3**
2	10.0	$2.37 \cdot 10^{-8}$	6.29	$2.63 \cdot 10^{-8}$	**-9.9**
3	20.0	$3.16 \cdot 10^{-9}$	13.73	$3.19 \cdot 10^{-9}$	**-1.0**
4	50.0	$1.38 \cdot 10^{-10}$	35.94	$1.38 \cdot 10^{-10}$	**0.1**
5	100.0	$8.54 \cdot 10^{-12}$	77.23	$8.15 \cdot 10^{-12}$	**4.8**
6	150.0	$1.47 \cdot 10^{-12}$	123.49	$1.48 \cdot 10^{-12}$	**-0.8**

4.4.3 Inverse modelling

In many cases the hydraulic conductivities obtained from steady-state permeameter tests are subsequently to be used for the analysis of transient unsaturated flow or transport problems. This often implies the application of numerical methods. For this purpose the conductivity data has to be integrated into suitable constitutive models. In this case, an attractive method to improve the biased conductivity data from the permeameter tests is their inverse modelling.

A suitable inverse modelling framework was already presented in chapter 2. This framework is adapted to the purpose of interest and is further on called COPEDA (for: COrrect PErmeability DAta). In order to not mixing up the steady-state tests with time-dependent flow behaviour, only steady-state measurements are used for the optimizations. That means that for each conducted permeameter test, the final water pressure in the reservoir at the base below the ceramic plate is an observation value. If available, also steady-state pore water pressure measurements inside the sample could be used.

Figure 4.13 shows a flowchart with the principal functioning of COPEDA. The program starts with a calibration of the constitutive model of choice against the hydraulic conductivities obtained from the permeameter tests. UCODE_2005 (Poeter et al. 2005) is employed for the optimization process. Due to the erroneous conductivity data, the optimized parameters are obviously biases as well. They are, however, used as suitable starting parameters for the final calibration process.

After this first step, COPEDA initializes the main optimization cycle. A forward run of the numerical simulations of the conductivity tests is carried out. For each single test a numerical model is required. The computed final water pressures below the lower ceramic plate are compared to the steady-state measurements of water pressure. UCODE_2005 carries out a sensitivity run and computes an updated parameter set. This second optimization cycle is repeated until convergence is reached, see Figure 4.13.

The main difference to the inverse modelling framework presented in chapter 2 is that COPEDA works as a superordinate program to UCODE_2005. Furthermore, a batch-file is employed to run the various permeameter simulations (according to the number of tests) that are used for one optimization cycle. In the original framework, only one process model is used. A simplification is that the boundary conditions do not change during the tests. Theoretically, the first optimization cycle would not be required. However, the quality of the initial guess parameters is of high importance for the successful calibration of flow models (Hill &

Tiedemann 2007). It is thought that the chosen two-stage approach allows a successful parameter optimization even in the case of a low number of available conductivity tests.

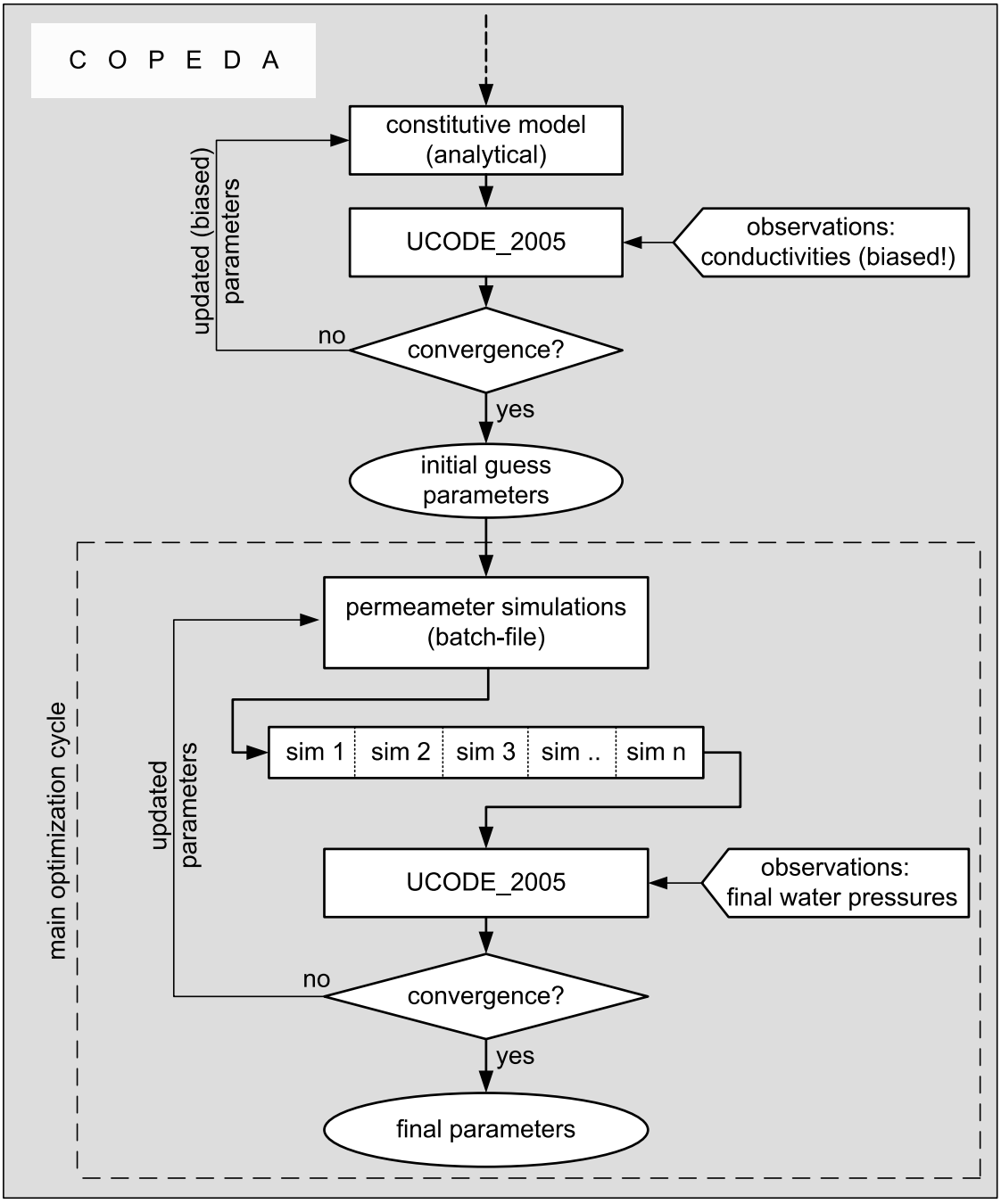

Figure 4.13: Flowchart of the principal functioning of COPEDA

- **Example of use:**
  In order to demonstrate the program capability, an exemplary optimization run with synthetic observation data sets is conducted. The results of the six simulated permeameter tests of the example of use in section 4.3.2 (see Table 4.8) are used for this purpose. The computed conductivities, referred to

the linear mean suction, constitute the first observation set. The computed steady-state water pressures below the lower ceramic plate constitute the second observation set.

The Van Genuchten-Mualem model (Van Genuchten 1980, Mualem 1976) is chosen as hydraulic conductivity function. Theoretically, five parameters could be optimized. The saturated water conductivity k and the saturated water content θ_{ws} can be determined with ease and high reliability in laboratory tests. The tortosity factor τ, following a common approach, is fixed with 0.5. Therefore, the pore size distribution factor n and the residual water saturation S_{wr} are optimized with COPEDA. Optimizing more parameters, e.g. the tortuosity factor, would probably require more observation data, i.e. more conductivity tests.

In the first optimization cycle, the conductivity values are calibrated against the analytical expression of the Van Genuchten-Mualem model. The optimized n-value is 1.56, and the S_{wr}-value is 0.080. The maximum and average deviations from the true conductivity values are 24.2 and 11.1 %, respectively.

Obviously, the parameters obtained from the preliminary optimization are biased. They are, however, used as initial guess parameters for the subsequent main optimization process. Here, in six iterations convergence is reached. The optimized parameters are practically identical with the parameters used for the forward simulation respectively the generation of the synthetic observation sets. The final n-value is 1.600, and the final $S_{w,r}$-value is 0.0442. With these parameters, the errors of the obtained conductivities are negligibly small, as can be seen from the last line of Table 4.9.

Table 4.9: Example of a COPEDA-run.

parameter	**n-value**	**$S_{w,r}$**	**maximum error**	**average error**
unit	[-]	[-]	[-]	[-]
forward simulation	1.600	0.0440	0.0	0.0
preliminary optimization	1.561	0.0800	24.2	11.1
main optimization	1.600	0.0442	0.17	0.08

4.5 Summary and conclusions

In this chapter, a numerical investigation of the steady-state method for unsaturated conductivity tests was carried out. A key interest of the research was to investigate the appropriateness of the common practice of assigning the measured conductivities to the linear mean value of suction of the sample. Further, the distribution of matric suction and hydraulic conductivity across the soil specimen were of interest.

The conducted numerical simulations illustrated the strong non-linear distribution of matric suction across the soil specimen especially for higher flow rates. Accordingly, a wide range of hydraulic conductivities over the length of the specimen was obtained. Since the correct hydraulic conductivities can be computed with the employed constitutive model function, a comparison of the conductivity values obtained from the permeameter tests was enabled. High deviations of the measured permeameter conductivities from the correct values were encountered.

The non-uniform distribution of suction and its adherent problems can theoretically be reduced by application of lower flow rates respectively head differences. However, it can never be completely avoided, and especially testing soils with low water retention potential will necessarily require flow rates that result in high suction gradients. Beyond, several arguments speak in favour of applying higher flow rates. Firstly, testing times can be reduced. Secondly, shorter testing times diminish the effects of experimentally caused errors. Thirdly, low flow rates imply very low gradients and thus, possible non-Darcyan flow behaviour is likely to interfere with the experimental results. Due to the latter considerations, the experimental investigator may not ignore the effects of the non-uniform suction distribution (which in fact is the common practice).

Three different methods of dealing with the hydraulic conductivity data obtained from steady-state tests were developed respectively investigated. Their performance and the conclusions that were drawn are summarized in the following:

- **The Smiles and Towner method (1968):**
  This method requires a number of tests at the same applied suction head at one end face of the specimen. The slope of a plot derived from the readily manipulated experimental data is a measure for the hydraulic conductivity at specific suction values. The method was applied to two simulation series that were conducted with parameters for Esperance Sand and Beit Netofa Clay. The derived hydraulic conductivities showed very good agreement with the correct values. For conductivities at suction values that approach the applied

suction head at the upper ceramic plate, the Smiles and Towner method becomes less effective respectively accurate.

- **A new reference suction:**
  The analysis of the numerically computed suction distributions showed that the actual mean suction for all simulated tests is larger than the linear mean value of suction. Further investigations showed that true mean suction corresponds closely to the average conductivity value which is obtained from steady-state permeameter tests. Consequently, a formula for a new reference suction aiming at matching the hydraulic conductivity was developed. The expression was calibrated against all of the conducted simulation series. The formula is simple and includes only the applied respectively measured suction values at the lower and upper end face of the specimen as variables. In order to show its correctness, the new reference suction was applied to an artificial set of simulated conductivity tests. The obtained results showed an average error of only 4 %.

- **Inverse modelling:**
  For cases in which the results of the permeameter tests are meant to be used in a numerical investigation of transient flow or transport problems, the conductivity values need to be incorporated into suitable constitutive models. Here, inverse modelling of the tests was suggested as an attractive method to obtain unbiased parameters. An existing inverse modelling framework was adapted to the purpose of interest. A two-stage optimization procedure of the hydraulic parameters was developed. In order to not mix up the steady-state measurements of the permeameter tests with transient flow behaviour, it was suggested to use only steady-state measurements for the optimization. The program was subsequently tested against synthetically generated observation value sets. The program was able to correctly identify the two optimized parameters from only six employed observations of the final pressures at the water reservoir where the flow is imposed.

Summarized, all three investigated methods for dealing with the effects of the non-uniform distribution of suction yield much better results than the common practice of employing the linear mean suction. Sticking to this practice means taking into account the possibility of highly erroneous conductivity values. For the future interpretation of hydraulic conductivity data derived from steady-state tests it is therefore strongly recommended to make adequate use of one of the proposed alternative approaches.

5 Installation, calibration and first results of a triaxial testing device

5.1 Introduction

At the Institute of Soil Mechanics and Foundation Engineering of the Graz University of Technology, tunnelling under compressed air has been a means of research during the last two decades. Because a prediction of the air losses has been of primary interest, most of the experimental and theoretical work focused on two-phase flow in unsaturated soils. Growing interest in the surface settlements and the tunnel face stability during a compressed air tunnel advance yielded an extension of the research to mechanical aspects. Chinkulkijniwat (2005) developed a coupled fluid-mechanical computation framework. Here, the implementation of appropriate constitutive models is work in progress.

The mechanical behaviour of unsaturated soils differs significantly from saturated soils. Thus, in order to experimentally investigate the mechanical behaviour and to subsequently derive parameters for the constitutive models, it was decided to equip the geotechnical laboratory with a double-walled triaxial cell for unsaturated soils. In this chapter, the installation and calibration process of the triaxial apparatus as well as the first results of a testing programme with fine-sandy silt are presented.

The chapter begins with theoretical aspects and a literature review of the mechanical behaviour of unsaturated soils. Additionally, the employed stress-state variables and the corresponding constitutive modelling approaches are recalled. Thereafter, the double-walled triaxial testing device for unsaturated soils is presented. The initial problems of the device and the improvements in order to overcome these deficiencies are described. The sensibility of the volume change-measuring device to temperature and pressure variations is investigated. Finally, the double-walled cell is calibrated against different cell pressures in order to enable accurate volume change measurements of the soil specimens during the tests.

After the completion of the installation and calibration process, a first testing series using a fine-sandy silt is started. The investigation of the mechanical behaviour of such soil types is of interest with respect to tunnelling under compressed air. The triaxial tests are conducted under drained conditions. The testing paths comprise an initial suction equilibration phase, a subsequent isotropic consolidation phase and a final shearing phase. The consolidation and shearing take place at constant suction. The effects of the degree of saturation

(hysteresis of the water retention curve) on the shear strength and strain behaviour are investigated by rigorous testing on main drying respectively wetting paths. The obtained results are discussed with respect to published experimental results of similar materials. The chapter closes with a summary and suggestions for further improvements on the triaxial testing device.

5.2 Theoretical aspects and literature review: mechanical behaviour of unsaturated soils

5.2.1 Micro-mechanical considerations

The suction in unsaturated soils affects their mechanical behaviour in two different ways (Wheeler and Karube 1995): firstly, by modifying the soil skeleton stress through changes in the average fluid pressure acting in the pores; and secondly, by providing an additional bonding force at the particle contacts as a consequence of capillary phenomena in the water menisci.

In order to better understand the two different mechanisms, first of all the distribution of pore water in unsaturated soils is considered: it may either appear as bulk water in within water-filled voids or as meniscus water at the inter-particle contacts around air-filled voids (Wheeler et al. 2003), see Figure 5.1. A soil specimen at a high degree of water saturation will have more bulk water and less meniscus water than a soil at a lower degree of saturation and vice verse.

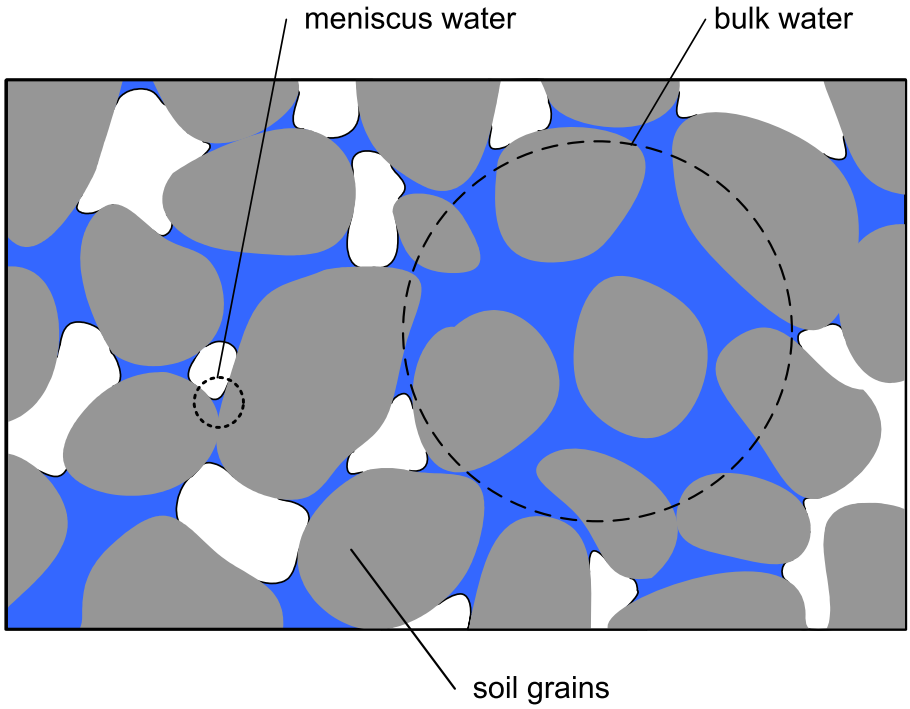

Figure 5.1: Bulk water and meniscus water in unsaturated soils.

In order to demonstrate the different effects of bulk water and meniscus water on the mechanical behaviour, an idealized macro-mechanical consideration is undertaken. Two identical spheres, which are in contact with each other, are considered. In one case the contact is saturated (= bulk water) and in the case the contact is unsaturated (= meniscus water), see Figure 5.2.

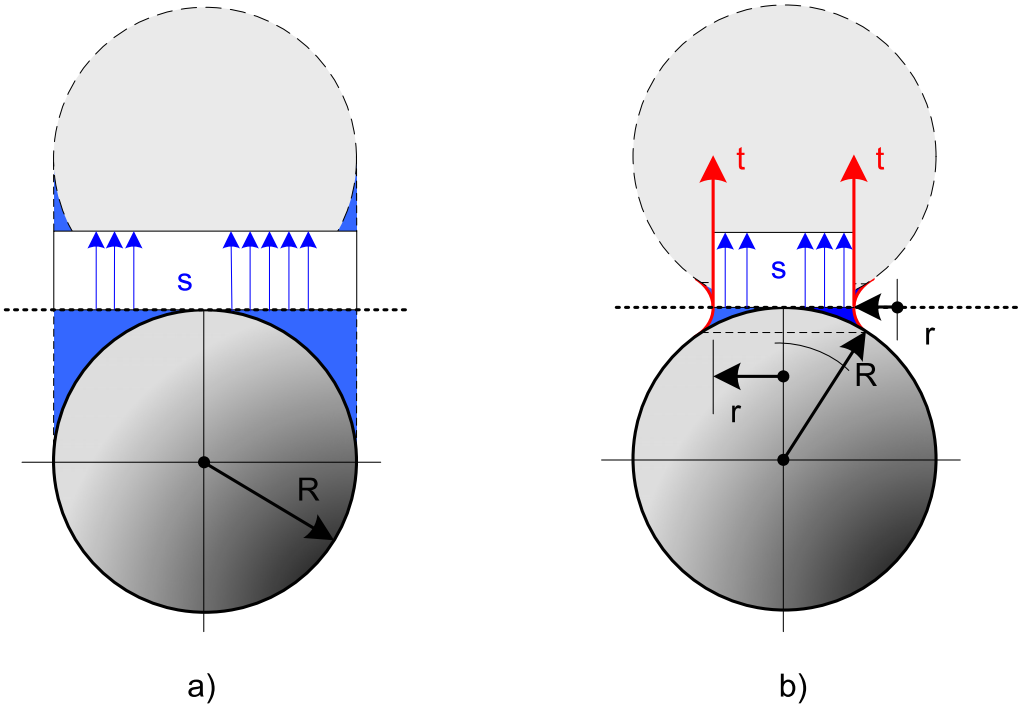

Figure 5.2: Idealized saturated (a) and unsaturated particle contact (b).

If the space between the spheres is completely filled with bulk water (Figure 5.2 a) at a given suction *s*, the intergranular stress σ_i^{bulk} is obviously equal to the magnitude of suction:

$$\sigma_i^{bulk} = \frac{s \cdot A}{A} = s \tag{5.1}$$

A cross section of the spheres

Now, a meniscus water contact is considered (see Figure 5.2 b). The magnitude of suction in the nodoide between the two spheres is given by the Young-Laplace-equation:

$$s = t_s \left(\frac{1}{r_1} - \frac{1}{r_2} \right) \tag{5.2}$$

t_s surface tension of water
r_1 radius of the meniscus surface
r_2 radius of the liquid bridge at the neck

The magnitude of suction in the meniscus between two contacting spheres can be computed as a function of the particle radius R and the half-filling angle θ of the meniscus (Figure 5.2 b). Rearranging Equation (5.2) yields:

$$s = t_s \left(\frac{1}{R\left(\frac{1}{\cos\theta} - 1\right)} - \frac{1}{R\left(1 + \tan\theta - \frac{1}{\cos\theta}\right)} \right) \tag{5.3}$$

It can be recognized that Equation (5.3) is linear with respect to the radius R of the spheres. The function has a singularity at $\theta = 0$. Here, the theoretical value of suction is infinite. Another characteristic point of the function is given for an aperture angle of θ = 53.13°. Here, the suction in the meniscus vanishes, independently of the sphere radius; this means that pore air and pore water pressure have equal magnitudes. Moreover, positive pore water pressures are obtained for all menisci, in which the half-filling angle is larger than 53.13°. In order to show the influence of the half-filling angle on the magnitude of suction, Figure 5.3 depicts plots of Equation (5.3) for three different radii R.

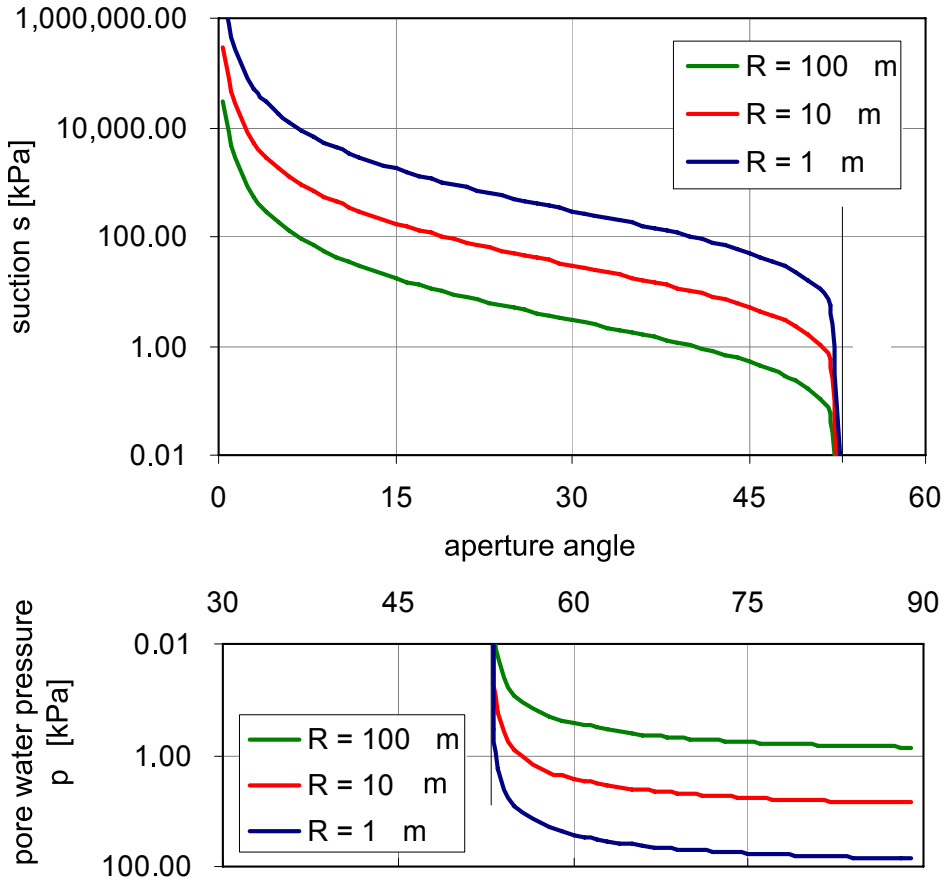

Figure 5.3: Theoretical suction values respectively pore water pressures between two spheres as a function of the half-filling angle θ.

In order to allow a logarithmic illustration of the plots, the diagram in Figure 5.3 is divided into two parts: the upper diagram depicts the distribution of suction for half-filling angles between 0 and 53.13°. Here, the strong decrease of suction with increasing aperture angle can be recognized. In contrast, the lower diagram shows the distribution of the positive pore water pressures (~ negative suction) for half-filling angles larger than 53.13°. Note that the absolute values of the pore water pressures are significantly smaller than in the range from 0 to 53.13°.

In addition to externally applied stresses, the intergranular stress of the unsaturated contact is a function of the pore water pressure in the liquid bridge and the surface tension around the perimeter of the neck of the liquid bridge (Figure 5.2 b):

$$\sigma_i^{menisucus} = \frac{r_2^{\,2}\pi \cdot \left(\frac{1}{r_1} - \frac{1}{r_2}\right) + t_s \cdot 2r_2\pi}{R^2\pi} \tag{5.4}$$

The development of the intergranular forces is not a priori obvious from Equation (5.4). If the suction in the meniscus increases, this goes necessarily hand in hand with a reduction of the cross section and the perimeter of the liquid bridge. This fact reduces the increase of an elevated suction to the intergranular stress. If instead of the radii r_1 and r_2 the half-filling angle θ of the water meniscus is introduced, the following expression is obtained:

$$\sigma_i^{menisucus} = \frac{\frac{t_s \cdot 2R\pi}{1+\tan(\theta/2)}}{R^2\pi} = \frac{2t_s}{R} \cdot \frac{1}{1+\tan(\theta/2)} \tag{5.5}$$

Equation (5.5) is evaluated for different angles θ and particle radii of 1, 10 and 100 µm. The obtained distributions of the intergranular stresses are depicted in Figure 5.4. It can be seen that the variation of the intergranular stresses with increasing suction is only moderate. As a first approximation, a constant value for all evaluated particle radii can be assumed. It can be recognized that even at zero suction there is a positive intergranular stress for the unsaturated contact. This is due to the surface tension along the perimeter of the liquid bridge. Schubert (1982) presented an analysis, which showed that the normal forces between two spheres always remain positive, even for positive pore water pressures in liquid bridges.

In order to demonstrate its different nature, the intergranular stress for the saturated contact is also shown in Figure 5.4. The development is linear proportional to the magnitude of suction and is independent of the particle radius. A converse feature is the intergranular stress at zero suction. Whereas for unsaturated contacts a distinct positive value is obtained, the intergranular stress is always zero for saturated contacts. Consequently, from zero suction to the

intersection of the two different curves, higher values are obtained for unsaturated contacts than for saturated contacts. Therefore, in an unsaturated soil at zero suction the intergranular stresses are higher than in a saturated soil at zero suction (Boso et al. 2005).

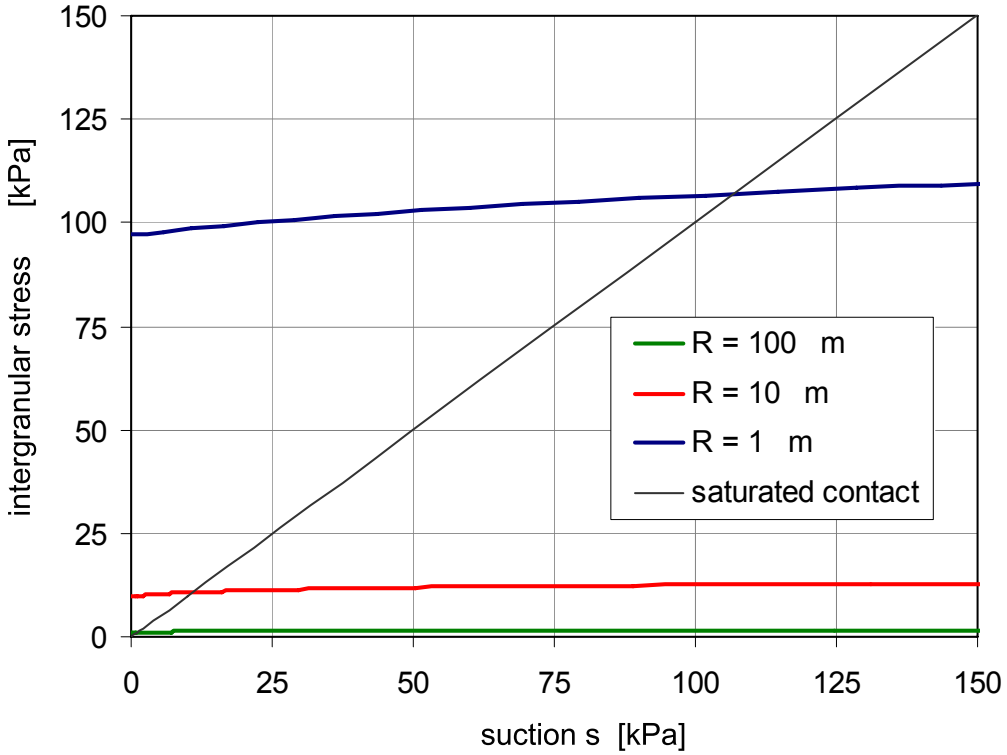

Figure 5.4: Exemplary distributions of intergranular stresses for saturated and unsaturated sphere contacts.

Similar results as shown in Figure 5.4 are obtained for non-contacting spheres respectively spheres with different particle radii. Concerning the magnitude of the intergranular stresses, it is emphasised that intergranular stresses are not comparable to effective stresses. Consequently, these micro-mechanical considerations are not suitable to compute effective stresses in unsaturated soils. Rather, they indicate some general trends in the mechanical behaviour of unsaturated soils respectively are helpful for the interpretation of experimental results and inherent phenomena. Examples are the linear increase of the shear strength at suctions lower than the air entry value (predominance of bulk water), the subsequent plateau (changeover from saturated contacts to unsaturated contacts) or the shrinkage limit of unsaturated soils (predominance of meniscus water).

The division of pore water in bulk water and meniscus water is also of importance with respect to hysteretic effects on the mechanical behaviour of unsaturated soils. As a consequence of the hysteretic water retention behaviour of most soils, two samples may have the same magnitude of suction but may exhibit significantly different degrees of saturation. Moreover, even if the values of net

stress, suction and specific volume were the same for these samples, they would be likely to show different mechanical behaviour, because the inter-particle forces in the soil structure would be different in both cases. Consequently, the degree of saturation has a direct influence on the mechanical behaviour, in addition to any other influence of suction (Wheeler et al. 2003).

5.2.2 Experimental evidence

The mechanical behaviour of unsaturated soils is not only significantly different from that of saturated soils, but is also characterised by non-unique trends in particular of the volume change properties. For example, converse material behaviour may be obtained, depending on whether a soil is compacted at the wet side or at the dry side of the optimum water content. In the following, the most important mechanical features of unsaturated soils are highlighted based on experimental observations. Highly expansive soils like bentonites are a topic of its own and are not covered by this review.

- **Isotropic compression**
  Isotropic compression tests are usually conducted on unsaturated specimen at constant suction. It is generally found that suction has little or no effect on the stiffness in the elastic range (Delage and Graham 1995). However, suction affects both the yield stress and the post yielding behaviour.

  Experimental evidence that is consistent in the majority of cases is that the apparent preconsolidation stress respectively the yield stress increases with suction (Iwasaki 1978, Josa et al. 1987, Wheeler and Sivakumar 1995). On the contrary, the encountered virgin compression lines show rather converse trends. Iwasaki (1978), Josa et al. (1987) and Estabragh and Javadi (2008) found that the soil stiffness increases with increasing suction. In contrast, Wheeler and Sivakumar (1995) conducted compression tests on compacted kaolin that indicated exactly the opposite, namely a decrease of soil stiffness at increasing suction. Yudhbir (1982) and Josa et al. (1992) presented data that indicate a mixed behaviour, which depends on the isotropic stress level p.

  Based on the differently observed isotropic compression behaviour, Wheeler and Karube (1995) identified three characteristic normal compression lines, see Figure 5.5. In the first case (Figure 5.5 a), the normal compression lines are diverging straights in the specific volume v- ln p plane. The slope $\lambda(s)$ of the lines decreases with increasing suction, i.e. the stiffness increases.

  In the second case (Figure 5.5 b), the normal compression lines are straights that show a converging trend in the v- ln p plane. The slope $\lambda(s)$ of the lines

increases with increasing suction, i.e. the stiffness decreases. Finally, in the third case the normal compression lines are curves that initially diverge and then converge for higher values of p (Figure 5.5 c). This type of behaviour probably represents the complete picture if a wide range of consolidation stress is investigated (Wheeler et al. 2002).

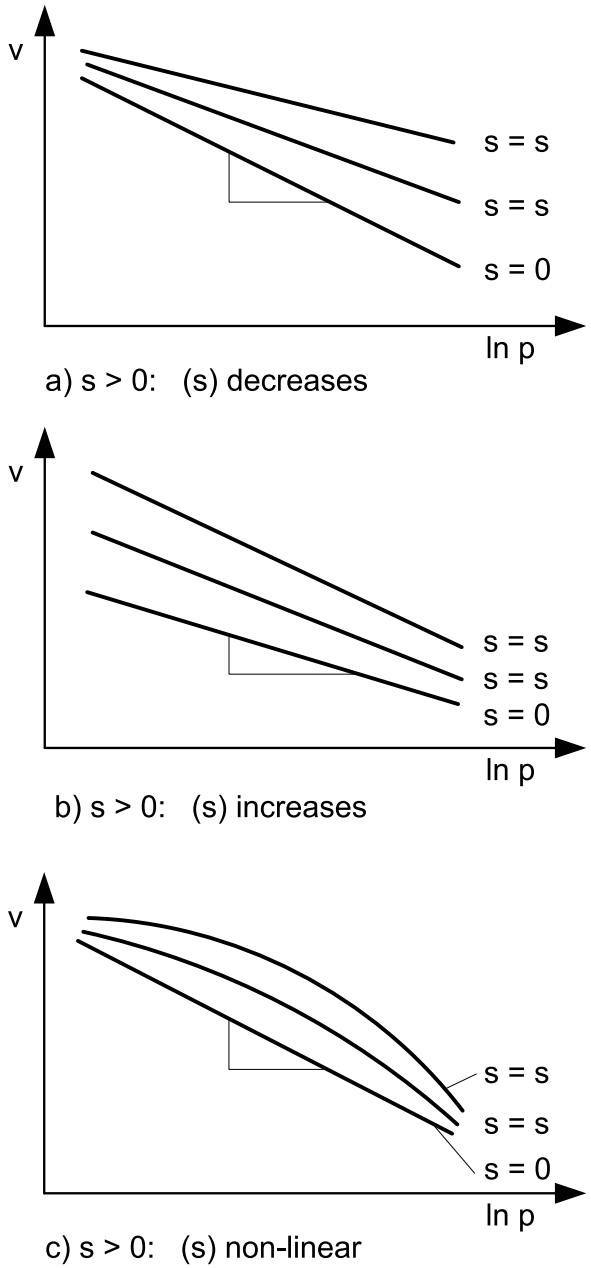

Figure 5.5: Types of normal compression lines for unsaturated soils (after Wheeler and Karube 1995).

- **Volumetric behaviour on wetting and drying**
  Unsaturated soils may exhibit swelling or compression behaviour on wetting respectively drying, depending on the externally applied stress level. The results of drying and wetting tests at constant isotropic stress can be displayed on so-called state surfaces. In these diagrams, the specific volume v or the

porosity *n* is shown over the net stress (σ-u_a) and the suction (u_a-u_w). In Figure 5.6, experimental results of Matyas and Radhakrishna (1968) are presented. The investigated soil exhibits strong swelling behaviour at low net stress and turns over to compression behaviour at higher net stresses.

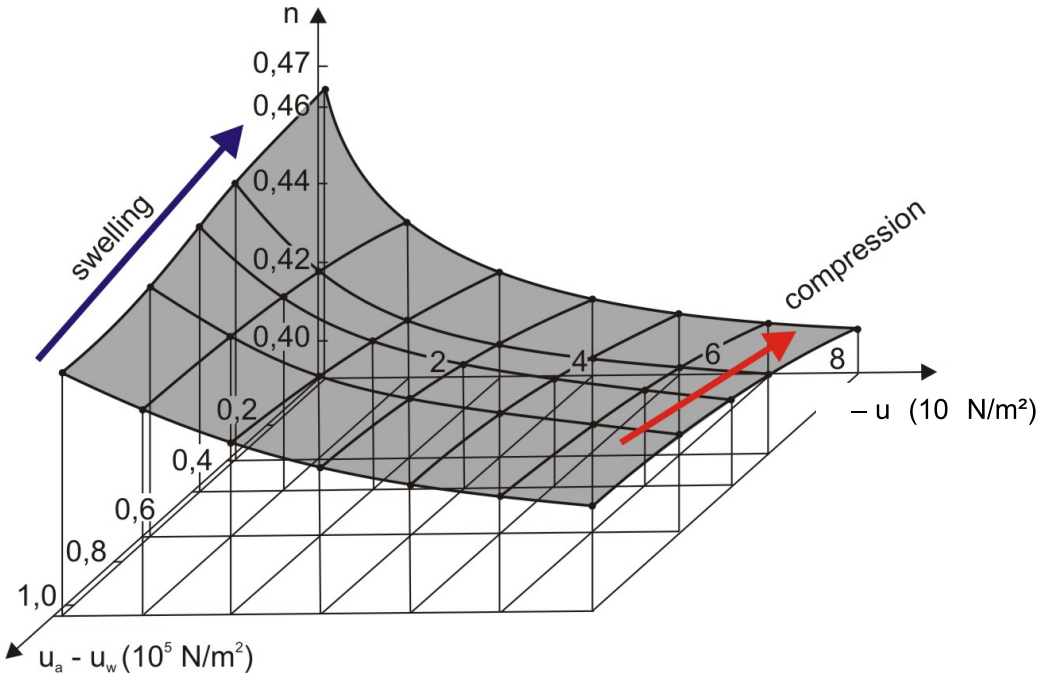

Figure 5.6: State surface after Matyas and Radhakrishna (1968).

A phenomenon that may occur during wetting of unsaturated soils is collapse; this describes an irreversible reduction of volume when the specimen is wetted under a constant load. Delage and Graham (1995) state that collapse relates to a condition in which the specimen moves to a net stress-suction state that has never been experienced in the past; in a more general sense, it yields. The microstructure, mineralogical and physico-chemical phenomena have a major influence on the collapse potential (Delage and Graham 1995).

Similarly to the isotropic compression behaviour, rather different collapse conditions respectively criteria have been identified. The presented normal compression lines in the last paragraph are directly linked to the collapse behaviour. If $\lambda(s)$ decreases monotonically with suction (Figure 5.5 a) this implies that the potential of wetting induced collapse increases indefinitely with the isotropic stress p (Wheeler et al. 2002). If in contrast $\lambda(s)$ increases monotonically with suction (Figure 5.5 b) this implies that the collapse potential is largest at low isotropic stress states. A further observation is reported by Yudhbir (1982) who identified the maximum collapse potential at intermediate stress states (Figure 5.5 c). Figure 5.7 displays an example of the collapse behaviour (after initial swelling) of compacted kaolin.

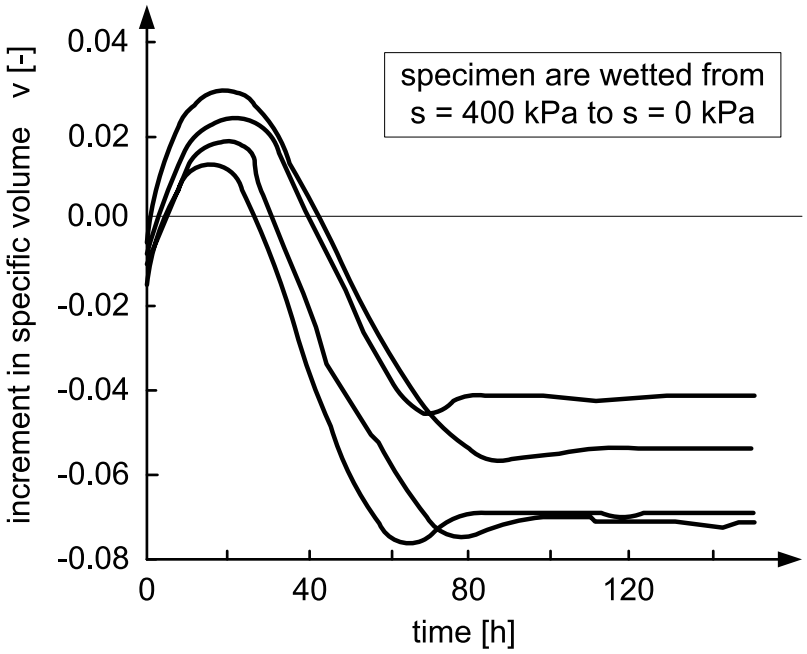

Figure 5.7: Collapse of compacted kaolin (after Wheeler and Sivakumar 1995).

An irreversible change in volume may also occur when a soil is dried under constant net stress to a suction magnitude that has never been experienced before. Alonso et al. (1990) state that a constant slope of virgin drying lines in a specific volume (*v*) – ln suction (*s*) plane can be assumed, independent of the applied net stress level. Chen et al. (1999), however, obtained experimental results that indicate a dependence of both the elastic and the virgin drying on the net stress level, see Figure 5.8.

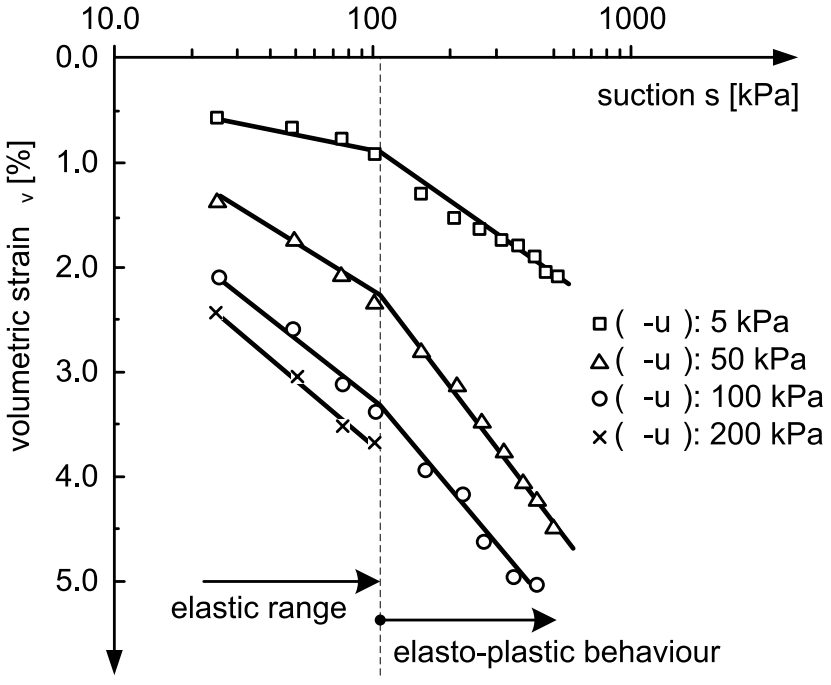

Figure 5.8: Soil stiffness at different suction levels (after Chen et al. 1999).

- **Shear strength**
  Early experimental results (e.g. Fredlund et al. 1978) indicated a (1) linear increase of the shear strength with suction and (2) an independence of the effective friction angle of suction. However, experimental evidence in the subsequent years often yielded contradictory results. For example, Escario and Saez (1986) tested the unsaturated shear strength of three different materials, among these Madrid clayey sand. They detected a non-linear, hyperbolic increase of the shear strength with suction. The initial increase corresponds to the effective friction angle φ', which for this material was found to vary only insignificantly with suction. Figure 5.9 shows the corresponding test results on a net stress-shear stress plane (a) and on a suction-shear stress plane (b).

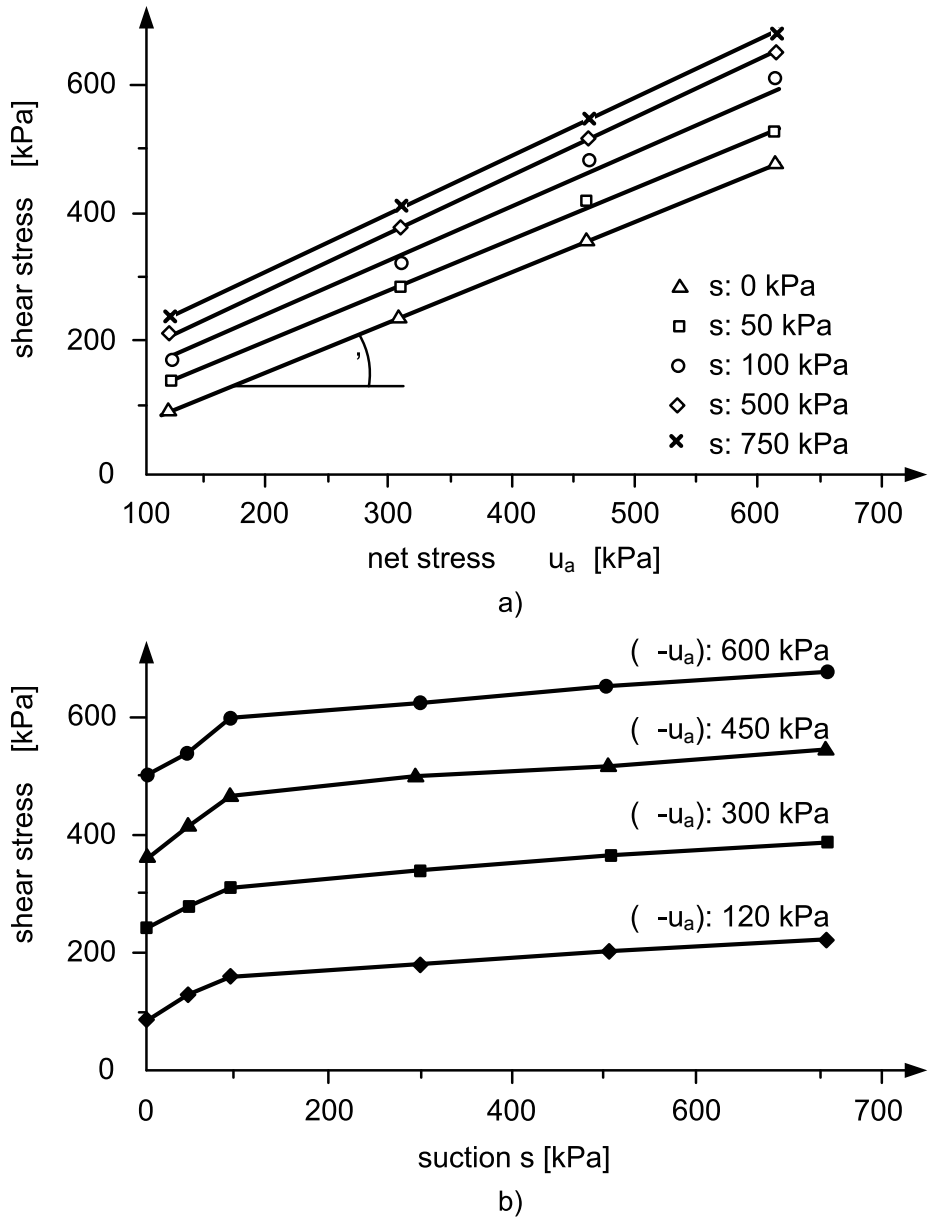

Figure 5.9: Shear strength envelopes for Madrid clayey sand (after Escario and Saez 1986).

Similar results were obtained from direct shear tests on glacial till by Gan et al. (1988), and triaxial shear tests on silty sand by Gallage and Uchimura (2006). In contrast to the formerly cited authors, Delage et al. (1987), Maatouk et al. (1995) and Escario and Saez (1986; for the two additionally investigated materials) detected a significant variation of the effective friction angle with increasing suction. Decreases as well as increases of the friction angle were observed.

Today it is commonly agreed that the increase of shear strength with suction is identical with the effective friction angle for saturated states respectively high degrees of water saturation (Escario and Saez 1986, Fredlund et al. 1987, de Campos and Carillo 1995, Fredlund et al. 1995). The further development of the shear strength in the unsaturated range is strongly soil-type dependent. However, in general the increase of shear strength develops towards a plateau at higher suction values and may even exhibit a decrease in the residual suction range. No such general statement can be made for the effective friction angle, which shows extremely converse properties in the unsaturated state for different soil types (compare Delage and Graham 1995).

5.2.3 Stress-state variables and constitutive model classes

The discussion of adopting appropriate stress-state variables for unsaturated soils arose shortly after Bishop's (1959) proposal of an extended effective stress concept in analogy to Terzaghi's (1936) effective stress concept for saturated soils. Bishop introduced a so-called effective stress parameter χ that relates the different magnitudes of pore water and pore air pressure to the effective stress σ':

$$\sigma' = \{(\sigma - u_a) + \chi \cdot (u_a - u_w)\} \tag{5.6}$$

σ total stress
u_a air pressure
u_w water pressure

The effective stress parameter χ is soil-type dependent and has to be determined experimentally. It is, however, quantitatively closely related to the degree of water saturation. For $\chi = 0$ (full air saturation) and $\chi = 1$ (full water saturation), Equation (5.6) reduces to the effective stress equation formulation by Terzaghi.

Jennings and Burland (1962), Matyas and Radhakrishna (1968) or Fredlund and Morgenstern (1977) doubted the validity of Bishop's effective stress. Jennigs and Burland stated that according to their experimental investigations the effective

stress parameter χ would be different for the shear strength and the volumetric behaviour. Matyas and Radhakrishna argued that Bishop's effective stress was not able to predict the collapse upon wetting of unsaturated soils. Fredlund and Morgenstern stated that the effective stress parameter showed constitutive character and should thus not enter into a stress state variable. As a consequence, the use of independent stress-state variables for unsaturated soils was proposed.

Fredlund and Morgenstern (1977) suggested the use of three possible pairs of independent stress-state variables:

$$(\sigma - u_a),(u_a - u_w) \text{ or } (\sigma - u_w),(u_a - u_w) \text{ or } (\sigma - u_a),(\sigma - u_w) \quad (5.7)$$

σ total stress
u_a air pressure
u_w water pressure

The theoretical assumptions were successfully confirmed by so-called "null tests" (Fredlund und Morgenstern 1977). Soil samples were subjected to converse variations of (1) total stress, (2) water pressure and (3) air pressure. As predicted, zero volume change was measured for all pressure variations and the validity of the independent stress-state variable approach was considered as correct. In the subsequent years, the first pair of stress-state variables, $(\sigma - u_a)$ and $(u_a - u_w)$, found the most widespread use in unsaturated soil mechanics.

Despite the relative success of the independent stress-variable approach, today many of the arguments criticising Bishop's extended effective stress have been proven misleading. For example, the collapse upon wetting is an elasto-plastic process, which includes particle slippage caused by a decrease of stabilizing forces of the water meniscus lenses. Obviously, this process could not be captured with the elastic frameworks used by Jennings and Burland (1962) or Matyas and Radhakrishna (1968).

Houlsby (1997) stated that the choice of stress-state variables in principle is arbitrary as long as they are work-conjugate respectively mechanically consistent. That means that the rate of work-input to the soil is equal to the sum of the product of the stresses with their corresponding strain rates. Houlsby (1997) presented a theoretical derivation of the work input into unsaturated granular materials. Incompressibility of the soil solids and the water phase was assumed. Further, the work dissipated by the relative movement of the air-water interface was neglected. The following expression for the work input is obtained:

$$\begin{aligned} dW = &-u'_{w,j} \cdot v_{w,j} - u'_{a,j} \cdot v_{a,j} - n \cdot (u_a - u_w) \cdot dS_w + n \cdot (1 - S_w) \\ &\cdot u_a \cdot d\rho_a / \rho_a + \{\sigma_{ij} - [S_w \cdot u_w + (1 - S_w) \cdot u_a] \cdot \delta_{ij}\} \cdot d\varepsilon_{ij} \end{aligned} \quad (5.8)$$

u' excess pore pressure gradient of air (u'_a) and water (u'_w)
v seepage velocities of air (v_a) and water (v_w)
n pore volume
S_w degree of water saturation
δ_a density of the air phase

In the majority of cases, a constant air pressure can be assumed. If further steady-state conditions respectively insignificant work rate contributions from the fluid flow are imposed, Equation (5.8) simplifies to the following expression:

$$dW = -n \cdot (u_a - u_w) \cdot dS_w + \left\{\sigma_{ij} - [S_w \cdot u_w + (1 - S_w) \cdot u_a] \cdot \delta_{ij}\right\} \cdot d\varepsilon_{ij} \tag{5.9}$$

The first term in Equation (5.9) describes the necessary work input due to a change of the degree of saturation. The corresponding work conjugate quantity is suction (u_a-u_w). The second term describes the work input caused by static straining of the soil skeleton. The work conjugate stress variable is shown to be a generalised version of Bishop's stress with the parameter $\chi = S_w$.

A logical consequence of Equation (5.9) is that desirable stress variables are the generalized Bishop's stress and suction; with the soil skeleton strains ε_{ij} and the change in the degree of saturation dS_w as their work conjugate strain variables (Wheeler et al. 2003). However, the expression for the work input rate can be achieved by different linear combinations. For example, if net stress is associated with the soil skeleton strain, the quantity $(-n \cdot dS_w + S_w \cdot \varepsilon_{jj})$ should be associated with suction (Jommi 2000).

If changes in the degree of saturation are neglected, Bishop's stress respectively net stress and suction may be equally chosen as stress variables, showing both an inconsistency with Equation (5.9). Thus, neither arguments favouring Bishop's stress as single stress-state variable approach nor the independent stress-state variable approach can be drawn from the theoretical analysis of Houlsby (1997). On the other hand, the analysis also does not imply that the choice of the latter types of stress-strain variables is mechanically inconsistent as long as the action of the interfaces is incorporated into the model (Jommi 2000). It becomes clear, however, that constitutive models lacking the degree of saturation in their stress definitions and the change of the degree of saturation in their strain quantities are likely to be incomplete from a hydro-mechanical point of view.

A large number of elasto-plastic constitutive models for unsaturated soils have been published so far (roughly 30). A variety of different stress-strain variables were adopted in these models. Most of these models may be classified into one of the following three categories:

- **The single stress-state variable approach**
  Constitutive models of this type are based on a single stress-state variable, which is explicitly Bishop's extended effective stress or a variation of Bishop's stress. The work conjugate strains are the soil skeleton stresses ε. The generic form of a constitutive model for unsaturated soils written in terms of a single stress-state variable is:

$$d\varepsilon_{ij} = C^{ep}_{ijhk} \cdot d\sigma'_{ij} \tag{5.10}$$

ε_{ij} strain tensor
σ'_{ij} effective stress tensor
C^{ep}_{ijhk} elasto-plastic constitutive matrix

  Here, C^{ep}_{ijhk} is the same elasto-plastic constitutive matrix as for saturated soils. The necessary modifications of a constitutive model for saturated soils in order to capture also the unsaturated soil behaviour are outlined by Jommi (2000). The challenge associated with this type of models is to account for a proper definition of the effective stress. Due to the unification of externally applied stresses and suction into one effective stress, only one yield surface is necessary. This usually results in a smaller number of soil parameters than in independent stress-state variable constitutive models.

  Model examples are Jommi and di Prisco (1994), Gudehus (1995), Bolzon et al. (1996), Loret and Khalili (2000), Jommi (2000) or Russell and Khalili (2006). Different definitions of the effective stress σ' are adopted in these models. Jommi uses the generalized Bishop's stress with $\chi = S_w$, whereas Russel and Khalili define χ as a function of suction.

- **The classical independent stress-state variable approach**
  This class of models is based on the independent stress-state variables suggested by Fredlund and Morgenstern (1977). The most commonly used combination of stress variables are net stress (σ-u_a) and suction (u_a-u_w). A constitutive model written in terms of two independent stress-state variables has the following generic form:

$$d\varepsilon_{ij} = C^{ep}_{ijhk} \cdot \left(d\sigma_{hk} - du_a \cdot \delta_{hk}\right) + C^{s}_{ijhk} \left(du_w - du_a\right) \cdot \delta_{hk} \tag{5.11}$$

C^{s}_{ijhk} additional constitutive matrix which relates suction increments to strain increments; independent of changes in net stress

  Models of this class do not incorporate the degree of saturation and are therefore not able to account for the hysteretic behaviour of unsaturated soils. Additionally, in numerical modelling these models show difficulties in the transition from a saturated to an unsaturated state (Gens et al. 2006).

Because of the two employed independent stress variables, usually also two yield surfaces are needed. In analogy, a higher number of parameters is required than in effective stress based models (Nuth and Laloui 2008). Model examples are Alonso et al. (1990), Wheeler and Sivakumar (1995), Cui and Delage (1996) and Chiu and Ng (2003).

- **Enhanced effective stress approaches**
  This category of models uses two or more constitutive variables, of which one is a Bishop-type of effective stress. Here, the generalized Bishop stress is most commonly employed. The second stress-state variable is function of suction, the degree of saturation or other soil parameters (e.g. porosity). The generic form of these models is identical with Equation (5.11). The difference to the classical independent stress-state variable approach is that these models do not strictly separate external stresses and suction into different constitutive variables. Instead, the suction respectively the degree of saturation may appear in both constitutive variables. In a general form, the two stress-state variables can be written as (Gens et al. 2006):

$$\sigma' = \left\{(\sigma - u_a) + \mu(s,\ S_w)\right\} \quad \text{and} \quad \xi = \xi(s,\ S_w,..) \tag{5.12}$$

μ function of suction s and/or the degree of water saturation S_w
ξ additional constitutive variable, which is a function of suction and/or degree of saturation respectively other soil parameters

The effective stress and suction in this sense are independent stress variables but their strain-like quantities are not because the degree of saturation depends on the pore volume and therewith on the soil strains.

Stress frameworks of this category are particularly appropriate to directly account for the two different mechanism of suction. Firstly, the generalized Bishop's stress describes the increase of the isotropic stress due to suction. The degree of saturation serves as a weighing term. Secondly, the additional stress variable may be employed to account for the second effect of suction - the bonding effect due to the single water meniscus lenses. Beyond, the effects of hydraulic hysteresis can be incorporated in a direct manner.

A challenge associated with the enhanced effective stress models is the representation of stress paths in the space of the employed stress variables, which is not as straight forward as in the classical independent stress-state variable approach. In fact, in many cases the stress path in the effective stress space can only be computed simultaneously with the constitutive equations (Wheeler et al. 2003). Enhanced effective stress based models have been published by Wheeler et al. (2003), Gallipolli et al. (2003), Sheng et al. (2004), and Nuth and Laloui (2008).

5.3 Triaxial apparatus for unsaturated soils

5.3.1 General principles and techniques

The mechanical testing of unsaturated soils in triaxial cells in principal is challenged by (1) the control of the desired suction level and (2) the accurate volume change measurement of the specimens. In the case of saturated soils, the specimen volume change is directly related to the water exchange, i.e. pore water entering or leaving the sample, and can be measured readily. In unsaturated soils, the volume change measurement is additionally complicated by the presence of air in the soil pores.

Different techniques have been developed in order to match the formerly described requirements. For the control of the suction, the axis-translation technique (e.g. Wheeler 1988), osmotic techniques (e.g. Cui and Delage 1996) and relative humidity control (e.g. Blatz and Graham 2000) are used. In order to accurately detect the volume change of unsaturated soil samples, cell liquid measurements (e.g. Wheeler 1988), air-water volume measurements (e.g. Laudahn et al. 2005) respectively direct measurements on the sample (e.g. Romero et al. 1997) are employed.

Probably the most commonly used experimental system is the axis-translation technique in combination with the double-cell method (e.g. Wheeler 1988, Yin 2003, Gallage and Uchimura 2006). By the axis-translation method (Hilf 1956), a distinct suction value is generated by independent control of the pore water and pore air pressure. For this purpose, the lower porous stone of a conventional triaxial device is replaced by a high air-entry value ceramic disc. Below the ceramic disc, the water pressure is controlled at a given value (usually in the range of the atmospheric pressure). In contrast, the air pressure is applied through the porous stone at the top of the specimen. The difference between the applied pore water respectively pore air pressure determines the suction level in the specimen.

The double-cell method is a variant of the cell liquid measurement. Here, the volume change of the specimen is deduced by measuring the volume change of the liquid in the confining cell. In order to increase the accuracy of the method, a second cell (double cell) is installed around the inner cell. The same magnitude of pressure acts in both cells. Thus, the volume of the inner cell (of which the liquid change is monitored) is theoretically not affected by changes of the confining pressure. However, calibration tests are also required in order to account for small deformations of the cell in axial direction, temperature effects or the absorption of water by the acrylic cylinder forming the cell wall.

5.3.2 Double-walled triaxial cell

In order to investigate the mechanical properties of unsaturated soil specimen, a double-walled triaxial system was installed in the Geotechnical Laboratory of the Institute of Soil Mechanics and Foundation Engineering. Matric suction is controlled by the axis-translation technique. The cell was fabricated by Wille Geotechnik, Göttingen (Germany). The cell is designed in such a way as to accommodate specimens of 5, 7 or 10 cm diameter. For this purpose, an exchangeable pedestal is situated at the base plate of the inner cell. Figure 5.10 shows the layout of the triaxial apparatus.

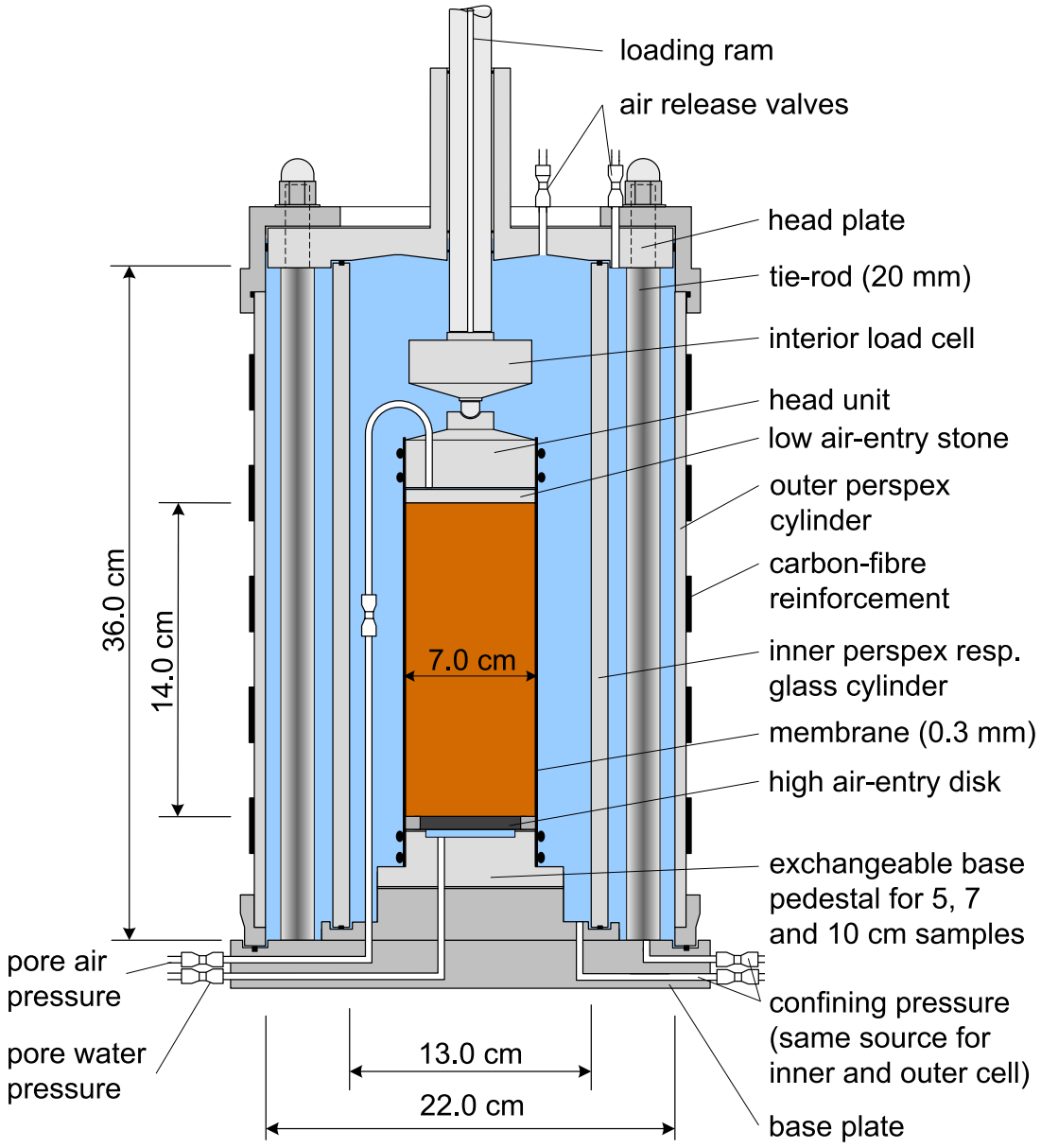

Figure 5.10: Illustration of the double-walled triaxial cell for unsaturated soils.

The inner and outer cell have a diameter of 13 and 22 cm, respectively. The clear height is 36.0 cm. The outer cell is reinforced with five carbon-fibre bands. This is not necessary for the inner cell; because of the equal confining pressure at both sides of the cell wall, it is only exposed to a minor mechanical stress. Three tie-rods with a diameter of 20 mm are used to fix the inner and outer cell to the base plate. O-ring seals and vacuum grease are used to ensure air and water tight connections. Air valves in the head plate serve to release accumulated air bubbles during the filling of the inner and outer cell with de-aired water. To facilitate the bleeding of air bubbles, the lower surface of the head plate was fabricated with a double inclination in the area of the inner cell.

The specimen is collocated on a 7 mm thick ceramic disc, which is fixed on the exchangeable base pedestal. On top of the specimen, a low air-entry porous stone and a head unit are collocated. Around the specimen, a 0.3 mm thick rubber membrane is installed. In this case, O-rings and vacuum grease are also used to impede water leakage from the inner cell into the soil sample. An interior load transducer cell is used to measure the shear force. Thus, friction between the loading ram and the guidance does not affect the shear force measurements. Figure 5.11 shows a picture of the triaxial cell with an installed specimen.

Figure 5.11: Photo of the double-walled triaxial cell for unsaturated soils.

5.3.3 Volume change device

The measurement of the change of the cell liquid volume respectively of the specimen volume is a key issue of the triaxial apparatus. Therefore, a high precision measurement is required. In order to meet this requirement, an electronic volume change device, based on the differential-pressure principle, is employed. Figure 5.12 shows the idealized layout and a photo of the device.

The main parts of the device are the base unit with the integrated differential pressure transducer, the measuring burette, a perspex hollow shaft and a head unit. The lower membrane of the pressure transducer is exposed to the confining pressure, which is applied by an air pressure source. In contrast, the upper membrane of the transducer is exposed to the confining pressure plus the weight of the water column in the burette. Thus, if the specimen volume changes, water from the inner cell flows into respectively leaves the burette and changes the electronic resistance of the sensor of the pressure transducer. The corresponding Volt-signal is transmitted continuously to the control unit and is transformed into the volume change measurement.

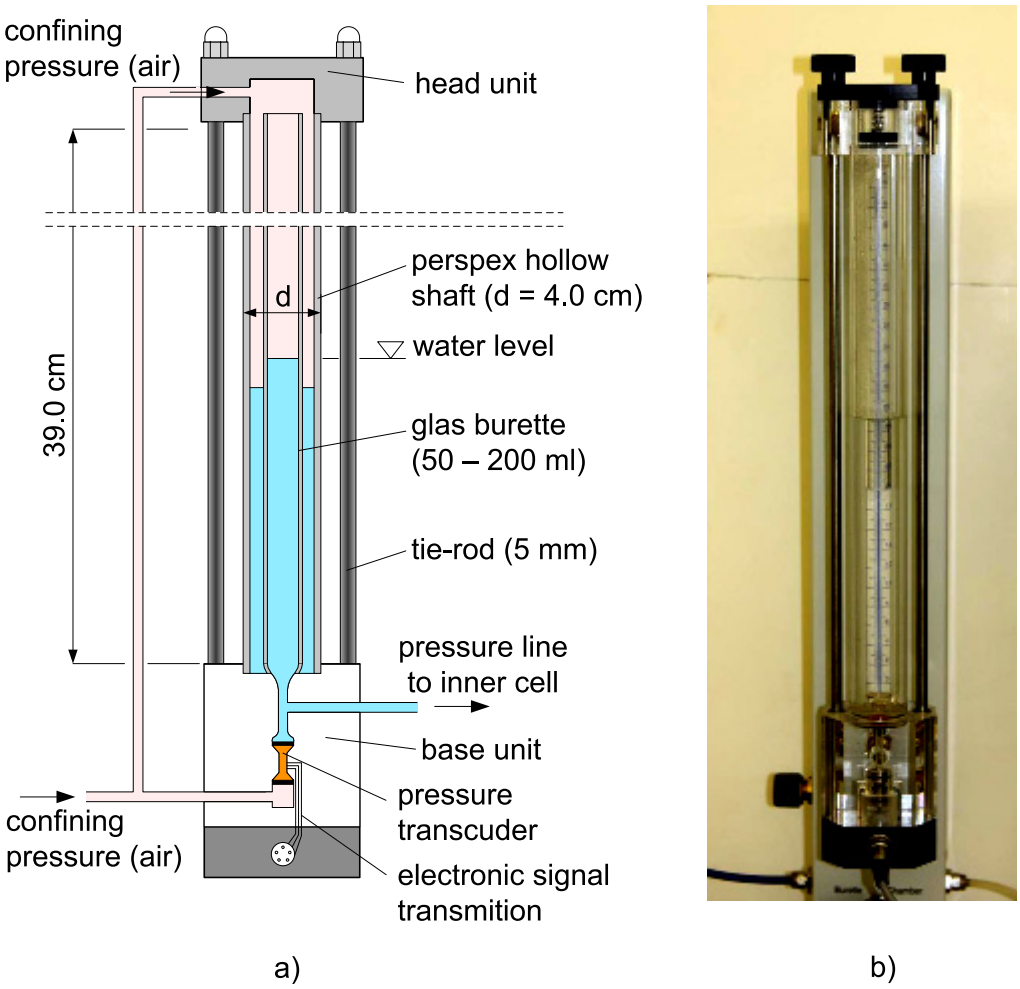

Figure 5.12: Idealized graphic (a) and photo (b) of the volume change device.

The perspex hollow shaft stabilizes the burette (in a similar manner as the outer cell of the triaxial apparatus stabilized the inner cell) and maintains the distance between the base and the head unit. The water level in the hollow shaft is arbitrary and remains constant during a test.

The volume change device can be equipped with 50, 100, 150 and 200 ml burettes. In order to achieve the best accuracy, it is best to choose the smallest possible capacity of the burette, i.e. the maximum expected volume change during a triaxial test. The scale on the burette is solely used for the visual control of the volume change. Each time a new burette is installed, an electronic calibration of the volume change device is necessary. Additionally, the complete device must be flushed before a test start in order to remove air bubbles from the connections and tubes.

The installed pressure transducer can measure differential pressures up to 70 mbar. The accuracy of the sensor is 0.1 % of the maximum value. The transducer must not be exposed to pressure differences higher than 1 bar. Otherwise, the sensor is destroyed. Thus, great care is needed while connecting and disconnecting the water pressure line to respectively from the inner cell.

5.3.4 Complete testing system

After the installation of the specimen into the cell, the execution of the triaxial test is fully automated and controlled by the software Asturix (Wille Geotechnik, Göttingen). The software navigates the pressure transmitters as well as the hydraulic system and manages the data acquisition. Consolidated-drained, consolidated-undrained respectively unconsolidated-undrained tests can be conducted by the programme. An illustration of the complete triaxial testing system is depicted in Figure 5.13.

Two DV-10 pressure transmitters are used to control the confining pressure respectively the pore air pressure. For both transmitters, an external air tank which is supplied by a compressor, is used as pressure source. The confining pressure line has a bifurcation and runs to the volume change device (inner cell) respectively an air water interface (outer cell). The pore air pressure is applied by means of a tube in the inner cell to the top of the specimen.

A DR-20 pressure transmitter is used to control the pore water pressure of the specimen. In contrast to the DV-10, it has an internal water reservoir and the water pressure is applied directly. In addition to the pressure control, the DR-20 also measures the water volume flow in order to be able to determine the water content change of the specimen during the test conduction.

The software Asturix also controls the UPR-100 hydraulic system during the execution of shear phases; they can be conducted either force-controlled or displacement-controlled. Vertical forces up to 100 kN can theoretically be applied. The vertical deformation of the specimen is measured by a high-precision digital displacement gauge.

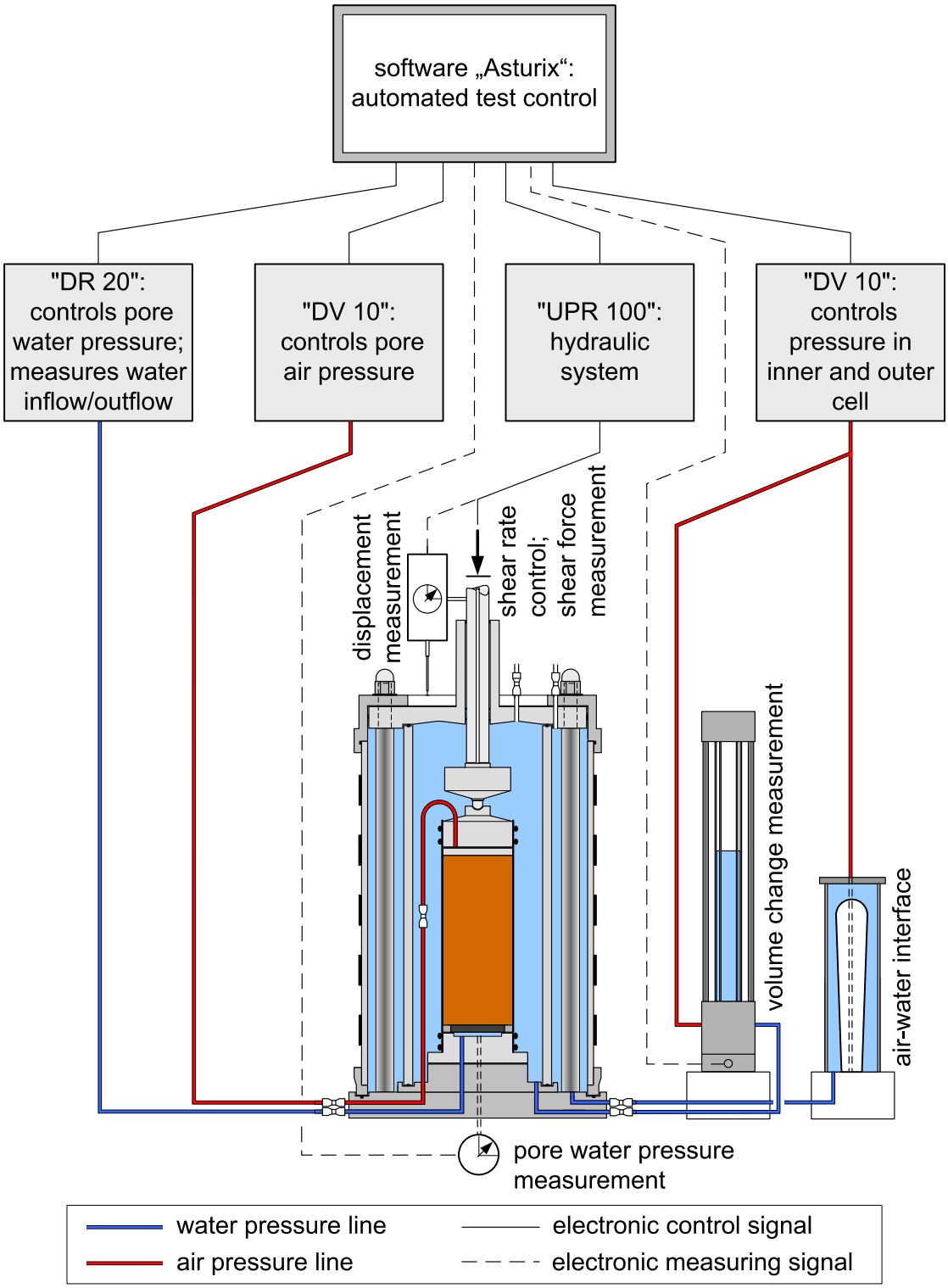

Figure 5.13: Complete testing system of the triaxial apparatus.

5.4 Initial problems and improvements

The successful putting into operation of the triaxial testing device has been extremely tedious. The conduction of preliminary tests indicated some severe deficiencies of the triaxial apparatus. In particular the volume change measurements of the specimen were inconsistent respectively indicated a water leakage problem. Despite careful assemblage of the cell and the replacement of selected seals, the water leakage could not be reduced below a rate of 0.20 cm³/d. Additionally, the control software appeared to have various bugs, which often resulted in an erroneous test conduction and/or abortion of the tests. Moreover, several pressure transducers did not work properly.

Figure 5.14 illustrates the described water leakage problem based on the volume change measurements of one of the preliminary tests. During the increase of the cell pressure σ_3 from 10 to 50 kPa, a volume change of ΔV = 3.3 cm³ is measured; this means that water flows from the volume change device into the inner cell. After reaching the final value of 50 kPa, the volume change rate shows a decreasing trend and seems to have reached a maximum after 40 hours. However, subsequently the volume change rate increases again and stabilizes approximately at a value of $\Delta V \approx 0.20$ cm³/d; this behaviour continues, even after 140 hours of testing time. Thus, the supposed volume change of the specimen can only be attributed to a water leakage problem somewhere at the device. Interestingly (as tests with varying cell pressures showed), it proved that the water leakage rate was relatively independent of the applied cell pressure.

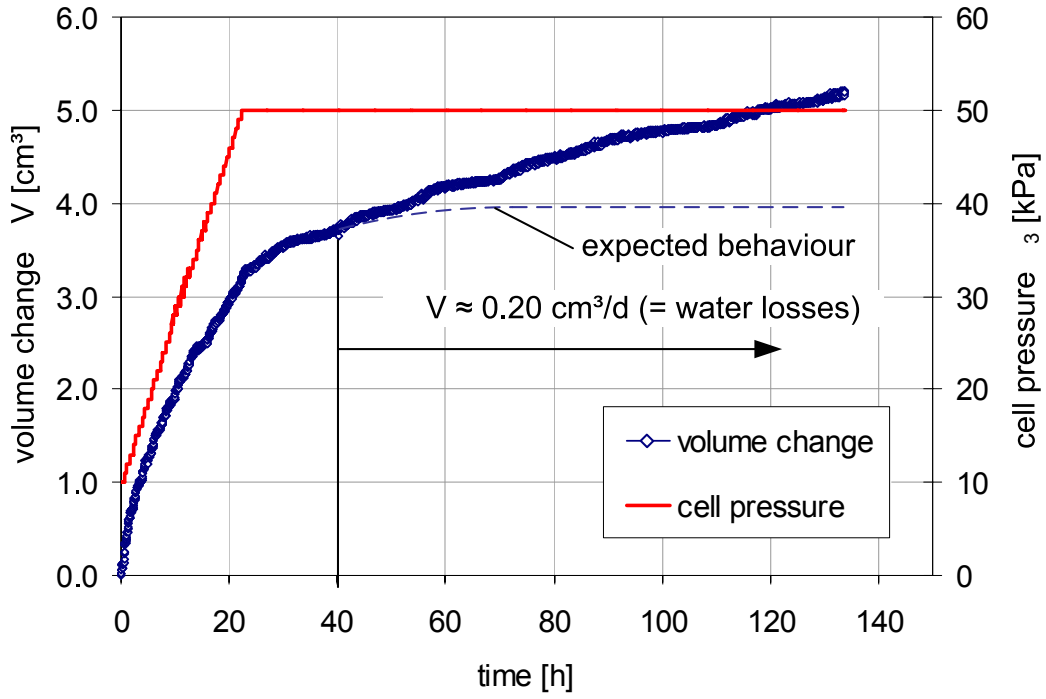

Figure 5.14: Erroneous volume change measurement due to leakage problems.

The delivered triaxial testing system for unsaturated soils had several other shortcomings. The correction of the defects was troubled by limited experience of the manufacturer on unsaturated laboratory testing devices and extremely long waiting periods for the repair of malfunctioning components. Finally, it was decided to take over the necessary works. A bundle of measures was carried out in order to eliminate the severe defects and to improve the overall performance of the triaxial apparatus.

The putting into operation of the device has was complicated by other aspects too, which may be categorized under "learning by doing". In the following, the principal problems, the identified reasons and the measures to eliminate the deficiencies of the triaxial testing system are described. The first three points are in direct relation with the volume change measurement.

- **Exchange of fittings; additional sealing efforts**
  The exchange of single suspect seals respectively fittings could not stop the leakage problem. In order to avoid a tedious search, it was finally decided to exchange all connections and seals of the cell. Several mobile connections were replaced by fixed connections. Additionally, connections which were identified as critical (e.g. the connections of the pore air pressure line inside the inner cell) were surrounded by removable glue, in addition to the use of vacuum grease at the seals. The O-ring seals at the top and bottom of the inner and outer cylinder were replaced by flat seal rings. With these measures, the leakage problem could be completely eliminated.

- **Replacement of the inner perspex cylinder by a glass cylinder**
  Perspex has the property to absorb water respectively humidity. The water-uptake rate depends on the relative humidity respectively on the pressure. The long term measurements of the cell liquid volume will consequently be influenced by this process. Wheeler (1988) already described this problem and used tedious calibration procedures in order to account for the water uptake of the inner perspex cylinder. To avoid these complications, the inner perspex cylinder of the triaxial apparatus was replaced by a glass cylinder.

- **Using 0.3 mm latex membranes instead of 0.1 mm membranes**
  Some of the preliminary tests were carried out with a silty, medium-sandy material. In the first place, 0.1 mm latex membranes were used to cover the specimen. The procedure of the leakage identification also included an investigation of the membranes after the completed tests. It was found that in some cases the sharp-edged sand grains caused small gaps in the latex membrane, which probably occurred at higher cell pressures. Non of these problems were encountered when 0.3 mm latex membranes were used instead.

- **Using ceramic discs with higher air entry values than theoretically required**
  In the literature (e.g. Fredlund and Rahardjo 1993) it is generally recommended to use ceramic discs with an air entry value which as low as possible, i.e. with an air entry value not much higher than the maximum applied suction. The reason for this recommendation is that ceramic plates with low air entry values allow shorter equilibrium times due to their higher water permeability. However, the conducted tests showed that after longer testing periods, in several cases an air break-through occurred at suctions considerably lower than the discs could theoretically withstand (e.g. a 75 kPa suction test failed when using a 1 bar ceramic). As a consequence, a 2 bar ceramic was used for the tests in the suction range from 50 to 100 kPa.

- **Testing of the control software against weaknesses**
  The bugs in the control software caused various computer crashes, which resulted in test stops. Because the control software is not open-source and due to the lacking efforts of the manufacturer of the triaxial testing system to improve the software, there were only two options left: either the purchase of a new control software or the detection of configurations, which caused the crashes. Finally, the software was debugged, “problematic” instructions were identified and subsequently avoided.

- **Installation of an emergency power supply system**
  The power supply system of the TU Graz experienced several expected and unexpected power cuts as well as short voltage fluctuations. These power supply problems resulted in the failure of two tests, because the computer running the control software crashed. Thus, it was decided to equip the triaxial testing system with an emergency power supply, which compensates voltage fluctuations and can bridge power cuts of up to 10 hours.

5.5 Calibration and sensitivity tests

5.5.1 General information

Although a double-walled triaxial cell is used, this does not imply that the liquid volume in the inner cell is solely influenced by the deformation of the specimen. The increase of the cell pressure results in the extension of the tie-rods and small flexures of the top and bottom plates, which increase the volume of the inner cell. Also, small variations of the room temperature may cause a falsification of the volume change measurements. Therefore, calibration tests are necessary. First, the behaviour of the volume change device alone, and thereafter the behaviour of the triaxial cell in combination with the volume change device are investigated.

5.5.2 Volume change device

During the calibration respectively sensitivity tests of the volume change device, the connection to the inner cell is maintained blocked. Therefore, the obtained measurements solely reflect the behaviour of the volume change device.

Figure 5.15 shows the influence of pressure variations on the volume change device. The pressure was increased stepwise from 5 to 50, 175 and 300 kPa, and subsequently decreased again. The total duration of the test was 9 hours. In order to no mix-up the pressure dependence of the device with temperature effects, the room temperature was controlled carefully around 19 ± 0.1 °C during the test. The accurate temperature control required manual interaction of the air conditioning system.

It can be seen from Figure 5.15 that the influence of the applied cell pressure on the volume change measurements is rather small. In the pressure range from 175 to 300 kPa, the measured deviations are principally between -0.01 and -0.02 cm³. The sensitivity of the differential pressure transducer and short-term temperature variations cause some scatter of the measurements. Particularly during the decrease periods of the pressure, the sensor gives some erroneous results. However, these are only isolated values that can be easily distinguished from the correct measurements.

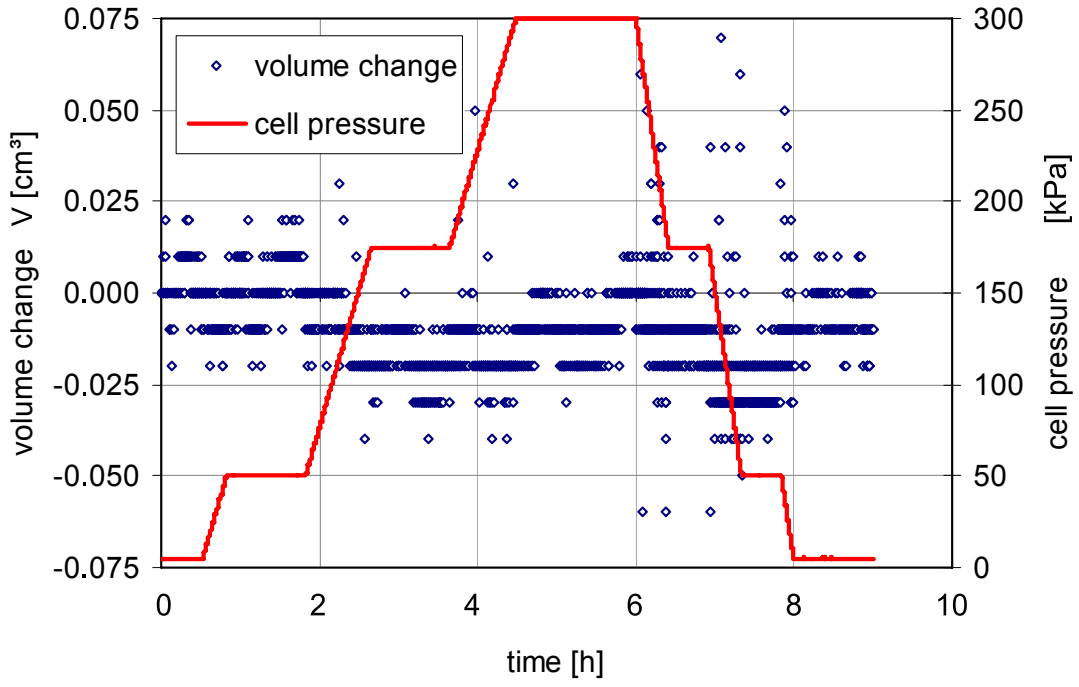

Figure 5.15: Influence of the applied cell pressure on the volume change device.

Subsequently to the pressure calibration test, the influence of the room temperature on the volume change device was investigated. For this purpose, a

long-term test with a time duration of 49 hours was conducted. During this period, the room temperature was controlled automatically by the air conditioning system at 19 °C. The recorded temperature showed variations of ± 0.2 °C, which were principally governed by the day-night cycles.

Figure 5.16 depicts the recorded room temperature and the obtained volume change measurements. Daytime temperatures were approximately 0.1 – 0.2 °C higher than the controlled value of 19 °C, whereas nighttime temperatures were approximately 0.1 – 0.2 °C lower. The cited temperature deviations are mean values over half an hour (short-term variations were up to ± 0.6 °C). The influence on the volume change measurements is clearly visible from Figure 5.16. However, the measured deviations of maximal 0.075 cm³ are generally low. The comparison with the pressure calibration test indicates a higher influence of temperature variations on the volume change measurements than on cell pressure variations.

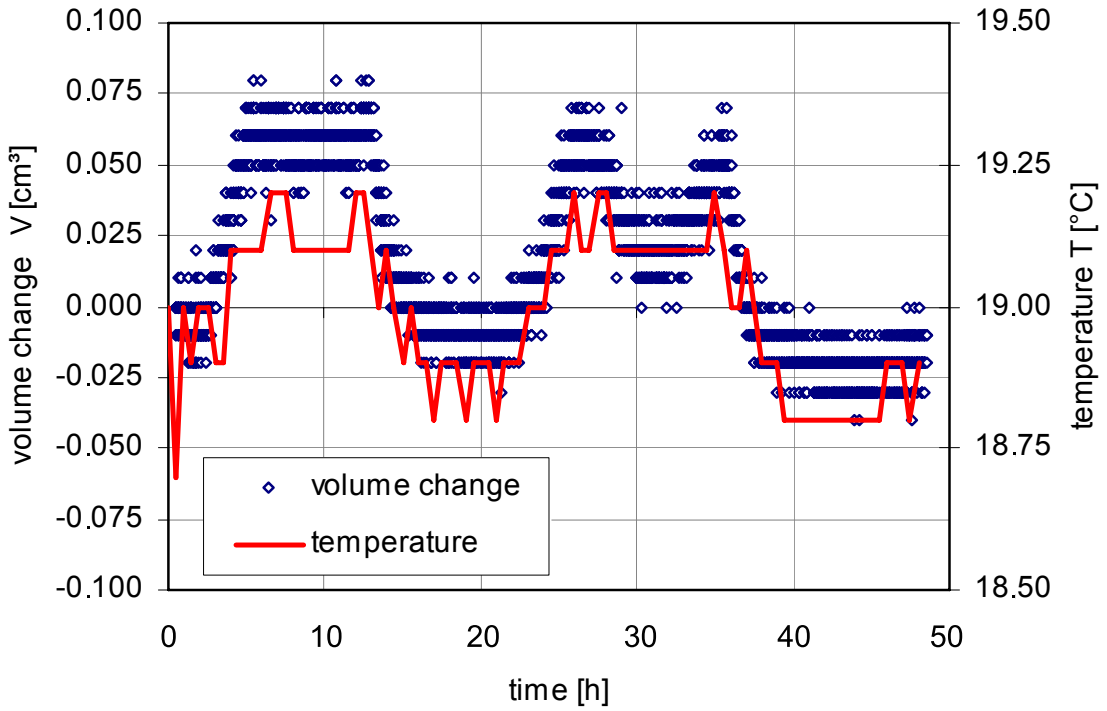

Figure 5.16: Influence of the room temperature on the volume change device.

5.5.3 Double-walled cell

For these calibration tests, the connection between the volume change device and the inner cell is maintained open. The behaviour of the outer cell, whose only purpose is to stabilize the inner cell, is not of interest and thus not investigated. A steel specimen of 7.0 cm diameter and 14.0 cm height was used for the calibration tests. A 0.3 mm membrane was put over the steel cylinder. The

triaxial apparatus and all connections were assembled as if in a common test with a soil specimen. Due to this equivalence, the obtained measurements can be directly used for the correction of the volume change measurements of actually conducted triaxial tests.

Figure 5.17 depicts the results of two pressure calibrations tests of the double-walled cell. The confining pressure σ_3 was increased from 10 to 350 kPa. The two tests were conducted with time durations of 22 and 110 hours, respectively. Rather similar volume change measurements were obtained for both tests. However, the distributions are non-linear, in particular in the pressure range from 10 to 250 kPa. It is supposed that this behaviour is due to restraints of the cell construction and due to the slackness of valves and tube fittings.

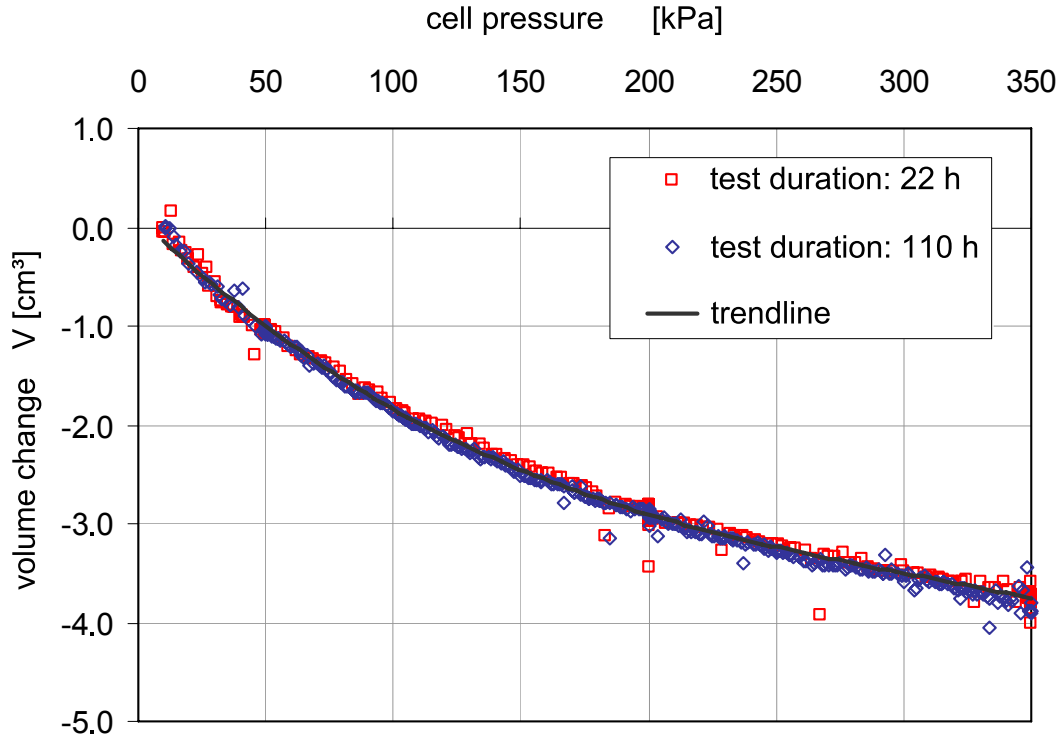

Figure 5.17: Influence of the cell pressure on the volume change measurement.

The negative values indicate the extension of the inner cell; this means that a larger volume change is measured than actually occurs at the specimen. In order to correct the volume change measurements, a polynomial trendline was matched to the measurements of the calibration tests. The obtained correction function reads:

$$\Delta V_{corr} = -7.01 \cdot 10^{-8} \sigma_3^{\,3} + 6.54 \cdot 10^{-5} \sigma_3^{\,2} - 0.0251\ \sigma_3 + 0.112 \quad (5.13)$$

ΔV_{corr} volume change correction
σ_3 cell pressure

Subsequently to the pressure calibration test, the influence of the room temperature on the volume change measurements was investigated. As expected, variations of the room temperature resulted in significant falsifications of the volume change measurements due to the thermal extension of the cell water and cell components. Figure 5.18 illustrates one of the temperature sensitivity tests. The test lasted for about 48 hours and started at a room temperature of 19° C. After two hours the temperature was elevated to 20 °C, subsequently dropped to 18 °C and again elevated to the initial temperature of 19 °C. It can be seen that the cell is relatively quickly affected by the temperature variations. However, it takes more than a day until the full volume change develops. On the other hand that means that short-term variations of the room temperature (e.g. caused by the passing of people) do not severely affect the volume change measurements.

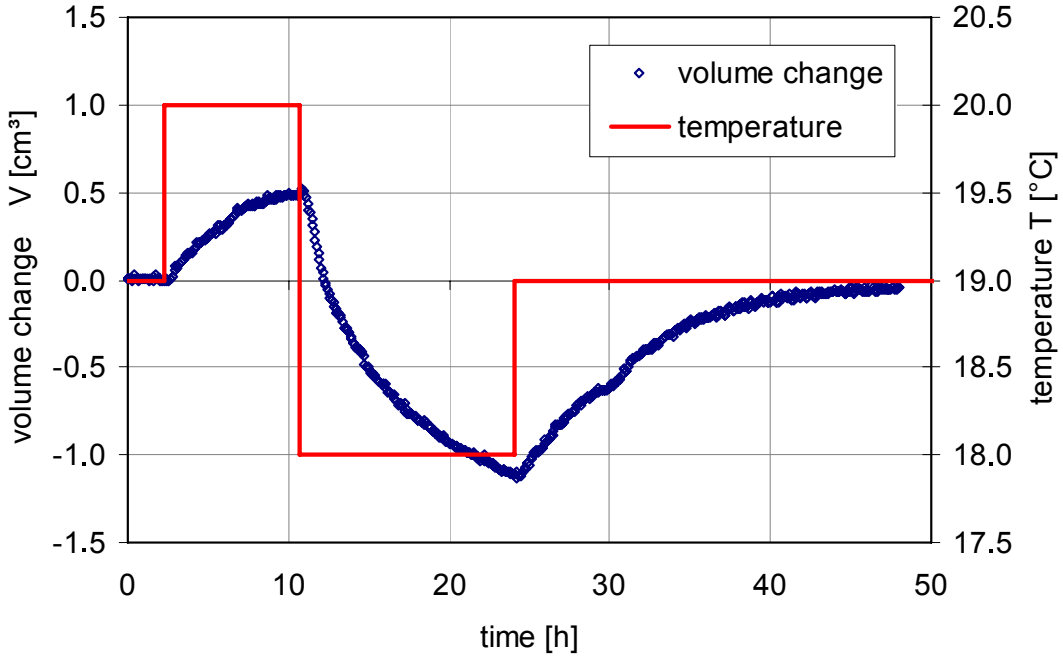

Figure 5.18: Influence of room temperature variations on the volume change measurement.

A definite conclusion from the sensitivity tests is that an accurate temperature control during the conduction of the triaxial tests is indispensable. A temperature calibration respectively correction of the volume change measurements is possible to a greater or lesser extent, but is complicated by the long time delay of the effects of a temperature variation.

The test of the air conditioning system revealed that temperature variations of up to ±0.6 °C cannot be prevented. As such variations usually occur in the form of day-night cycles, the full effects on the liquid volume of the inner cell do not develop. It was found that maximal variations of ±0.35 cm³ are the consequence

of the inaccuracy of the temperature control. Such a volume change is small in comparison to the total liquid volume of the cell (approx. 4,000 cm³).

In an attempt to reduce the effects of the uncontrollable variations of the room temperature it was decided to put a thermal insulation around the outer cell during the conduction of the tests. A flexible 5 cm rubber foam layer is used for this purpose. In this way, the short-term and the day-night variations of the room temperature can be equilibrated very well. However, it is important to make sure that the average room temperature over the course of the days does not vary. If such a tendency is recognizable, a manual interaction of the air conditioning system is necessary.

Based on the experience gained from the pressure and temperature calibration tests, the achievable accuracy of the volume change measurements is estimated by approximately ±0.5 cm³. Relating this value to a soil specimen of 7 cm diameter and 14 cm height, the accuracy is within the range of 0.1 %.

5.6 Experimental study

5.6.1 General description

The basic idea of the experimental study is to investigate the influence of hydraulic hysteresis respectively the degree of water saturation on the isotropic compression and shear strength behaviour of compacted unsaturated fine-sandy silt. The tests are conducted at constant suction respectively under drained conditions. Some experimental studies on this subject have already been published but they primarily focused on wetting-drying cycles of highly expansive clays (e.g. Alonso et al. 1995, Sharma 1998).

The investigated soil is recompacted and constitutes of 5.9 % clay, 56.3 % silt and 37.8 % fine-sand. The uniformity-coefficient of the grain size distribution curve is 13.3. The specific gravity of the solids is ρ_s = 2.77 g/cm³. The specimens are compacted to an initial dry density of ρ_d = 1.40 g/cm³, which results in a void ratio of e = 0.98. Direct shear tests with saturated specimens yielded an effective friction angle φ' = 30,6° and an effective cohesion c' = 13.0 kPa.

It has already been outlined in section 5.2.1 that due to the hysteresis of the water retention curve, a soil at equal suction may exhibit different degrees of water saturation. For a given suction, the minimum and the maximum degree of water saturation are determined by the main wetting and main drying curve of the soil, respectively. The experimental study focuses on isotropic compression and shear tests exactly at these two extremes of the water retention behaviour. Figure 5.19

shows the water retention behaviour of the investigated silt and illustrates the basic idea of the experimental study. The depicted water retention curves were obtained by fitting Tempe-pressure cell and additionally contact-filter paper measurements to the van Genuchten model (van Genuchten 1980).

After compaction, the soil specimens exhibit a suction in the range of 16 – 19 kPa. The corresponding water saturation degree S_w is 0.42. This hydraulic state is close to the measured main wetting curve of the material. In order to conduct a triaxial test on the main drying curve, the specimen is first wetted along a scanning curve, and subsequently dried to the desired suction value. Conversely, for testing along the main wetting curve, the specimen is first dried along a scanning curve, and subsequently wetted to the desired suction value. The red dotted lines in Figure 5.19 indicate exemplarily the necessary paths in order to reach the main drying respectively main wetting state at 50 kPa suction. The resulting large difference in the degree of saturation can be recognized.

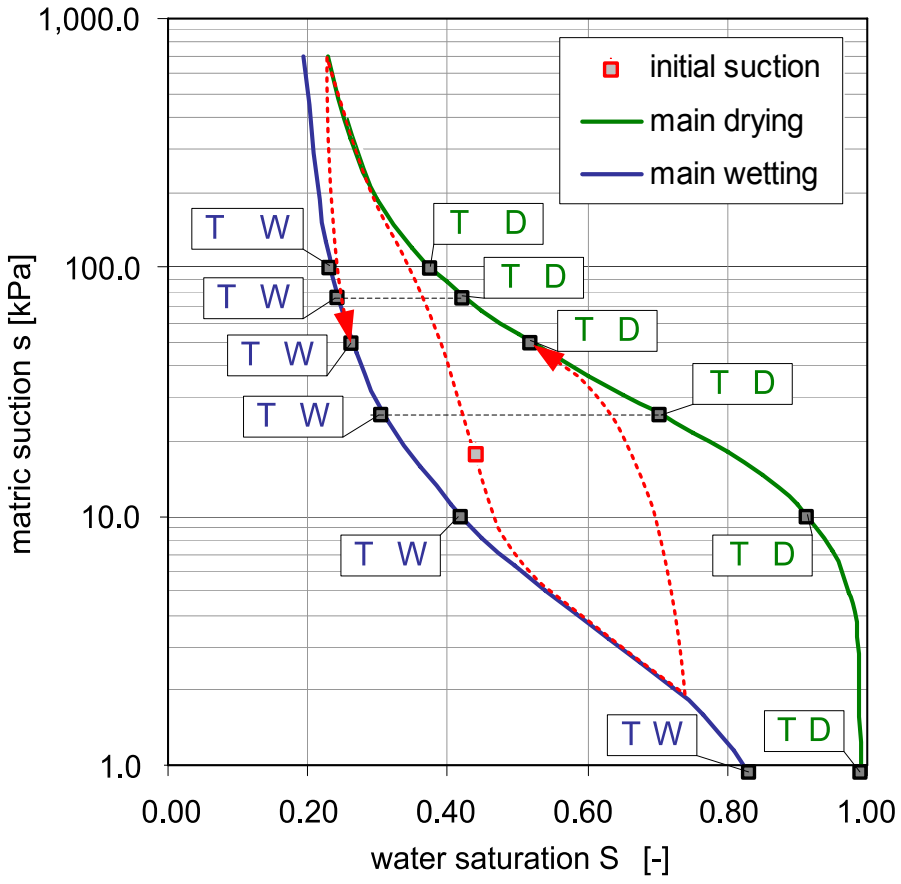

Figure 5.19: Water retention curves and illustration of the experimental study.

The suction respectively hydraulic states at which the planned triaxial consolidation and shearing tests take place are also indicated in Figure 5.19. A total number of 12 tests were planned. The tests are labelled according to the suction values at which the tests are conducted and depending on whether the suction state is achieved by main wetting or main drying. For example, "$T_{50}D$"

means that the specimen is brought to a suction of 50 kPa on the main drying side of the water retention curve, before the mechanical testing is initiated.

Before the soil sample is brought to the desired suction level, it is exposed to an net stress of $(\sigma_3\text{-}u_a)$ = 40 kPa. After the equilibration phase at the desired suction level, the specimen is consolidated under drained conditions to a net stress $(\sigma_3\text{-}u_a)$ of 225 kPa. Thereafter, the sample is allowed to rest for 36 hours in order to allow the dissipation of any excess pore water pressure and of creep effects. Subsequently, the specimen is sheared under a constant axial strain rate. Figure 5.20 illustrates the stress paths of the planned triaxial tests plotted as suction s over the net stress $(\sigma\text{-}u_a)$.

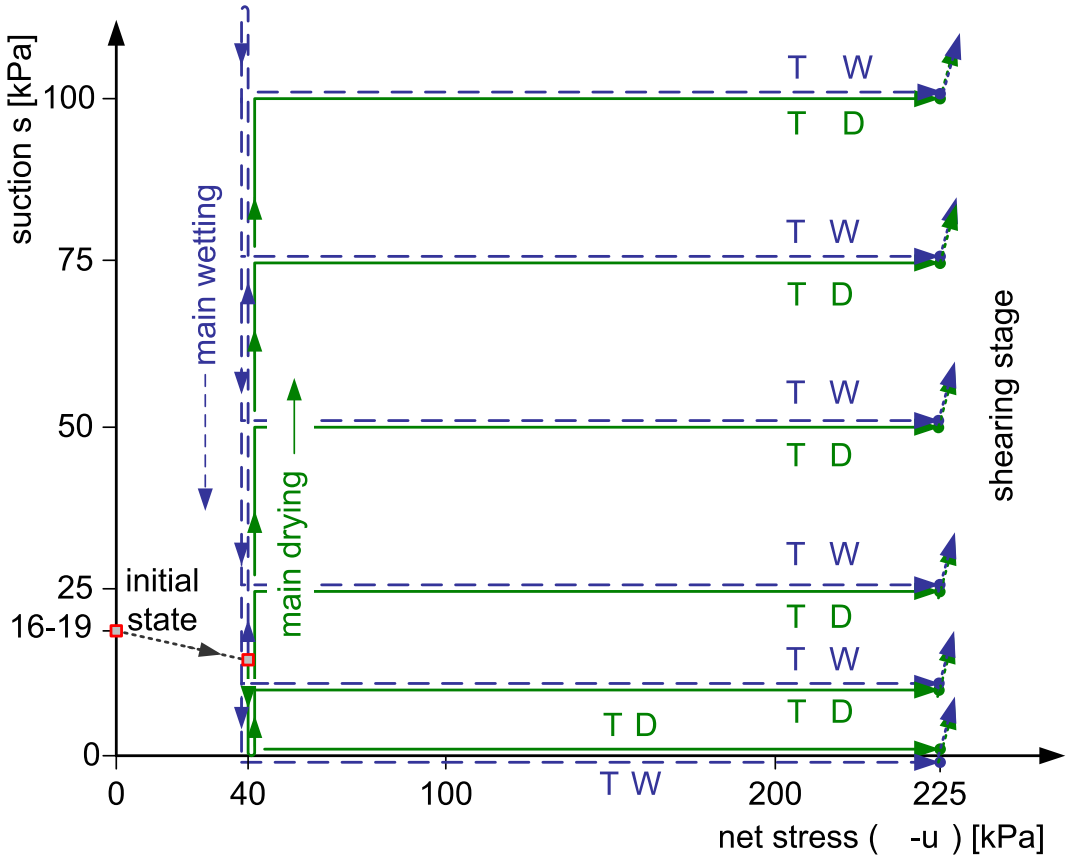

Figure 5.20: Stress paths during equalization and consolidation phases.

5.6.2 Testing procedure

The triaxial specimens have a diameter of 7.0 cm and a height of 14.0 cm. They are prepared in a mould by dynamic compaction of 10 subsequent layers to a dry density of ρ_d = 1.40 g/cm³. The initial water content is w = 15 % (approximately 7 % less than the optimum), which theoretically yields a water saturation degree of S_w = 0.42. After the preparation, the specimens are left in the mould until they are collocated into the triaxial cell.

Meanwhile, the triaxial testing device is prepared; this includes the saturation of the ceramic disc, the de-airing of tubes and fittings by flushing with water and de-airing of the volume change device. Subsequently, the mould is dismantled and the specimen is placed on the high-air entry disc at the base pedestal of the triaxial cell. A porous stone is placed on the top of the sample. Finally, a 0.3 mm latex membrane is put over the specimen. Two O-rings at the base and at the top are used to prevent the leakage of water from the inner cell into the specimen.

Thereafter, the double-walled triaxial cell is assembled as depicted in Figure 5.10 respectively 5.11. In order to favour the bleeding of air bubbles from the cell walls and the latex membrane the inner and outer cell are slowly filled with de-aired water within a time duration as long as one hour. Finally, the cell pressure lines are connected to the inner and outer cell. This takes place with the help of a specifically fabricated jar, which allows the fittings to be connected under water. This way, no air can enter into the water pressure lines during this process.

The triaxial testing starts with the elevation of the net stress from an initially manually set value of $(\sigma_3\text{-}u_a)$ = 10 kPa to 40 kPa. The subsequent procedure depends on whether a drying or wetting test is intended. For tests following a main drying path, an external cylinder is connected to the pore water pressure line and the sample is allowed to saturate. Thereafter, the pore air and pore water pressure lines are connected and the soil is dried to the desired suction value. For tests along the main drying path at high suction levels, the saturation only takes place for a short period (approximately 1 – 2 days), just to make sure that a main drying state can be achieved and not only a state on a scanning curve.

Conversely, for tests following a main wetting path, the suction is first raised to a high level in the residual range, before it is decreased to the desired value. Also in this case, the maximum applied value of the suction is adapted to the final value; i.e. very high maximum values are applied for triaxial tests at higher suction levels, whereas lower maximum values are applied for tests at lower suction values.

The distinct suction values are applied to the specimens in two steps. First, the pore water and pore air pressures are simultaneously increased to a value of $u_a = u_w$ = 20 kPa; this allows the pore water pressure line to be flushed during the test in order to remove diffused air below the ceramic disc. Subsequently, the water pressure is maintained constant, whereas the pore air pressure is raised to its final value. The cell pressure must be elevated simultaneously with the pore air pressure in order to maintain a constant net stress in the specimen ($\sigma_3\text{-}u_a$ = 40 kPa). Subsequently, a time period of 5 – 12 days is generally needed for the suction to equilibrate throughout the sample. The equilibration stage is terminated when the water inflow respectively outflow into the sample falls below a rate of ΔV_w = 0.1 cm³/day.

After the suction equilibration stage, the soil specimen is consolidated under drained conditions to a final net stress of σ_3-u_a = 225 kPa. The cell pressure is increased at a stress rate of $\Delta\sigma$ = 0.01 kPa/min and $\Delta\sigma$ = 0.02 kPa/min for the tests with zero and non-zero suction, respectively. Thus, the consolidation stage takes 7.8 respectively 15.6 days. The lower pressure increase rate for the tests at zero suction is chosen because here the tests are saturated or quasi-saturated, and excess pore pressures are more likely to develop.

Before the shearing phase is initiated (at the final consolidation net stress of σ_3-u_a = 225 kPa), a rest period of 36 hours ensures the dissipation of any excess pore water pressure. Subsequently, a constant displacement rate of 0.0025 mm/min is applied to the specimen. Time to failure varies between 10 and 15 days.

The triaxial tests require typically 9 testing stages in order to conduct the suction equilibration, consolidation and shearing phase. Table 5.1 describes exemplarily the test phases for the $T_{50}D$ test and gives the applied cell pressure σ_3, pore air and pore water pressure (u_a and u_w, respectively) as well as the pressure increments and the time durations of the individual stages.

Table 5.1: Exemplary stages for the triaxial test $T_{50}D$.

nr.	**description**	**σ_3**	**u_a**	**u_w**	**increment $\Delta\sigma$; duration t**
-	-	[kPa]	[kPa]	[kPa]	-
1	application of initial cell pressure	10 – 40	-	-	1.0 kPa/min; 0.5 hours
2	resting period	40	-	-	1.0 hour
3	saturation phase	40	-	-	2 days
4	application of suction-step 1	40 – 60	0 – 20	0 – 20	1.0 kPa/min; 20 min
5	application of suction-step 2	60 – 110	20 – 70	20	1.0 kPa/min; 50 min
6	suction equilibration	110	70	20	8 days
7	consolidation	110 – 295	70	20	0.02 kPa/min; 8 days
8	resting period	295	70	20	1.5 days
9	shearing	295	70	20	0.0025 mm/min; 10 days

5.6.3 First test results

The testing program has not yet been completed due to the long time needed for the successful putting into operation of the triaxial apparatus. Up to now four tests on the main drying side and two tests on the main wetting side have been completed (T_0D, $T_{25}D$, $T_{50}D$ and $T_{75}D$ respectively $T_{25}W$ and $T_{50}W$). Therefore, an analysis and modelling of the test is only possible to a limited extent. However, the presently available results of the consolidation and shear phases are presented and discussed in the following. The observed volume changes during the suction equilibration stage were generally small. Collapse phenomena or significant swelling could not be observed. Thus, the volumetric behaviour during this initial test phase is not further considered here.

- **Results and discussion of isotropic compression**
  Figure 5.21 shows the change of specific volume *v* during the consolidation phases. The net stress $(\sigma\text{-}u_a)$ is depicted on a logarithmic scale. The soil sample at zero suction (T_0D) experienced by far the largest decrease of specific volume. At all other tests, the soil compressibility decreased continuously with increasing suction. Moreover, the two tests on the main wetting curve ($T_{20}W$ and $T5_0W$) experienced considerably less volume decrease than their counterparts on the main drying side ($T_{20}D$ and $T_{50}D$).

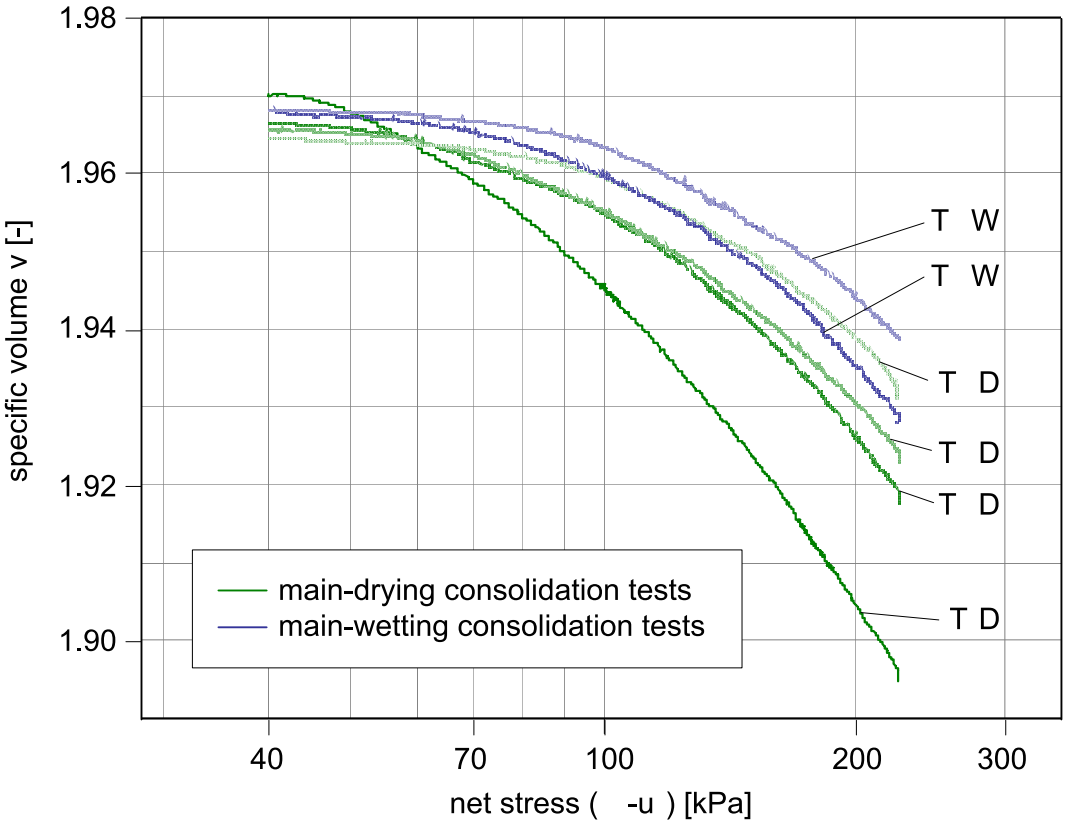

Figure 5.21: Variation of specific volume during consolidation.

The consolidation plots do not exhibit a clear yield point but show a rather gradual transition from elastic to plastic behaviour. Moreover, the slopes of the consolidation lines in the virgin compression range are not constant in the plastic range. This type of compression behaviour probably origins in the silty-fine sandy constitution of the tested soil respectively is a general trend for unsaturated soils (see Figure 5.5 c). It is interesting to recognize from Figure 5.21 that the slopes of the main wetting respectively main drying tests at the same magnitude of suction ($T_{20}W$ and $T5_0W$ resp. $T_{20}D$ and $T_{50}D$) tend to become increasingly parallel at higher levels of isotropic stress.

A small vertical drop of specific volume can be recognized at the end of most of the consolidation plots in Figure 5.21. These volume decreases occurred during the 36 hour resting period at the end of the consolidation phase before the shearing was initiated; this demonstrates that creep effects or excess pore water pressures slightly influenced the experimental results.

Despite the smooth transition from elastic to plastic behaviour, it can be recognized by visual inspection from the plots in Figure 5.21 that the isotropic yield stress p_0* increases with suction. Subsequently, it was tried to roughly estimate the yield points by determination of the maximum curvature of the consolidation curves. The so obtained yield points and the approximated yield curves serve for a qualitative interpretation of the observed material behaviour and are shown in Figure 5.22.

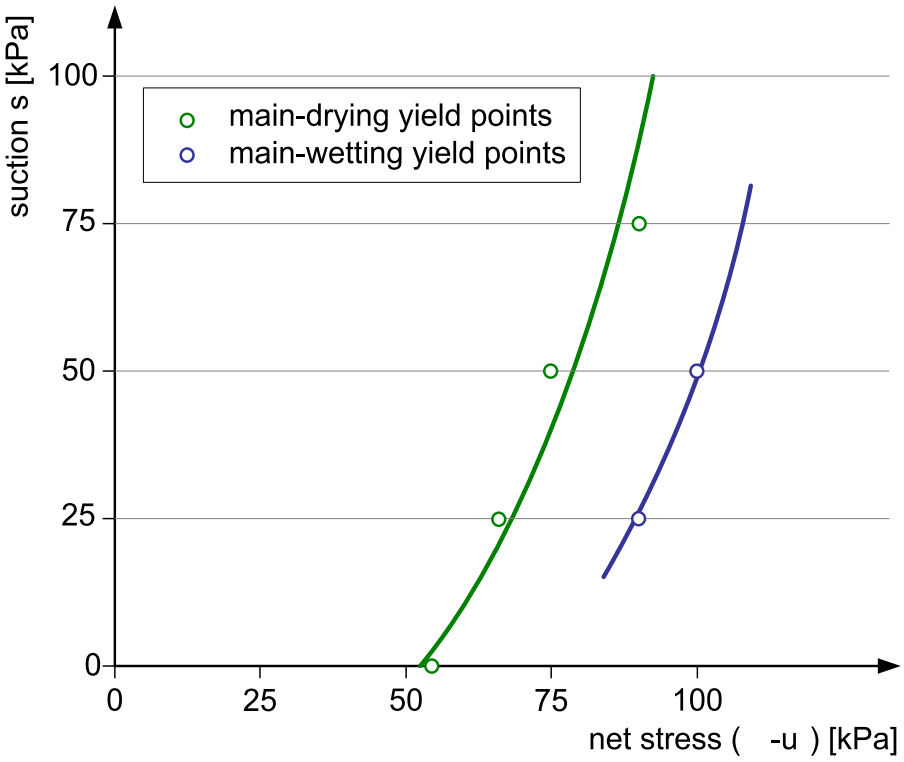

Figure 5.22: Yield points and approximated yield curves for isotropic compression.

It can be seen from Figure 5.22 that the two yield points obtained from the consolidation tests on the main wetting path are considerably higher than their counterparts on the main drying side ($T_{20}W$ and $T5_0W$ respectively $T_{20}D$ and $T_{50}D$). These experimental results can be explained by the consideration of coupled hydro-mechanical material behaviour.

Alonso et al. (1990) incorporated two yield surfaces into their model: the so-called loading collapse yield surface (LC) and the suction increase (SI) yield surface. An increase of the isotropic stress beyond the plastic limit causes a shifting of the LC yield surface and an increase of suction to virgin ranges causes shifting of the SI yield surface. Both yield surfaces are independent of each other. On the other hand, Wheeler et al. (2003) and Sheng et al. (2004) argued that the change of the degree of saturation along the main wetting or the main drying curve is an irreversible process which results in a different mechanical behaviour even at the same suction.

In relation to the obtained experimental results, the interpretation is as follows: for a test on the main wetting side, the initial drying of the specimen shifts the SI yield surface; this also results in a coupled movement of the LC yield surface. Thus, if the specimen is finally wetted to the desired suction value and subsequently compressed isotropically, the yield stress p_0* will be higher than for a test on the main drying side, in which the original position of the LC yield surface remains unchanged, see Figure 5.23.

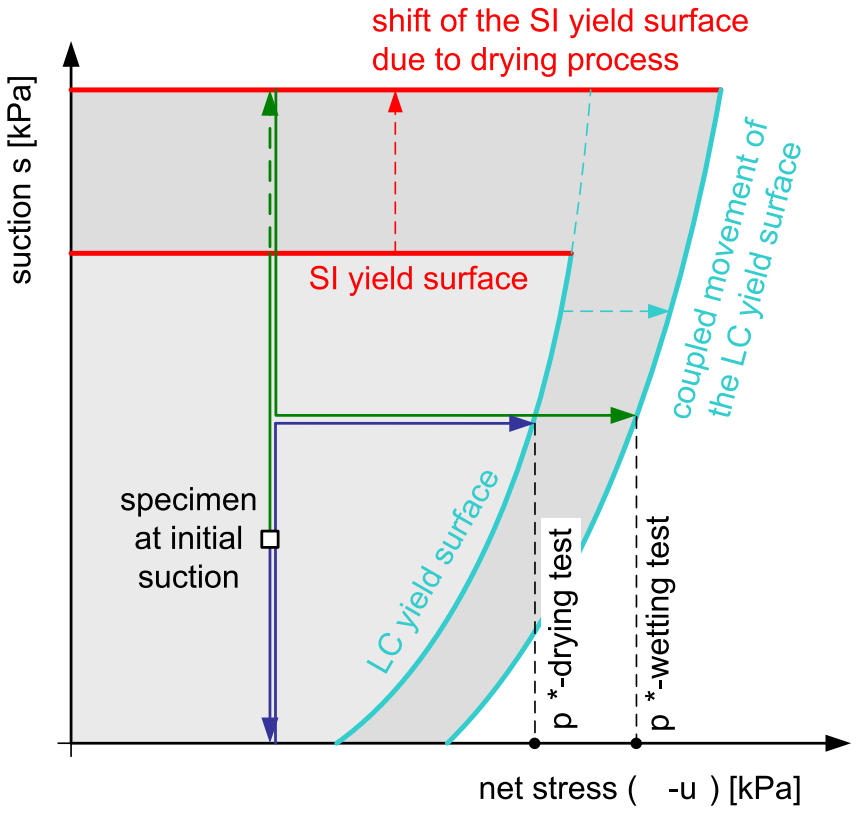

Figure 5.23: Illustration of the assumed coupled hydro-mechanical behaviour.

- **Results and discussion of shear strength tests**
  Figure 5.24 a) shows the axial strain ε_1 - deviatoric stress q graphs and Figure 5.24 b) the corresponding axial strain ε_1-volumetric strain ε_v plots of the conducted constant-suction shear tests. The specimens were sheared under a constant isotropic net stress of 225 kPa. The test $T_{25}D$ was erroneously conducted at a lower net stress and is therefore not depicted.

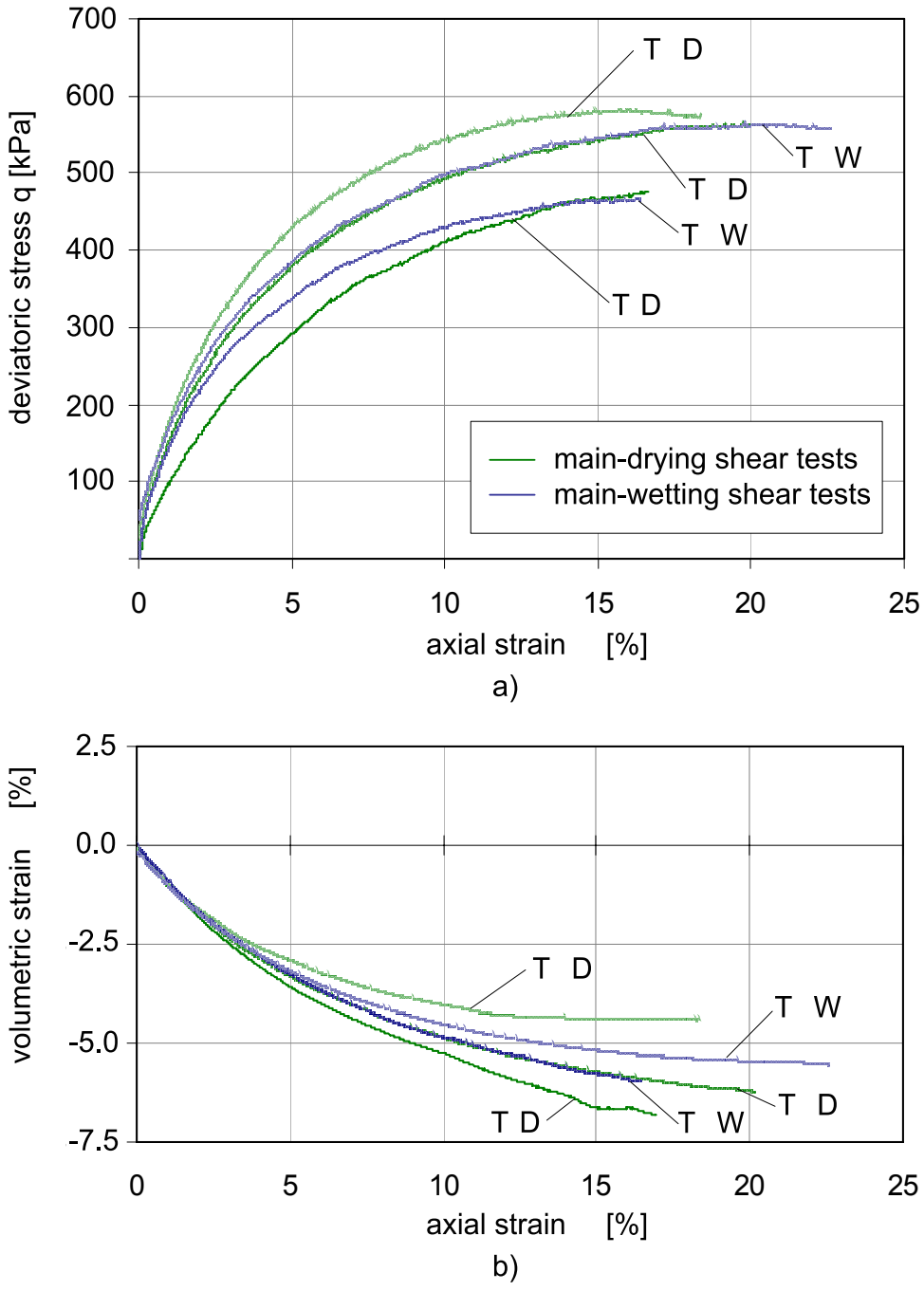

Figure 5.24: Deviatoric stresses (a) and volumetric strains (b) over axial strains of the conducted constant-suction shear tests.

The results of the shear tests are largely consistent, i.e. tests a higher suction level yielded higher shear strength and shear stiffness as well as lower

volumetric strains. An exception is the test $T_{25}W$, which apparently yielded lower shear strength than the test at zero suction (T_0D). It is therefore desirable to repeat both shear tests. Because of this contradictory result and the overall low number of tests, a meaningful interpretation of the presently available shear test results has yet not been possible.

However, it is remarkable that the main wetting and main drying shear test at s = 50 kPa suction yielded an almost identical material behaviour. It will be interesting to see in further experiments whether the shear strength is less affected by hydraulic hysteresis respectively the degree of water saturation than the isotropic compression behaviour. The literature results on this topic are inconsistent. Han et al. (1995) reported higher shear strength of shear tests on the main drying path, whereas Gallage and Uchimura (2006) reported exactly the opposite behaviour, namely higher shear strength on the main wetting path.

Figure 5.25 illustrates the large influence of suction on the shear strength of the tested silt. The coloured area between the upper envelope of the peak shear strength values and the horizontal base line through the peak shear strength of the test T_0D is representative for the capillary cohesion respectively the apparent cohesion induced by the suction. Additionally, the deviation of the measured shear strength of the Test $T_{25}W$ from the general trend can be recognized.

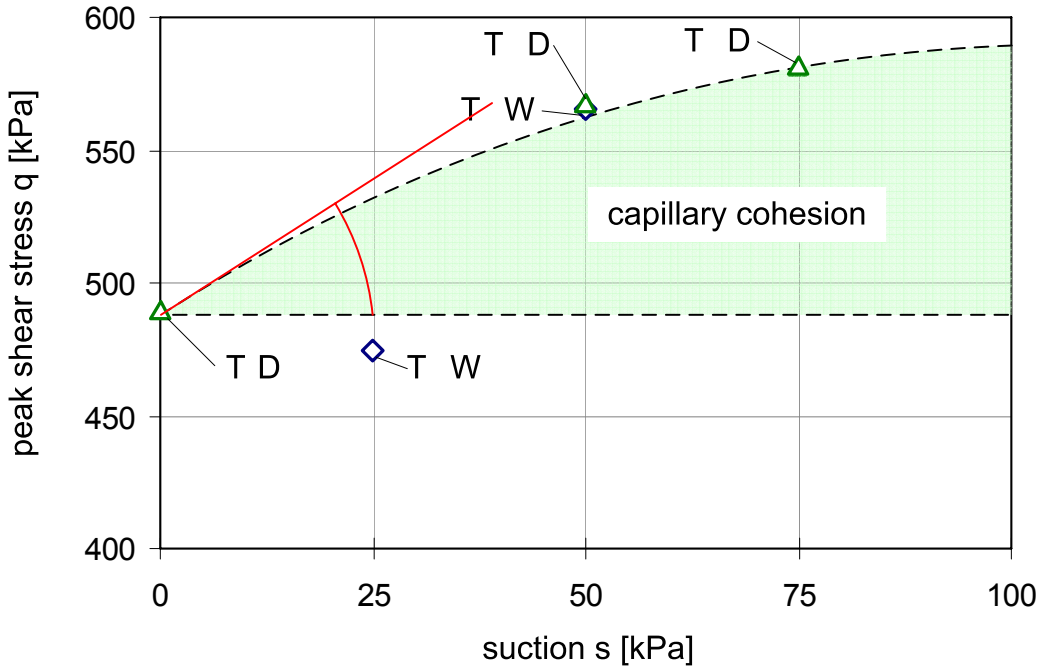

Figure 5.24: Increase of shear strength with suction for the tested silt.

It is remarkable that the initial increase φ_b of the capillary cohesion is significantly higher than the effective friction angle φ' (62° respectively 31°).

This is in contradiction to a number of published experimental evidence respectively to the theoretical assumption that φ_b must not be larger than φ' (e.g. Fredlund et al. 1987). However, the direct shear tests of Escario and Saez (1986) and recent triaxial shear tests of Estabragh and Javadi (2008) on unsaturated compacted silt also indicate that φ_b may be significantly larger than φ'.

5.7 Summary and conclusions

A triaxial apparatus for unsaturated soil specimen was installed in the laboratory. The device has a double-walled cell and uses the axis-translation technique to apply distinct suction values. Intensive efforts were necessary in order to overcome some shortcomings of the apparatus, among these the detection and elimination of a water leakage problem. After the successful putting into operation, the volume change device and the double-walled triaxial cell were calibrated in order to allow accurate volume change measurements. Finally, a testing program which included the investigation of hydraulic hysteresis on the mechanical behaviour of unsaturated silt was started. Due to the long time period needed to put the triaxial apparatus into operation, it has yet not been possible to complete the testing program.

The tedious installation process of the triaxial testing system showed that the successful putting into operation of complex laboratory equipment is complicated, particularly if there is a lack of support by the manufacturer. On the other hand, triaxial testing devices for unsaturated soils are not standard machines that can simply be put into operation by pressing a button. Each of these devices is unique and has its specific features that require special considerations. Thus, in addition to apparent defects of the device, the initial testing phase was a necessary development phase, in which the know-how respectively experience for the further work was gained by the execution of a number of preliminary tests.

The conducted calibration tests showed that despite the use of a double-walled triaxial cell, great care is needed in order to obtain accurate volume change measurements. The influence of pressure and temperature variations solely on the volume change device was found to be negligibly small. On the contrary, a significant influence on the double-walled cell was detected. A calibration function was derived in order to correct the volume change measurements for the cell pressure variation during consolidation phases. Further, it showed that the inner cell is relatively quickly affected by small variations of the room temperature. However, there is also a long time delay until the full effect of a temperature variation develops. A correction of the volume change

measurements is therefore only possible to a limited extent. As a consequence, a careful control of the room temperature is the best measure to avoid a falsification of the measurements. In any case it is indispensable to continuously record the room temperature.

After the completion of the installation and calibration process, a first testing series was started. Fine-sandy silt with a low initial dry density was investigated. The investigation of the saturated and unsaturated mechanical behaviour of such soil types is of interest with respect to tunnelling under compressed air. The experimental study particularly focused on the effects of hydraulic hysteresis respectively the degree of water saturation on the isotropic compression and shear strength behaviour; this was achieved by rigorous testing on main drying respectively wetting paths. The triaxial tests were conducted under drained conditions.

A number of six triaxial tests have been successfully completed presently. The outcome of these tests can be summarized as follows:

- **Isotropic compression tests**
  The experimental results of the consolidation phases indicated an increase of the isotropic yield stress as well as a decrease of the soil compressibility with suction. Moreover, the consolidation tests conducted on the main wetting side exhibited a larger isotropic yield stress and lower soil compressibility than their counterparts at the same suction level on the main wetting side. This type of material behaviour was attributed to coupled hydro-mechanical behaviour, in which preliminary applied high suction values caused the increase of the apparent preconsolidation stress; this means that in contrast to the model of Alonso et al. (1990) the shifting of the SI yield surface additionally results in a coupled movement of the LC yield surface.

- **Shear tests**
  The obtained results of the shear tests yielded a non-linear increase of shear strength with suction. Moreover, it was found that the initial increase of the capillary cohesion is significantly higher than the saturated friction angle. Although this type of material behaviour is in contradiction to other experimental evidence and theoretical assumptions, it is arguably consistent with recently published experimental results from triaxial tests on compacted unsaturated silt by Estabragh and Javadi (2008). Concerning the differences between the shear strength on the main wetting respectively main drying path, there has only been one pair of tests at the same suction level available for analysis. A comparison of the experimental results of the two specific tests suggested that the shear strength is not affected by the hydraulic hysteresis of the water retention curve. However, this single experimental result is much too sparse to allow decisive statements on this specific aspect.

It is therefore desirable to complete the initiated experimental study. Beyond, equivalent isotropic compression tests with different initial dry densities and shear tests at different confining pressures should be conducted; the additional experimental evidence would allow a generalisation of the so far observed effects of hydraulic hysteresis and would allow detecting a possible influence of suction on the effective friction angle respectively on the slope of the critical state line.

Finally, a slight modification respectively enhancement of the triaxial cell is suggested. The high air-entry ceramic at the base respectively the low air-entry filter at the top should both be replaced by combined end plates. This modification, which only required minor mechanical works would cut the drain length for water and air by half. As a consequence, particularly the suction equilibration phase but also the other testing stages could be conducted in significantly shorter time periods. An accelerated testing procedure is a major interest in the triaxial testing of unsaturated soils, where the long testing times often allow only a limited experimental investigation.

6 Case study: Tunnel Fritzens - analysis and prediction of air losses

6.1 Introduction

There is a worldwide trend towards situating new traffic-infrastructure in urban areas in underground space. In order to meet this requirement, the construction of shallow tunnels is necessary. Existing buildings, traffic-infrastructure and often groundwater hinder the tunnel advance. In many cases, a number of collateral measures are necessary to allow for a safe construction of these tunnels.

In Austria and Germany, a frequently used driving method for shallow tunnels in groundwater bearing soils is the NATM (New Austrian Tunnelling Method) in combination with compressed air. A characteristic feature of the NATM is the application of a reinforced shotcrete layer as primary support of the lining. The combination with compressed air is used to prevent groundwater inflow into the tunnel, especially in the excavation area.

The considered project, the Tunnel Fritzens is also driven under compressed air support. The complex environment of tunnel construction requires a number of additional measures, e.g. sealing injections, roof-umbrellas and bulk heads. These measures ensure the stability of the tunnel advance. On the other hand, unexpectedly high air losses were encountered during the excavation of the first sections of the top-heading of the tunnel. The excessive air losses presented a risk for the safe and economic construction of the tunnel.

As a consequence, the building owner, the Brenner Eisenbahn GmbH, decided to commission an extensive investigation of the air losses that had occurred. Key tasks were the identification of the reasons for the high air losses and the elaboration of measures to reduce the air losses in the course of the further top-heading advance. Additionally, a prediction of the air losses for the subsequent bench advance of the tunnel was commissioned. A further interest was to clarify whether or not the high air losses origin in a higher soil permeability than specified in the tender documents.

The investigations are carried out by means of numerical simulations. A finite difference program, developed by Steger (2004) is employed. As a starting point for the investigations, the measured air losses during the advance of the first 12 sections of the top-heading of the tunnel are available. In a first step, the focus is on identification of air losses taking place through the tunnel lining respectively through the tunnel face. Two- and three-dimensional numerical simulations are

used to analyze the permeability values of the ground and other materials involved in the tunnel construction (e.g. shotcrete or grouted soil).

In a second step, different construction variants are simulated numerically in order to identify appropriate measures for the reduction of the air losses. Based on the computation results, exemplary air loss predictions are elaborated. They allow for a comparison of the effectiveness of the studied measures. Finally, an estimation of the air losses and total air need for the bench advance is conducted. Different scenarios, assuming a thoroughness of the tunnel support measures to a greater or lesser extent, are considered.

The results of the conducted investigations and the gained knowledge are presented in this chapter. First, a short introduction into the principles of compressed air tunnelling is given. Thereafter, the Tunnel Fritzens and its challenging construction environment are presented. The subsequent section of the numerical investigations starts with a description of the employed simulation tool. The numerical investigations are split up in three parts: air losses through the tunnel lining, air losses during the advance phase and air losses for the bench excavation. A summary of the computation results and recommendations for the further tunnel advance close this chapter.

6.2 Tunnelling under compressed air

Tunnelling under compressed air is an economic driving method in appropriate ground conditions. An excess air pressure inside the tunnel is employed to prevent groundwater inflow. In order to apply the excess pressure, the tunnelling area is separated from atmospheric conditions by means of a bulk head. One or two air locks are accommodated in the bulk head. Personnel, machinery and construction material enter respectively leave the tunnel through the air locks. A pressure chamber is employed to pass the workmen through the air lock. Compressed air is constantly pumped into the tunnel in order to maintain a constant excess air pressure.

The magnitude of the applied air pressure p_a inside the tunnel corresponds to the hydrostatic pressure at the base of the tunnel $p_{w,b}$. Due to the low gravity potential, the air pressure is approximately constant over height, whereas the water pressure increases linearly. Consequently, a pressure difference Δp acts at the tunnel walls. At the crown of the tunnel it reaches a maximum and it is approximately zero at the invert of the tunnel. The maximum pressure difference depends on the diameter d of the tunnel, but not on the depth below the groundwater level. Figure 6.1 illustrates the described pressure difference in longitudinal and cross section.

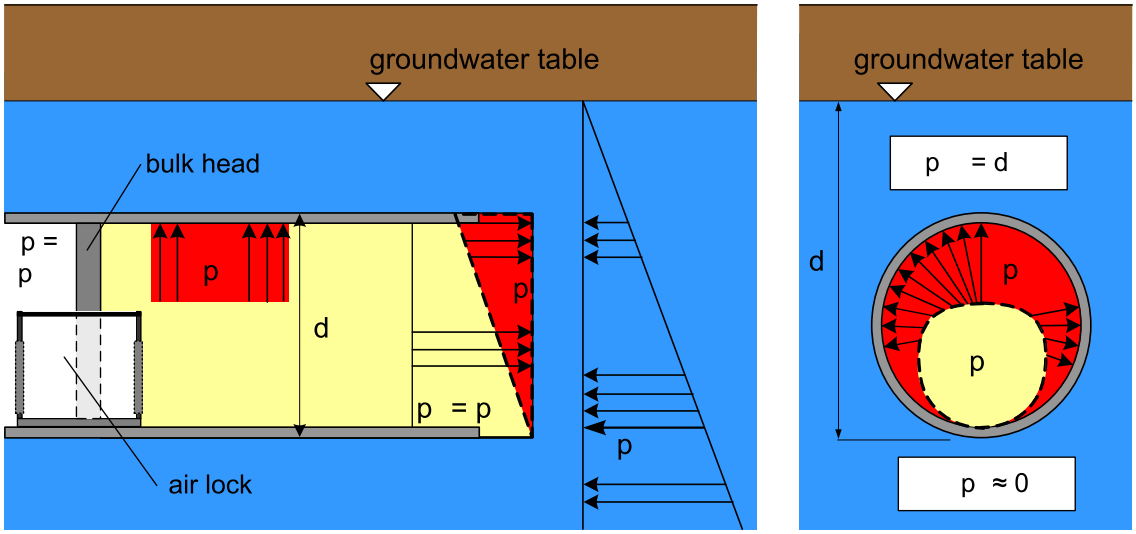

Figure 6.1: Air and water pressure difference at the tunnel face and lining.

The described pressure difference represents a driving potential for air flow out of the tunnel. The compressed air may escape both through the unsupported tunnel face, and through shrinkage cracks and gaps of the tunnel lining. For the tunnel designer and the contractor, it is important to correctly estimate the maximum air loss rate q_a [m³/min] and the total amount of air need Q_a [m³] previously to the construction of the tunnel. These values are needed to determine the capacity of the air supply equipment and to compute the energy costs for the generation of the compressed air, respectively. The costs related to compressed air can reach several thousand Euros per meter of tunnel length.

The use of compressed air is especially well-suited for grounds with a saturated water permeability of $k_{ws} \approx 10^{-5}$ - 10^{-7} m/s. At higher soil permeability, additional measures like grouting are necessary, and the method may lose its economic advantage. On the other hand, compressed air has been successfully used in combination with grouted soils in a number of cases, e.g. Tunnel Siegaue (Gattermann and Wittke-Gattermann 2003). At lower ground permeability, the water infiltration rates are usually too low to need compressed air support.

6.3 The Tunnel Fritzens

6.3.1 Situation

The Tunnel Fritzens is a complex tunnelling project of the Brenner Zulaufstrecke, situated in the lower Inn-valley, Tirol. The Brenner Zulaufstrecke is a section of a future high-speed European north-south connection that crosses the Alps and runs from Munich, Germany, to Verona, Italy.

The routeing of large parts of the Brenner Zulaufstrecke is narrowed by the limited space between the river Inn, the Inntal-highway and an existing railway line. The rail traffic has to be maintained in operation throughout the construction works of the new connection, and beyond. Further requirements are the protection of the inhabitants against the impact of noise and vibrations. The restrictive boundary conditions require a number of tunnel buildings in all different variations, i.e. cut-and-cover tunnels, top-cover tunnels and conventionally driven tunnels.

In the area of Fritzens, the new railway line crosses under the station and the adjacent tracks in an extremely oblique-angled manner. A 430 m long tunnel, the Tunnel Fritzens, is a necessary intersection between two top-cover tunnels. In totally, the tracks run for approximately 5 km subterraneously. Figure 6.2 shows an areal view of the location of the Tunnel Fritzens and illustrates the narrowed conditions for the construction of the new railway line in this area.

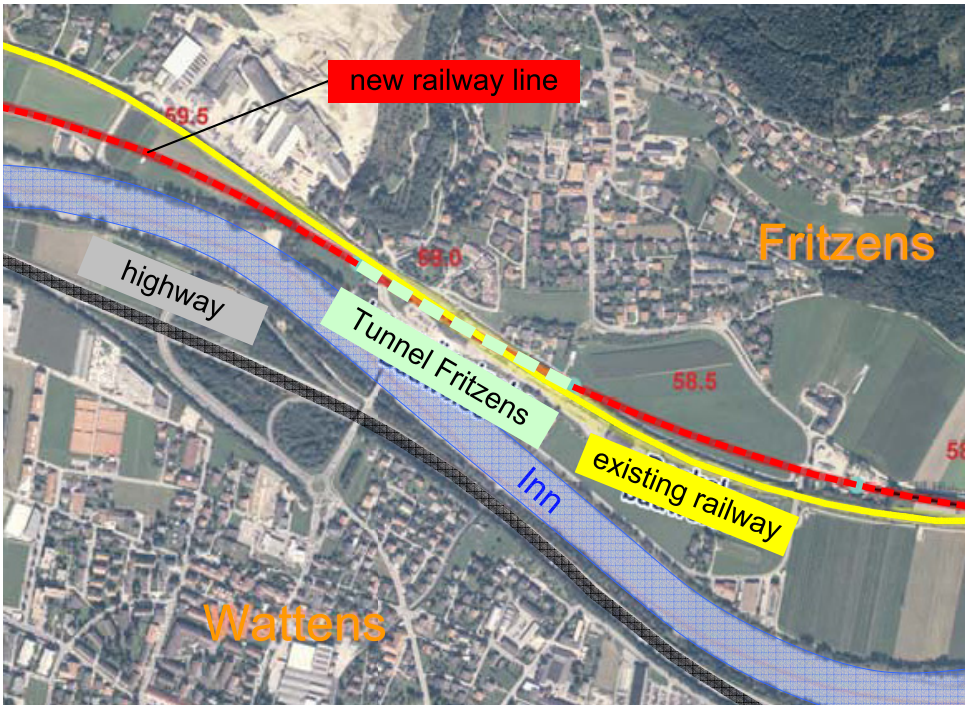

Figure 6.2: Areal view of the location of the Tunnel Fritzens.

The Tunnel Fritzens is a two-tracked tunnel. The mandatory railway loading gauge requires an inner radius of 5.70 m respectively an inner diameter of 11.40 m. The thickness of the inner shell is 50 cm. Figure 6.3 shows the standard cross section of the tunnel. The top rail is the reference level. The final tunnel crown is situated at a height of +8.00 m, and the final invert at a level of -1.30 m. The reference level for the tunnel radius is at +2.30 m. The tunnel crosses directly under the railway sidings of the station Fritzens with an average overburden of only 6 m.

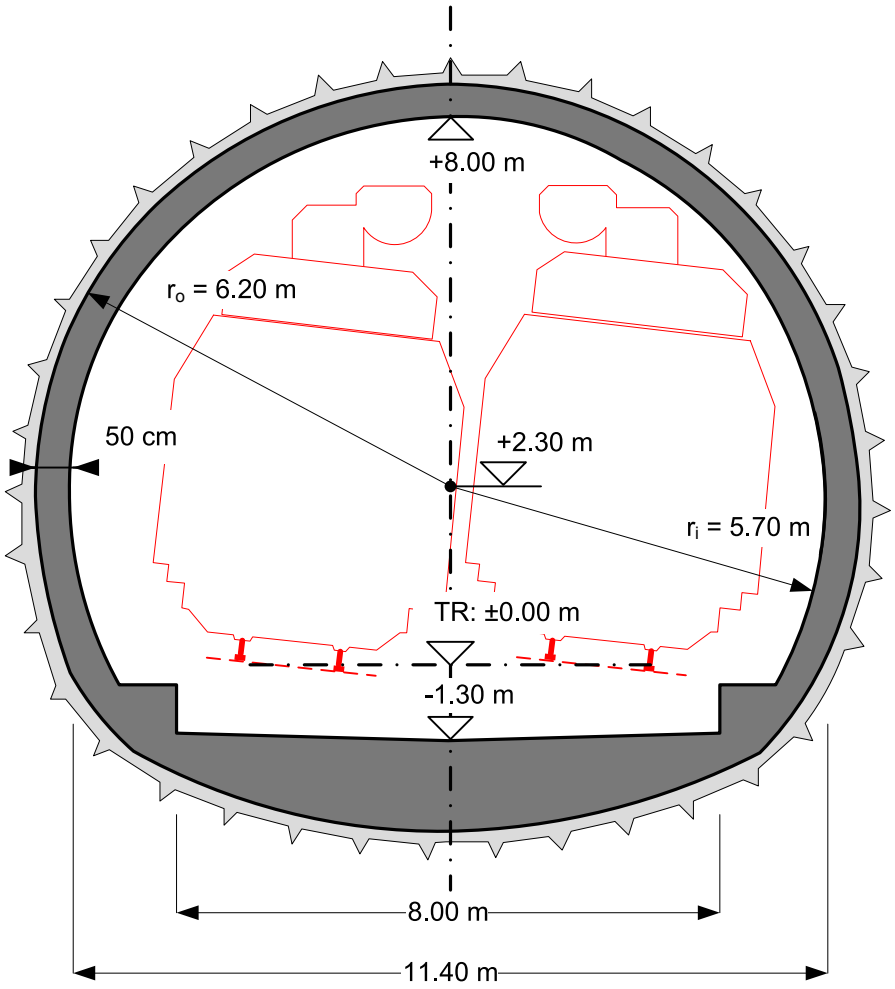

Figure 6.3: Standard cross section of the Tunnel Fritzens.

6.3.2 Geological and hydrogeological conditions

The ground consists of gravels with low sand content, deposited by the Inn and the Fritzener Bach. Earth deposits up to 5 m thickness are encountered on the surface. The deposits also consist of pebbly material. In the tender documents, the permeability range of these soils is specified with $1 \cdot 10^{-2}$ m/s to $1 \cdot 10^{-4}$ m/s. Pumping tests in the immediate environment of the tunnel alignments yielded water permeabilities between $0.4 \cdot 10^{-3}$ m/s and $4.0 \cdot 10^{-3}$ m/s.

Due to the proximity of the Tunnel Fritzens to the Inn, the groundwater conditions directly correspond with the Inn water level. The groundwater level is encountered approximately at the tunnel crown during spring and summer months, and various meters below during autumn and winter months. The tunnel gradient is approximately parallel to the Inn water level, thus the position of the groundwater level relative to the tunnel cross section is the same over the length of the tunnel. For the top-heading and bench advance, the average groundwater levels are +7.30 m and +8.50 m, respectively.

6.3.3 Driving scheme

The difficult boundary conditions, i.e. the low overburden with continuous rail traffic on the surface and the high groundwater table in combination with a highly permeable soil, lead to the design of an innovative but laborious driving method. Compressed air, jet grout column-roof-umbrellas, pipe-roof-umbrellas and bulk heads are employed to allow for a successful construction of the tunnel.

The top-heading of the 430 m long tunnel is driven preliminary to the bench excavation. The top-heading is driven under protection of a two-rowed jet grout column-roof-umbrella. The single columns have a length of 15 m and a diameter of 60 cm. In the area of the crown of the tunnel, the jet grout column-roof-umbrella is partly replaced and extended by a roof-pipe-umbrella. Due to the fan-shaped roof-umbrellas, the radius of the tunnel lining varies between 6.23 m and 7.22 m. A temporary top-heading invert is installed to support the stability of the tunnel advance. For protection of the bench advance, a lateral surround of 1.0 m thickness consisting of overlapping jet grout columns, is installed. Temporary fillings are used to facilitate the numerous grouting works inside the tunnel, see Figure 6.4.

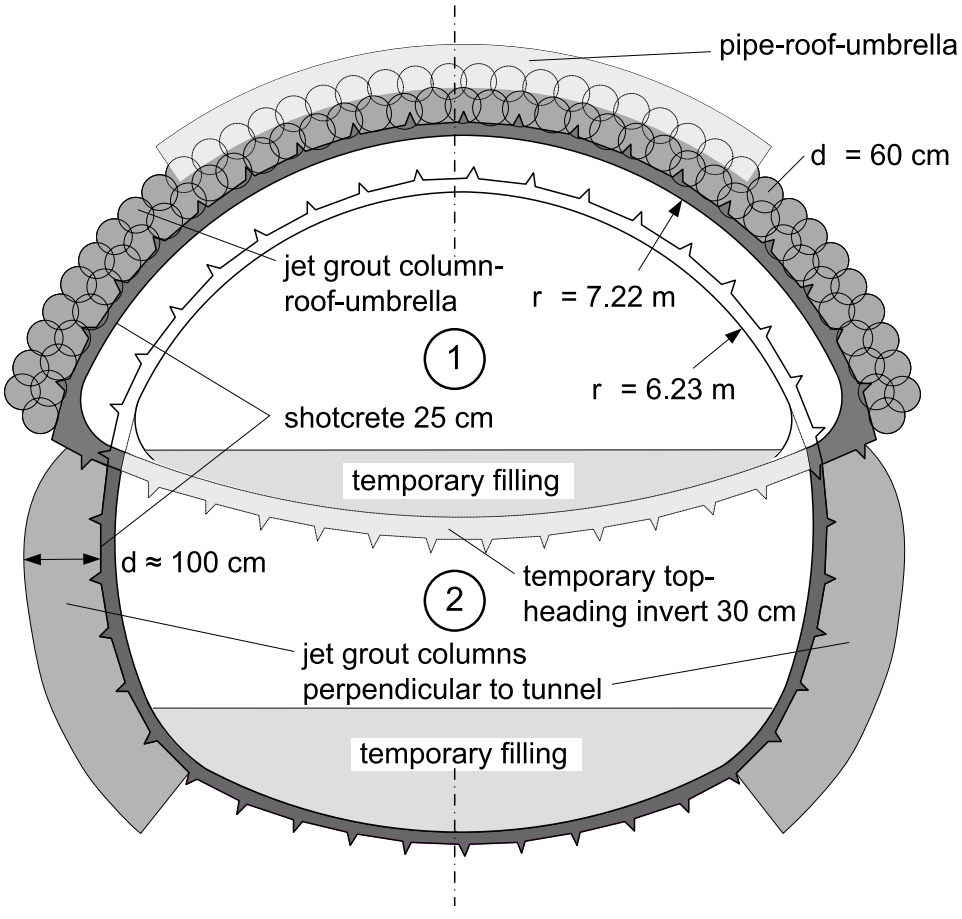

Figure 6.4: Support measures and driving sequence of tunnel.

The top-heading and the bench are both driven under the application of compressed air. In order to prevent excessive air escapes in longitudinal direction, a 1.5 m thick bulk head is installed by means of a series of low pressure pore space injections at the end of each roof-umbrella. The 15 m long roof-umbrellas are overlapping 3 m. Thus, the usable length of each section is reduced to 12 m. Figure 6.5 illustrates the construction process of the top-heading in sectional (a) and ground view (b).

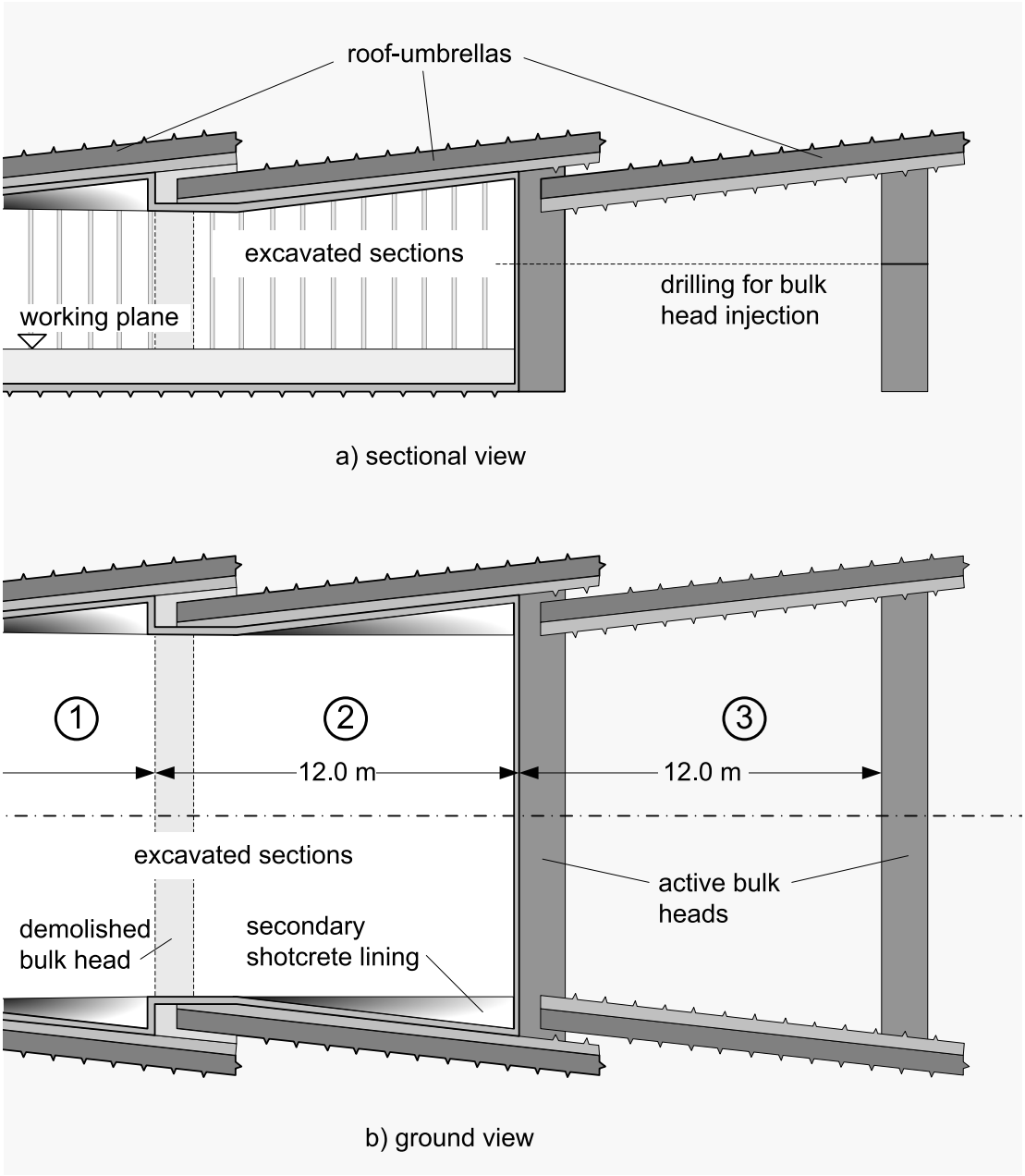

Figure 6.5: Sectional driving scheme of the top-heading.

After completion of the injection works for a new section, the excavation cycle of the top-heading starts with the demolition of the bulk head of the preliminary section. The excavation is carried out in 1.2 m round lengths. Lattice girders

and 25 cm shotcrete are installed as primary support of the tunnel lining. The temporary top-heading invert is installed in 2.0 to 6.0 m long sections. A 20 cm thick shotcrete layer is sprayed on the bulk head at the end of the 12 m long excavation sequence. After completion of the excavation and support measures, the injections works for the subsequent section are started. The described construction procedure is cyclically repeated in 12 m units, see Figure 6.5.

The applied excess air pressure during the injection works varies between 0.30 and 0.35 bar, depending on the present ground water level. For the excavation of the sections, the air pressure has to be increased intermittently to 0.42 – 0.48 bar. The injection works need 10 – 15 days on the average, whereas the excavation and support works are carried out in 5 – 7 days.

The lateral jet grout body of the bench is fabricated subsequently to the advance of the top-heading. After completion of the top-heading advance and the jet grouting works, the excavation of the bench and invert is started. In order to ensure a structural integrity of the support, the lattice girders of the top-heading are extended and 30 cm shotcrete is applied. The excess air pressure which is needed to counterbalance the water pressure varies between 1.0 and 1.3 bar. This excess pressure acts on the entire 430 m long lining of the top-heading from the beginning of the bench advance. Therefore, high air losses are to be expected throughout the advance period.

The concreting of the 50 cm thick inner shell is planned to begin approximately one month before the completion of the excavation works. The tender prescribes the installation of the inner shell under compressed air.

6.3.4 Measured air losses

During the advance of the tunnel, the air losses are continuously measured and recorded. For the objective investigations, the data of the air losses during the advance of the first 12 sections of the top-heading are available. Figure 6.6 shows the measured air losses (daily mean values) over time and the applied excess air pressures inside the tunnel.

The distribution of the air losses is characterized by peak values and pronounced valleys between them. The peak values appear during the actual excavation of the individual sections (referred to as S1 – S12 in Figure 6.6), whereas the the local minima typically appear during the standstill time for the injection works. Also, the influence of the magnitude of the excess pressure on the air losses is evident. Excess air pressures between 0.30 and 0.37 bar are applied during the standstill time, and for the excavation works values between 0.40 and 0.48 bar are applied.

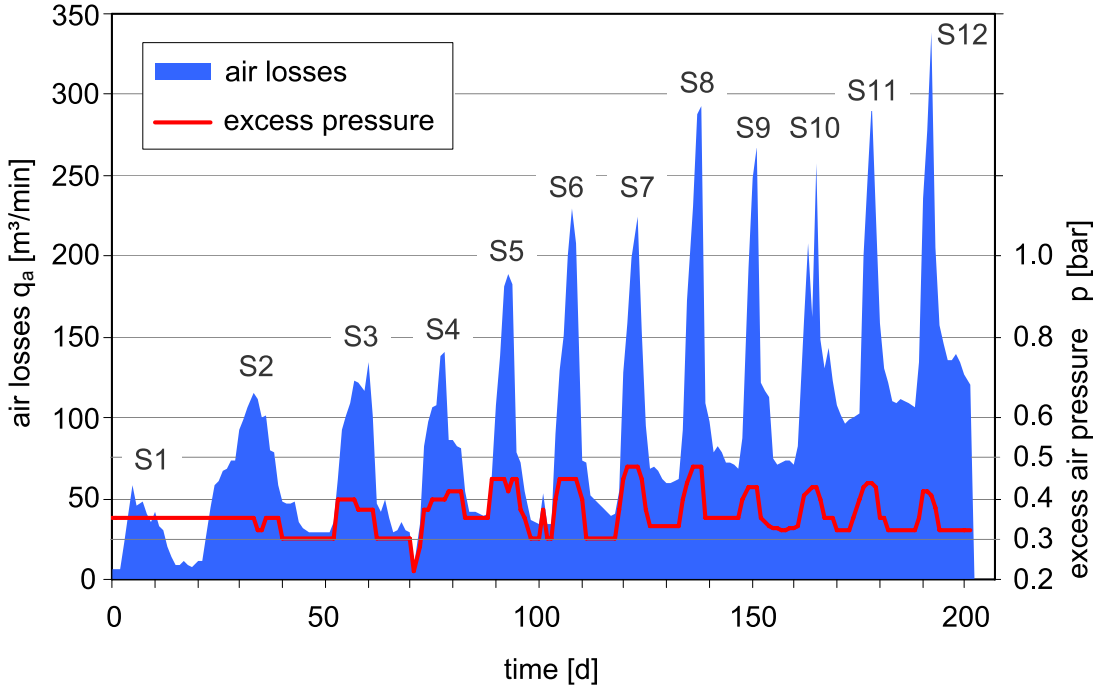

Figure 6.6: Air losses for the first 12 sections of the top-heading advance.

A rather inconsistent development of the air losses was obtained for the sections 1 – 4. Thus, they are not considered in the further analyses. During the advance of the sections 5 – 12, peak values between 183 and 339 m³/min were measured, whereas a reduction to flow rates between 39 and 107 m³/min was encountered during the standstill times,. More detailed overview on the measured air losses is given in the site reports of Putz (2008).

6.4 Computation method

The numerical simulation of air losses in compressed air tunnelling is a transient two-phase flow problem of water and air. The excess pressure inside the tunnel constitutes the driving potential for air flow through the unsupported tunnel face and through gaps and cracks of the shotcrete lining into the surrounding ground. The escaping air penetrates into the originally saturated soil and continuously increases the air saturation and thus the air conductivity of the soil. Accordingly, also the magnitude of the air losses increases with time. Whether or not a steady-state flow is reached during one round length depends on the soil type and the advance velocity of the tunnel.

The numerical investigations of the air losses are carried out with ASCATA (for: Automated Simulation of Compressed Air Tunnel Advance). ASCATA allows for an automated simulation of the tunnel advance and a concurrent evaluation of the air outflow off the tunnel. The program was developed by Steger (2004) and

is based on the numerical model presented by Scheid (2003). ASCATA makes use of the TOUGH2-EOS3 (Pruess et al. 1999) finite difference procedure in order to solve the governing equations for two-phase flow of water and air. The principle functioning of ASCATA is briefly described below. A detailed programme description can be found in Steger and Semprich (2006). Figure 6.7 illustrates the working principle of the programme.

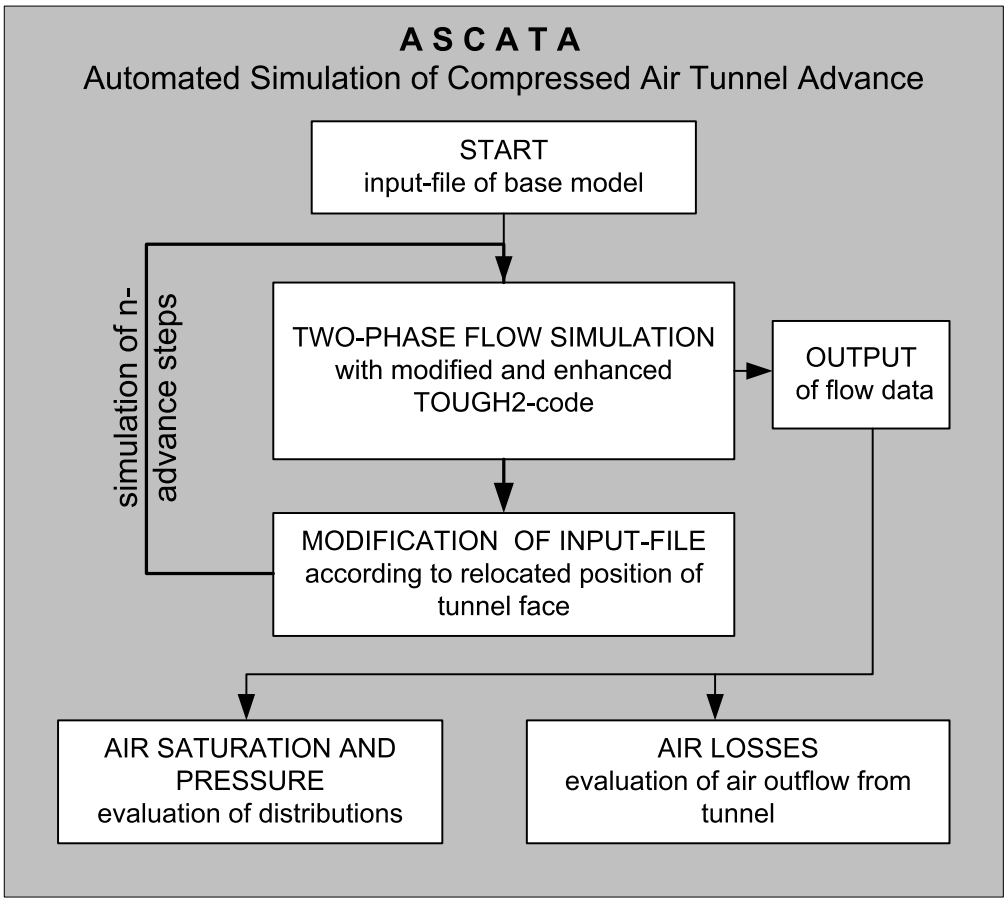

Figure 6.7: Working principle of the programme ASCATA.

After the initialization, ASCATA reads the input file of the numerical model of the tunnel advance. In this model, the ground conditions over the whole length of the tunnel have to be specified. The cross section of the tunnel has to be modelled in its starting positions only. ASCATA asks the user to specify the advance length of the tunnel and the corresponding advance velocity. If the tunnel axis is inclined, the gradient may be defined as sequence of straights.

In the next step, ASCATA identifies the position of the tunnel face and initializes the first flow simulation. The assigned simulation time corresponds to the advance rate of the tunnel. All connections between elements, which specify the boundary condition for “constant excess air pressure” inside the tunnel, and adjacent soil elements are identified in order to evaluate the air outflow.

After the completion of the flow simulation, a subroutine relocates the position of the tunnel face in advance direction. For this purpose, the soil elements behind the current tunnel face are replaced by elements with the boundary condition "constant excess air pressure". Additionally, a new layer of shotcrete elements is installed along the lining of the tunnel. Finally, a new input-file with the updated geometry and the updated initial and boundary conditions of the model is generated. The next numerical flow simulation is carried out, and so forth.

The described procedure is repeated until the specified tunnel length is reached. ASCATA then produces a number of output-files. If the focus is on air losses, the flow data of all identified tunnel-soil element connections are evaluated and written as time series into an EXCEL-file. For each time step, the air saturation and pressure distributions in the ground are stored in further output-files that may be used for further applications, e.g. flow-deformation computations.

6.5 Investigation of air losses through the tunnel lining

6.5.1 Analysis of the measured air losses

For the interpretation of the measured air losses, the diagram of Figure 6.6 in combination with the site records of Putz (2008) is used. Putz provides detailed information on the context between occurred air losses and different construction sequences.

In Figure 6.8, air loss rates q_a, which were measured directly before the excavation of a new section was started, are depicted. This time, the tunnel face respectively the bulk head of the excavated section is covered by a 20 cm thick shotcrete layer. The surface of the tunnel face is small in comparison to the surface of the lining. Thus, the depicted data points are characteristic for the air losses through the tunnel lining.

In order to enable a subsequent linear regression of the development of the air losses, the values are standardized linearly to the average excess air pressure of 0.32 bar. The actual pressures during the injections works vary between 0.30 and 0.35 bar. Although a linear relationship of the air losses at different applied excess pressures can usually not be supposed, the linear standardization is sufficiently accurate due to the low pressure variations.

The development of the air losses for the sections 1 – 4 is rather inconsistent, see Figure 6.8. It is supposed that the inconsistencies are related to a differing fabrication of the roof-umbrellas and bulk heads of the first sections. For example, parts of the injection works were carried out from the surface. For the

regression of the air losses through the tunnel lining, the measured values before the excavation of the sections 5 – 12 are employed.

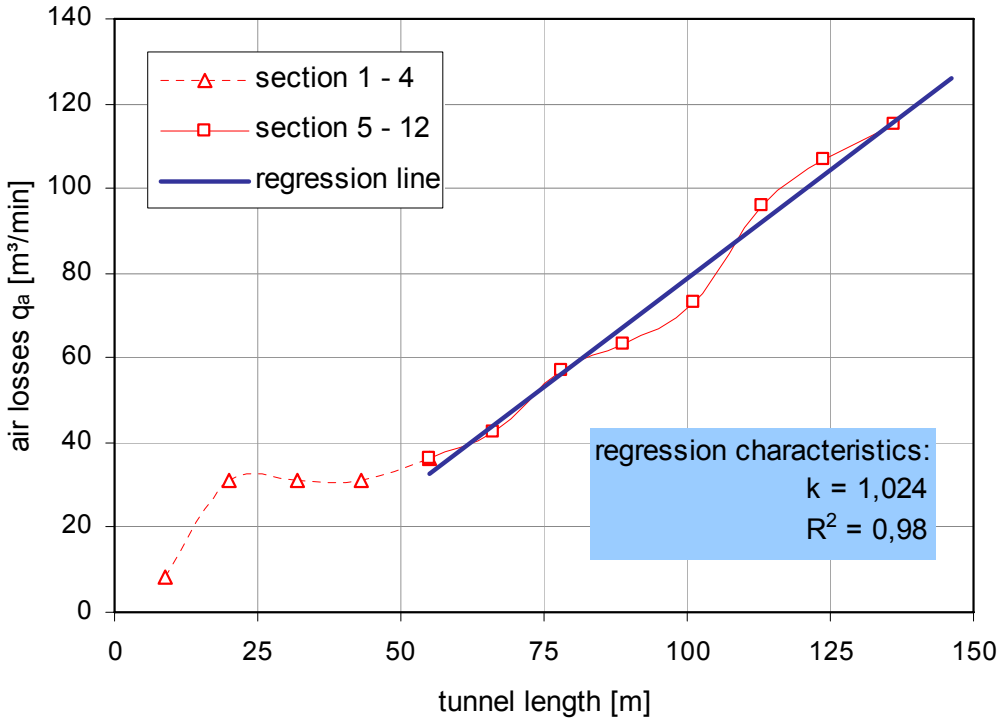

Figure 6.8: Calibration of air losses through the tunnel lining.

The linear regression yields a slope k of 1.024 and a coefficient of determination R^2 of 0.98; that means that at the reference pressure of 0.32 bar, air losses of 1.02 m³/min occur per meter tunnel length on the average. This value is the basis for the subsequent analysis of the air losses through the lining of the tunnel.

6.5.2 Numerical model and calibration procedure

A two-dimensional model is employed for the analysis of the permeability values of the soil, shotcrete, grout column-roof-umbrella and pipe-roof-umbrella. The geometry of the tunnel is modelled with an average radius of 6.72 m, according to the descriptions in section 6.3.2. The natural ground and the pebbly fillings on the surface have similar properties. For the numerical simulations, no difference is made between these two materials.

The model dimensions are 11 m and 13 m in horizontal and vertical direction, respectively. A rectangular grid with 26 element rows in vertical and 43 rows in horizontal direction is used. Taking advantage of the symmetry, only half of the cross section is modelled. According to the actual construction of the tunnel, the secondary shotcrete lining in the angular interspaces of the roof-pipes is not considered for the calibration procedure. The jet grout-column- and pipe-roof-

umbrella are modelled with average thicknesses of 90 and 120 cm, respectively. The cross section of the model is depicted in Figure 6.9.

The modelling of the shotcrete lining as single grid blocks requires the adoption of a harmonic weighting scheme for the intrinsic permeabilities. Similar arguments apply to the modelling of the roof-umbrellas. Following the recommendations of Pruess et al. (1999), the mobilities respectively relative permeabilities are upstream-weighted. The simulations are carried out isothermally at a ground temperature of 10° Celsius.

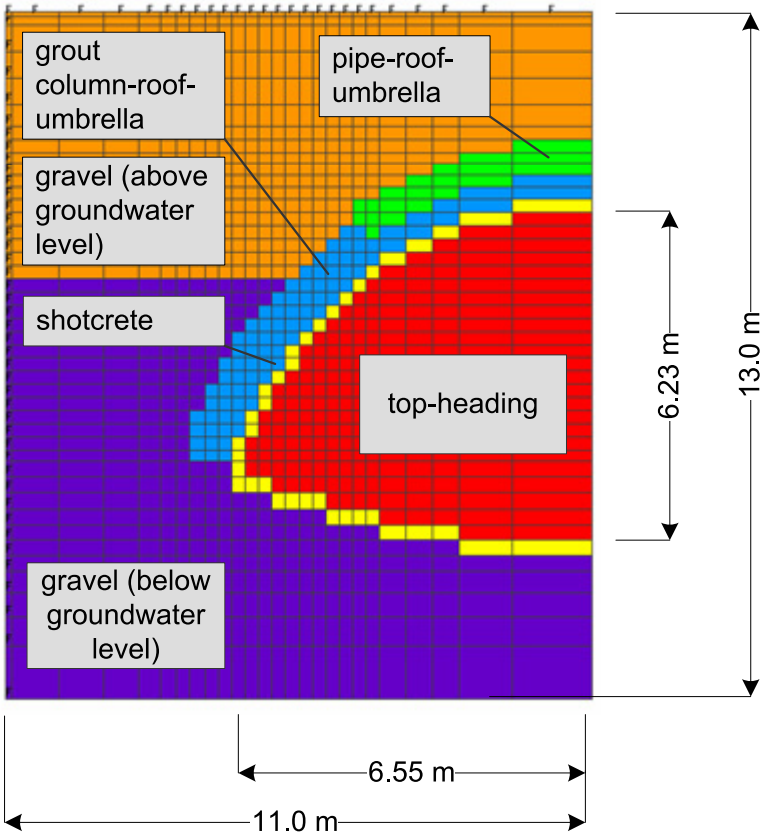

Figure 6.9: Two-dimensional numerical model of top-heading cross section.

For the analysis of the material properties, the permeabilities are perturbed manually. Due to the large heterogeneity and variations of the construction process, a model calibration by systematic inverse modelling cannot be applied advantageously to the considered case study. Instead, assumptions and a procedure based on engineering judgement are required. In the following the calibration process and its results are described.

The water permeability k_w of the ground is fixed in a first step at an average value of $1.0 \cdot 10^{-3}$ m/s. The influence of the ground permeability is investigated subsequently to the model calibration. The Mualem-model (1976) is employed to describe the relative permeability. Due to the high intrinsic permeability, a

steady-state is reached rapidly and the Mualem-parameters are only of secondary importance. An *m*-value of 0.67 and a tortuosity τ of 0.5 are adopted. Matric suction in sandy gravels is negligibly small and therefore not modelled.

The intrinsic permeability of the pipe-roof-umbrella is related to the soil permeability. It is assumed that a reduction by a factor of 100 is achieved by the injections. The relative permeability of water and air is modelled with linear functions. Zero residual saturation is assigned for both phases, thus the relative permeabilities are identical to the corresponding phase saturations ($S_i = k_i$).

The intrinsic permeability of the shotcrete and the jet grout column-roof-umbrella is varied respectively calibrated against the derived increase of the air losses by 1.02 m³/min per meter of tunnel length. The horizontal, fan-shaped direction of the single jet grout columns favours gaps and imperfections of the roof-umbrella. It is therefore assumed that the permeability of this material is significantly higher than the permeability of the shotcrete. The ratio of the permeabilities is varied between 1 : 5 and 1 : 10. The relative permeabilities of water and air are described by linear functions for this material, too.

Table 6.1 shows the determined permeability values. For a better overview, both, the saturated air and water permeability are given in addition to the calibrated intrinsic permeabilities. The air permeability is computed for use in combination with a driving potential expressed in terms of water pressure head. This is a common practice for empirical air loss predictions (e.g. Kramer and Semprich 1989) and is maintained here.

Table 6.1: Back-calculated permeability values.

material	**intrinsic permeability**	**water permeability**	**air permeability**
-	K_i [m²]	k_w [m/s]	k_a [m/s]
shotcrete	$1.60 \cdot 10^{-13}$	$1.15 \cdot 10^{-6}$	$8.10 \cdot 10^{-5}$
grout column-roof-umbrella	$1.60 \cdot 10^{-12}$	$1.15 \cdot 10^{-5}$	$8.10 \cdot 10^{-4}$
soil (sandy gravel)	$> 1.39 \cdot 10^{-11}$	$> 1.15 \cdot 10^{-6}$	$> 8.10 \cdot 10^{-5}$

The determined intrinsic permeability K_i of $1.60 \cdot 10^{-13}$ m² of the shotcrete is relatively high. Steger and Semprich (2005) derived a value of $5.0 \cdot 10^{-14}$ m² based on back-analyses of other projects, and Scheid (2003) suggests a value of

$7.0 \cdot 10^{-14}$ m². Reasons for the elevated permeability may be a want of care during the spraying of the shotcrete or a thinner sprayed layer than designed.

Subsequently to the back-calculation of the other permeability values, the influence of the soil permeability is investigated. According to the geotechnical report, the water permeability may vary between $1 \cdot 10^{-2}$ m/s to $1 \cdot 10^{-4}$ m/s. Even if the lower given value is employed in the simulations, the magnitude of the computed air losses remains equal. It follows that a two-dimensional consideration does not allow any conclusions on the ground permeability, except that it is larger than $1 \cdot 10^{-4}$ m/s. On the other hand, the large permeability of the soil ensures a high reliability of the back-calculated permeability values of the shotcrete and the jet grout column-roof-umbrella.

6.5.3 Computations with different excess air pressures

For a better interpretation and understanding of the measured air losses, computations with the calibrated model at different simulated excess air pressures, ranging from 0.30 to 0.55 bar, are carried out. The obtained results in particular are meant to allow for a differentiation of the air losses occurring through the shotcrete lining from the total air losses.

The computations are conducted with the standard numerical model and an extended model, where additionally the secondary shotcrete lining in the angular interspaces (see Figure 6.5) of the roof-umbrellas is considered. An average thickness of 50 cm of the secondary lining is modelled. In a first assumption, the back-analyzed permeability value for shotcrete is assigned to the secondary shotcrete lining. For a further simulation series, the (lower) permeability value derived by Steger and Semprich (2005) is employed. This assumption is based on the fact that the construction environment for the spraying of the secondary shotcrete layer is more favourable than for the primary layer.

Figure 6.10 shows the results of the three simulation series. It can be seen that the secondary shotcrete has a significant influence on the magnitude of the air losses. A reduction of the air losses up to 40 % respectively 20 % is obtained. For all variants, a linear increase of the air losses up to an excess pressure of 0.40 bar can be recognized. However, an elevation of the air pressure by 1% yields an increase of the air loss rate by 1.6 %. These computation results are supported by similar observations of disproportional increases of the air losses by Putz (2008).

At excess air pressures of 0.40 bar and higher, the development of the air losses becomes disproportionately high. This is of importance for the excavation works of the top-heading sections, where excess pressures of 0.42 - 0.48 bar are applied.

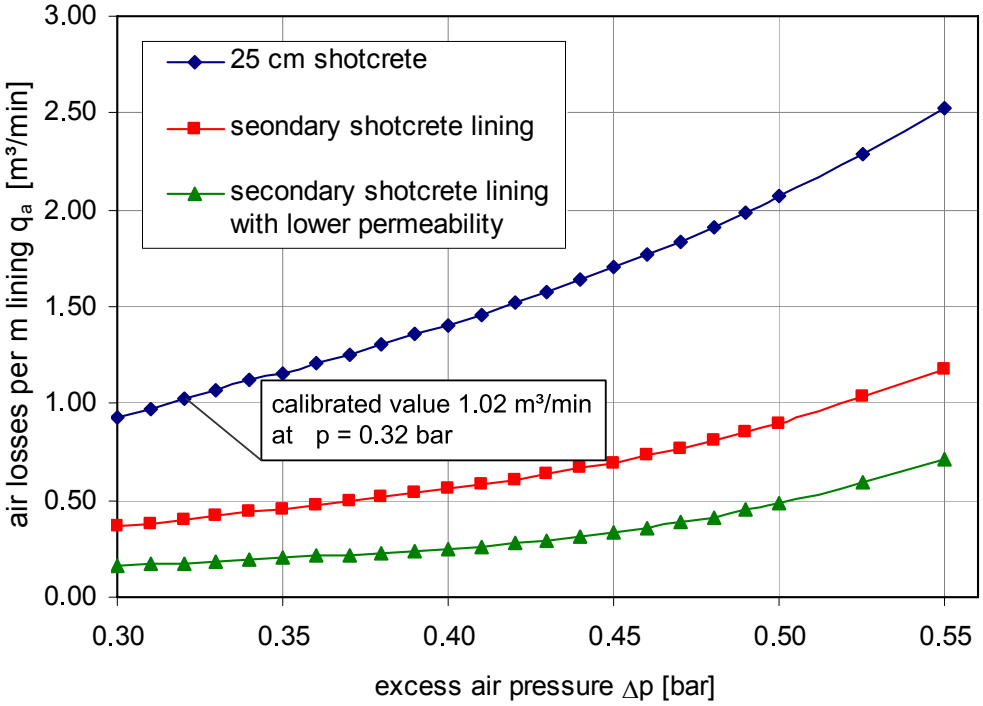

Figure 6.10: Air losses at different excess air pressures and lining variants.

6.5.4 Identification of air losses through the lining

The measured air losses during the execution of the injection works are relatively low in comparison to the air losses during the excavation works of a new top-heading section. On site, this circumstance yielded the conclusion that the magnitude of the air losses is almost exclusively governed by the escaping air in the immediate area of the tunnel face of a new section (Putz 2008). However, in the previous section it is shown that at excess pressures which are required for the excavation works, disproportionally high air losses take place through the tunnel lining.

Considering the applied excess pressures during the top-heading advance, the correct air losses through the tunnel lining can be computed. In Figure 6.11, the dashed line indicates the theoretical air losses for a constant excess air pressure of 0.32 bar for the tunnel advance from 50 – 150 m. The blue full line gives the air losses that were computed based on the actually applied air pressures and the simulation results of the previous section. The area between the two lines is representative for the air losses through the lining which are due to elevated excess air pressures up to 0.48 bar, which are necessary for the excavation and support works of a new tunnel section. This consideration clearly indicates that large parts of the peak values of the total air losses are in reality due to strongly increased air flow through the tunnel lining.

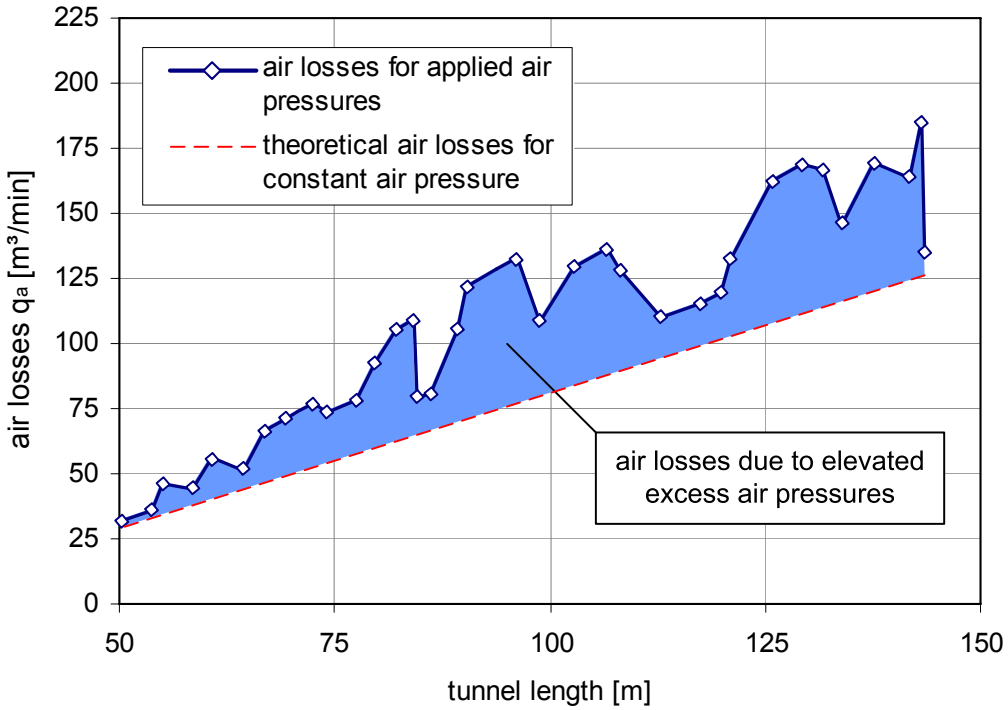

Figure 6.11: Corrected air losses through the tunnel lining.

Similar results as presented in Figure 6.11 are also obtained when the secondary shotcrete lining is modelled. The computation results show the strong influence of the shotcrete lining on the magnitude of the total air losses. If it is further taken into account that the time effort for the execution of the injection works is 2 – 3 times higher than for the excavation of the sections, the importance of a high quality (i.e. low permeability) of the tunnel lining is emphasized once again.

6.6 Investigation of air losses through the tunnel face

6.6.1 Analysis of the measured air losses

For the subsequent investigation of the air losses in the immediate excavation area of a new section, a three-dimensional numerical model is employed. In order to enable a calibration of the model, the air losses taking place through the tunnel face have to be isolated from the total air losses shown in Figure 6.6. To allow for a better interpretation, the site records of Putz (2008) are additionally used.

The air losses for the sections 1 – 4 are inconsistent. Therefore, only the sections 5 – 12 are considered. In order to obtain the air losses through the tunnel face, the corrected air losses through the lining (see 6.5.4) are subtracted from the total air losses. Additionally, an air amount of 7 m³/min is subtracted in order to account for the passing of personnel and material through the air locks. The so computed

air losses are depicted in Figure 6.12. The dashed graph indicates the air losses at the actually applied pressures (0.42 – 0.48 bar) and the full graph shows the standardized values for a reference pressure of 0.45 bar.

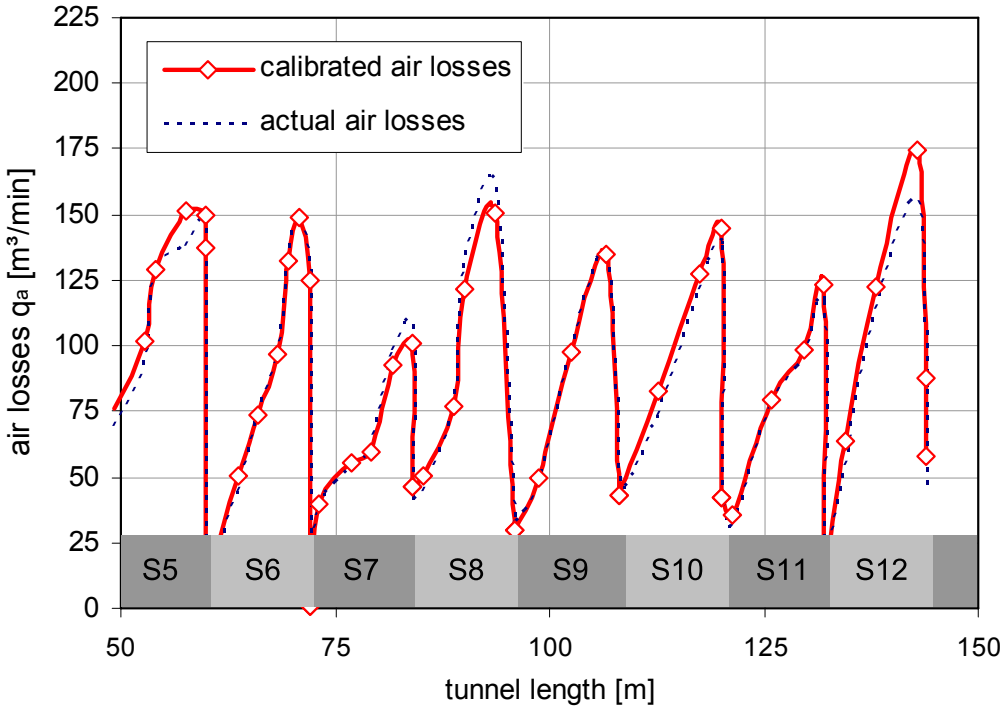

Figure 6.12: Corrected air losses through tunnel face for section 5 - 12.

Figure 6.12 gives a good overview of the real air losses through the tunnel face. On the average, the maximum air losses reach a magnitude of approximately 145 m³/min. Strong deviations are encountered for the sections 7 and 12, where the corrected air losses are 100 and 175 m³/min, respectively. Consequently, they are not considered for the mean computation of the mean values. Further, it is notable that the peak values appear towards the end of the sections.

Putz (2008) assumes that the ring closure distance, i.e. the distance between the tunnel face and the installed temporary top-heading invert, has a governing influence on the air losses. However, the corrected air losses for the sections 5 – 12 do not support this assumption. For example, at section 8 the invert was installed in 5 units (average distance 2.4 m) whereas at various other sections the invert was installed in 2 units only (average distance 6.0 m). Notwithstanding, the corrected air losses for section 5 are the second largest of all sections.

Moreover, no predominant influence of the magnitude of the applied excess air pressure can be recognized. The largest air losses occurred at section 12, where the applied excess air pressure of 0.42 bar was the lowest of all sections. These considerations yield the conclusion that the peak values of the air losses are decisively influenced by variations of the achieved quality of the roof-umbrellas and the bulk heads of the different sections.

6.6.2 Numerical model and calibration procedure

A three-dimensional numerical model with 23.000 elements is employed for the investigations. The excavation of one section is simulated. The cross section is identical with the two-dimensional model (Figure 6.8). In a simplified manner, the roof-umbrellas are modelled with a fixed radius. According to site reports, the excavation is simulated in 1.2 m round lengths and the ring closure distance is modelled with 3.6 m. The excavation takes 5 days on the average. Thus, the advance velocity is simulated with 2.4 m/d. The applied excess air pressure inside the tunnel is 0.45 bar. The simulation of the tunnel advance is carried out with ASCATA (Steger and Semprich 2005, 2006). The longitudinal section of the numerical model after six round lengths is depicted in Figure 6.13.

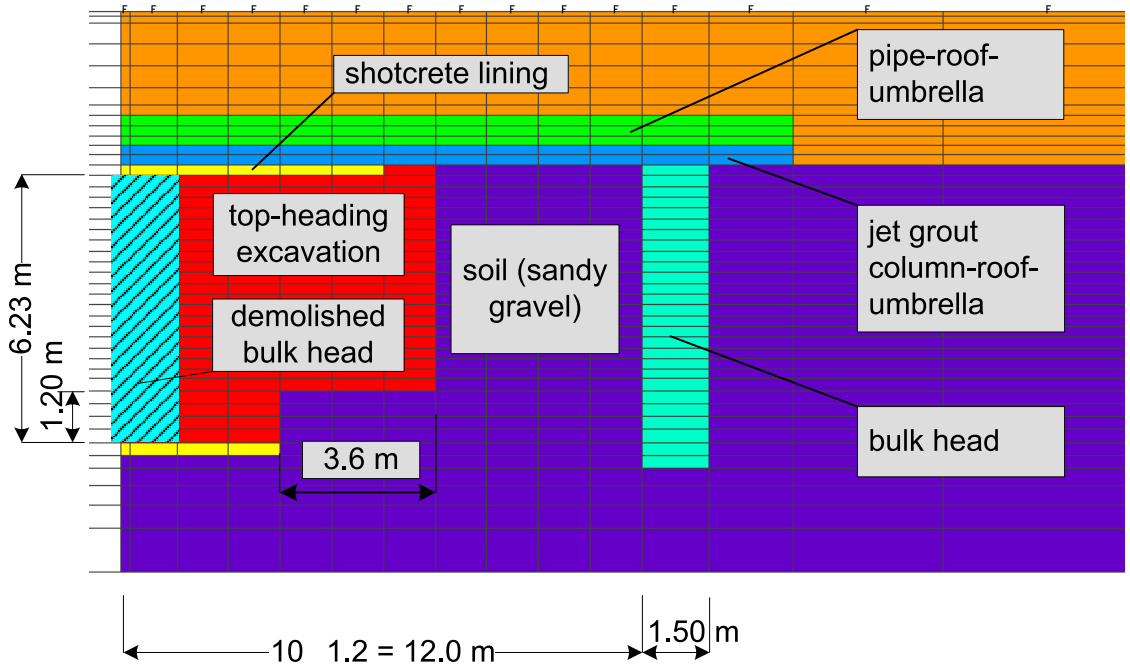

Figure 6.13: Longitudinal section of the numerical model.

The simulation of the tunnel advance starts with the demolition of the bulk head at the beginning of the section. Subsequently, the single round lengths are simulated by the sequential replacement of soil grid blocks behind the tunnel face by boundary conditions, which simulate the excess air pressure in the tunnel. Shotcrete elements are installed along the perimeter of the tunnel. After the tenth round length, the simulated excavation is completed with the application of a 20 cm thick shotcrete layer on the bulk head at the end of the section. Thereafter, the ring closure is simulated by simultaneous installation of three rows of shotcrete elements at the invert of the top-heading. The final state of the model corresponds to the on-site conditions during the downtime of the tunnel advance for execution of the injection works for the next section.

The calibration of the numerical model follows the same procedure as outlined in section 6.5. In principle, solely the determination of the soil permeability is required. The permeability of the shotcrete lining and of the jet grout column-roof-umbrella have been determined with high reliability in section 6.5, and the permeability of the pipe-roof-umbrella and the bulk head are directly linked to the soil by a factor of 100.

Pumping tests in the immediate environment of the tunnel alignments yielded ground permeabilities between 0.4 $\cdot 10^{-3}$ m/s and 4.0 $\cdot 10^{-3}$ m/s. This range is largely covered by five conducted advance simulations. The results are presented in Figure 6.14. The jumps of the graphs each time after 0.5 days are due to the discrete simulation of the tunnel advance in 1.2 m round lengths.

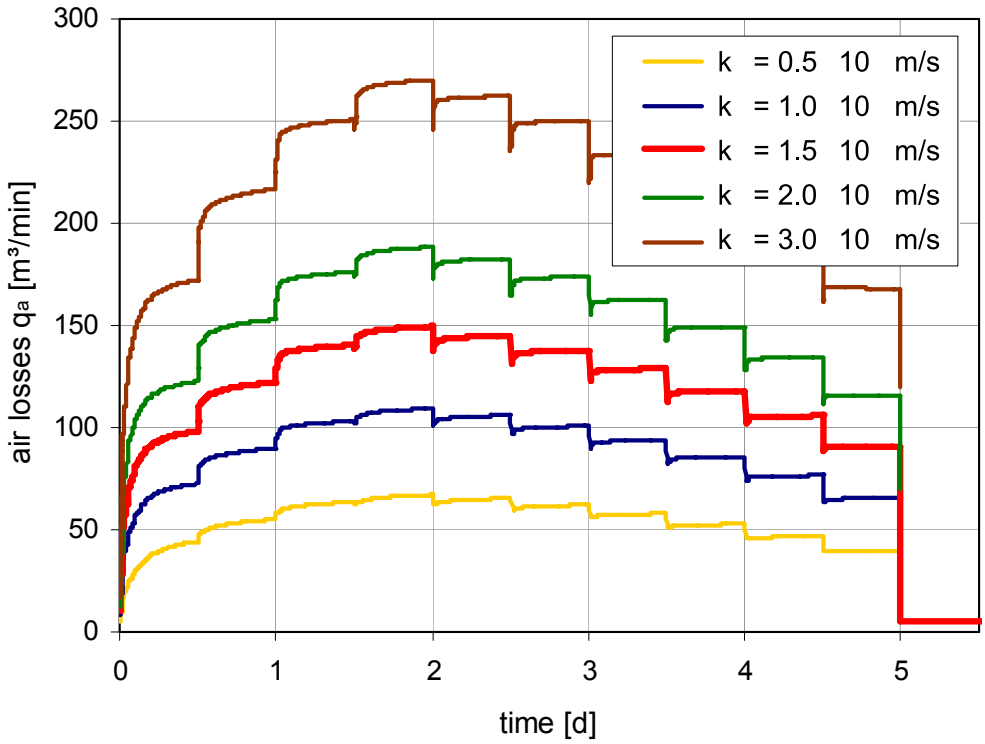

Figure 6.14: Air losses at different simulated soil permeability values.

The peak values for all five simulations appear after 2 days respectively an advance length of approximately 5 m. This is a characteristic difference to the corrected measurements of the air losses, where the peak values appear at the end of the sections. The most probable reason is the partial demolition of the bulk head, which is installed by low pressure pore injections in the course of the excavation works. Putz (2008) remarks that the bulk heads extended in several cases various meters into the excavation area.

For the conducted simulations, the maximum and minimum peak values of the air losses are 73 and 275 m³/min, respectively. The water permeability k_{ws} of 1.5 $\cdot 10^{-3}$ m/s corresponds best to the corrected average air loss of 145 m³/min

through the tunnel face. This value is therefore assumed to be representative for the ground permeability and is employed for the further investigations. Table 6.2 shows the derived permeability values for soil, pipe-roof-umbrella and bulk head.

Table 6.2: Back-calculated permeability values.

material	**intrinsic permeability**	**water permeability**	**air permeability**
-	K_i [m²]	k_w [m/s]	k_a [m/s]
soil (sandy gravel)	$2.09 \cdot 10^{-10}$	$1.50 \cdot 10^{-3}$	$1.05 \cdot 10^{-1}$
pipe-roof-umbrella and bulk head	$2.09 \cdot 10^{-12}$	$1.50 \cdot 10^{-5}$	$1.05 \cdot 10^{-3}$

6.6.3 Bottom extension of grout column-roof-umbrella

The deepest level of the temporary top-heading invert is situated 2.0 m below the bottom edge of the jet grout column-roof-umbrella. In order to prevent water inflow, the excess air pressure has to be adjusted to this excavation level. Consequently, it is to be expected that parts of the air losses through the tunnel face are due to the incomplete encapsulation of the excavation area with the roof-umbrella. Figure 6.15 illustrates the described problem (right side) and a possible extension of the roof-umbrella (left side).

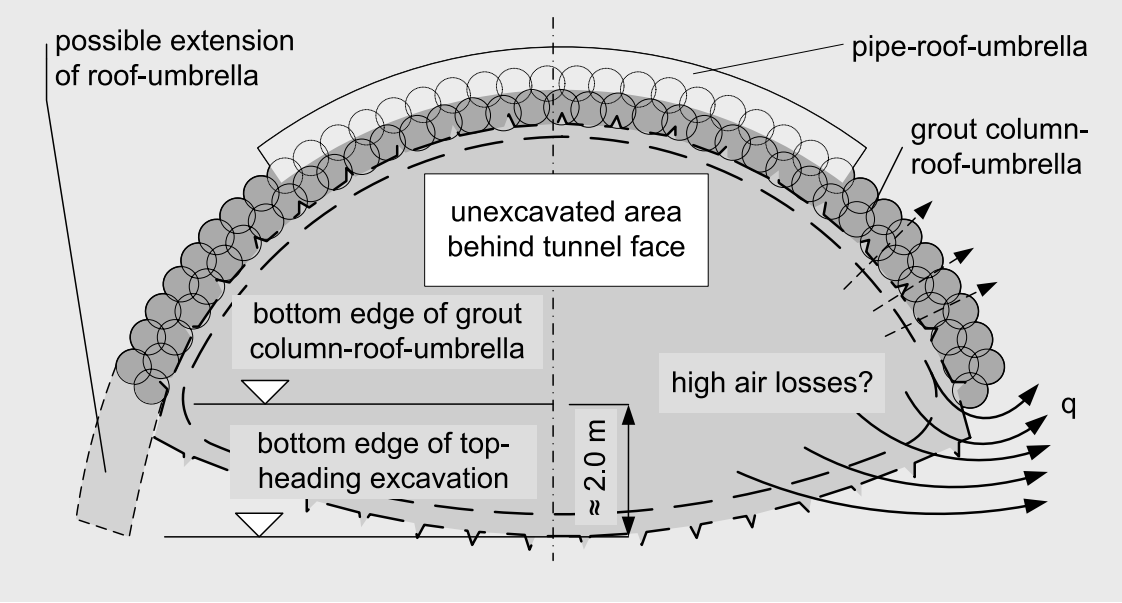

Figure 6.15: Air outflow below the bottom edge of the roof-umbrella.

For the calibrated model with $k_w = 1.50 \cdot 10^{-3}$ m/s, the computed peak air losses are 149.5 m³/min. A detailed evaluation of the flow data of the single elements yields that 95.1 m³/min are due to the air outflow below the bottom edge of the jet grout column-roof-umbrella. That means that only a portion of 36.4 % escapes directly through the roof-umbrella.

Further simulations are carried out in order to investigate the use of an extended roof umbrella (see Figure 6.15) to reduce the air losses. For two simulations, the bottom edges are modelled 30, 60 and 90 cm lower than the design prescribes. A further simulation is carried out, in which the roof-umbrella extends 200 cm to the bottom level of the top-heading invert. This simulation is mainly of theoretical interest, because the extension to this level would require a disproportionally high jet grouting effort.

The results of the investigations are summarized in Table 6.3. Additionally to the peak air losses, the amount of air losses due to the outflow below the roof-umbrella is given. Further, the achievable reductions of the air losses for the simulated extensions of the jet grout column-roof-umbrella are given.

Table 6.3: Air losses for extended jet grout column-roof-umbrellas.

extension of roof-umbrella	**peak air losses**	**outflow below roof-umbrella**	**reduction (of peak air losses)**
[cm]	[m³/min]	[m³/min]	[%]
0 cm	149.5	95.1	-
30 cm	116.4	59.0	22.1
60 cm	94.9	34.6	36.5
90 cm	80.3	16.9	46.3
200 cm	74.2	0.0	50.4

It can be seen that a deeper bottom edge of the jet grout column-roof-umbrella yields significant reductions of the air losses. For extensions of 30 and 60 cm, the peak air losses are 22.1 and 36.5 % lower, respectively. However, for larger extensions, the measure loses on effectiveness and the additional jet grouting effort may no longer be economic. Theoretically, a decrease of 50 % of the peak air losses can be achieved with an extension of the jet grout column-roof-umbrella to the level of the top-heading invert.

6.6.4 Two-staged top-heading excavation

A further possibility to reduce the air losses is the conduction of the top-heading excavation in a two-staged manner. The first step consists in the complete excavation of a new section to a level not lower than the bottom edge of the grout column-roof-umbrella. During this phase, the excess air pressure of 0.32 bar, which is applied during the downtime for execution of the injection works, does not have to be increased. In the second step, the excavation and installation of the temporary top-heading invert is carried out at an elevated air pressure of 0.45 bar.

Two advantages are gained by the outlined excavation sequence. Firstly, the period in which the tunnel face and the shotcrete lining are exposed to the elevated excess air pressure, is reduced. Accordingly, the disproportionally high air losses through the shotcrete lining at air pressures of 0.40 bar and higher are reduced as well. Secondly, when the air pressure is increased to 0.45 bar, the lining and the bulk head of the new section are already protected by shotcrete. On the other hand, however, high air losses may occur after the pressure increase due to the large ring closure distance of initially 12 m.

Figure 6.16 shows the result of a simulated two-staged top-heading excavation according to the described manner. The excavation and support of the upper part of the top-heading is simulated in three days, and the subsequent excavation and installation of the temporary invert in two sections in two more days. For a comparison, the air losses of the reference simulation are depicted as well.

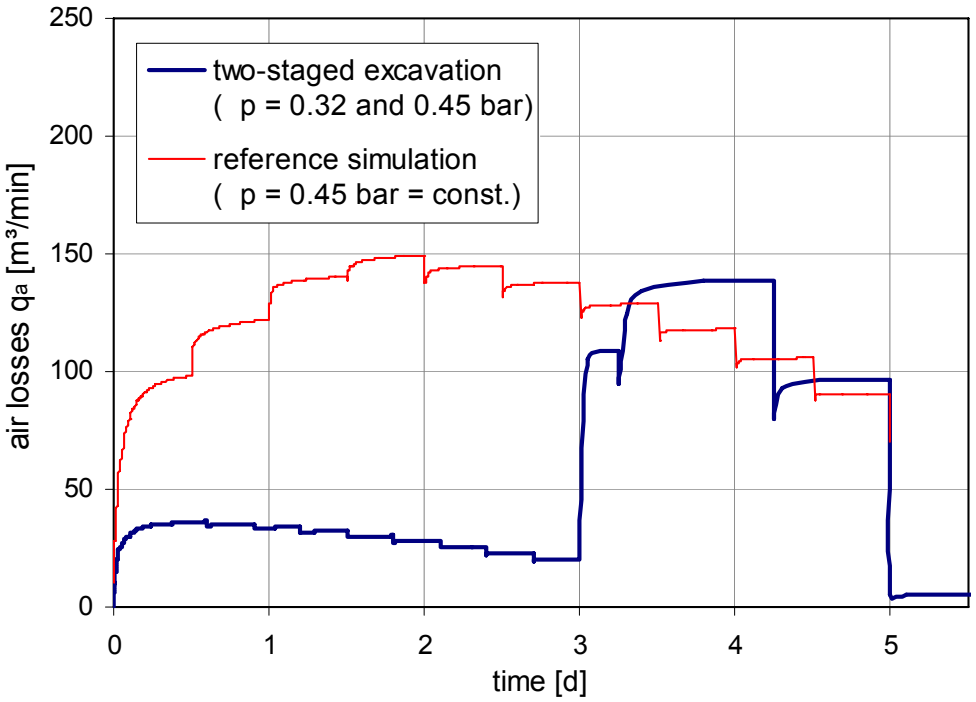

Figure 6.16: Air losses for a two-staged top-heading excavation.

Figure 6.16 indicates strongly reduced air losses during the excavation of the upper part of the top-heading. For this construction step, the computed peak value of 36.2 m³/min is four times lower than the corresponding value of the reference simulation. This reduction is largely due to the avoided air losses below the bottom edge of the grout column-roof-umbrella. The pressure elevation to 0.45 bar leads to an increase of the air losses to 115 m³/min. A further increase is obtained for the excavation of the first section of the invert. The peak value of 140.4 m³/min is only insignificantly smaller than the corresponding value of the reference simulation (149.5 m³/min). After the complete installation of the temporary top-heading invert, the remaining air losses losses of 4.0 m³/min are equal for both simulations.

The possible excavation of the top-heading in a two-staged sequence certainly depends on the structural requirements of the tunnel construction. On the other hand, it is particularly cost-effective because it allows a large economization of the air losses at no additional costs for construction measures.

6.7 Characteristic air loss predictions

6.7.1 General concept

The conducted analyses and numerical investigations allow for a deeper understanding of the encountered air losses at the Tunnel Fritzens. Further, the simulated alternatives indicate a high economization potential of the air losses respectively the total air need. In order to enable a quantitative comparison between the currently carried out excavation method and the considered alternatives, characteristic air loss predictions are elaborated in this section.

For the air loss predictions, it is assumed that the advance length of the tunnel is already 100 m. In this case, the idealized, back-calculated air losses are 102 m³/min. From this starting point, the injection works, excavation and support of three further tunnel sections are simulated. The assumed time effort for the injection works is 10 days, and for the excavation and support measures 5 days. The assigned excess air pressures are 0.32 and 0.45 bar, respectively. The simulated advance velocity for the excavation works is 2.4 m/d. These boundary conditions are average values derived from site reports of Putz (2008).

For all numerical simulations, the back-analyzed permeability values of the previous sections are employed. However, the permeability of the secondary shotcrete layer is simulated with the permeability value suggested by Steger and Semprich (2005). The elaborated air loss predictions for a better impression of the total air need are presented over time.

6.7.2 Default advance scheme

The conducted numerical simulation corresponds to the currently practiced tunnel advance scheme. The characteristic air loss prediction is shown in Figure 6.17. The total air losses and the air losses through the tunnel lining are depicted separately.

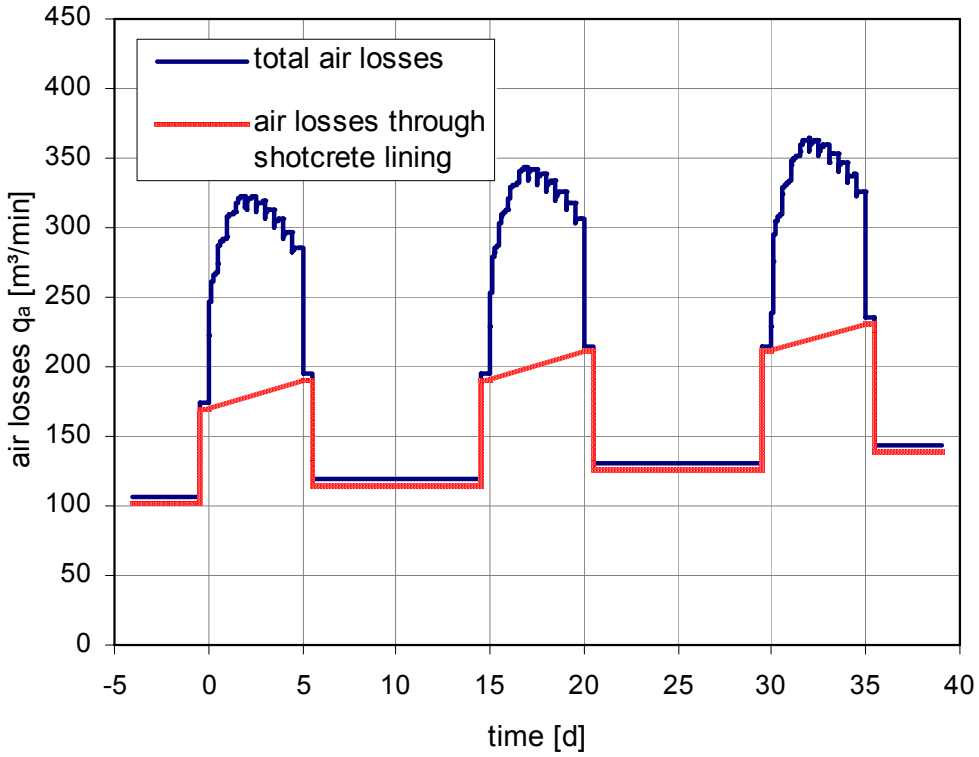

Figure 6.17: Air loss prediction for the design tunnel advance scheme.

The pressure elevation from 0.32 to 0.45 bar yields an increase of the air losses through the shotcrete lining from 102 m³/min to 170 m³/min (day -0.5). The demolition of the bulk head and the tunnel excavation yield a peak value of 330 m³/min (day 2.0). In the course of the excavation of the 12 m long sections, the air losses through the tunnel lining increase by 20.4 m³/min. After completion of the excavation and the application of a shotcrete layer to the tunnel face, the air losses decrease to 190 m³/min (day 5.0). The subsequent reduction of the excess pressure from 0.45 to 0.32 bar yields a further drop to 114 m³/min (day 5.5). The net increase of the air losses is 12 m³/min and corresponds to the 12 m of gained tunnel length with air losses of 1.02 m³/min per meter of lining.

A similar picture is obtained for the injection and excavation of the further two sections. During the downtime of the tunnel advance, a difference of 4 m³/min between the total air losses and the air losses through the tunnel lining can be recognized. These are the remaining air escapes through the tunnel face after the application of a shotcrete layer on the bulk head.

6.7.3 Alternative advance schemes

Characteristic air loss predictions are evaluated for selected alternative tunnel advance schemes. In Figure 6.18, the computed total air losses for an extended jet grout column-roof-umbrella (60 cm) and for a secondary shotcrete layer in the angular interspaces of two subsequent sections are depicted, respectively. For comparison, the graph for the design tunnel advance is shown as well.

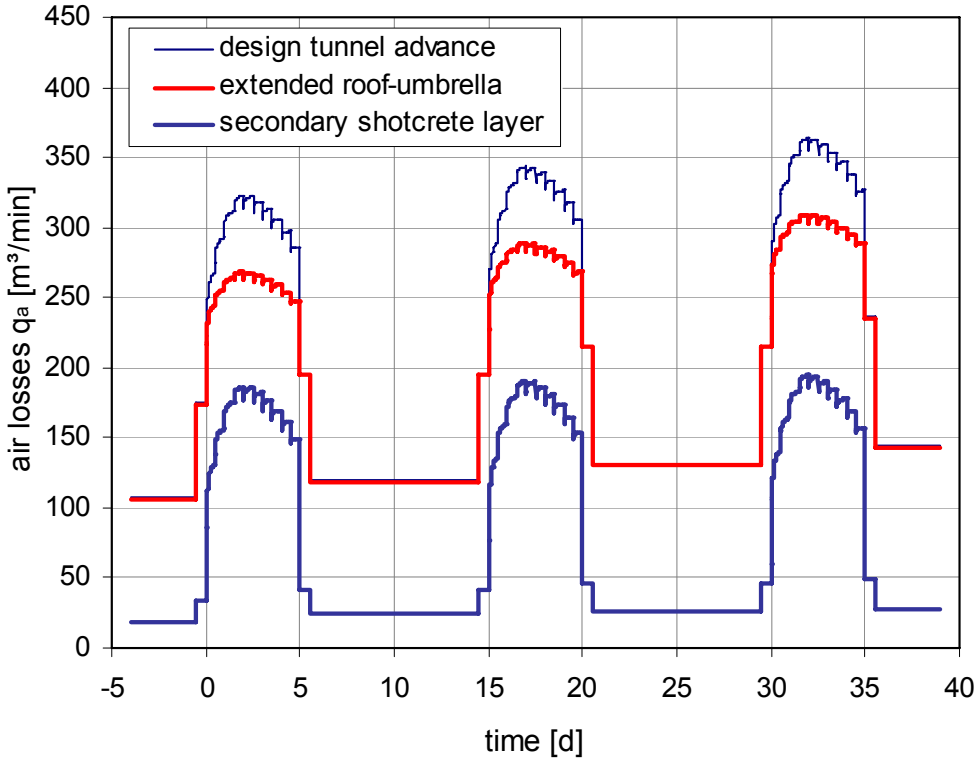

Figure 6.18: Prediction of the air losses for an extended roof-umbrella and a secondary shotcrete layer.

The extended roof-column umbrella reduces the peak value of the air losses by approximately 52 m³/min during the excavation phase, but it has only an insignificant influence on the air losses through the shotcrete lining. During the downtime for the injection works, the air losses are virtually equal with the design tunnel advance.

A different picture is obtained for the simulation with the secondary shotcrete layer. The air losses through the tunnel lining are strongly decreased both during the downtime and the advance sequence. The same total increase of air losses as for the design tunnel advance occurs during the excavation of the sections. However, the obtained peak values of the total air losses are 135 m³/min lower.

Two further alternative tunnel advance schemes are investigated. The first one considers a two-staged excavation of the tunnel section, as described in

section 6.6. For the second one, a combination of measures is simulated. Additionally to the two-staged excavation, an extended jet grout column-roof-umbrella (60 cm) and an installed secondary shotcrete layer are taken into account. The obtained air loss predictions are shown in Figure 6.19.

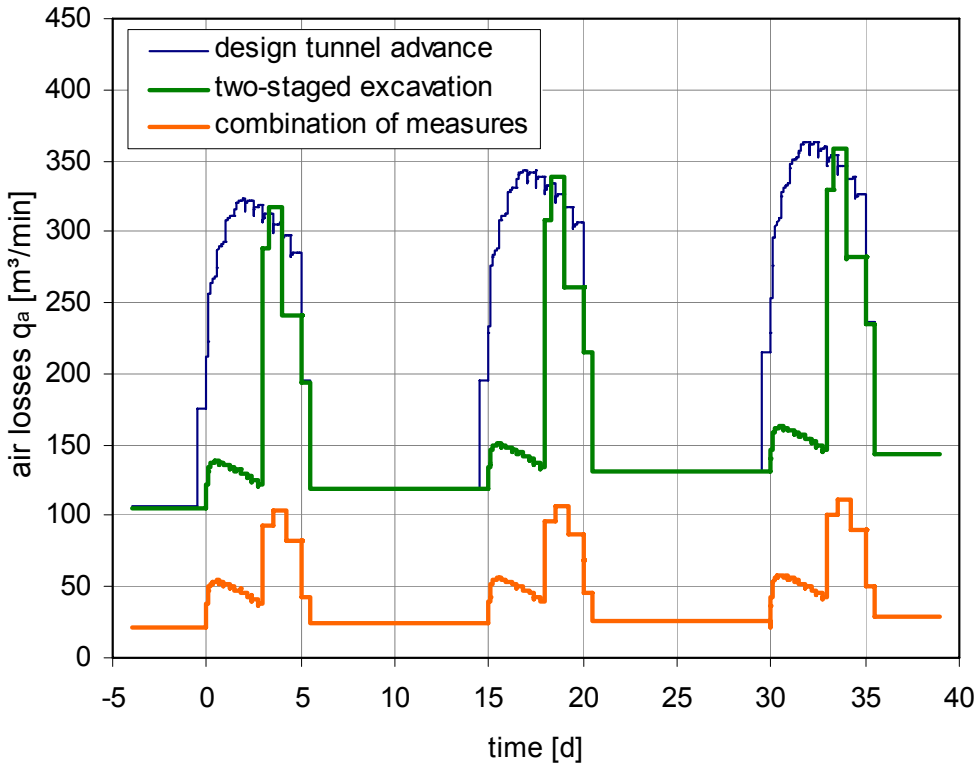

Figure 6.19: Prediction of air losses for two-staged tunnel excavation and combination of alternative measures.

The two-staged tunnel excavation yields significantly lower air losses during the first phase of the tunnel advance. Because the excess air pressure does not need to be increased for the excavation of the upper part of the top-heading, both, the air losses through the tunnel face and lining are strongly reduced. However, the subsequent elevation of the excess pressure for the installation of the temporary top-heading invert increases the air losses to almost the same magnitude as for the design tunnel advance scheme. For the combination of the two-staged excavation scheme with the extended roof-umbrella and the secondary shotcrete lining, strongly reduced air losses are obtained throughout the construction time.

6.7.4 Comparison of the total amount of air need

The characteristic air loss predictions show the different use of the investigated tunnel advance schemes for economization of air losses. In order to quantify the possible economizations, the total amount of air need is evaluated for the design advance scheme and the alternative methods. Obviously, alternative tunnel

advance schemes are only of interest if the costs for additional efforts are lower than the achieved cost savings by the economization of compressed air. To provide a basis for these considerations, an estimation of the costs for compressed air generation is carried out. For this purpose, costs of 1.5 Cent per m³ of air are assumed. The results are summarized in Table 6.4.

Table 6.4: Comparison of investigated advance schemes.

tunnel advance method	**max. air losses**	**total air need**	**costs per m tunnel**	**percent-age**
-	[m³/min]	[m³] · 10^6	[€]	[%]
default tunnel advance	362.5	11.68	4,866	100
extended jet grout-roof-umbrella	308.5	10.71	4,462	91.7
secondary shotcrete lining	194.0	4.61	1,920	39.4
two-staged excavation	355.0	9.04	3,765	77.4
combination of measures	111.5	2.42	1,008	20.7

The costs of compressed air generation vary between 4.866 €/m for the currently practiced tunnel advance scheme and 1.008 €/m for the alternative with a combination of measures. The extended roof-umbrella yields the lowest saving potential, and requires relatively high effort because the fabrication of additional jet grout columns at the level of the working plane is tedious.

As single measure, the secondary shotcrete lining is by far the most effective method for the economization of air losses. The spraying of the additional shotcrete layer can be carried out in a straightforward manner. A comparison between additional costs and gained savings is easily feasible. Alternatively, the spraying of the secondary shotcrete layer can be done with a reduced thickness.

The execution of the tunnel excavation in a two-staged manner allows for savings of 23 %. No additional costs for structural measures are required. However, due to the initially 12 m long ring closure distance, the stability of the tunnel advance has to be investigated for this advance scheme. With a combination of measures, the total air need can be reduced to only 20 %. However, high efforts and thus costs would be required for the realization of all of the structural measures.

6.8 Air loss prediction for bench excavation

6.8.1 General information

The excavation of the bench is planned after completion of the top-heading of the 430 m long tunnel. For stability reasons and to enable compressed air maintenance, the bench advance takes places under protection of a lateral surround of the lining, consisting of a 1 m thick jet grout body (Figure 6.4).

The advance works take place from both access points. The advance lengths are 285 m and 145 m, starting from the westward respectively eastward portal. A subdivision of the advance in different sections by means of bulk heads is not designed. The planned time duration for the bench excavation is 4.5 months. Including planned downtimes, the average advance velocity is 3.4 m/d.

An average excess air pressure of 1.15 bar inside the tunnel is required to counterbalance the groundwater pressure. Already at the beginning of the bench advance, the whole top-heading of the 430 m long tunnel is exposed to the full excess air pressure. Consequently, high air losses during the whole period of the bench excavation are to be expected.

6.8.2 Numerical model and material parameters

The air losses for the bench excavation can be divided into three different groups. Immediately after the pressure elevation from 0.32 to 1.15 bar, the air losses are exclusively determined by air flow through the shotcrete lining of the top-heading. With the proceeding bench advance, air losses additionally occur through the lining of the full cross section. This type of air losses progressively replaces the air losses solely through the lining of the top-heading. The third type of air losses consists in air escapes over the bench face.

The complete simulation of the bench excavation would require high modelling and computational effort. However, the high permeability of the ground leads to a quick steady-state of the air flow, and thus allows for a simplified approach. Corresponding to the described types of air losses, three different models are employed. For the computation of the air losses through the lining of the top-heading and the full cross section, two two-dimensional models are employed. Depending on the position of the bench advance, the obtained air losses are multiplied by the effective length of the top-heading respectively completed cross section.

A three-dimensional model is used to compute the air losses through the bench face. The cross section of this model is a combination of 2 two-dimensional models. Because of the highly permeable ground and missing bulk heads, air can flow over a long distance in longitudinal direction below the temporary top-heading invert. Finally, the air escapes through the jet grout-encapsulation of the bench. The necessary length of this model is 150 m. Details of the modelled cross sections are shown in Figure 6.20.

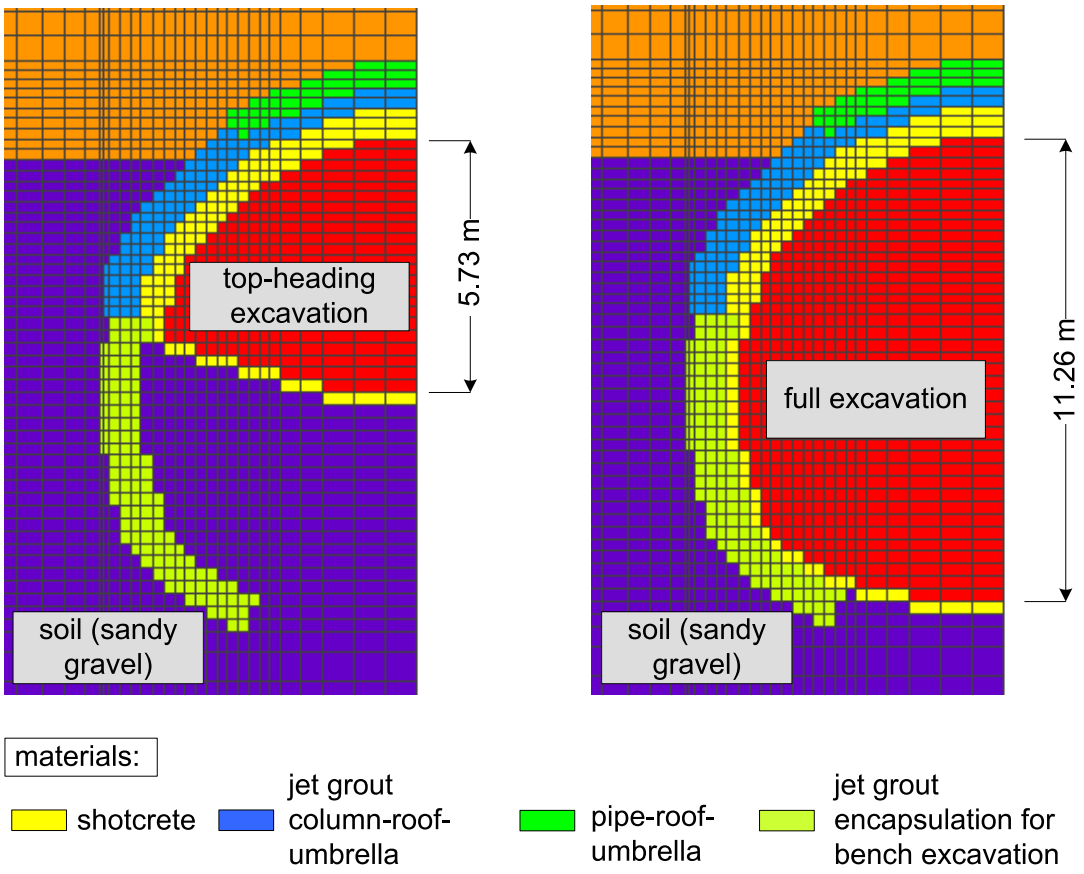

Figure 6.20: Details of modelled cross sections for bench advance.

The elaboration of appropriate air loss predictions for the bench excavation heavily depends on the quality of the jet grout encapsulation of the bench and the shotcrete. In order to take into account different scenarios, three different variants are investigated in the following. For all variants it is assumed that the secondary shotcrete lining in the angular interspaces of the sections is completed.

For the first variant, the back-analyzed permeability values of section 6.5 respectively 6.6 are employed. Furthermore it is assumed that the permeability of the jet grout encapsulation of the bench is equal to the permeability of the jet grout column-roof-umbrella of the top-heading.

The second variant takes into account a reduced permeability of the jet grout surround of the bench by 50 %. This assumption is based on the considerations that the single columns are shorter and that their parallel collocation yields fewer voids and imperfections than the 15 m long, fan-shaped columns of the roof-umbrella. The other parameters are identical with variant 1.

For variant 3 it is assumed that the permeability of the shotcrete lining of the bench and of the secondary lining of the top-heading corresponds to a value suggested by Steger and Semprich (2005). Furthermore, taking into account a careful fabrication of the encapsulation of the bench, its permeability is modelled with a ratio of 10 : 1 to the shotcrete of the bench. The employed permeability values for the different variants are summarized in Table 6.5.

Table 6.5: Intrinsic permeability values of materials for the variants 1 – 3.

material	**variant 1**	**variant 2**	**variant 3**
-	K_i [m²]	K_i [m²]	K_i [m²]
jet grout encapsulation of bench	$1.60 \cdot 10^{-12}$	$8.00 \cdot 10^{-13}$	$5.00 \cdot 10^{-13}$
shotcrete bench	$1.60 \cdot 10^{-13}$	$1.60 \cdot 10^{-13}$	$5.00 \cdot 10^{-14}$
soil (sandy gravel)	$2.09 \cdot 10^{-10}$		
pipe-roof-umbrella	$2.09 \cdot 10^{-12}$		
jet grout column-roof-umbrella	$1.60 \cdot 10^{-12}$		
shotcrete top-heading	$1.60 \cdot 10^{-13}$		

6.8.3 Air loss predictions

The computation results of the three employed numerical models are summarized in Table 6.6. For each of the three variants, the air losses per meter of top-heading and full cross section, and the air losses over the face of the bench are given.

Variant 1 yields almost identical air losses per meter of top-heading and full tunnel cross section (2.23 respectively 2.29 m³/min). Approximately 15 % lower values are computed for variant 2 (1.92 respectively 1.84 m³/min). The air losses through the bench face are 114.0 and 73.9 m³/min, respectively. The outcomes of the favourable assumptions of the permeability of the shotcrete and jet grout-

surround of the bench are significantly lower air losses of 1.33 and 1.57 m³/min, respectively. The corresponding air losses through the tunnel face are 54.3 m³/min.

Table 6.6: Air losses per meter of top-heading, full tunnel cross section and bench face.

type	**variant 1**	**variant 2**	**variant 3**
-	[m³/min]	[m³/min]	[m³/min]
per m full cross section	2.23	1.92	1.33
per m top-heading	2.29	1.84	1.57
bench face	114.0	73.9	54.3

The computation results of Table 6.6 are used to elaborate air loss predictions respectively the total air need for the bench advance. It is assumed that during excavation and installation of the invert, the bench face is covered by a shotcrete layer. Therefore, the air losses through the bench face are taken into account with 50 %, only. Air losses due to the passing of materials and personnel through the air locks are not considered. The obtained air loss predictions for the three variants are depicted in Figure 6.21.

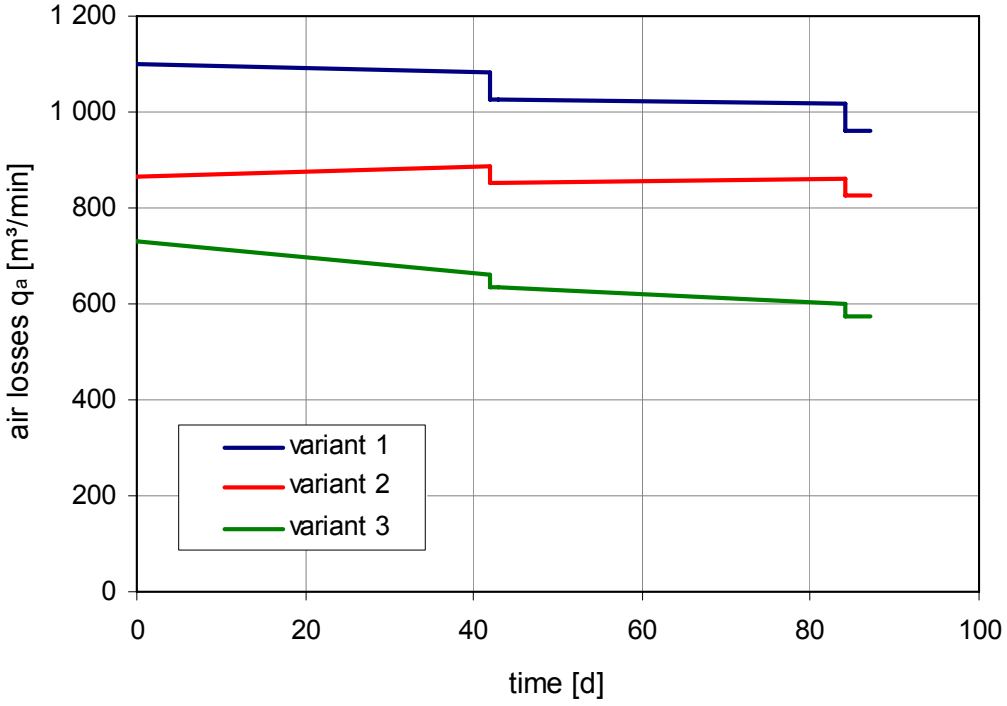

Figure 6.21: Air loss predictions for the bench advance of Tunnel Fritzens.

High air losses are predicted for all of the three investigated variants. The maximum air losses are 1099, 888 and 729 m³/min for the variants 1, 2 and 3, respectively. Depending on the variant, a slight reduction respectively increase of the air losses over the tunnel length can be seen. This is due to the gradual shifting of air losses through the lining of the top-heading to air losses through the lining of the full cross section. The characteristic jump of the graphs after 42 days is due to the termination of the bench excavation from the eastside.

For the three variants, the maximum air losses, the total air need and the estimated costs for the generation of the compressed air are summarized in Table 6.7. If the inner concrete shell is installed under compressed air use as well, the given total air need and total costs increase approximately by 30 %.

Table 6.7: Summary of air loss predictions for the bench excavation.

	max. air loss	**total air need**	**costs per m**	**total costs**
-	[m³/min]	$[m^3] \cdot 10^6$	[€]	$[€] \cdot 10^6$
variant 1	1,088.7	131.8	4,598	1.977
variant 2	888.3	108.4	3,781	1.626
variant 3	729.4	81.8	2,852	1.226

6.9 Summary and conclusions

In this section, an analysis and prediction of the air losses for the construction of the Tunnel Fritzens was carried out. The investigations focused on the analysis and interpretation of the encountered air losses during the excavation of the first 12 sections of the top-heading, and on the elaboration of appropriate measures for an economization of the air losses of the further tunnel advance. Additionally, a prediction of the air losses for the bench advance was conducted.

The investigations are based on numerical simulations of the two-phase flow of water and air, which is induced in the ground by the escaping compressed air. The program ASCATA (Steger and Semprich 2005, 2006) was employed to simulate the tunnel advance and to evaluate the according air losses. Two-dimensional and three-dimensional numerical simulations were carried out.

In a first step, the results of the numerical simulations were used to back-calculate the permeability values of the ground and of the tunnel construction materials. The numerical models were calibrated against the corrected air losses of the first twelve sections of the top-heading. The calibration was carried out manually, with a procedure based on engineering judgement and experience. The main findings of the conducted numerical simulations with the calibrated models are:

- The permeability of the shotcrete lining (K_i = 1.60 · 10^{-13} m²) of the top-heading is significantly higher than reference values given by Steger and Semprich (2005) and Scheid (2003).

- The permeability of the ground (k_w = 1.50 · 10^{-3} m/s) coincides well with the permeability values given in the tender documents.

- Significant parts of the air losses during the excavation and support works of the top-heading are in reality due to disproportionally high air losses through the shotcrete lining at the elevated excess air pressure.

- Approximately 65 % of the air losses through the tunnel face of the top-heading are due to air escapes below the bottom edge of the jet grout column-roof-umbrella.

In a second step, extended models were used to study the effectiveness of measures to reduce the magnitude of the air losses respectively total air need. Investigated alternatives were a secondary shotcrete layer in the angular interspaces of the excavation sections, an extended grout column-roof-umbrella, a two-staged excavation method and a combination of different measures. Characteristic air loss predictions were elaborated with the obtained computation results. The main findings from conducted numerical simulations with the extended models and the characteristic air loss predictions are:

- The installation of the secondary shotcrete layer in the angular spaces between two subsequent suctions is extremely effective. The total air need can be reduced to 40 %. Also, the maximum air losses are strongly reduced.

- An extended jet grout column-roof-umbrella only yields a moderate reduction of the total air need and the maximum air losses (approximately 10 % each), and is difficult to install.

- A two-staged top-heading excavation yields a 25 % lower air need at no additional costs for structural measures. However, the stability of the tunnel may be a concern here. Furthermore, only a minor reduction of the maximum air loss rate can be achieved.

- With a combination of measures, the total air need can be minimized to 20 % in comparison to the currently employed excavation method. Similarly, a significant reduction of the maximum air losses can be achieved.

Obviously, the realization of one or more of the proposed alternatives for the top-heading advance depends on the cost-benefit ratio. From this point of view, the execution of the excavation in a two-staged manner seems especially attractive if the stability of the tunnel face can be ensured. Alternatively, the proposed modifications of the design tunnel advance may be realized in parts, only. For example, the application of a thin additional shotcrete layer in combination with a slightly extended jet grout column-roof-umbrella also provides a high economization potential for the total air need and air loss rates. In any case it is recommended to increase the thickness of the primary shotcrete lining especially towards the end of the excavation sections, where an increased number of voids due to the fan-shaped collocation of the jet grout columns is to be expected.

The upcoming bench advance of the Tunnel Fritzens in terms of air losses is to be considered as critical. From the beginning of the excavation works, the whole lining of the top-heading is exposed to the elevated excess air pressure of 1.15 bar. The three investigated variants yielded air losses ranging from 729 up to 1,000 m³/min. Accordingly, total air needs ranging from 81,800,000 m³ to 131,800,000 were estimated. If a sufficiently impermeable encapsulation of the tunnel cannot be achieved, the air losses may turn uncontrollably high. Consequences like long construction delays, or in the worst case a blow out, provide serious risk potentials for the successful tunnel construction. Therefore, in addition to the installation of the secondary shotcrete lining in the top-heading, special care is recommended for the fabrication of the jet grout surround of the bench. Based on the gained knowledge from the numerical simulations, it is estimated that a flow rate of 500 m³/min represents a lower limit for the air losses during the bench advance.

A final consideration concerns the modification of the construction sequence of the tunnel. The designer prescribes the advance of the bench from both access points and a subsequent installation of the inner shell after completion of the advance works under compressed air. An alternative is the advance of the bench from one access point, only. The excavation material could be removed along the competed top-heading in direction of the second access point. The inner shell of the tunnel could be installed subsequently to the bench excavation from the first access point. Thus, the surface of the shotcrete lining which is exposed to the excess air pressured could be reduced progressively, and therewith the air losses. The adoption of the suggested alternative construction sequence would allow for a reduction of the total air need of the bench advance and the installation of the inner shell by approximately 50 – 60 %.

7 Conclusions and outlook

The main topics of the present thesis have been the development and realisation of a two-phase flow field test, the numerical investigation of steady-state unsaturated conductivity tests and triaxial tests on unsaturated soil specimen. The research has experienced a practical application in the numerical investigation of the air losses at the Tunnel Fritzens. The described topics have been treated exhaustively in individual chapters, including summary and conclusions. However, the purpose of the closing chapter is to present the state of the conducted research respectively the achieved progresses of each topic. The most important findings are highlighted. Suggestions for further developments and further research activities are made. The potential applications of the conducted research to practical problems in civil engineering are discussed.

- **A new two-phase flow field test**
  The developed test concept and the used experimental set-up proved to work well in the field. Also the measuring instrumentation and the data acquisition system showed a good performance, except for the TDR-probes. Due to the complicated installation below the groundwater level, the obtained data was not considered as qualified, particularly not for the inverse modelling. More robust instruments should be used in future field tests.

  The original idea of the field test was to conduct a preliminary water infiltration and a subsequent air injection phase. Presently, only air injection field tests into originally saturated ground below a shallow groundwater table have been carried out. In situ, the extended test procedure would only require a water supply system in addition to the existing experimental set-up. However, because of the significant hysteretic water retention behaviour of most soils, an implementation of hysteretic constitutive models would be necessary. Here, it will be a challenge to find efficient numerical algorithms.

  The inverse modelling of the conducted field tests proved to be partly unsuccessful. The suspected reasons are, for example, that the erosion of finer soil particles or an extension of the pore space occurred, which could not be captured by the employed modelling approach, occurred. It is an open issue how to deal with these complications. If such processes are to be expected in the site-specific problem too, it is indispensable to incorporate them into the modelling approach. On the other hand, if this required the introduction of additional constitutive parameters, it could make the flow parameters unidentifiable. The best solution will be to find an approach which approximately accounts for the described complications but still maintains a well-posed, identifiable inverse problem.

- **Steady-state unsaturated conductivity tests**
  The conducted numerical simulations revealed that the distribution of suction across the specimens is strongly non-linear in many cases. Accordingly, the degree of water saturation and therewith the hydraulic conductivity varies within a wide range. Since it is common to use the linear mean of suction as reference value, the described nonlinearities often result in significant misinterpretations of the unsaturated hydraulic conductivity. Particularly high errors are likely to be obtained if soils with dominating sand fraction, in which already low suction gradients result in large saturation differences across the samples, are tested.

  As a consequence, three different methods in order to ensure an improved interpretation of the hydraulic conductivity were developed respectively evaluated. Each of these methods has its particular advantage: the proposed new reference suction is very simple and does neither require additional experimental efforts nor theoretical analyses; the Smiles and Towner method is well applicable if a number of steady-state tests at the same suction value are available; and an inverse modelling of the conductivity tests is particularly recommendable if the derived flow parameters are meant for a subsequent use in numerical investigations of a practical problem.

  The conducted research on the steady-state unsaturated conductivity tests has been completed to a large extent. However, it is desirable to conduct even more parametric studies for the further validation respectively refinement of the suggested formula for the new reference suction.

- **Triaxial apparatus and triaxial tests**
  After initial problems and improvements, the triaxial testing device was successfully put into operation. The subsequent calibration tests showed the importance of a careful control of the room temperature and the necessity of correcting the volume change measurements for cell pressure changes. The initiated experimental study focused on the investigation of the effects of hydraulic hysteresis on the mechanical behaviour of fine-sandy silt. A number of six controlled-suction compression and shear tests have been completed so far.

  The experimental results of the compression tests indicated an increase of the isotropic yield stress as well as a decrease of the soil compressibility with suction. Moreover, the consolidation tests conducted on the main wetting side exhibited a larger isotropic yield stress and lower soil compressibility than their counterparts at the same suction level on the main wetting side. The obtained results of the shear tests yielded a non-linear increase of shear strength with suction. Further, it was found that the initial increase of the capillary cohesion is significantly higher than the saturated friction angle.

There was also limited experimental evidence that the shear strength at the same suction level is not affected by the degree of water saturation.

In order to validate the so far encountered experimental results, the initiated experimental study should be completed and then extended to other soil types. It will also be of interest to investigate whether or not the initial dry density and water content have a significant influence on the hydro-mechanical behaviour. In order to allow an accelerated conduction of the controlled-suction tests, the triaxial apparatus should be equipped with combined high-air entry respectively low air-entry discs.

- **Numerical simulation of air losses at the Tunnel Fritzens**
  The recorded air losses during the advance of the first 12 sections of the top-heading were used to back-calculate the permeability values of the ground, grouted ground and shotcrete. Two- and three-dimensional numerical simulations of the occurring two-phase flow of water and air were carried out for this purpose. Subsequently, different construction measures for reducing the air losses in the course of the further top-heading advance were developed and assessed.

  The conducted computations showed that the maximum air loss rate and the total air need can be significantly reduced by employing slightly enhanced tunnel advance schemes. Beyond, a low permeability of the shotcrete was found to be of major importance in this context. Finally, a prediction of the air losses respectively of the total air need for the bench advance was carried out. Here, it was shown that a modified construction sequence, which required no additional structural measures, could reduce the air need by more than 50 %.

  The completed case study has shown that the theoretical concepts of multi-phase flow can be applied successfully to civil engineering problems. In this context, an extensive understanding of the site-specific problems and interests by the engaged research institution is crucial.

It is a tradition in the Institute of Soil Mechanics and Foundation Engineering that the research activities are undertaken with the focus on subsequent applications to practical problems in civil engineering. In the present thesis the application has been limited to two-phase flow simulations at the case study Tunnel Fritzens. However, the developed field test and the triaxial tests are important contributions, which will finally yield a comprehensive framework that allows the investigation of a wide range of encountered problems in tunnelling under compressed air: air losses, surface settlements, tunnel face stability and blow-outs. The conducted research may also find a wider use in other engineering applications, e.g. geo-environmental remediation by soil venting or the bearing capacity and settlements of shallow foundations.

8 Bibliography

Akaike, H. (1973)
Information theory and an extension of the maximum likelihood principle. Proc. Int. Symp. on Information Theory, Petrov & Csaki (eds.), Akadémiai Kiadó, Budapest, 267-281.

Akaike, H. (1974)
A New Look at the Statistical Model Identification. IEEE Transactions on Automatic Control, Vol. 19, No. 6, 716–721.

Akaike, H. (1978)
Time series analysis and control through parametric models. Applied Time Series Analysis, Findley (ed.), Academic Press, New York, 1-25.

Alonso, E.; Gens, A.; Josa, A. (1990)
A constitutive model for partially saturated soils. Géotechnique, Vol. 40, No. 3, 405-430.

Alonso, E.; Yang, D.; Lloret, A.; Gens, A. (1995)
Experimental behaviour of highly expansive double-structure clay. Proc. 1st Int. Conf. Unsaturated Soils, Alonso & Delage (eds.), Balkema, Rotterdam, Vol. 1, 11-16.

Arya, L.; Leij, F.; Shouse, P.; van Genuchten, M. (1999)
Relationship between the hydraulic conductivity function and the particle size distribution. Soil Sci. Soc. Am. J., Vol. 63, 1063-1070.

Arz, P.; Schmidt, H.; Seitz, J.; Semprich, S. (1994)
Grundbau. Abschnitt B des Beton-Kalenders 1994, Teil II. Wilhelm Ernst & Sohn, Berlin, 487-729.

Bear, J. (1988)
Dynamics of Fluid in Porous Media. Elsevier, New York.

Benson C.; Gribb, M. (1997)
Measuring hydraulic conductivity in the laboratory and in the field. Unsaturated soil engineering practice, Houston & Fredlund (eds.), ASCE Geotechnical Special Publication, No. 68, 113-168.

Bishop, A. (1959)
The principle of effective stress. Teknisk Ukeblad, Vol. 106, No. 39, 859-863.

Blatz, J.; Graham, J. (2000)
A system for controlled suction in triaxial tests. Géotechnique, Vol. 50, No. 4, 465–469.

Bolzon, G.; Schrefler, B.; Zienkiewicz, O. (1996)
Elastoplastic soil constitutive laws generalized to partially saturated states. Géotechnique, Vol. 46, No. 2, 279-289.

Boso, M., Tarantino, A.; Mongiovì, L. (2005)
A direct shear box improved with the osmotic technique. Proc. Int. Symp. Advanced Experimental Unsaturated Soil Mechanics, Tarantino, Romero & Cui (eds.), Taylor & Francis, London, 85–90.

Brockwell, P.; Davis, R. (1987)
Time Series, Theory and Methods. Springer Verlag, New York.

Brooks, R.; Corey, A. (1964)
Hydraulic properties of porous medium. Hydrology Paper, No. 3, State University Fort Collins, Colorado, 1-27.

Brutsaert, W. (1967)
Some methods of calculating unsaturated permeability. Transactions of the ASAE, Vol. 10, No. 3, 400–404.

Burdine, N. (1953)
Relative permeability calculations from pore-size distribution data. Transactions of the AIME, Vol. 198, 71–77.

Burland, J.B. (1964)
Effective Stresses in Partly Saturated Soils. Correspondence to: Some Aspects of the Effective Stress in Saturated and Partly Saturated Soils, Blight and Bishop, Géotechnique, Vol. 14, No. 1, 64-68.

Burnham, K.; Anderson, D. (2002)
Model Selection and Multimodel Inference: A Practical Information-Theoretic Approach. Springer Verlag, New York.

Carrera, J.; Neumann, S. (1986)
Estimation of aquifer parameters under transient and steady state conditions. Water Resources Research, Vol. 22, No. 2, 199-242.

Chen, J.; Hopmans, J.; Grismer, M. (1999)
Parameter estimation of two-fluid capillary pressure–saturation and permeability functions. Advances in Water Resources, Vol. 22, No. 5, 479–493.

Childs, E. (1957)
The physics of land drainage. Drainage of Agricultural Lands, Agronomy Monographs VII, Luthin (ed.), American Society of Agronomy, Madison, 1–78.

Chinkulkijniwat, A. (2005)
Multiphase Flow in Unsaturated Soils and the Induced Deformation with Respect to Compressed Air Tunneling. Gruppe Geotechnik Graz, Graz University of Technology, Vol. 27.

Chinkulkijniwat, A. Semprich, S. Steger, G. (2005)
Unsaturated hydraulic properties for compressed air tunnelling by inverse modelling. Proc. XVIth Int. Conf. on soil mechanics and geotechnical engineering, Balkema, Rotterdam, Vol. 3, 1599-1602.

Chiu, C.; Ng, C. (2003)
A state-dependent elasto-plastic model for saturated and unsaturated soils. Géotechnique, Vol. 53, No. 9, 809-829.

Cooley, R.; Naff, R. (1990)
Regression modelling of ground-water flow. U.S. Geological Survey in Techniques in Water-Resources Investigations, Book 3, Chapter B4.

Corey, A. (1954)
The Interrelation between Gas and Oil Relative Permeabilities. Producers Monthly, 38-41.

Crank, J. (1964)
The Mathematics of Diffusion. Oxford University Press, Oxford.

Cui, Y.; Delage, P. (1996)
Yielding and plastic behaviour of an unsaturated compacted silt. Géotechnique, Vol. 46, No. 2, 291–312.

de Campos, T.; Carillo, C. (1995)
Direct Shear Testing on an Unsaturated Soil From Rio-De-Janeiro. Proc. 1st Int. Conf. on Unsaturated Soils (UNSAT 95), Alonso & Delage (eds.), Balkema, Rotterdam, Vol. 1, 31-38.

Delage, P.; Suraj de Silva, G. ; De Laure, E. (1987)
Un novel appareil triaxial por les sols non saturés. Proc. 9th European Conference on Soil Mechanics and Foundation Engineering, Hanrahan, Orr & Widdis (eds.), Balkema, Rotterdam, 26-28.

Delage, P.; and Graham, J. (1995)
Mechanical behaviour of unsaturated soils: Understanding the behaviour of unsaturated soils requires reliable conceptual models. Proc. 1st Int. Conf. on Unsaturated Soils (UNSAT95), Alonso & Delage (eds.), Balkema, Rotterdam, Vol. 3, 1223-1292.

Draper, R.N.; Smith, H. (1998)
Applied Regression Analysis. John Wiley and Sons, New York.

Durner, W.; Schultze, B.; Zurmühl T. (1999)
State-of-the-art in inverse modeling of inflow/outflow experiments. Proc. Int. Workshop on Characterization and Measurement of the Hydraulic Properties of Unsaturated Porous Media, van Genuchten and Leij (eds.), Riverside, California, 661–681.

Durner, W. (1994)
Hydraulic conductivity estimation for soils with heterogeneous pore structure. Water Resources Research, Vol. 30, No. 2, 211-223.

Eching, S.; Hopmans, J. (1993)
Optimization of hydraulic functions from transient outflow and soil water pressure data. Soil Sci. Soc. Am. J., Vol. 57, 1167-1175.

Eching, S.; Hopmans, J.; Wendroth, O. (1994)
Unsaturated hydraulic conductivity from transient multi-step outflow and soil water pressure data. Soil Sci. Soc. Am. J., Vol. 58, 687–695.

Escario, V. and Saez, J. (1986)
The shear strength of partly saturated soils. Géotechnique, Vol. 36, No. 3, 453-456.

Estabragh, A.; Javadi, A. (2008)
Critical state for overconsolidated unsaturated silty soil. Canadian Geotechnical Journal, Vol. 45, No. 3, 408-420.

Finsterle, S. (1999)
iTOUGH2 User's Guide. Lawrence Berkeley National Laboratory, Berkeley, California, LBNL-40040.

Finsterle, S. (2004)
Multiphase Inverse Modelling, Review and iTOUGH2 Applications. Vadose Zone Journal, Vol. 3, 747-762.

Fredlund, D.; Morgenstern, N. (1977)
Stress state variables for unsaturated soils. Geotechnical Engineering Division, ASCE, Vol. 103, No. 5, 447-466.

Fredlund D.; Morgenstern N.; Widger R. (1978)
The shear strength of unsaturated soils. Canadian Geotechnical Journal, Vol. 15, No. 3, 313-321.

Fredlund, D.; Rahardjo H.; Gan, J. (1987)
Non-linearity of strength envelope for unsaturated soils. Proc. 6th Int. Conf. Expansive Soils, Francis & Taylor, Vol. 1, 49-54.

Fredlund, D.; Rahardjo, H. (1993)
Soil Mechanics for Unsaturated Soils. John Wiley & Sons, New York.

Fredlund, D.; Vanapalli, S.; Xing, A.; Pufahl, D. (1995)
Predicting the Shear-Strength Function for Unsaturated Soils Using the Soil-Water Characteristic Curve. Proc. 1st Int. Conf. on Unsaturated Soils (UNSAT 95), Alonso & Delage (eds.), Balkema, Rotterdam, Vol. 1, 63-69.

Gallage, C.; Uchimura, T. (2006)
Effects of wetting and drying on unsaturated shear strength of silty sand under low suction. Proc. 4th Int. Conf. on Unsaturated Soils, Miller, Zapata, Houston & Fredlund (eds.), ASCE Geotechnical Special Publication, No. 147, 1247-1258.

Gallipoli, D.; Gens, A.; Sharma R.; Vaunat, J. (2003)
An elastoplastic model for unsaturated soil incorporating the effects of suction and degree of saturation on mechanical behaviour. Géotechnique, Vol. 53, No. 1, 123–135.

Gan, J.; Fredlund, D.; Rahardjo, H. (1988)
Determination of the Shear Strength Parameters of an Unsaturated Soil Using the Direct Shear Test. Canadian Geotechnical Journal, Vol. 25, No. 3, 500-510.

Gan J.; Fredlund D. (2000)
A new laboratory method for the measurement of unsaturated coefficients of permeability of soils. Proc. Int. Conf. on Unsaturated Soils for Asia, Rahardjo, Toll and Leong (eds.), Balkema, Rotterdam, 381-386.

Gardner, W. (1958)
Some steady-state solutions of the unsaturated moisture flow equation with applications to evaporation from a water table. Soil Science, Vol. 85, 228-232.

Gattermann, J.; Wittke-Gattermann, P. (2003)
Tunnel Siegaue - Interpretation des Druckluftverbrauchs und des Luft-Wasser-Strömungsfeldes. Geotechnik, Vol. 4, 244-252.

Gens, A.; Sanchez, M.; Sheng, D. (2006)
On constitutive modelling of unsaturated soils. Acta Geotechnica, Vol. 1, No. 3, 137-147.

Grant, M. (1977)
Permeability Reduction Factors at Wairakei. Proc. AICHE ASME Heat Transfer Conf., Salt Lake City, Utah, paper 77-HT-52.

Gudehus, G. (1995)
A Comprehensive Concept for Nonsaturated Granular Bodies. Proc. 1st Int. Conf. on Unsaturated Soils (UNSAT 95), Paris, Alonso & Delage (eds.), Balkema, Rotterdam, Vol. 2, 725-737.

Han, K., Rahardjo, H., Broms, B. (1995)
Effect of hysteresis on the strength of a residual soil. Proc. 1st Int. Conf. on Unsaturated Soils (UNSAT 95), Paris, Alonso & Delage (eds.), Balkema, Rotterdam, Vol. 2, 499-504.

Hilf, J. (1956)
An Investigation of Pore Water Pressure in Compacted Cohesive Soils. Ph.D.-thesis, US Bureau of Reclamation, Denver, Colorado, Technical Memo. 654.

Hill, M. (1998)
Methods and Guidelines for Effective Model Calibration. U.S. Geological Survey Water-Resource Investigations, Reston, Virginia, Report 98-4005.

Hill, M., Tiedeman, C. (2007)
Effective groundwater model calibration with analysis of sensitivities, predictions and uncertainty. Wiley and Sons, New York.

Hirscher, B. (2010)
Bestimmung der Luftdurchlässigkeit gering kohäsiver Böden für die Anwendung im Tunnelbau unter Druckluft. Master thesis, Institute of Soil Mechanics and Foundation Engineering, Graz University of Technology.

Hirschfelder, J.; Curtiss, C.; Bird, R. (1954)
Molecular Theory of Gases and Liquids. John Wiley & Sons, New York.

Hopmans, J.; Vogel, T.; Koblik, P. (1992)
X-ray tomography of soil water distribution in one-step outflow experiments. Soil Sci. Soc. Am. J., Vol. 56, 355–362.

Houlsby, G.T. (1979)
The Work Input to an Unsaturated Granular Material, Géotechnique, Vol. 47, No. 1, 193-196.

Huang, S., Fredlund, D.; Barbour, S. (1998)
Measurement of the coefficient of permeability for a deformable unsaturated soil using a triaxial Permeameter. Canadian Geotechnical Journal, Vol. 35, 426-432.

Huang, K.; Tsang, Y.; Bodvarsson, G. (1999)
Simultaneous Inversion of Air-Injection Tests in Fractured Unsaturated Tuff at Yucca Mountain. Water Resources Research, Vol. 35, No. 8, 2375–2386.

Hwang, S.; Powers, S. (2003)
Estimating unique soil hydraulic parameters for sandy media from multistep outflow experiment. Advances in Water Resources, Vol. 26, 445-456.

International Formulation Committee (1987)
A Formulation of the Thermodynamic Properties of Ordinary Water Substance. IFC Secretariat, Düsseldorf, Germany.

Iwasaki, Y. (1978)
Reassessment of the effective stress coefficient in unsaturated soils. Master of Science thesis, Kobe University, Japan.

Jackson, R. (1972)
On the calculation of hydraulic conductivity. Soil Sci. Soc. Am. J., Vol. 36, 380–383.

Jennings, J.; Burland, J. (1962)
Limitations to the use of effective stress in partly saturated soils. Géotechnique, Vol. 12, No. 2, 125-144.

Jommi C.; Di Prisco, C. (1994)
A simple theoretical approach for modelling the mechanical behaviour of unsaturated soils. Conf. Il ruolo dei fluidi nei problemi di Ingegneria geotecnica, Mondovi, Vol. 1, No. 2, 167–188.

Jommi, C. (2000)
Remarks on constitutive modelling of unsaturated soils. Experimental evidence and theoretical approaches in unsaturated soils, Proc. of Int. Workshop on unsaturated soil, Trento, Italy, Tarantino & Mancuso (eds.), Balkema, Rotterdam, 139–154.

Josa, A.; Alonso, E.; Lloret, A.; Gens, A. (1987)
Stress-strain behaviour of partially saturated soils. Proc. 9th European Conference on Soil Mechanics and Foundation Engineering, Hanrahan, Orr & Widdis (eds.), Balkema, Rotterdam, Vol. 2, 561-564.

Josa, J.; Balmaceda A.; Gens A.; Alonso, E. (1992)
An elastoplastic model for partially saturated soils exhibiting a maximum of collapse. Proc. 3rd Int. Conf. Computational Plasticity, Barcelona, Vol. 1, 815-868.

Kammerer, G. (2000)
Experimentelle Untersuchungen von Strömungsvorgängen in teilgesättigten Böden und in Spritzbetonrissen im Hinblick auf den Einsatz von Druckluft zur Wasserhaltung im Tunnelbau. Mitteilungshefte Gruppe Geotechnik Graz, Graz University of Technology, No. 8.

Kosugi, K. (1994),
Three parameter lognormal distribution model for soil water retention. Water Resources Research, Vol. 30, No. 4, 891-901.

Kramer, J.; Semprich, S. (1989)
Erfahrungen über Druckluftverbrauch bei der Spritzbetonbauweise. Taschenbuch für den Tunnelbau, Verlag Glückauf GmbH, Essen, 91-153.

Kunkel, J.; Olsen, H.; Meyer, D.; Host, L. (1995)
Comparison of Unsaturated Zone Hydraulic Properties Using a New Laboratory Testing Procedure. Water Resources at Risk, Hotchkiss, Downey, Gutentag & Moore (eds.), American Institute of Hydrology, Minneapolis, 80-88.

Laudahn, A.; Sosna, K.; Boháč, J. (2005)
A Simple Method for Air Volume Change Measurement in Triaxial Tests. Geotechnical Testing Journal, Vol. 28, No. 3, 6.

Levenberg, K. (1944)
A method for the solution of nonlinear problems in least squares. Quarterly of Applied Mathematics, Vol. 2, 164-168.

Loret, B.; Khalili, N. (2000)
A three-phase model for unsaturated soils. Int. Journal for Numerical and Analytical Methods in Geomechanics, Vol. 24, 893-927.

Lu, N.; Wayllace, A.; Carrera, J. ; Likos, W. (2006)
Constant Flow Method for Concurrently Measuring Soil-Water Characteristic Curve and Hydraulic Conductivity Function. Geotechnical Testing Journal, Vol. 29, No. 3, 230-241.

Lu, N.; Likos, W. J. (2004)
Unsaturated soil mechanics. John Wiley & Sons, New York.

Maatouk, A.; Leroueil, S.; La Rochelle, P. (1995)
Yielding and critical state of a collapsible unsaturated silty soil. Géotechnique, Vol. 45, No. 3, 465-477.

Marquart, D.W. (1963)
An Algorithm for Least-Squares Estimation of Nonlinear Parameters. SIAM Journal on Applied Mathematics, Vol. 11, No. 2, 431–441.

Matyas, E.; Radhakrishna, H. (1968)
Volume change characteristics of partially saturated soils. Géotechnique, Vol. 18, No. 4, 432-448.

Moncada, M. (2008)
Avaliação da curva de retenção e da função de permeabilidade em solos não saturados. PhD thesis, Pontifícia Universidade Católica do Rio de Janeiro.

Mualem, Y. (1976)
A New Model for Predicting the Hydraulic Conductivity of Unsaturated Porous Media. Water Resource Research, Vol. 12, No. 3, 513-522.

Nimmo, J.; Akstin, K. (1988)
Hydraulic conductivity of a saturated soil at low water content after compaction by various methods. Soil Sci. Soc. Am. J., Vol. 52, 303-310.

Nimmo, J.; Akstin K.; Mello, K. (1992)
Improved apparatus for measuring hydraulic conductivity at lower water content. Soil Sci. Soc. Am. J., Vol. 56, 1758-1761.

Nuth, M.; Laloui, L. (2008).
Effective Stress Concept in Unsaturated Soils : Clarification and Validation of an Unified Framework. Int. Journal of Numerical and Analytical Methods in Geomechanics, Vol. 32, No 771-801.

Ott, L. (1993)
An Introduction to Statistical Methods and Data Analysis. Duxbury Press, Belmont, California, 4th ed.

Poeter, E.; Hill, M.; Banta, E.; Mehl, S.; Christensen, S. (2005)
UCODE 2005 and six other computer codes for universal sensitivity analysis, calibration, and uncertainty evaluation. US Geological Survey Techniques and Methods, US Geological Survey, Reston, Virginia, Report 6-A11.

Pruess, K.; Oldenberg, C.;Moridis, G. (1999)
TOUGH2 User's Guide, Version 2.0. Earth Science Division, Ernest Orlando Lawrence Berkeley National Laboratory, LBNL – 43134.

Putz, G. (2008)
Sicherheitsmanagement auf Tunnelbaustellen. Diploma thesis, Institute of Soil Mechanics and Foundation Engineering, Graz University of Technology.

Richards, L. (1931)
Capillary Conduction of Liquids through Porous Mediums. Physics, Vol. 1, 318-333.

Romero, E.; Lloret, F.; Gens, J.; Alonso, E. (1997)
A new suction and temperature controlled triaxial apparatus. Proc. 14th Int. Conf. Soil Mechanics and Foundation Engineering, Balkema, Rotterdam, Vol. 1, 185–188.

Russell, A.; Khalili, N. (2006)
A unified bounding surface plasticity model for unsaturated soils. Int. Journal for Numerical and Analytical Methods in Geomechanics, Vol. 30, 181–212.

Sagis (2009)
Salzburger Geographisches Informationssystem.
http://www.salzburg.gv.at/landkarten.htm

Samingan, A.; Leong, E.; Rahardjo, H. (2003)
A flexible wall permeameter for measurements of water and air coefficients of permeability of residual soils. Canadian Geotechnical Journal, Vol. 40, No. 3, 559-574.

Scheid, Y. (2003)
Einfluss der Strömungsmechanik teilgesättigter Böden beim Tunnelbau unter Druckluft nach NATM, PhD-thesis, Institute of Soil Mechanics and Foundation Engineering, Graz University of Technology.

Schubert, H. (1982)
Kapillarität in porösen Feststoffsystemen. Springer Verlag, Berlin.

Schultze, B.; Ippisch, O.; Huwe, B.; Durner, W. (1999)
Dynamic non-equilibrium during unsaturated water flow. Proc. Int. Workshop on Characterization and Measurement of the Hydraulic Properties of Unsaturated Porous Media, van Genuchten and Leij (eds.), Riverside, California, 877–892.

Sharma, R. (1998)
Mechanical behaviour of unsaturated highly expansive clays. PhD thesis, University of Oxford, United Kingdom.

Sheng, D.; Sloan, S.; Gens, A. (2004)
A constitutive model for unsaturated soils: thermomechanical and algorithmic aspects. Computational Mechanics, Vol. 33, No. 6, 453–465.

Simunek, J.; van Genuchten, M. (1996)
Estimating Unsaturated Soil Hydraulic Properties from Tension Disc Infiltrometer Data by Numerical Inversion. Water Resources Research, Vol. 32, No. 9, 2683–2696.

Smiles, D.; Towner, G. (1968)
The steady-state measurement of the relation between hydraulic conductivity and moisture content in soils. Water Resources Research, Vol. 4, No. 5, 1029-1030.

Steger, G. (2004)
Implementierung der Vortriebssequenz in ein räumliches numerisches Modell eines Tunnelvortriebs unter Druckluft zur Ermittlung von Luftströmungsvorgängen. Diploma thesis, Institute of Soil Mechanics and Foundation Engineering, Graz University of Technology.

Steger, G.; Semprich, S. (2005)
Numerische Erstellung von Luftbedarfsprognosen für den Tunnelbau unter Druckluft, Geotechnik, Vol. 28, No. 4, 263-270.

Steger, G., Semprich, S. (2006)
ASCATA – a TOUGH2 based program for automated simulation of compressed air tunnel advance. Proc. TOUGH Symposium 2006, Lawrence Berkeley National Laboratory, Berkeley, California, on CD-ROM.

Steger, G., Semprich, S.; Chinkulkijniwat, A. (2006)
Recent Advances and Encountered Problems in Computing Air Losses in Compressed Air Tunnelling by Consideration of Unsaturated Soil Mechanics. Proc. International Conference on Unsaturated Soils, Miller, Zapata, Houston & Fredlund (eds.), 451-462.

Steger, G.; Vargas, E.; Semprich, S. (2007)
Design of suitable field tests for inverse modelling of unsaturated soil parameters using numerical procedures. 5th Brazilian Symp. Unsaturated Soils, Brazilian Association of Soil Mechanics and Geotechnical Engineering, Salvador, Brazil, 57-66.

Steger, G.; Semprich, S.; Moncada, M.; de Campos, T.; Vargas Jr., E. (2008)
A numerical investigation of steady-state unsaturated conductivity tests. Proc. 1st European Conf. on Unsaturated Soils: Advances in Geo-Engineering, Toll, Augarde, Gallipoli & Wheeler (eds.), CRC press/Balkema, Leiden, 747-754.

Sugiura, N. (1978)
Further analysis of the data by Akaike's information criterion and the finite corrections. Communication in Statistics, Vol. 7, No. 1, 13-26.

Terzaghi, K. (1936),
The Shear Resistance of Saturated Soils. Proc. 1st International Conference on Soil Mechanics and Foundation Engineering, Cambridge, USA., Vol. 1, 54-56.

Van Dam, J.; Sticker, J.; Droogers, P. (1992)
Inverse method for determining soil hydraulic functions from one-step outflow experiments. Soil Sci. Soc. Am. J., Vol. 56, 1042-1050.

Van Dam, J.; Stricker, J.; Droogers, P. (1994)
Inverse method to determine soil hydraulic functions from multistep outflow experiments. Soil Sci. Soc. Am. J., Vol. 58, 647-652.

Van Genuchten, M. (1980)
A closed-form equation for predicting the hydraulic conductivity of unsaturated soils. Soil Sci. Soc. Am. J., Vol. 44, 892-898.

Vargas, E. (2006)
Personal communication, December 2006, Rio de Janeiro.

Velloso, R.; Vargas Junior, E.; Castro Filho, G.; Vaz, L. (2007)
Desenvolvimentos de Procedimentos de Campo para a Determinação de Propriedades Hidráulicas de Solos Saturados-Não Saturados. Proc. XIII Congresso Brasileiro de Mecânica dos Solos e Engenharia Geotécnica, Curitiba, Brasil.

Vesselinov, V.; Neumann S. (2001)
Numerical inverse interpretation of single-hole pneumatic tests in unsaturated fractured tuff. Groundwater, Vol. 39, No. 5, 685-695.

Vesselinov, V.; Neumann, S.; Illman, W. (2001)
Three-dimensional numerical inversion of pneumatic cross-hole tests in unsaturated fractured tuff: 1, Methodology and borehole effects. Water Resources Research, Vol. 37, No. 12, 3001-3017.

Wheeler, S. (1988)
The undrained shear strength of soil containing large gas bubbles. Géotechnique, Vol. 38, No. 3, 399–413.

Wheeler S.; Gallipoli D.; Karstunen M. (2002)
Comments on use of the Barcelona Basic Model for unsaturated soils. Int. Journal for Numerical and Analytical Methods in Geomechanics, Vol. 26, No. 15, 1561 – 1571.

Wheeler S.; Karube D. (1995)
Constitutive modelling. Proc. 1st Int. Conf on Unsaturated Soils UNSAT95, Alonso & Delage (eds.), Balkema, Rotterdam, Vol. 3, 1323-1356.

Wheeler, S.; Sivakumar, V. (1995)
An elasto-plastic critical state framework for unsaturated soil. Géotechnique, Vol. 45, No. 1, 35-53.

Wheeler, S.; Sharma, R.; Buisson, M. (2003)
Coupling of hydraulic hysteresis and stress–strain behaviour in unsaturated soils. Géotechnique, Vol. 53, No. 1, 41–54.

Wösten, J.; van Genuchten, M. (1988)
Using texture and other soil properties to predict the unsaturated soil hydraulic functions. Soil Sci. Soc. Am. J., Vol. 52, 1762-1770.

Yin, J. (2003)
A Double Cell Triaxial System for Continuous Measurement of Volume Changes of an Unsaturated or Saturated Soil Specimen in Triaxial Testing. Geotechnical Testing Journal, Vol. 26, No. 3, 353-358.

Yudhbir, Y. (1982)
Collapsing behaviour of residual soils. Proc. 7th Southeast Asian Geotechnical Conference, Hong-Kong, Vol. 1, 910-930.